Laser powder bed fusion produced Ti-6Al-4V: Microstructural transformations and changes in deformation behaviour through thermal treatments

by
Gerrit Matthys Ter Haar

Dissertation presented for the degree of Doctor of Philosophy in the Faculty of Mechanical and Mechatronic Engineering at Stellenbosch University

Supervisor: Prof Thorsten Hermann Becker

December 2021

Declaration

By submitting this thesis electronically, I declare that the entirety of the work contained therein is my own, original work, that I am the sole author thereof (save to the extent explicitly otherwise stated), that reproduction and publication thereof by Stellenbosch University will not infringe any third-party rights and that I have not previously in its entirety or in part submitted it for obtaining any qualification.

This dissertation includes two original papers published in peer-reviewed journals or books, one paper under review and one unpublished paper. The development and writing of the papers (published and unpublished) were the principal responsibility of myself and, for each of the cases where this is not the case, a declaration is included in the dissertation indicating the nature and extent of the contributions of co-authors.

Date: December 2021

Abstract

The current 4th Industrial Revolution has brought about enormous potential for social-economic development in South Africa. Additive manufacturing, a key technology of the 4th Industrial Revolution, and titanium, an abundantly mined but under-developed mineral commodity, collectively inspired industrial embracing of titanium-powder additive manufacturing, and specifically, laser powder bed fusion produced Ti-6Al-4V. Manufactured part quality concerns and the limited understanding of the innovative process-structure-property interactions impede its industry acceptance. Through developing fundamental insights into interactions between the microstructure and thermal treatments, mechanical performance can be improved, tailored, and optimised. Since conventional process routes cannot be applied to additively manufactured components, novel thermal treatments need to be developed. This dissertation documents experimental research into thermal treatments of laser powder bed fusion produced Ti-6Al-4V. By developing novel insights into the material's unique metallurgical response to thermal treatments, tensile behaviour of the material is improved.

The research investigates three temperature regions for thermal treatments post-fabrication and one *in-situ* approach. Thermal treatments between 750 – 960 °C are used to develop insight into the microstructure's large-scale morphological transformation. Thermal treatments at 960 °C achieve fragmentation and grain globularisation. This is followed by quenching to attain a superior bi-modal microstructure.

Thermal treatments at temperatures below 650 °C are used to develop insight into the initial stages of martensite decomposition phase transformation and material stress relief. Microhardness and tensile properties revealed material embrittlement. Fine precipitates in the microstructure were identified using high-resolution transmission electron microscopy. Based on these findings, two theories for the cause of material embrittlement based on two possible transformation routes of the initial stages of martensite decomposition are proposed.

Mechanical properties of laser powder bed fusion produced Ti-6Al-4V depend on build orientation. Although the unique columnar-shaped and textured prior-β microstructure is identified as a probable cause of deformation anisotropy, limited insight into the cause of anisotropic deformation exists. Thermal treatments above 975 °C are used to globularise the columnar prior-β grain morphology. Microstructural anisotropy between two orientations is quantified using electron backscatter diffraction maps, and the influence of microstructure on deformation and crack initiation is studied. Insight into the deformation behaviour and the identified relation between prior-β crystallographic texture and α-lath morphological texture is used to formulate a theory of the probable cause of material deformation anisotropy.

The study lastly investigates a novel approach to thermal treatments by using high-energy process parameters to achieve *in-situ* heating. An iterative approach for part optimisation using non-default process parameters is undertaken. While findings indicate that an improved microstructural and residual stress state can be achieved, detrimental effects of part oxidation and part-edge bulging are also observed.

Beknopte samevatting

Die huidige 4de Industriële Rewolusie het enorme potensiaal vir sosiale-ekonomiese ontwikkeling in Suid-Afrika teweeggebring. Additiewe vervaardiging, 'n belangrike tegnologie van die 4de Industriële Revolusie, en titaan, 'n oorvloed ontginde, maar onderontwikkelde minerale kommoditeit, het gesamentlik die aanvaarding van titanium-poeier additiewe vervaardiging, of spesifiek laser-poeierbedfusie geproduseerde Ti-6Al-4V, geïnspireer. Bekommernisse oor die kwaliteit van vervaardigde onderdele en die beperkte begrip van die interaksies tussen die proses-struktuur-eienskap belemmer die aanvaarding daarvan deur industrie. Deur die ontwikkeling van fundamentele insigte in interaksies tussen die mikrostruktuur en termiese behandelings, kan meganiese eienskappe verbeter, aangepas en geoptimaliseer word. Aangesien konvensionele verwerkings roetes nie op additiewe vervaardigde komponente toegepas kan word nie, moet nuwe termiese behandelings ontwikkel word. Hierdie proefskrif dokumenteer eksperimentele navorsing oor termiese behandelings van laser-poeierbedfusie vervaardigde Ti-6Al-4V komponente. Deur die ontwikkeling van nuwe insigte in die unieke metallurgiese reaksie van die materiaal op termiese behandelings, word die trekgedrag van die materiaal verbeter.

Die navorsing ondersoek drie temperatuurstreke vir termiese behandeling na-vervaardiging en een *in-situ* benadering. Termiese behandelings in die temperatuurstreek 750 – 960 °C word gebruik om insig te ontwikkel in die grootskaalse morfologiese transformasie van die mikrostruktuur. Termiese behandelings by 960 °C bewerk fragmentering en bolvorming van korrels. Dit word gevolg deur te blus om 'n beter tweemodale mikrostruktuur te verkry.

Termiese behandelings onder 650 °C word gebruik om insig te ontwikkel in die aanvanklike fase van transformasie van martensietontbinding en materiële spanningsverligting. Mikrohardheid en trekkeienskappe het materiële broosheid aan die lig gebring. Fyn korrels in die mikrostruktuur is geïdentifiseer met behulp van hoë resolusie transmissie-elektronmikroskopie. Op grond van hierdie bevindinge word twee teorieë oor die oorsaak van materiële broosheid voorgestel, gebaseer op twee moontlike transformasie-roetes van die aanvanklike stadiums van martensietontbinding.

Laser-poeierbed-versmelting vervaardigde Ti-6Al-4V meganiese eienskappe hang af van die bou-oriëntasie. Alhoewel die unieke kolomvormige en tekstuur voorafgaande-β mikrostruktuur geïdentifiseer is as 'n waarskynlike oorsaak van vervormingsanisotropie, bestaan daar beperkte insig in die oorsaak van anisotropiese vervorming. Termiese behandelings bo 975 °C word gebruik om die kolomvormige morfologie van voorafgaande-β korrels te laat bolvorm. Mikrostrukturele anisotropie tussen twee oriëntasies word gekwantifiseer aan die hand van elektron-terugspreid-diffraksiekaarte, en die invloed van mikrostruktuur op vervorming en ineenstorting van die krake word bestudeer. Insig in die vervormingsgedrag en die geïdentifiseerde verband tussen voorafgaande-β kristallografiese tekstuur en α-korrel morfologiese tekstuur word gebruik om 'n teorie te formuleer oor die waarskynlike oorsaak van materiële vervorming anisotropie.

Die studie ondersoek laastens 'n nuwe benadering tot termiese behandelings deur gebruik te maak van hoë-energie prosesparameters om *in-situ* verwarming te bewerkstellig. 'n Iteratiewe benadering vir onderdeeloptimalisering met nie-standaard prosesparameters word onderneem. Alhoewel bevindinge aandui dat 'n verbeterde mikrostruktuur- en residuele spanningstoestand bereik kan word, word nadelige gevolge van oksidasie en gedeeltelike bulting ook waargeneem.

Acknowledgements

Table of contents

List of figures

List of tables

List of abbreviations

3D	Three-dimensional
4IR	Fourth Industrial Revolution
AB	As-built
ABF	Annular bright field
AC	Air cool
ADF	Annular dark field
AF	As-fabricated
AM	Additive manufacturing
AMS	Aerospace materials specification
APT	Atom probe tomography
ASTM	American standard testing method
at%	Atomic percent
bcc	body centred cubic
BSE	Backscattered electrons
CAD	Computer-aided design
CAF	Central analytical facilities
CAGR	Cumulative average growth rate
CHRTEM	Centre for high resolution transmission electron microscopy
CPAM	Collaborative program in additive manufacturing
CSIR	Centre for scientific and industrial research
DED	Direct energy deposition
DFM	Design-for-manufacturability
DfAM	Design for additive manufacturing
DSI	Department of science and innovation
EBM	Electron beam melting
EBSD	Electron backscatter diffraction
EDS	Energy-dispersive spectrograph
EELS	Electron energy loss spectroscopy
ELI	Extra low interstitial
FC	Furnace cool

FOD	Focal-offset distance
FWHM	Full-width half-maximum
GDP	Gross domestic product
HAADF	High-angle annular dark-field
hcp	hexagonal close-packed
HIP	Hot isostatic pressing
HSV	Hue-saturation-value
IPF	Inverse pole figure
KU	Katholieke Universiteit
LOM	Light optical microscopy
MAUD	Material analysis using diffraction
ppm	Parts per million
RAPDASA	Rapid product development association of South Africa
RDI	Research development and innovation
SEM	Scanning electron microscopy
SLM	Selective laser melting
SSTR	Solid solution temperature region
SU	Stellenbosch University
TEM	Transmission electron microscopy or Transverse electromagnetic
TiCoC	Titanium centre of competence
TMP	Thermomechanical processing
USGS	United states geology survey
UTS	Ultimate tensile strength
wt%	Weight percent
WQ	Water quench
XCT	X-ray computed tomography

List of symbols

d	Laser spot diameter
D	Gauge diameter
d_0	Laser-waist spot diameter
$d_{10,50,90}$	10th, 50th and 90th percentile particle diameter
E	Young's modulus
G	Magnitude of temperature field gradient of Shear modulus
h	Hatch distance
I	Maximum laser intensity
K	Twin plane
l	Layer thickness
v	Scan velocity
P	Laser power
R	Solid-liquid interface velocity
m	Schmid factor
m'	Transmissibility factor
T_0	Critical temperature
T_{diss}	Dissolution temperature
E_v	Volumetric energy density
T_β	Beta transus temperature
Z_R	Rayleigh length
α	stable alpha phase
α'	meta-stable (martensitic) alpha phase
α_1	Solute-lean intermediate phase
α_2	Ti_3Al precipitate or Solute-rich intermediate phase
α_p	Primary alpha
α_s	Secondary alpha
β	beta phase
∇***T***	Gradient of temperature field
ε_f	Elongation to failure
η	Twin direction

θ	Bragg's angle
λ	X-ray wavelength
//	Parallel
~	Approximately equal

1 Introduction

Many consider the current scale of technological advancement and industrial transformation to signify a fourth industrial revolution (4IR, also called "industry 4.0"). Key to the 4IR is technological advancements in digital and cybernetic technologies, which have paved the way for human cyber-physical integrated systems (Abubakr *et al.*, 2020). These systems allow for the interconnectivity between physical, biological, and digital spheres enabling innovative design and manufacturing approaches, such as "digital twins" and "smart factories," which are expected to fundamentally change conventional work and life, leading to societal transformation.

Additive manufacturing (AM)[1] is considered a chief invention of the fourth industrial revolution due to its reforming and perhaps disrupting impact on conventional design and manufacturing practices (Bogue, 2013; Prince, 2014; Bonneau *et al.*, 2017; Dilberoglu *et al.*, 2017). AM could, and in many cases, has already had profound geopolitical, economic, social, demographic, environmental, and security implications (Campbell *et al.*, 2011). AM is the umbrella term for historical synonyms such as rapid/additive fabrication, 3D-printing, additive processes techniques and layer manufacturing, and solid freeform fabrication.

A key indicator of AM's role in industrial transformation is its explosive market growth over the past decade. A key catalyst was the termination of ~225 key early 3D-printing patents from 2002 to 2014, of which 16 key patents related to material extrusion, powder bed fusion, and vat photopolymerization expired in 2013 – 2014 (Hornick, 2016). This meant that 3D-printing technology, which at the time was at least 20 years old, became available for wider public use.

The projected total revenue for AM products and services is approximately $15.8 billion for 2020 and $27.5 to $35.6 billion for 2024 (Forbes, 2019; Wohlers Associates, 2019). This is at a cumulative average growth rate (CAGR) of ~22 % for the period of 2019 to 2024 (BCCPublishing, 2019). This is comparable to the market growth rate of personal computers when they first became inexpensive and commercially available in the early 1970s. To put this in perspective, the growth rate of the global manufacturing industry was only ~3 % in 2019 (BCCPublishing, 2019). Global manufacturing currently contributes 30 % to the global GDP with a global market size of $12 trillion. Although AM contributes less than 1 % to the global manufacturing market (AMFG, 2020), the current growth rate of AM's adoption by industry indicates a likely increase in its global manufacturing share.

Industrial-sized AM machines used for fabrication of functional parts (as opposed to desktop-sized machines, which are predominantly used for prototyping) saw a sharp increase in AM market share from 28 % in 2013 to almost a third in 2019 (Wohlers Associates, 2013; Ernst & Young Global Limited, 2019). Since functional parts, in most cases, require high-strength materials such as metals, the demand for parts fabricated from metal has resulted in the

---

[1] Defined by ASTM F2792 Standard Terminology for AM technologies as "the process of joining material to make objects from 3D model data, usually layer upon layer, as opposed to subtractive manufacturing methodologies, such as traditional machining."

significant growth of the metal AM market. The 2018 Wohlers Report indicated a sharp rise in metal AM with 1,768 metal AM systems sold in 2017, compared to 983 systems in 2016, marking an increase of nearly 80 %. For a fifth consecutive year, the AM metal materials market saw strong growth of 41.9 % in 2017 – 2018 (Wohlers Associates, 2019).

An increase in metal AM machines manufacturers also accelerated from 97 companies in 2016 to 135 companies globally in 2017. Currently, metal AM accounts for the largest market share. A survey conducted on 582 companies in 2019 indicated that 49 % of the companies use metal. Although this is lower than the percentage of companies using polymers (72 %), metal tops the list of materials surveyed companies wish to use in their next AM build (65 %). This is a growth from 46 % in 2016 (Ernst & Young Global Limited, 2019).

Since metal is primarily used for functional parts, as opposed to prototypes, this indicates a shift in AM market from dominantly prototyping, tooling and modelling to metal manufacturing of fully functional production parts. This means that instead of AM being an additional fabrication process, as was the case when the technology was born, it is gradually replacing decades-old conventional manufacturing processes.

Leading AM adopters are in the medical and aerospace industries. For a review of AM technologies and its application in the aerospace industry, see Najmon *et al.* (2019). Aerospace was one of the earliest adopters of AM, going back as far as 1989. In 2018, aerospace represented 12 % of the total AM market. This industry accounted for 16.8 % of the 3D-printing market in 2019 and is likely to grow at one of the fastest rates in years to come (Stratview Research, 2020). In a survey of 900 companies, 78 % of aerospace companies claimed to use AM technology (Ernst & Young Global Limited, 2019). The aerospace AM market is expected to grow at a CAGR of 16.9 % over the next seven years to reach $6,717.4 million in 2027 (Stratview Research, 2020).

The AM's market growth's key driving force is the various advantages it boasts over conventional fabrication methods. Customisation/personalisation of part design, as opposed to mass-production, is a growing trend in manufacturing (Hu, 2013). Conventional manufacturing routes for part customisation, are however, expensive and time-consuming due to the specialised tooling that must be acquired and installed. The advantage of AM is that personalised part fabrication can be achieved without added tooling. This capability is critical in, for example, the medical industry where customisation of medical devices, such as bone implants, need to fit each patient's unique, organic structure precisely.

Conventional manufacturing entails multiple operation steps to achieve a final part shape with desired mechanical performance. Multiple bulk forming operations, discussed in Subsection 2.1.2, are followed by multiple material removal operations such as cutting, turning, milling, grinding and chemical machining until finally, the end-component is achieved by joining/assembly operations such as welding, brazing, soldering and mechanical fastening. Each process step requires specialised tooling, expertise, process management and labour, causing the accumulation of processes to result in an expensive and time-consuming endeavour. AM, on the other hand, eliminates many conventional process steps. Apart from the direct cost

reductions in materials and labour, this has the effect of a decentralised and democratised production.

Whereas conventionally produced parts are transported either by ground, air, or sea, AM allows for a so-called fourth form of part logistics (also called the fourth modality of logistics) (Skapinyecz *et al.*, 2018) in which parts are "transported" through the Internet in the form of computer-aided design (CAD) data. Since parts can be stored digitally, this eliminates the need to warehouse spare parts. Since manufacturing can be done on-demand, AM allows for responsive and flexible production with reduced supply chains. A part that previously required weeks of manufacturing due to multiple process steps can be manufactured in a single step on a single machine, at one location. This results in reduced manufacturing lead time and costs due to shorter transport routes.

Another key advantage of AM is its ability to fabricate complex shapes not manufacturable through traditional processes, such as internal cavities and conformal cooling channels (Jahan & El-Mounayri, 2016). This design capability is especially useful in orthopaedic and dental implantation where fine grid/lattice/scaffold/porous structures are ideal for biocompatibility (Hollander *et al.*, 2006; Stamp *et al.*, 2009; de Damborenea *et al.*, 2015; Yang *et al.*, 2017) (see Appendix B). High achievable part complexity allows for freedom of part design in which completely new part designs are possible. This means that the decades-old principles of design-for-manufacturability (DFM) are replaced by what has come to be known as design for additive manufacturing (DfAM) (Thompson *et al.*, 2016; Hanson, 2020; Leary, 2020).

Designs can be mathematically optimised, such as stiffness-and-weight topology optimisation (Panesar *et al.*, 2018), greatly improving aspects of the final part such as weight and performance. This has led to a function-driven design strategy as opposed to a manufacturing-driven design strategy (Leutenecker *et al.*, 2015). A key aspect of this capability is reducing the number of separate parts making up the final component (examples of successful commercialisation of this are provided in Appendix B).

Lastly, AM is claimed to be a long-term environmentally sustainable manufacturing route (Fraţila & Rotaru, 2017). This advantage has become particularly relevant, considering human-induced global warming (Santer *et al.*, 1996; Ramaswamy *et al.*, 2006). AM significantly reduces material waste due to its net-shape manufacturing route. Freedom of design allows for less material to be used, but the same or improved strength-to-weight ratio can be achieved due to strategic structural optimisation. Weight reduction has a primary advantage in structural application (for example, aircraft fuel consumption) and a secondary advantage in fuel reduction of down-chain processes (for example, transportation costs). Shorter product development cycles also require fewer employees, which has the effect of lowering energy consumption. For further reading on the sustainability of AM, see Ford and Despeisse (2016).

The following sections introduce the project by providing background on the South African economic and industrial landscapes, the governmental strategy for beneficiation from the 4IR and mineral resources, and the material quality concerns and knowledge gaps of metal AM. A summary of the project aims, and the outline of the dissertation concludes the chapter.

1.1 The South African economic and industrial landscapes

South Africa's industrial and socio-economic climate is key catalysts of this study. South Africa is an upper-middle-income economy and the most industrialised and diversified economy in Africa (InvestSA, 2020). In 2017, the industrial sector (comprising of mining, manufacturing, energy production and construction) contributed an estimated 29.7 % of the national gross domestic product (GDP) (Central Intelligence Agency, 2020).

Despite being the most industrialised country on the African continent, South Africa has not reaped the full benefits of the previous industrial revolution and is classified by the International Monetary Fund as a developing country (International Monetary Fund, 2018). South Africa's GDP growth was only 0.2 % in 2019. Due to a technical recession at the end of 2019, several factors, including revenue shortfalls, government debt, persistent electricity shortages and the outbreak of the COVID-19 pandemic, caused a projected growth of negative GDP growth of 8 % for 2020 (International Monetary Fund, 2020).

The project forms part of a collective research effort initiated by a governmental strategy to aid the struggling economy by focusing on three asset areas: (1) South African research, development, and innovation (RDI) capabilities, (2) an abundance of local titanium in mineral form, and (3) local market interest. These three asset areas will be discussed followed by South Africa's AM strategy in the next section.

A key aspect of South Africa's RDI capabilities is the available experience, technical knowledge and infrastructure from past, large-scale aerospace, and military projects. South Africa has an established aerospace industry with extensive experience in large military air force projects (see Appendix A.1.). However, the novelty of AM requires training of the next generation of skills and knowledge needed to benefit from AM in the 4IR successfully. Local aerospace companies, such as Aerosud, have already implemented AM for prototyping and final part production (see Appendix A.3). Furthermore, in 2017, Boeing and Airbus were reported to be considering international collaboration agreements for building parts locally, as well as metal AM development and job creation in South Africa (Clarke, 2017).

Historically, mining was the main driving force behind South Africa's developing economy. South Africa is one of the world's leading mining and mineral-processing countries and the largest producer of platinum, gold and chromium (Yager, 2015). South Africa's position in the titanium mineral market and key social-economic and techno-economic opportunities, challenges and strategies have been addressed in detail elsewhere (van Vuuren, 2009; Dworzanowski, 2013; Rokita, 2017).

According to the 2020 mineral commodity summary of the U.S. Geological Survey (USGS), South Africa is currently the second-largest producer of titanium mineral concentrate (TiO_2 – also referred to as ore, slag, or rutile), which is either extracted through carbothermal reduction of ilmenite, $FeTiO_3$ or mined directly. South Africa holds the 6th largest titanium reserve in the world, with approximately 30 % of the world's minerals used to produce the global titanium supply (de Beer et al., 2016). South Africa exports most of its titanium-bearing slag to countries

such as China and the United States (Yager, 2015). For example, America imports 36 % of its titanium from South Africa (U.S. Geological Survey, 2020).

Unfortunately, South Africa lacks the costly infrastructure in key value-chain sectors to transform the mineral to a high-valued titanium sponge and pure titanium. For example, the import cost of finished titanium parts is 100 times the raw mineral export price(de Beer *et al.*, 2016). Primary processing industry (so-called upstream industry) lacks the needed capabilities of reducing the slag to commercially pure titanium, with only 7 % of raw mineral ore being processed to final metal (Roskil, 2013). A primary reason for the underdeveloped processing infrastructure is the poor local market demand for the finished product due to lack of "downstream" beneficiation.

In recent years, the Department of Science and Innovation (DSI) has identified local market opportunities that will benefit from AM RDI based on stakeholder workshops, international trends and local capabilities (de Beer *et al.*, 2016). Opportunities were prioritised based on "attractiveness" (need, value, and potential) and "strategic fit" (capability, national objectives, and likelihood of realisation). Identified high priority opportunities included the production of medical devices and implants, the production of parts for the aerospace industry and raw material development for AM processes. Other high priority market opportunities identified were in the medical and dental industries, such as tooling, casting, refurbishment, automotive, and machine platform development. Medium priority opportunities in the small, medium and macro enterprise sectors were also identified, and include jewellery, prosthetics, audiology, archaeology, and the creative arts.

1.2 The South African AM strategy through titanium beneficiation

Positioning South Africa to exploit the advantages of the 4IR fully has become a governmental priority. At his presidential inauguration, the president of South Africa, Cyril Ramaphosa, urged the country to embrace and use the 4IR for socio-economic development:

> *Africa is poised once again to rise, to assume its place among the free and equal nations of the world. We must use that innovative talent that originated in Africa to embrace and use the Fourth Industrial Revolution to develop Africa and create jobs for the youth and empower the women of our continent.*

Subsequently, on 7 February 2019, President Cyril Ramaphosa announced the appointment of the Presidential Commission on the Fourth Industrial Revolution. The commission serves as a principal national advisory group on the 4IR to capitalise on advances brought upon by technologies in different sectors of the economy, such as AM. For the latest report of the commission published in the Government Gazette, 23 October 2020, see the Presidential Commission on the Fourth Industrial Revolution (2020). For the National Planning Commission's draft report of South Africa's readiness for the 4IR, see the National Planning Commission (2020).

South Africa imported the first AM machine in 1990 from 3D systems (de Beer *et al.*, 2016). AM has since grown in the country due to the uptake of the technology by industry. The USGS for mineral commodities further found that aerospace companies' demand for titanium continues to grow as the growth in the application of metal AM becomes more popular (U.S. Geological Servey, 2018). A commercial opportunity was therefore realised, which led the DSI, through the Council for Scientific and Industrial Research (CSIR), to establish the Titanium Centre of Competence (TiCoC) in 2009 as part of its titanium beneficiation strategy. The TiCoC is a research initiative aimed at locally developing titanium processing knowledge and skills to grow the country's manufacturing industry and economy (du Preez, 2014).

In the Department of Trade and Industry's Industrial Policy Action Plan (2014/15 – 2016/17), a key action program aimed at the titanium value-chain with the focus on downstream manufacturing (a secondary industry contributor to GDP) was formulated. The aim is to develop and prepare the "local manufacturing industry to effectively exploit the current opportunities as well as the future potential of titanium production in South Africa." (The Department of Trade and Industry, 2014). The Action Plan highlights two key economic motivations for focusing on titanium beneficiation: (1) to position South Africa as a leading supply chain within the global titanium manufacturing industry, concentrating on aerospace and defence products and innovative technologies; and (2) to increase the spill-over effects of these innovative technologies into related activities and adjacent industries such as medical, energy, automotive, chemical processing, marine, and oil-and-gas.

Two of the programmes supported within this titanium beneficiation value chain are metal powder production (primary industry) and metal AM (downstream manufacturing industry). The prior program is headed by the CSIR, while a combined university research initiative heads the latter with industrial projects by the CSIR and AeroSwift (see Appendix A).

The powder-based AM process of LPBF became the focus for research and development to stimulate the value chain and local market demand for titanium powder. According to Professor Willie du Preez, previous director of the TiCoC and a founding member of the Rapid Product Development Association of South Africa (RAPDASA), "there exists a limited insight in the ability of local metal AM technologies to consistently deliver parts that comply with the required physical and mechanical properties" (du Preez, 2014). This is also in agreement with internationally published research on LPBF-produced Ti-6Al-4V discussed in the next section.

This gap in understanding led to establishing a collaborative research project led by the Central University of Technology, titled the Collaborative Program in Additive Manufacturing (CPAM). Collaborators include the CSIR, Stellenbosch University, North-West University, Vaal University of Technology, and the University of Cape Town. This joint research program aims to develop knowledge and skills in the local metal AM industry towards the qualification of the technology for application in the aerospace and biomedical industries. For more on the DSI's strategy on developing market opportunities, AM research, development and innovation for the 2014 – 2023 period, see de Beer *et al.* (2016). This shortcoming in material performance and knowledge gaps in metal AM is discussed in more detail in the next section.

1.3 Material quality concerns and scientific knowledge gaps

This section provides scientific motivation for the study on LPBF-produced Ti-6Al-4V. Although as-fabricated (i.e., in its non-post-processed state) LPBF produced Ti-6Al-4V components can achieve a high material strength ranging from ~1100 – 1300 MPa (Yan & Yu, 2015; Liu & Shin, 2019), studies have indicated poor ductility, poor fatigue properties (Leuders *et al.*, 2013; 2014) and mechanical anisotropy (Ren *et al.*, 2019) among the most concerning quality aspects. Consequently, quality and reproducibility are still areas of development and are often referred to as the "Achilles' heel" of AM technologies. For an overview of metal AM material qualification needs, see Seifi *et al.* (2016).

LPBF-produced Ti-6Al-4V components in the AF condition do not meet the standard quality requirements for application in biomedical and aerospace industries (ASTM F136 and AS9100, respectively). Particularly, the achievable material ductility (measured as percentage elongation-to-failure) of LPBF-produced components range from 3 – 8 % (Yan & Yu, 2015; Liu & Shin, 2019). This is lower than, for example, the 10 % elongation-to-failure required of wrought Ti-6Al-4V parts for application as surgical implants (ASTM F 136 for Grade 23 and ASTM F1472 for Grade 5) and by the LPBF-specific standard ASTM F2924-14.

Furthermore, AF LPBF-produced Ti-6Al-4V does not achieve the same level of mechanical ductility, toughness and fatigue properties as its wrought-produced counterpart (Nalla *et al.*, 2002; Leuders *et al.*, 2013; Yan & Yu, 2015). In comparison, depending on the processing route, wrought-produced Ti-6Al-4V can achieve up to 19 % elongation-to-failure (see Donachie (2000: 101)).

Various structural integrity aspects are to blame for poor mechanical performance. These include poor part density, high residual stress, high surface roughness and a martensitic microstructure. Post-processing operations such as heat treatments and surface finishing are required to improve part quality.

Studies have shown that post-process heat treatments can increase the material's ductility above 10 % and improve its fatigue properties. ASTM F2924 advises thermal processing as per standard AMS 2801 or AMS H81200 (although it should be noted that these were developed for wrought-produced titanium alloys). A standard practice for post-process heat treatment of LPBF-produced metals has also recently been released (ASTM F3301).

In contrast to the long developmental history of conventionally produced Ti-6Al-4V, LPBF-produced Ti-6Al-4V is a very novel process. This is not only because the technology has only recently been invented, but more importantly, because various critical patents have only recently expired. Therefore, the development of the technology is in its preliminary stages, which causes gaps in understanding of, for example, the influence of the process (laser-and-build parameters as well as post-process thermal treatments) on structural aspects. Due to the manufacturing process' novelty, only a few published studies address these issues. Therefore, the understanding of the links between the process, structure, and mechanical properties (Figure 1.1) is limited. This makes improving, controlling and tailoring tensile properties a challenge.

Mechanical property
- Ductility
- Yield and tensile strength
- Anisotropy
- Fracture toughness
- Fatigue properties

Structure
- Density / defects
- Microstructure
- Residual stress
- Surface roughness
- Oxygen, nitrogen content

Process
In-situ
- Build parameters
Post-process
- Thermal treatments
- Hot-isostatic pressing

LINK LINK LINK
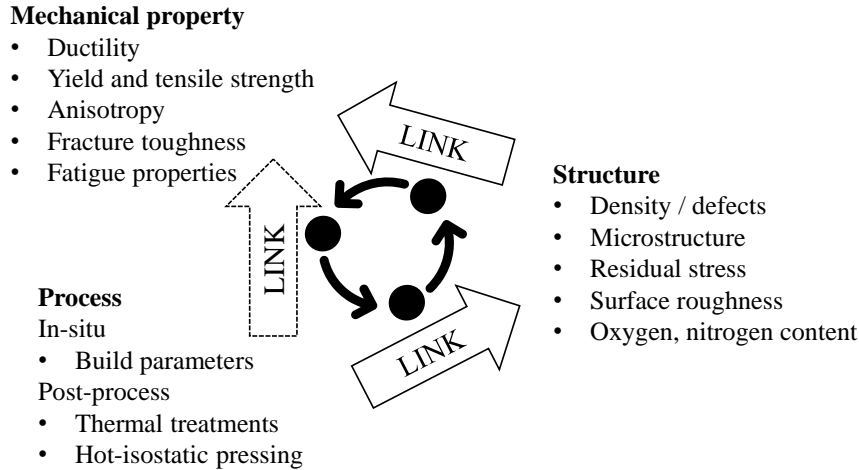
Figure 1.1. Process-structure-property interactions.

Microstructure is a key controlling aspect of the material's mechanical behaviour and, perhaps most crucially, can be tailored to improve mechanical properties. Since conventional optimised process routes that involve material deformation cannot be applied to net-shaped metal AM parts, new process operations need to be developed that rely on post-process and *in-situ* heat treatment methods alone. Due to the need to improve LPBF-produced Ti-6Al-4V's mechanical properties for industry application, and the lack of understanding in this field, this study aims to contribute to an understanding of the thermal response of microstructure and subsequent microstructural influence on tensile behaviour.

1.4 Summary of project aims

The core purpose of the project is to develop an understanding of the process-structure-property interactions of LPBF-produced Ti-6Al-4V. The project aims to develop a fundamental understanding of the thermal response of the material's microstructure and, secondly, determine the influence of resultant microstructures on deformation behaviour.

1.5 Dissertation outline

This section summarises the document's structure for readers who wish to direct their focus to specific chapters instead of a front-to-back approach.

The dissertation's core chapters that address the central project aim are Chapters 4, 5, 6, and 7. Each core chapter addresses one of the four project objectives defined in Section 3.2 and are presented in the form of self-contained journal articles that have either been submitted or published. The chapters that have been published are presented in their original (pre-revised) state. Each core chapter contains a brief overview of the literature relevant to its core objective.

Due to this formatting, only a general overview of key technical concepts is revised in the form of a background reading (Chapter 2).

Chapter 2 briefly reviews three core knowledge areas of the study and aims to provide a background to the dissertation's technical aspects. These knowledge areas are (1) titanium metallurgy, (2) metal AM, and (3) experimental techniques. In each case, specific focus is placed on their relevancy to the project's aim. Therefore, the overview of titanium metallurgy and metal AM is focused on Ti-6Al-4V, although, in most cases, concepts are generally applicable to a broader range of titanium alloys and metal AM processes.

Chapter 3 presents the development of the project's central hypotheses. This includes the motivation for the project's experimental approach, the four core research objectives with their specific aims and tasks, and the project's scope and limitations.

Chapter 4 addresses the first project objective by studying the influence of post-process heat treatments in the temperature range of 750 – 960 °C on microstructures' morphological transformation. Likely mechanisms of microstructural transformation are proposed. The study uses the insight gained from this to develop heat treatment strategies to achieve tensile properties comparable to wrought-produced Ti-6Al-4V.

Chapter 5 addresses the second project objective by studying the influence of post-process heat treatments in the temperature range below 700 °C on martensite decomposition and residual stress. X-ray diffraction is used to monitor slight changes in phase lattice parameters which are used to assess the degree of phase transformation. The study uses high-resolution transmission electron microscopy to observe the formation of nano-scale precipitates in the material. Two proposed mechanisms of martensite decomposition are presented to explain the observed microstructural changes and material embrittlement.

Chapter 6 addresses the third project objective by investigating the cause of material deformation anisotropy by using β-annealing to alter the prior-β grain morphology. Large electron backscatter diffraction maps of α' grains and reconstructed prior-β grains of two sample orientations are quantitatively characterised in terms of their morphology and texture to determine the degree of microstructural anisotropy. Material deformation is studied through grain Schmid- and transmissibility factors. Based on the findings, a mechanistic cause of material anisotropy is proposed.

Chapter 7 addresses the fourth project objective by developing process parameters that achieve *in-situ* heating of the material to decompose and relieve residual stresses during the build. Process parameters of laser hatch distance and scan speed are varied to determine the influence of laser energy density on microstructural transformation and residual stress. X-ray diffraction is used to monitor slight changes in phase lattice parameters which are used to assess the degree of phase transformation and oxygen/nitrogen pickup. Prior-β grain texture is used to estimate the solidification front angle to account for indications of columnar-to-equiaxed morphological transition.

Chapter 8 provides a discussion of key questions that remain unanswered, lessons learnt, merits and downfalls, and recommended future experimental investigations. Chapter 9 concludes the dissertation's main body of with a succinct summary of contributions made by the work in line with the research objectives.

2 Background reading

This chapter provides an overview of the metallurgy of Ti-6Al-4V, the working principles of metal AM technologies and a detailed description of LPBF. An overview of the experimental techniques and technologies applied is also provided. The chapter aims to provide the reader with a broad understanding of the technical aspects presented in the dissertation.

2.1 Ti-6Al-4V physical metallurgy

This section provides a summary of the most relevant aspects of Ti-6Al-4V's physical metallurgy. This includes the alloy's chemical composition, phase transformations, morphological and crystallographic structures, and plastic deformation behaviour. Even though the focus is on Ti-6Al-4V, most aspects of the fundamental science can also be applied to a broader spectrum of titanium and other alloys. Recent reviews (Boyer *et al.*, 1994; Leyens & Peters, 2003; Lütjering & Williams, 2007; Banerjee & Williams, 2013) provide exhaustive descriptions of the science, technology and application of titanium metallurgy. Furthermore, a summary of literature on metallurgy is available in the author's master's thesis (Ter Haar, 2017).

Originally developed in the 1950s for aircraft structural components, today Ti-6Al-4V occupies almost half of the market share of titanium products globally. Its application in aircraft-components is popular due to its numerous advantages (Boyer, 1996). Of key structural advantage is titanium's light weight. The alloy has a density of 4.43 g/cm^3 compared to 8.05 g/cm^3 of steel, making it ~56 % lighter. This allows for a reduction in fuel consumption while still achieving a high tensile strength comparable to that of steel.

While the aerospace industry still dominates Ti-6Al-4V demand, the alloy's application has also been extended to other fields such as automotive, oil-and-gas, marine, chemical, and biomedical. This is not only due to the alloy's high strength-to-weight ratio but also due to the alloy's moderate-to-high temperature corrosion resistance (315 – 400 °C) (Boyer *et al.*, 1994) and its biocompatibility. This latter advantage is most notably applied to the dental and biomedical industries. Titanium is suitable for medical bone-replacement implantation due to it being non-poisonous and biologically inert (Niinomi, 2008; Geetha *et al.*, 2009). The main disadvantage of Ti-6Al-4V is that it is expensive compared to steel due to titanium's energy-intensive mineral extraction process (called the Kroll Process, see Donachie (2000)).

2.1.1 Overview

Ti-6Al-4V is a dual-phase (α+β) titanium alloyed with 6 wt% aluminium (10.2 at%) and 4 wt% vanadium (3.6 at%). While aluminium chemically stabilises the α-phase, the vanadium concentration in the alloy allows for approximately 10 % volume of β-phase at chemically equilibrium conditions and atmospheric temperature and pressure. Due to its highly symmetric body centred cubic (bcc) lattice structure, the β-phase aids in material deformation. This is advantageous in improving the ease of material bulk-forming processing and mechanical properties such as ductility, toughness, and fatigue life.

11

The aluminium-stabilised α-phase has a hexagonal close-packed (hcp) crystal structure of space group symmetry P63/mmc (international space group no. 194). The hcp lattice structure's low symmetry aids in strengthening the material, which is advantageous for its application in structural load-bearing parts.

Figure 2.1 plots the simulation-calculated temperature-dependant α/β phase fraction and phase elemental composition diagrams of Ti-6Al-4V. Figure 2.1(a) and (b) respectively indicate that an increase in vanadium concentration lowers the temperature at which (α+β) ↔ β (called the β-transus temperature – $T_β$), while an increase in aluminium increases $T_β$. This temperature can be calculated based on the stabilising element's atomic percentage (Soundararajan Rajan *et al.*, 2020). Figure 2.1(c) indicates the relative phase fraction of α and β as a function of temperature. During a slow increase or decrease in temperature, phase transformation of α ↔ β occurs in which stabilising elements diffuse across phase boundaries.

Figure 2.1(d) and (e) depict the concentration of alloying elements in the β- and α-phase as a function of temperature, respectively. When comparing these figures, the β-phase can be seen to undergo a high elemental segregation of vanadium and titanium, while only a minor change in α composition occurs with temperature.
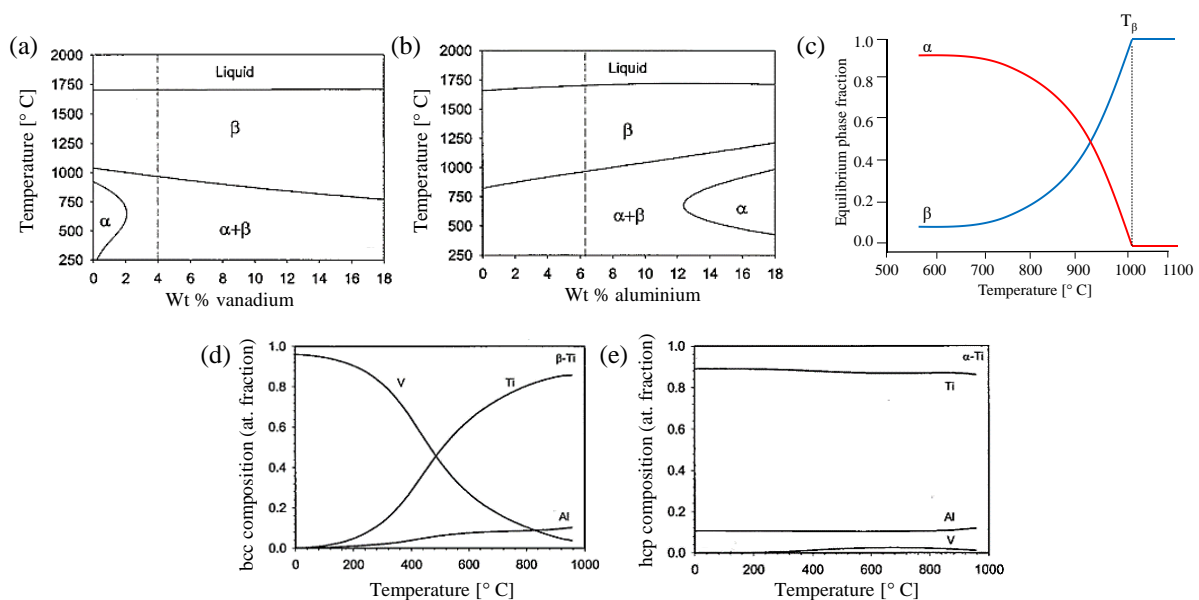
Figure 2.1. Temperature-phase diagram as a function of wt% of stabilising elements (a) vanadium and (b) aluminium (Elmer *et al.*, 2004). (c) Phase composition as a function of temperature (adapted from Kelly (2004)). Temperature-composition diagram of (d) β-phase (e) α-phase (Elmer *et al.*, 2004).

During the α↔β phase transformation, the resulting crystal structure shares an orientation relationship with the initial structure (called the "parent" structure). This has become known as the Burgers orientation relationship (BOR) (Burgers, 1934). This structural relationship

necessitates hcp and bcc structures to transform with parallel planes $\{0001\}_\alpha || \{101\}_\beta$ and parallel axis $\langle 12\bar{1}0 \rangle_\alpha || \langle 111 \rangle_\beta$. A total of 12 unique α orientation variants and 6 unique α/α misorientation angles exist for each parent β-grain orientation (Wang *et al.*, 2003), although only a number of variants are "selected" based on a number of proposed theories (Sargent *et al.*, 2012; Li, Li, *et al.*, 2016)

2.1.2 Solid-state phase transformations, conventional microstructural morphologies, textures, and mechanical properties

As mentioned, slow heating or cooling (< 20 °C/s) allows for slow solid-state atomic diffusion of alloying elements across phase boundaries. This results in equilibrium phase products, which is the focus of this section. Non-equilibrium cooling rates, on the other hand (i.e., fast cooling and heating), can result in unstable or metastable phases (such as martensite). These products are further discussed in the subsequent sections.

Equilibrium microstructural morphologies can be grouped into three categories: (1) acicular lamellar (i.e., elongated-shaped α+β "sandwiched" grains), (2) equiaxed (globular-shaped α-grains in a matrix of β-phase) and (3) bimodal microstructures—a combination of (1) and (2). While category (1) requires no mechanical processing, the latter two do require material deformation. The formation of (1) is discussed here, while the formation of microstructural morphologies (2) and (3) is discussed subsequently.

Figure 2.2(a) depicts the temperature-time-transformation (TTT) diagram for Ti-6Al-4V as modelled by Kelly (2004). Superimposed on this diagram are two cooling curves and their resultant microstructural morphologies depicted in (b) and (c). Depending on the cooling rate from above T_β, one of two distinctive acicular α+β lamellar microstructural morphologies will form.

The first is a grain boundary α morphology that nucleates and grows on the boundary of parent β-grains (called prior-β grains, PBG) together with an internal colony morphology, depicted in Figure 2.2(b). This morphology results from slow cooling rates represented by the blue cooling curve in Figure 2.2(a). Sketches of microstructural transformation at various temperature points indicate the formation of (i) grain boundary α at elevated temperatures followed by (ii) α+β lamellar colonies at lower temperatures. Colony size and lath width are determined by the rate of cooling, with slower cooling favouring larger structures.

The red cooling line represents intermediate cooling rates (such as air cooling). This results in a finer acicular "basketweave," also called Widmanstätten-patterned morphology, as depicted in Figure 2.2(c). Faster cooling rates facilitate finer lath structures. If the cooling rate is approximately > 410 °C/s, represented by the black broken line, a non-diffusive phase transformation occurs, resulting in a metastable martensitic phase.
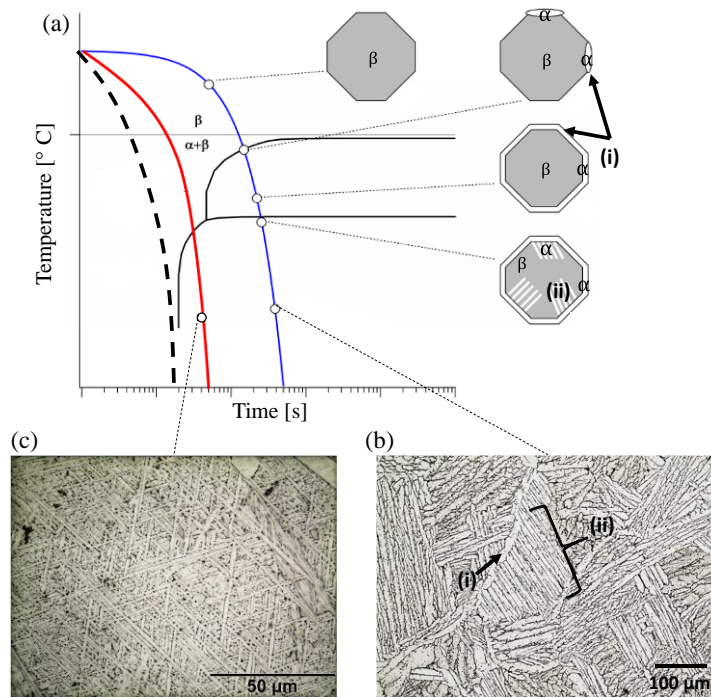
Figure 2.2. (a) TTT diagram of allotropic-structure nose and basketweave-structure nose (Kelly, 2004) with two cooling curves resulting in a (b) typical colony microstructure and (c) typical basketweave/Widmanstätten microstructure. (i) Grain boundary α and (ii) α+β lamellar colony.

The following section discusses the formation of equiaxed and bimodal microstructures. Most conventionally produced metal end-components are fabricated from a starting metal ingot. During the last step of titanium ingot production, the poor thermal conductivity of the material causes slow cooling rates and, therefore, extremely large grain sizes.

The first step in conventional part fabrication is bulk-forming operations such as rolling, extrusion, forging, drawing, and bending. Thermomechanical processing (TMP) entails extensive deformation processing above and below T_β (termed 'ingot breakdown') to refine the ingot's coarse as-cast grain size (Waziers *et al.*, 2009). TMP tailors both the alloy's microstructural morphology and crystallography. A range of microstructure morphologies and textures can be achieved depending on the TMP temperature, holding time, strain rate and intensity, number of process cycles and cooling rates. The TMP of Ti-6Al-4V has been researched and developed extensively (Lütjering, 1998; Weiss & Semiatin, 1999; Ding *et al.*, 2002; Motyka *et al.*, 2012). For a guide to conventional post-process heat treatments, see standard AMS H81200D (SAE International, 2014).

TMP usually consists of four process operations—homogenisation, plastic working, recrystallisation and stress relief, Figure 2.3(a). Each process step has a specific influence on microstructural morphology (Figure 2.3(c)). Operation 1 entails heat-treating above T_β to

14

homogenise the prior-β grain size. This is followed by slow cooling to achieve a lamellar microstructure.

Operation 2 plastically deforms the material by forging or rolling at elevated temperatures either above or below the β-transus. Working-temperature, deformation percentage and direction determine the resultant microstructural morphology and crystal texture. The aim of this step is to fragment the longitudinal α-grains, Figure 2.3(b), with stress-induced dislocations serving as nucleation sites for β-phase in the next heating process step.

Operation 3 entails annealing in the range of 700 °C – T_β. This step causes the dissolution of fine α-grains and nucleation of β-phase at previously induced dislocations which results in the globularisation of fragmented α-laths. Furnace cooling results in an equiaxed (i.e., globular) microstructure (Figure 2.3(d)).

To obtain a bi-modal microstructure, Figure 2.3(e), the sample is cooled at an intermediate-to-fast rate (such as quenching) from ~850 – 920 °C, which causes martensite to form between the globular α-grains. The martensite is usually decomposed into lamellar (α+β) in a subsequent heating step. Area fraction of globular α (called primary α or α_p) to lamellar (α+β) (called secondary α or α_s, + β) structure is controlled by the starting temperature of intermediate-to-fast cooling. The ratio α_p to α_s influences the strength versus ductility ratio and other mechanical properties of the resultant material.

Operation 4 is usually applied to quenched microstructures to serve as a "stress relief" (also called ageing) or to decompose the martensite into an α+β lamellar structure. This is usually done at a temperature below 700 °C.

The advantage and disadvantage of microstructural morphologies have been identified and are listed in Figure 2.4. Although a detailed discussion of these is outside the scope of this Subsection, the reader is encouraged to consult Chapter 12 of Donachie (2000) for further reading.
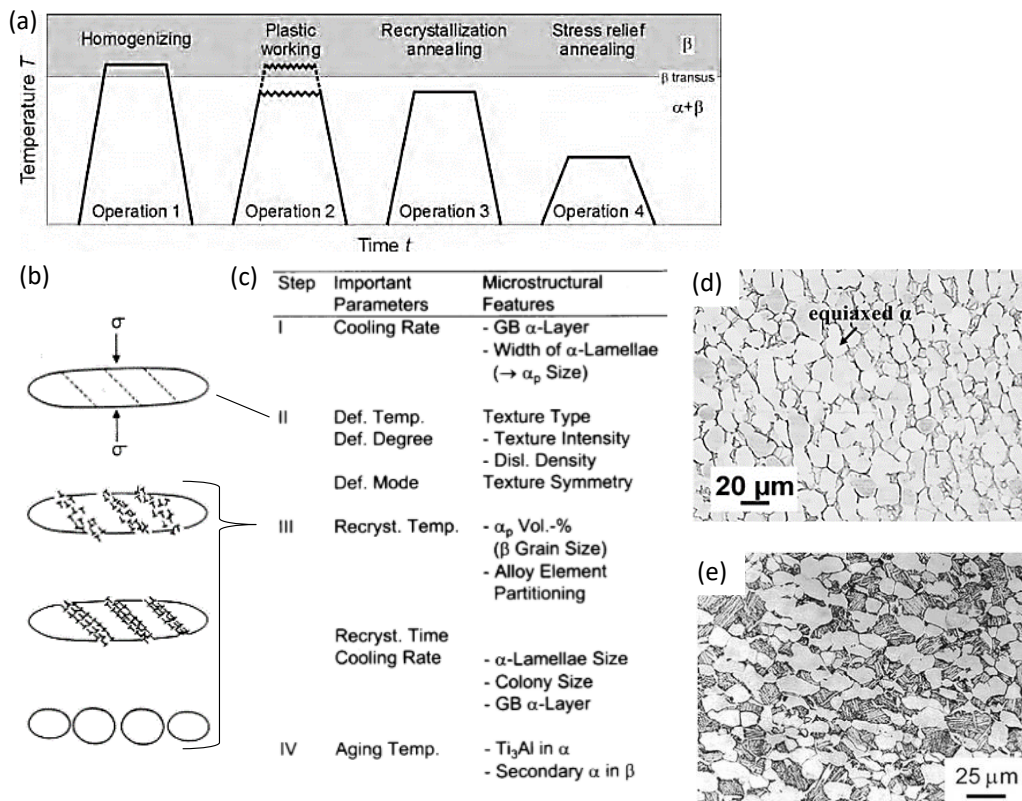
Figure 2.3. (a) TMP process operation, (b) schematic of lath fragmentation (Seshacharyulu *et al.*, 2000). (c) Summary of operation steps and their respective resultant microstructural features resulting in (d) typical equiaxed and (e) bi-modal microstructures (Liu & Shin, 2019).

	Strength	Ductility	Fracture Toughness	Crack initation	Crack propagation
	(UTS)	(ϵ_{frac})	(K_{IC})	(HCF)	(HCF+LCF)
Fine	+	+	-	+	-
Coarse	-	-	+	-	+
Lamellar	-	-	+	-	+
Equiaxed	+	+	-	+	-
Widmanstätten α	-	-	+	-	+
Colony α	-	-	+	-	+
Secondary α	+	+	-	+	-
GBα		-	+	-	+

Figure 2.4. Advantages (+) and disadvantages (-) of morphological structures for mechanical properties (Brandl, 2010).

As a result of preferential slip systems being activated during material deformation, crystallographic texture related to the direction of deformation is achieved. Figure 2.5 depicts four typical α crystallographic textures from rolling and forging operations at four different temperatures. Due to the elastic and deformation anisotropic of the hcp lattice (Tromans, 2011; Hémery *et al.*, 2020), crystallographic texture is an effective technique to tailor and improve mechanical properties.
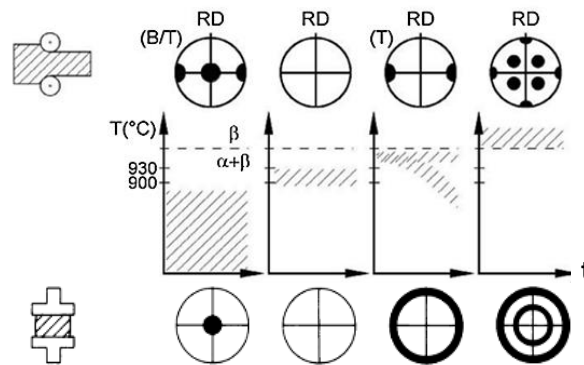
Figure 2.5. Four typical hcp crystallographic textures achieved through rolling and forging at four different temperature regions (Lütjering & Williams, 2007). Texture represented by {0001}$_α$ pole figures (see Subsection 2.5.7) (RD—roll direction, B—basal texture, T—transverse texture).

2.1.3   Crystal elastic anisotropy and plastic deformation modes

The titanium hcp lattice is elastically highly anisotropic with both the Young's modulus (E) and shear modulus (G) varying with load-angle from the lattice's [0001] axis (Tromans, 2011). Plastic deformation behaviour is also dependant on the lattice orientation. For an extensive technical overview of the latest findings of microplasticity in Ti-6Al-4V, see Hémery *et al.* (2020) and Sandala (2012).

The activation of slip depends on two factors: the slip system's critical resolved shear stress (CRSS) and the Schmid factor (*m*). Slip is initiated when the resolved shear stress (τ) (the in-plane component of the applied stress) equals the slip system's CRSS. The resolve shear stress is determined by multiplying the Schmid factor ($m = cos\theta \cdot cos\lambda$) with the applied shear stress, σ. This is schematically depicted in Figure 2.6(a).

Table 2.1 tabulates the slip and twinning deformation systems of the hcp lattice of titanium. Basal and prismatic hcp slip systems are the most common deformation systems due to their lower CRSS. Basal slip CRSS has been reported as 442 MPa, while the prismatic slip is slightly lower at 349 MPa (Habraken *et al.*, 2013). Slip systems of pyramidal-type $\langle c + a \rangle$, both 1st order and 2nd order, are typically 1.1 to 15 times higher than the CRSS for prismatic-$\langle a \rangle$ systems (Mayeur & McDowell, 2007). Twinning is also a deformation route of titanium alloys. The

17

tension type I twinning system is frequently observed in as-fabricated metal AM (Kazantseva *et al.*, 2018; Zhong *et al.*, 2018).

The β-phase bcc lattice has a higher crystal symmetry with a total of 48 slip systems along axis directions ⟨111⟩ and planes {101}. This phase also has a twin plane and direction of {112} and ⟨111⟩.

Since grain boundaries inhibit slip mobility, the ease of crystal slip transfer across grain boundaries is a key structural mechanism influencing material deformation and mechanical properties. Various approaches to quantify slip transmissibility across grain boundaries in metals have been developed. For an overview of these methods, see Bayerschen *et al.* (2016).
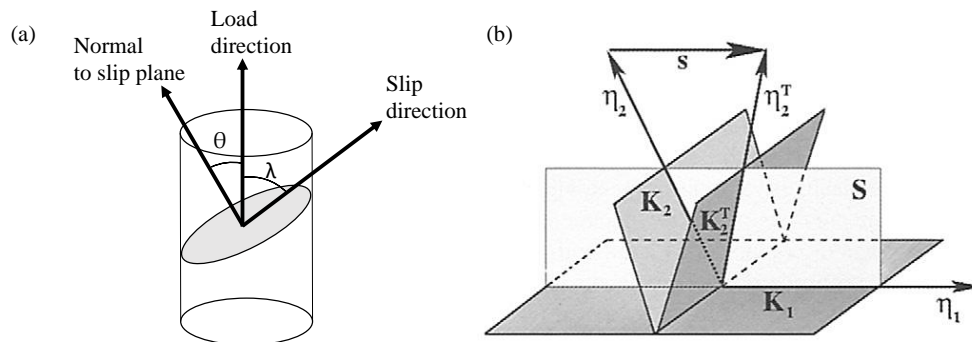
Figure 2.6. (a) Components of Schmid's law: θ – angle between slip normal and load; λ – angle between slip direction and load direction, (b) components of twinning: K_1, K_2 – undeformed twinning planes K_2^T – deformed plane ; η_1 – twinning shear direction; η_2 η_2^T – the reciprocal or conjugate twinning direction lying in K_2 and K_2^T respectively, S – the plane of shear; s – the magnitude of shear (Niewczas, 2007).

Table 2.1. Slip and twinning systems in α-titanium (Hémery *et al.*, 2020).

Slip mode	Slip direction	Slip plane	No. of slip systems
$\vec{a}$ (basal)	$\langle 11\bar{2}0 \rangle$	$\{0001\}$	3
$\vec{a}$ (prismatic)	$\langle 11\bar{2}0 \rangle$	$\{10\bar{1}0\}$	3
$\vec{a}$ (pyramidal)	$\langle 11\bar{2}0 \rangle$	$\{10\bar{1}1\}$	6
$\vec{c} + \vec{a}$ (pyramidal 1st order)	$\langle 11\bar{2}3 \rangle$	$\{10\bar{1}1\}$	12
$\vec{c} + \vec{a}$ (pyramidal 2nd order)	$\langle 11\bar{2}3 \rangle$	$\{11\bar{2}2\}$	6
Twinning mode	**Twin planes (κ_1) and (κ_2)**	**Twinning shear direction (η_1)**	**κ_1 - κ_2 angle, rotational axis**
Tensile Type I	$\{10\bar{1}2\}\{10\bar{1}2\}$	$\langle \bar{1}011 \rangle$	85° $\langle 11\bar{2}0 \rangle$
Tensile Type II	$\{11\bar{2}1\}\{0002\}$	$\langle \bar{1}\bar{1}26 \rangle$	35° $\langle 1\bar{1}00 \rangle$
Compression	$\{11\bar{2}2\}\{11\bar{2}\bar{4}\}$	$\langle 11\bar{2}\bar{3} \rangle$	65° $\langle \bar{1}100 \rangle$

2.2 Metastable phases, structures, and transformations

A broad range of unstable and metastable phases are known to form in titanium alloys. These phases form either due to (1) fast temperature changes that do not allow for the slow atomic diffusion to achieve an equilibrium chemical composition or, (2) subjecting the material to high stresses during deformation. Since their phase stability greatly influences these phases' formation, the chemical composition is the key determining factor in most cases.

2.2.1 Martensite α' and α''

The most common metastable phases of Ti-6Al-4V are the martensitic phases, α' and α''. The definition of martensite is ambiguous because it is more a description of the morphology than the chemical or crystal structure, and thus, can be somewhat subjective. Technically, α' is a phase that forms during fast cooling (> 410 °C/s) from above a critical temperature (T_0 = ~872 °C) to below the martensitic start temperature (M_s) (Ji *et al.*, 2016). Lattice parameters are approximately: 'a' = 0.293 nm and 'c' = 0.684 nm, with a 'c/a' of ~1.58. This is slightly lower than that of stable α, which has a 'c/a' ratio of 1.59 to 1.6 (Xu *et al.*, 2017). The martensitic start temperature has been calculated as 575 °C (Ahmed & Rack, 1998). However, upon cooling, M_s can reach much higher temperatures (up to ~800 °C) than its isothermally calculated counterpart, according to existing experimental observations and continuous cooling temperature diagrams. (Kelly, 2004; Ji *et al.*, 2016; Sallica-Leva *et al.*, 2016). Additionally, depending on the cooling rate, the critical temperature T_0 is also expected to shift. This temperature has been calculated based on a thermodynamic database by Lu *et al.* (2016) and Ji *et al.* (2016), who respectively found T_0 to be 893 °C and 872 °C. The phase forms through a shearing mechanism followed by nonthermal nucleation. For a technical description of the phenomenological theory of martensitic transformations, see Wang *et al.* (2003).

α' is characterised by a hierarchical structure that forms with thin needle-shaped grains in a "basketweave" structure, Figure 2.7. This phase obeys the BOR and has been observed to form habitually along $\{334\}_\beta$ and $\{344\}_\beta$ planes (Gaunt & Christian, 1959; Klostermann, 1972) according to five self-accommodation misorientation axis/angle types (Wang *et al.*, 2003).

Excessive twinning has been observed to occur in as-fabricated material. For an in-depth study on twinning of LPBF-produced Ti-6Al-4V see Zhong *et al.* (2018). A less common "massive transformation" of α' has also been observed in which large martensitic phase forms when theoretically fast-cooled from 800 – 893 °C (Lu *et al.*, 2016).
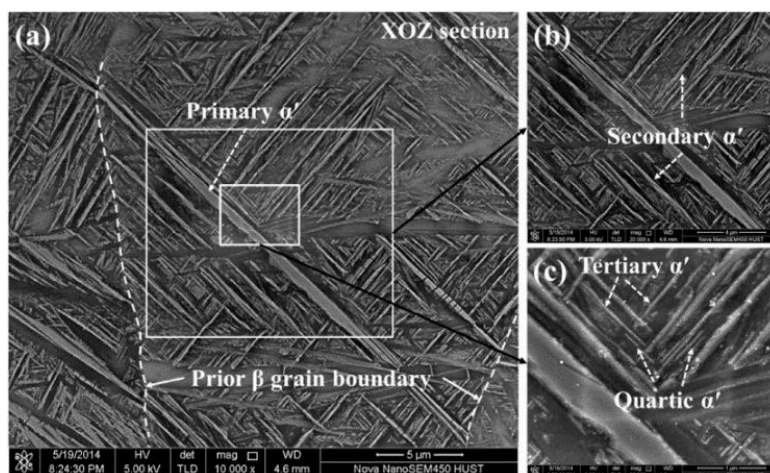
Figure 2.7. Hierarchical structure of α' according to lath size (Yang, Yu *et al.*, 2016).

A less common martensitic phase is the orthorhombic-structured α''. This phase has a base-centred orthorhombic structure, which has a space group of 'Cmcm' and lattice parameters of 'a' = 0.3152 nm, 'b' = 0.4854 nm, and 'c' = 0.4642 nm, although lattice parameters can vary with alloy composition (Kazantseva *et al.*, 2018). For a detail characterisation and description of the formation of α'' in LPBF-produced Ti-6Al-4V, see Kazantseva *et al.* (2018), Murr *et al.* (2009), and in conventional produced Ti-6Al-4V, see Lee & Welsch (1990).

In addition to the formation from fast cooling, α'' can also form athermally (i.e., stress-induced). The phase causes the softening of the material, which reduces yield stress, tensile strength, and Young's modulus. The latter has been reported as ~105 GPa (Vilaro *et al.*, 2011). The phase has been reported to form through hydrogen-induced phase transformations in EBM (Pushilina *et al.*, 2018) and is often observed in regions enriched with β-stabilizing elements (Kazantseva *et al.*, 2018). Since the phase is challenging to reveal under TEM, the best technique to identify this phase is through selected area transmission electron diffraction patterns.

2.2.2 Titanium aluminide (α$_2$)

Ti$_3$Al (α$_2$) precipitates have been found to form in near-α Ti-alloys and are known to cause an increase in material embrittlement (Zhang & Li, 2003; Jia, 2016; Radecka *et al.*, 2016; Bagot *et al.*, 2018). The precipitate has a D0$_{19}$ superstructure and forms in a cluster formation both internal to α-grains and at grain boundaries and dislocations (Zhang & Li, 2003; Karkina & Yakovenkova, 2012). Lattice parameters measured from XRD are 'a' = 0.289 nm and 'c' =

0.464 (Radchenko *et al.*, 2008). The phase is difficult to observe using SEM due to its fine structure. Figure 2.8(c) depicts α_2 particles that have been grown over 576 hours and are therefore easier to observe using SEM. This phase is also not easily observed using conventional XRD due to overlapping peaks and fine scale. Some studies have used a high energy X-ray diffraction approach via a synchrotron source to identify the phase (Haubrich *et al.*, 2019). The best technique to identify this phase, like α'', is selected area transmission electron diffraction patterns. This phase is commonly observed through superlattice reflections in the $[2\bar{1}\bar{1}0]$ or $[0\bar{1}\bar{1}0]$ directions, which produces α_2 atomic positions between hcp positions (Karkina & Yakovenkova, 2012).

The solvus temperature of α_2 in Ti-6Al-4V has been reported as 550 °C (Carreon *et al.*, 2014), 622 °C (Ji *et al.*, 2016), and 650 °C (Zhang & Li, 2003). Figure 2.8(a) depicts the influence of vanadium on the phase stability of α_2, of which the dissolution solvus temperature increases with an increase in vanadium concentration.

Oxygen promotes the formation of ordered phase α_2 (Bagot *et al.*, 2018) due to it causing a decrease in α's uptake of aluminium. Studies have reported α_2 in cases where the material's oxygen content is relatively high (~0.2 wt%) (Welsch *et al.*, 1977). Jia (2016) found evidence of the presence of α_2 particles at oxygen concentrations as low as 1200 ppm in LPBF-produced Ti-6Al-4V. In a study by Thijs *et al.* (2010), dark-etched layers in the ZX/ZY plane of LPBF-produced microstructure is attributed to the formation of α_2.
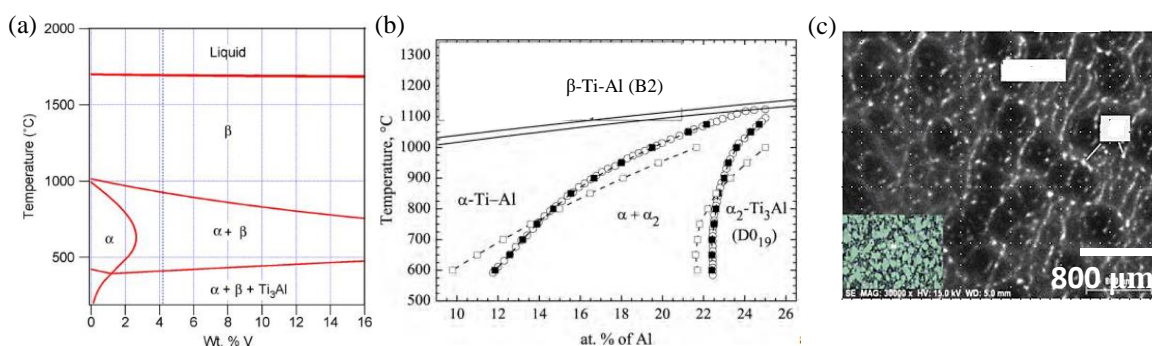
Figure 2.8. Temperature-phase diagrams of α_2 for (a) Ti-6Al-4V for varying vanadium (Elmer *et al.*, 2005) and (b) Ti-Al phase diagram with varying aluminium (Radchenko *et al.*, 2008), (c) bright α_2 particles image after a 576 hour anneal at 575 °C (Carreon *et al.*, 2014).

2.2.3   Less common metastable phases

Phases ω and β' form in Ti-alloys with much higher β-stabilising concentrations (i.e., near-β titanium alloys) and are therefore extremely uncommon in near-α Ti-6Al-4V. However, ω and β' can form under certain conditions. For example, with elemental additions such as hydrogen, oxygen, nitrogen (Pushilina *et al.*, 2018) and iron (Narayana *et al.*, 2019). Thermal undercooling (rapid solidification) has also shown to cause these phases' formation (Fan & Miodownik, 1994).

2.3 Overview of metal additive manufacturing technologies

Although a broad range of AM technologies with application in almost all industries exist today (Shahrubudin *et al.*, 2019), its application and sophistication in the 1980s were elementary (Wohlers & Gornet, 2014; Capucine Lonjon, 2017). The first commercially successful application of AM was in the fabrication of pre-production prototypes or "touch-and-feel" models (called rapid prototyping) purposed to support the design process, such as medical implant visualisation, architectural models, and other consumer goods. As the technology improved, it was applied to an increasingly broader range of applications such as in tooling and casting processes (called rapid tooling and rapid casting, respectively). Ultimately, the technology improved to be capable of fabricating end-use, functional parts.

Today, a general distinction is made between "3D printing" and "additive manufacturing." The former is associated with the fabrication of components using low capacity, low-cost "desktop" machines (segmented by the market below $5,000) using low-cost materials such as plastics. Application examples include educational, fashion and jewellery, dental, food, and others (Grand View Research, 2018).

On the other hand, additive manufacturing is associated with large industrial-sized, high-end, expensive (segmented by the market above $5,000), high-precision machines. Industrial machines are predominantly used to fabricate end-use, full functional components using expensive materials such as metals. Application examples include automotive, aerospace and defence, healthcare, consumer electronics, industrial, power-and-energy, and others (Grand View Research, 2018).

ISO/ASTM 52900:2015 defines seven process classifications for additive manufacturing: Binder Jetting, Directed Energy Deposition, Material Extrusion, Material Jetting, Powder Bed Fusion, Sheet Lamination, and Vat Photopolymerization. While the basic principles of layer-wise additive fabrication from computer-aided design (CAD) models remain the same, metal AM can be categorised into groups based on energy source (laser beam, electron beam or arc), feedstock state (powder, wire or sheet), or method of material feed (blown/fed powder or powder bed) (Liu *et al.*, 2017). Of the seven ASTM classified AM groupings, four are currently applied to metal powders. Two are considered indirect fabrication routes, binder jetting and material extrusion, and two are considered direct fabrication routes, direct energy deposition and powder bed fusion (Sames *et al.*, 2016). The following overview of metal additive manufacturing technologies is based on work by Zhang *et al.* (2017) and Sames *et al.* (2016).

Indirect methods use a relatively inexpensive process to fabricate a "green" part, after which several critical post-process operations densify and improve the material properties. While the fabrication of the green part is faster than other powder-based AM processes, extensive post-processing is required, which takes up most of the fabrication time. A major advantage of indirect methods is their affordability, production speed of the green part, and lower operation safety concerns.

In recent years, binder jetting has grown to become the most popular indirect metal AM technology. This method's working principle consists of bonding powder in a layer-wise

fashion through precisely jetting a polymer-based binding agent to form a green part. The binding medium is then either removed through ultra-violet radiation or during a sintering process.

An even more cost-effective indirect method is material extrusion (also referred to as bound powder extrusion), in which extruded bound metal rods—metal powder held together by wax and polymer binders—are bonded in a layer-wise fashion to form the green part ("Desktop Metal[TM]", 2020). The part is immersed in a de-binder fluid, dissolving the binder, and the resultant green part is then sintered at 0.7 – 0.9 of the metal's melting temperature to improve densification. The achievable final part density is reported up to 98 % by companies such as Desktop Metal ("Desktop Metal[TM]", 2020). Other post-processes that can be applied to improve density include liquid metal infiltration or hot isostatic pressing.

The main disadvantage of indirect metal AM fabrication is the resultant large and inconsistent internal part defects. The resulting effect of this on mechanical properties makes the parts unsuitable for application as functional load-bearing components. A common application of indirect metal AM is in rapid casting, in which the patterns, cores, and moulds can be fabricated much faster than conventional routes.

For metals to achieve consistent and high dimensional accuracy, high density, and adequate mechanical properties, direct metal AM is typically used instead of the indirect approach. Direct metal AM methods are more popular based on the volume of recent research, development and market growth (Liu *et al.*, 2017). For a brief overview of the history of direct metal AM, its development, and the latest technologies, see Hanson (2020). As mentioned, two direct powder-based metal AM routes are currently recognised by ASTM: direct energy deposition (DED) and powder bed fusion (PBF).

DED functions with either a laser, electron beam or arc as the energy source and the material is either wire-fed or powder-fed. DED is also commonly referred to as laser cladding, laser metal deposition, laser engineering net-shaping, direct metal deposition, direct laser deposition, electron beam free-form/additive manufacturing, and wire-and-arc additive manufacturing (Dutta & (Sam) Froes, 2015). In DED, material is deposited either through pressured powder injection or wire feed to the focus point of the heat source. DED processes are typically used for surface coating and repairing parts where material is missing due to wear or damage.

The direct metal AM method of powder bed fusion (PBF) operates with either a laser, electron, or arc source. PBF is also commonly referred to as direct metal laser schmelzen, selective laser melting and selective laser sintering (Dutta & (Sam) Froes, 2015). PBF process, developed and patented by the Fraunhofer Society in 1995 – 1996 (Meiners *et al.*, 1996), fabricates parts by irradiating pre-selected powder on a powder bed, fusing neighbouring tracks to solidify a layer. Detailed description and discussion of LPBF are provided in the next section.

PBF, in contrast to DED, is overwhelmingly used for manufacturing full-sized functional parts and is, therefore, the closest direct alternative to traditional manufacturing in terms of its industrial application. The most popular metal AM method is LPBF. This method's popularity

is largely due to its comparative higher dimensional accuracy, lower machine costs and shorter build times.

Electron beam melting (EBM) is the closest comparable metal AM method to LPBF. EBM is performed in a high-vacuum, below 10^{-4} mbar, providing an ideal low-contamination environment for the manufacturing of materials with a high affinity for reacting with oxygen and nitrogen, such as Ti-6Al-4V. Additionally, EBM generates a faster build rate than DED and LPBF due to its higher energy input and faster scan laser speed. Parts are usually built on a high-temperature built-plate (600 – 750 °C), which leads to the formation of stable α+β in Ti-6Al-4V parts (Tammas-Williams *et al.*, 2015). The shortcoming of electron beam melting is its inferior surface quality and high cost compared to LPBF. For an in-depth study of EBM applied to Ti-6Al-4V, see Tan *et al.* (2015).

2.4 Laser powder bed fusion

This section discusses the working principles of LPBF in further detail. An overview of current understandings of the influence of the LPBF process and post-processes on the material's structure is discussed. For a brief overview of the process, microstructure and economics of titanium AM, see Dutta and Froes (2015). For a comprehensive technical review of the metal additive manufacturing process, structure and properties, see Sames *et al.* (2016), DebRoy *et al.* (2018) and specifically Ti-6Al-4V see Liu & Shin (2019).

Even though LPBF of commercially pure Ti and Ti-6Al-4V are the focus materials of most studies, other Ti-alloys such as Ti-6Al-7Nb, Ti-Nb, Ti-5Al-5V-5Mo-3Cr, Ti-45Al-2Cr-5Nb, Ti-24Nb-4Zr-8Sn, Ti-50Ta and Ti-13Nb-13Zr have also been investigated (Attar *et al.*, 2018). Recent research also focused on AM produced Ti-based matrix composites (Attar *et al.*, 2018) and *in situ* alloying of Ti with master 60Al-40V (wt%) alloy (Ramosena *et al.*, 2019). Ti-copper alloying (Ti-8.5Cu) has also shown promising improvement in material performance (Zhang *et al.*, 2019).

2.4.1 Process description

As depicted in Figure 2.9, a LPBF machine consists of laser, optical, gas and pneumatic systems controlled and integrated by an onboard computer. Before starting a build, the CAD part is "sliced" at the desired layer height. This sliced file (typically in STL digital file format) is loaded onto the LPBF computer, and the technician sets the build parameters. The oxygen sensor in the build chamber is used to regulate the oxygen concentration during the build by opening and closing air valves. Due to titanium's high reactivity with oxygen and nitrogen at elevated temperatures and the negative effect of these elements on mechanical performance, further discussed in the next subsection, atmospheric control in the build chamber is critical. Once the oxygen concentration is below the required value (typically 1000 – 1200 ppm), the build starts. At the start of each layer, the powder feed plate is raised, and the build plate lowered by the increment of the part layer height. This allows for the deposition scraper blade to deposit a layer of powder onto the build plate. The laser-scanning system exposes powder according to the sliced CAD data. This process repeats for all part layers until the build job is complete. The

feed container is then sealed, the excess powder on the build plate is deposited into the overflow chamber, and the build plate is removed. The overflow chamber is also removed, and the powder is recycled into the powder-feed chamber before the next build.
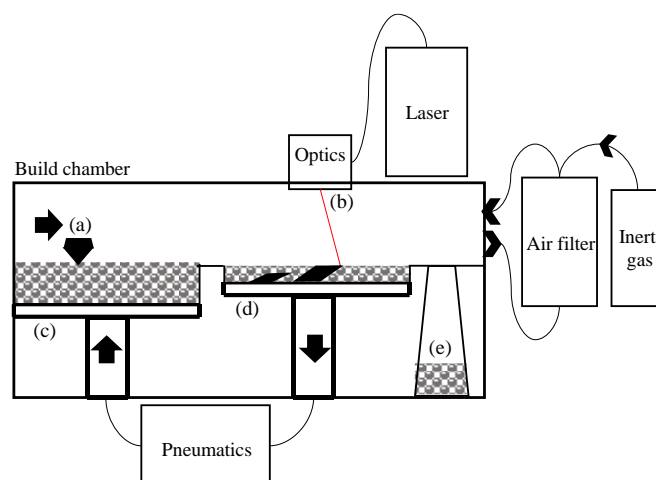
Figure 2.9. LPBF system components (a) deposition blade, (b) laser, (c) powder-feed chamber, (d) build plate, (e) over-flow container.

Ti-6Al-4V powder used for LPBF is commercially manufactured using either gas atomisation, plasma rotating electrode process or plasma atomisation (Sun *et al.*, 2017; Chen *et al.*, 2018). These processes are effective in achieving an extremely spherical morphology with homogeneous diameters. The typical 10th and 90th percentile diameters (d_{10} & d_{90}) are reported to range from 42 – 60 µm, and 92 – 120 µm, respectively. Although plasma atomisation generally achieves better powder quality, the disadvantages of plasma atomisation is a limited accepted feedstock type (wire or powder) and high process costs. Since Ti-6Al-4V part quality is extremely sensitive to oxygen and nitrogen, the elemental concentration in Grade 23—the so-called extra low interstitial (ELI) grade—is kept below 0.13 and 0.05 at% oxygen and nitrogen, respectively (ASTM F3001-14). Other important powder characteristics that influence part quality are powder flowability, porosity in powder particles and moisture content.

The primary LPBF process parameters are listed in Table 2.2. The lasers typically used for Ti-alloys are Ytterbium gaussian fibre lasers operated in continuous wave mode. The laser wavelength is typically 1070 nm, and the maximum output power of most commercial machines is in the range of 200 to 400 W. Laser spot size (defined as the diameter where the laser intensity falls to $1/e^2$ of the maximum laser intensity) is typically 50 – 100 µm. Due to the hourglass-shaped focal profile along the laser's length, laser spot size and intensity profile can be altered by changing the powder bed height. This is measured through the focal offset distance (FOD).

The strategy in which each layer is scanned varies depending on the machine manufacturer. A wide range of laser scan patterns have been investigated (Zhang & Liu, 2018). Popular manufacturers such as EOS and Concept Laser use a "zig-zag" strategy (i.e., tracks scanned in a to-and-fro fashion fusing neighbouring powder tracks) as building blocks. This strategy is

then fragmented into strips or squares/islands across each layer. The scan direction is typically rotated after each layer by 67° or 90° to reduce residual stress and other anisotropic structural effects.

Table 2.2. Primary LPBF process parameters.

Process parameter	Symbol	Typical units
Laser beam power	P	W
Laser spot diameter	d	µm
Scan speed	v	mm/s
Hatch distance	h	µm
Layer thickness	l	µm
Beam focal offset distance	FOD	mm
Scan strategy	-	-
Build plate pre-heat	-	°C
Powder bed pre-heat	-	°C
Chamber gas concentration	-	ppm

As a metric to compare studies of the same material, a linear or volumetric heat input is used. Linear heat input is defined by: $H = \frac{P}{v}$, and the volumetric heat (energy) density input: $E_v = \frac{P}{h \cdot l \cdot v}$. The multiplication of an absorptivity constant has also been used to calculate a modified E_v. More accurate but computationally intensive approaches that consider material properties such as melt- and boiling-points, thermal conductivity, and thermal diffusivity have also been developed. These include the normalised approach (Thomas *et al.*, 2016), the enthalpy-based approach (Rubenchik *et al.*, 2018) and the modified normalised enthalpy approach (Yang, Han, *et al.*, 2016).

Process monitoring is the most recent research field of PBF AM aimed at process optimisation. Process monitoring is typically done with optical systems consisting of high-speed CCD or intensified digital CCD-camera systems and CMOS-cameras combined with pyrometers (Chivel & Smurov, 2010; Lott *et al.*, 2011; Yadroitsev *et al.*, 2014).

2.4.2 The influence of the LPBF process on material structure

Some of the earliest research done on LPBF-produced part density and microstructure was published by Thijs (2014). Build defects, such as voids or unmelted powder particles, are caused by non-optimum energy density at the laser-part interface (Dilip *et al.*, 2017). Lack-of-fusion, Figure 2.10(a), voids are caused by below-optimum laser energy density. These voids are crack-like in morphology and cause high stress concentrations at their boundaries during load application. Therefore, lack-of-fusion defects are undesired due to their propensity to cause premature failure in tensile and fatigue loading (Li, Warner, *et al.*, 2016). Spherical-shaped voids, Figure 2.10(c), are caused by an above-optimum laser energy density and form during a keyhole melt pool mode or as a result of gas-formation (DebRoy *et al.*, 2018). These keyhole pores have been argued to have a negligible effect on tensile properties if they fall below a certain threshold

size (Gong *et al.*, 2015). Defects can lead to anisotropy if heterogeneously dispersed in the sample or geometrically textured according to a certain direction (Ren *et al.*, 2019). This can cause the initiation and/or coalescence of cracks according to a preferential direction causing anisotropic deformation/failure behaviour.
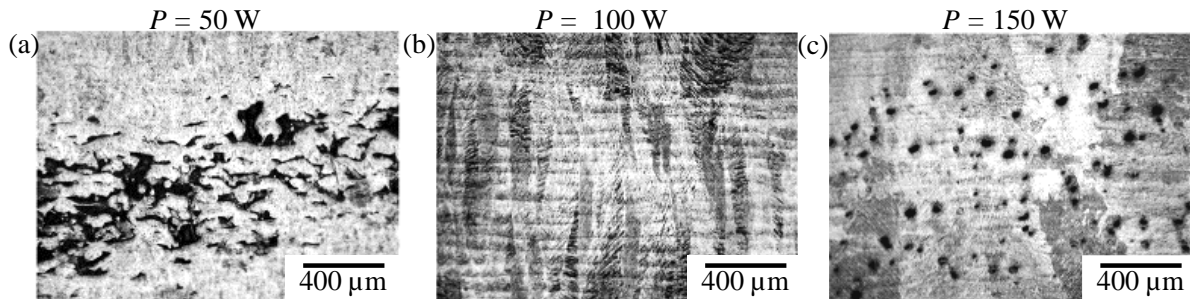
Figure 2.10. LPBF micrographs of (a) lack-of-fusion defects, (b) optimal density, (c) spherical keyhole or gas-induced defects (scanned at 500 mm/s) (Dilip *et al.,* 2017).

Part density can be improved by optimising process parameters of laser speed, hatch distance and laser power (Thijs *et al.*, 2010). Density optimisation has been done by various studies, which found that near dense parts in LPBF-produced Ti-6Al-4V can be achieved by volumetric energy densities in the range of $50 – 70$ J/mm^3 (Dilip *et al.*, 2017) and 117 J/mm^3 (Mishurova *et al.*, 2019a). This is, of course, given that the laser intensity is adequate to achieve a sufficient laser spot temperature.

The localised laser melting and solidification of LPBF causes high cooling rates, which result in a non-diffusive microstructural phase transformation route. This results in chemically metastable martensite formation—a microstructure that greatly differs from Thermomechanical-produced (TMP-produced) microstructures in terms of morphology, texture, and phase chemistry. Antonysamy *et al.* (2013) identified two mechanisms effecting α' variant selection in Ti-6Al-4V: (1) the nucleation of α variants at PBG boundaries with mutually beneficial orientation (for example, a basal plane that shares the PBGs {101} planes) and (2) the occurrence of thermal or transformational stresses that "bias" nucleation. Due to the high cooling rate of LPBF, the nucleation of grain boundary α is negligible, and therefore the second mechanism will likely dominate. In this way, LPBF is closely related to welding in that variant selection due to thermal stresses seem the most likely.

Process parameters have also been found to influence α' lath structure (Yang, Han, *et al.*, 2016; Yang, Yu *et al.*, 2016) and PBG morphology and texture (Gockel & Beuth, 2013; Louw & Pistorius, 2019). Figure 2.11 depicts a reconstructed cube from 3 micrographic planes of an LPBF-produced Ti-6Al-4V sample. Apart from the fine α' martensitic structure, notable features are the difference in PBG structure (indicated by red lines in (a) and (b)) between the two planes. The XY-plane PBG structure is globular/square and mimics the scan strategy and laser hatch distance, while the ZX-plane indicates a columnar morphological structure. Studies

27

have shown that PBG crystallographic texture forms epitaxially in the direction of maximum heat flow (Simonelli *et al.*, 2014a). Since this direction in most conventional LPBF processes is towards the meltpool, PBG texture forms with a strong $\langle 100 \rangle \parallel Z$-axis texture. Since build orientation determines the PBG texture, part build orientation has been shown to influence part mechanical properties such as fatigue, tensile properties (Liu & Shin, 2019; Xu *et al.*, 2019). Due to the large number of possible α' variant orientations due to the BOR (twelve per PBG orientation), α' texture in LPBF-produced Ti-6Al-4V is weak.
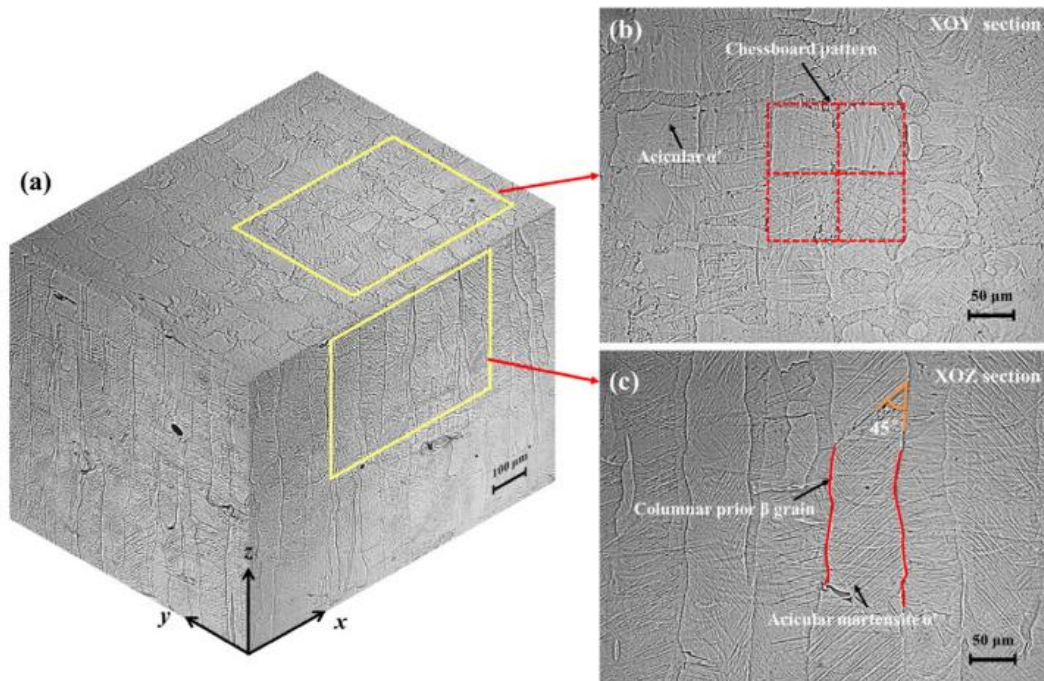
Figure 2.11. (a) 3D reconstruction of typical LPBF-produced Ti-6Al-4V microstructure, (b) XY-plane microstructure, (c) ZX-plane microstructure (Yang, Yu *et al.*, 2016).

A critical factor in LPBF processing is the oxygen and nitrogen concentration in the build chamber. As mentioned in the previous subsection, due to titanium's high affinity for oxidation at elevated temperatures, an inert build-chamber atmosphere is critical for high-quality part fabrication.

Oxygen, nitrogen and hydrogen atoms occupy octahedral interstitial positions in the hcp lattice (Nayak *et al.*, 2018). These point defects play a key role in the mechanical properties and diffusivity of elements in metallic materials. Ti-6Al-4V parts have been found to increase in strength while decreasing in ductility with an increase in oxygen and nitrogen in the material. As mentioned in Subsection 2.2.2, a higher oxygen concentration has been correlated with the formation of α_2 clusters.

Since the strain induced by the interstitials in the crystal lattice along the c-axis, perpendicular to the basal plane, is greater than that along the perpendicular axes (Blanter *et al.*, 2004), an increase in both 'a' and 'c' lattice parameters and the ratio 'c/a' occurs with an increase in interstitial oxygen and nitrogen concentration in the material (Montanari *et al.*, 2008; Jia, 2016).

Residual stress is an intrinsic part of LPBF fabrication due to the high rate of localised cooling during the process. Residual stress has two detrimental effects on part quality: (1) cracking, warping and delamination during the build leading to build failure, (2) the deterioration of mechanical properties such as fatigue life. One of the earliest publications on the experimental study of the formation of residual stress and its relation to process parameters in LPBF-produced metals was published by Mercelis and Kruth (2006). Generally, shorter laser scan tracks combined with scan rotations have been shown effective for reducing residual stress.

Residual stress can be measured through several techniques. For an overview of the state of the art methods employed to measure residual stress in LPBF-produced parts, see Anderson (2017). Traditionally, the most popular method has been hole-drilling (Knowles, 2012; Baldi, 2014). Non-destructive methods such as diffraction-based methods of X-ray diffraction (Robinson *et al.*, 1996) and neutron diffraction (Anderson *et al.*, 2018) have also been developed. These are further discussed in Subsection 2.5.2. A contour-method has also been used effectively (Vrancken, 2016). A simpler but less accurate method is through measuring part distortion angles of bridge-shaped specimens (Mishurova *et al.*, 2017).

2.4.3 The influence of post-processes on material structure

Hot isostatic pressing (HIPing) is a well-established technique for mending internal porosity in titanium castings and has been widely used to increase fatigue life in critical components (Leuders *et al.*, 2013). HIPing involves the concurrent application of elevated temperatures (~920 °C for Ti-6Al-4V) and pressures (~100 MPa), via an inert gas, to a component. Elevated temperatures reduce material yield stress and increases diffusion rates. This allows for the applied pressure to cause pore collapse that, under ideal conditions, also fuses the pore interface. (Atkinson & Davies, 2000). However, some studies have found porosity to reappear after HIPing when the part is β-annealed (Tammas-Williams *et al.*, 2016).

Since knowledge of the influence of thermal treatments on the microstructure is relatively limited, few publications address this topic. Furthermore, since the work presented in the body of this dissertation provides a detailed background to this field, a detailed description is omitted here to avoid repetition.

Most studies agree that a single heat treatment in the solid solution temperature region above ~750 °C followed by furnace or air cooling is effective for full stress relief and martensite decomposition to a stable α+β microstructure. For an overview of the influence of annealing strategies applied to LPBF-produced Ti-6Al-4V on deformation behaviour see Khorasani *et al.* (2017), Huang *et al.* (2015), and Qiu *et al.* (2013). Limited studies can be found that have investigated heat treatments at temperatures above T_β (Brandl & Greitemeier, 2012) or below 600 °C.

2.5 Experimental techniques

This section provides the technical background to the study's chief experimental techniques. Techniques used in the study for the acquisition of mechanical properties (micro-hardness indentation and uniaxial quasi-static tensile tests) are omitted from this section since they followed standard practises as described in the core chapters and do not involve any unique approaches. Structural characterisation techniques were more involved than mechanical testing and required detailed knowledge of the equipment, method, and data processing. Furthermore, structural characterisation techniques were used more extensively than mechanical testing methods. Therefore, this section includes a description of sample preparation, optical and electron microscopy, micro X-ray computed tomography, X-ray diffraction, and electron backscatter diffraction data acquisition, representation, and post-processing.

2.5.1 Sample preparation

Preparation procedures of grinding and polishing were applied to samples intended for microscopy, microhardness measurements and X-ray diffraction. Preparation by machining (i.e., turning) was applied to samples intended for tensile testing.

Although the author's polishing steps are derived from Buehler's recommendations (Buehler, 2020), steps were tailored to improve polishing quality or reduce sample preparation time. Samples were sequentially ground for one minute each with 600, 800, and 1200 grid SiC paper with a base speed of 150 rotations per minute at an applied load of 25 N while flushing with water.

The samples were polished with 9 μm Struers DiaPro Allegro/Largo suspension liquid for five minutes on a Struers Largo disk. A final polish was performed using 0.04 μm Struers OP-S solution for five minutes on a Struers DAC polishing cloth. These two polishing steps were done in the absence of water with an applied load of 25 N at base speed of 150 rotations per minute. Samples were cleaned with running water between grinding steps. Samples were cleaned in between polishing steps using an ultrasonic cleaner with the sample placed in a beaker of isopropanol or acetone.

The Standard Practice for Micro-etching Metals and Alloys (ASTM E407) and Gammon *et al.* (2004) were consulted for etching of samples. Depending on the required outcome, some samples were etched with Kroll's Reagent containing (vol%) 1.5 HF, 4 HNO_3 and 94 H_2O. Although not used, Keller's reagent was shown to be useful in LPBF studies of Ti-6Al-4V to distinguish the heat effected zone (Dilip *et al.*, 2017). Other etchants that are typically used for titanium alloys are oxalic reagent, ammonium bifluoride and lactic hydride reagent (see Gammon *et al.* (2004)).

2.5.2 X-ray diffraction

X-ray diffraction is a non-destructive technique applied to crystalline material or material in a crystalline phase to determine its structural dimensions on an atomic scale. These dimensions

are further used to attain information on the chemical composition and physical properties of the material.

The basic working principles of X-ray diffraction (Figure 2.12) in the causal sequence is (1) a source emits a monochromatic X-ray beam; (2) the beam penetrates the surface of the sample; (3) the angle between the incoming beam and the sample (θ) is varied by rotating the source and/or sample; (4) the in-phase reflected X-rays undergo constructive interference at certain angles depending on the structure of the material; and (5) the reflected constructive interference is recorded by the detector.

The position of interference peak intensities allows Bragg's Law to calculate atomic position within a lattice plane: $n\lambda = 2d\sin(\theta)$, where n is a positive integer, λ the X-ray wavelength and d the atomic spacing of diffracted lattice plane.
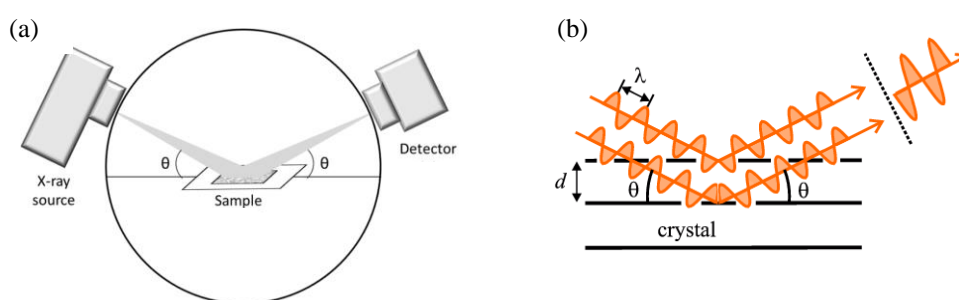
Figure 2.12. Schematic of (a) Simple X-ray diffraction setup (Unruh & Forbes, 2019), (b) incoming X-rays being reflected by crystal planes and undergoing constructive interference according to Bragg's Law (Paul *et al.*, 2006).

X-ray diffraction is used to determine the crystal structure of a material by measuring the pattern of peaks (i.e., their periodic arrangement) and correlating the pattern to a database of known patterns. The crystal structure's physical properties, such as crystal texture and crystallinity (collective term for crystal imperfections such as dislocations and average grain/particle/crystal size) can be approximated by parameterising the Gaussian-shaped Bragg peaks through methods such as the Scherrer equation or more advanced methods such as Rietveld refinement. Since material chemical composition has a pre-determined influence on atomic spacing in a lattice, chemical properties such as composition can be estimated.

For measurements of residual stress, the material strain is first determined through X-ray diffraction. This is done by (1) assuming or measuring the stress-free lattice dimensions; (2) measuring the lattice parameters of the stressed/strained sample using a specific X-ray diffraction approach and (3) calculating the difference between the strained and strain-free lattice dimensions to determine the material strain due to residual stress. The stress state of the material is then determined by assuming/measuring the directional dependant lattice stiffness parameters of the material and applying Hooke's Law to the measured strain. A range of techniques exist to measure residual stress through X-ray diffraction. For a comprehensive

31

summary of techniques, see Fitzpatrick *et al.* (2005), Anderoglu (2004), Prevéy and Hornbach (2019), or for a condensed summary see Anderson (2017).

2.5.3   Micro X-ray computed tomography

Micro X-ray computed tomography (XCT) is applied in a wide range of fields to image internal features of solid bodies. Although it is primarily used in the medical field, XCT has found useful applications in metal AM to determine the morphology, frequency, and distribution of internal defects, Figure 2.13(a & b). Defect morphology is relevant to mechanical properties since pores with rounded morphology produce a lower stress concentration than irregularly shaped lack-of-fusion pores. Defect distribution in a sample can also influence mechanical anisotropy. *In-situ* tensile tests combined with XCT have been performed to observe the initiation of facet fracture features in LPBF-produced Ti-6Al-4V, Figure 2.13(c).

The working principle of XCT relies on projecting X-rays through a rotating object and capturing the X-ray image on the other side of the sample. Images are then stitched together post-scan to construct a computer-generated 3-dimensional model of the object. The final model's resolution depends on the scan voxel size and contrast between internal features and the material. Achievable resolution (voxel size) depends on the sample size and X-ray power. With most commercial machines, small samples in the range of 1 – 2 mm can achieve a voxel size of ~2 µm, while larger samples of ~10 mm cube can achieve a voxel size of ~10 µm (Tammas-Williams *et al.*, 2015). For a standardised method for analysis for porosity in metal AM, see du Plessis *et al.* (2018).
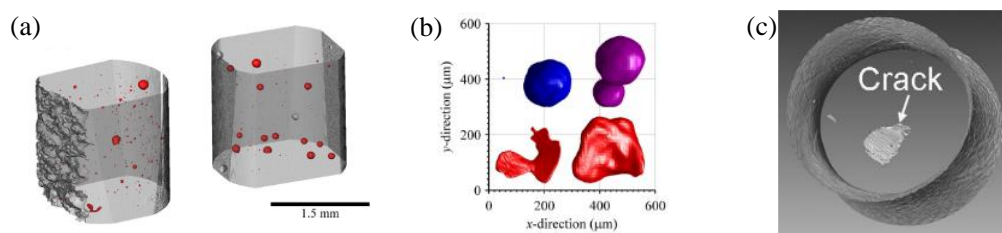
Figure 2.13. (a) Computer-generated internal topology from XCT scan data, (b) Pore morphology data obtained from XCT (Tammas-Williams *et al.*, 2015), (c) an internal crack imaged in a cylindrical tensile sample using *in-situ* XCT (Matsumoto *et al.*, 2011).

2.5.4   Optical imaging microscopy

Although electron microscopy was the dominant microscopy approach used in the study, optical methods were almost always used as a preliminary step to either determine if the sample preparation was adequate or as an initial investigation of microstructure or porosity. Electron microscopy has a much higher magnification capability compared to the available optical microscope, which has a maximum magnification of 1000×. An Olympus GX51 inverted

optical microscope (for technical information see (Olympus, n.d.)) was used to qualitatively characterise microstructure.

The microscope's differential interference contrast (DIC) tool was used to improve grain contrast. This tool functions as a sliding Nomarski prismatic lens that diffracts incoming light, thereby causing light to hit the sample surface at a controllable angle (Murphy *et al.*, 2012). Light hitting the sample at an angle increases topological differences in the surface, causing a shadow contrast effect. This was found especially useful when applied to etched martensitic microstructures. This is because the etching of martensitic microstructure only partially improves visible grain contrast. Subtle differences in grain relief/topology can be accentuated with DIC, thereby improving grain contrast.

2.5.5 Scanning electron microscopy

For higher magnification and added functionality, electron microscopy is preferred to optical microscopy. Electron microscopes use shaped magnetic fields to form electron optical lens systems that are comparable to the glass lenses of an optical light microscope.

The interaction of the primary electron beam with the imaged surface triggers several signal-generation types that can be used to image and quantify aspects of the sample, Figure 2.14. Common signals that are detected and used to describe the sample are secondary electrons (SE), backscattered electrons (BSE) and characteristic X-rays. The ejection generates SE electrons from the conduction of the primary beam electrons by valence bands of specimen atoms. Due to their low energy, SE originates from within a few nanometres from the sample surface. The brightness of the signal depends on the number of secondary electrons reaching the detector. Thus, SE imaging is useful to obtain surface topological information.

On the other hand, BSE is generated from electrons reflected or backscattered out of the interaction volume. Since heavy elements (high atomic number) backscatter electrons more strongly than light elements (low atomic number) and thus appear brighter in the image, BSE is used to detect contrast between areas with different chemical compositions. BSE also contains diffracted electrons. These diffraction electron patterns are used to derive crystal structure information through electron backscatter diffraction (EBSD) analysis, discussed in the next section.

Lastly, characteristic X-rays are generated by the incident beam exciting an inner shell electron and causing it to eject. This "electron hole" is then filled by an outer-shell electron. The difference in energy between the higher-energy shell and the lower energy shell may be released in the form of an X-ray. As the energies of the X-rays reflect the difference in energy between the two shells and of the atomic structure of the emitting element, EDS allows the elemental composition of the specimen to be measured, Figure 2.14(e – f).

Scanning transmission electron microscopy uses transmitted, diffracted, or scattered electrons through the sample to obtain a higher resolution than SEM. Sample thickness is usually required in the range of 100 nm, which is conventionally accomplished by ion-beam milling. STEM operational modes that are relevant to the study are dark field, bright field, and the technique of

electron energy loss spectroscopy (EELS). Bright field images are generated by intentionally selecting an objective aperture which only permits the non-diffracted beam to pass beyond the back focal plane. A dark field image is generated by blocking the central, non-diffracted beam. As a result, heavier/denser regions appear darker in bright field images. In EELS, electrons are separated into a spectrum based upon their velocity (which is closely related to their kinetic energy and thus energy loss from the beam energy), which can be used to determine the material's elemental composition.
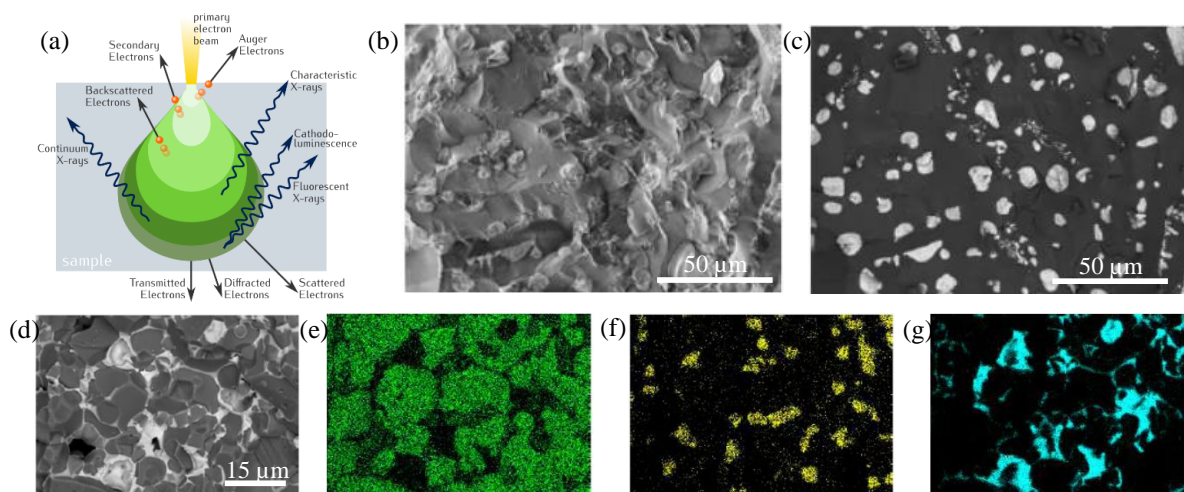
Figure 2.14. (a) primary electron beam and sample interaction with resultant generated signals (Ponor, 2020), comparison of (b) SE imaging versus (c) BSE imaging for the identical ROI. Example of EDS analysis (d) BSE image, and mapping of (e) zinc, (f) antimony and (g) bismuth (Masako *et al.*, 2016).

2.5.6   Electron backscatter diffraction

The working principles of EBSD rely on electron diffraction of crystalline material to determine both crystal structure and crystal orientation. Therefore, EBSD has two main application areas: (1) phase (crystal structure) identification and (2) orientation imaging microscopy.

Figure 2.15 depicts the sequential workflow of the EBSD process - adapted from Maitland & Sitzman (2007) and Brisset (2010). (a) A sample is mounted at ~70° with respect to the EBSD detector. The sample surface is scanned with an electron beam at increments (called steps) which causes electrons to diffract at angles that satisfy the Bragg equation see Subsection 2.5.2. (b) Diffracting electrons cause electron backscatter patterns, also called Kikuchi patterns. These are projected onto a phosphor screen which is fluoresced by the electrons. The scan position on the sample surface is stored at each increment, and the diffracted Kikuchi pattern image is captured by a sensitive charge-coupled device (CCD) camera.

(c) A computer then processes the image by applying a Hough transform to generate a unique pattern of points. This pattern is then compared to a crystallographic database to determine the

unique band-dependant crystal structure. (d) Lattice planes for each band can then be identified, and (e) their relative orientations are used to determine the crystal structure and lattice orientation. This process repeats for the entire region of interest (i.e., the imaged area). This data is popularly represented in an orientation map, Figure 2.16(b), although other mapping representations, discussed subsequently, are also popular. Due to the computationally intensive process, a single EBSD map scan can take many hours to complete.

The most popular orientation convention to describe lattice/crystal orientation relative to the sample orientation is the Bunge convention. This uses three sequential angular lattice rotation values (φ_1, Φ, φ_2) of the crystal Z-axis (miller notation [001]) from the sample/specimen coordinate system (ND – normal direction, RD – roll direction and TD – transverse direction) to describe the crystal orientation, Figure 2.15(e).
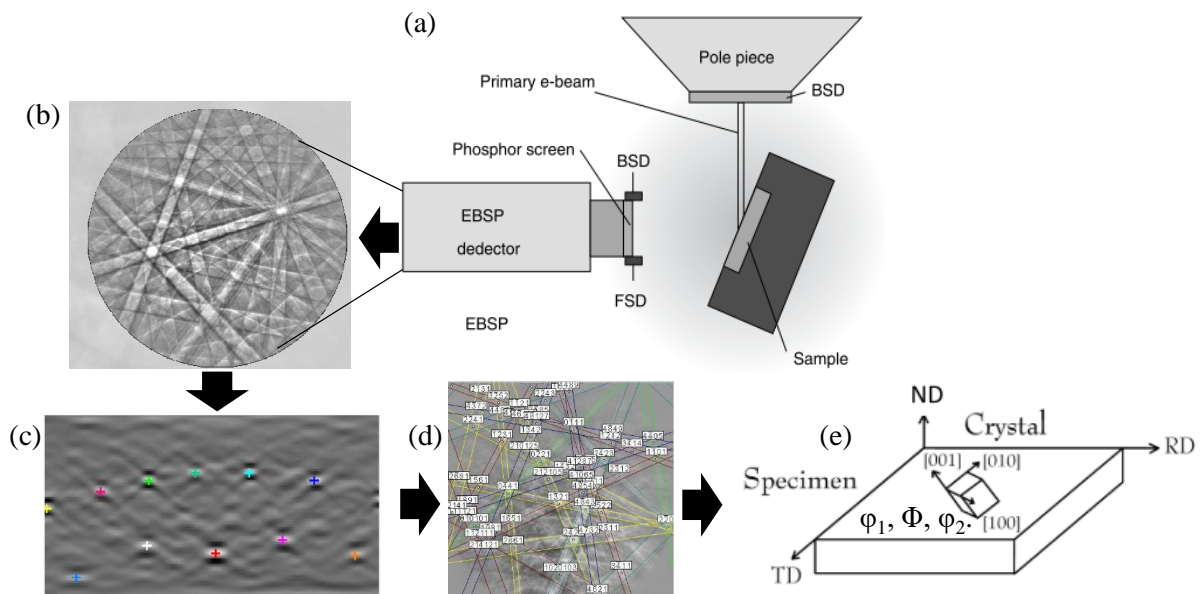
Figure 2.15. EBSD working process to obtain lattice orientation (description in text). Adapted from Maitland & Sitzman (2007) and Brisset (2010).

Image quality maps, Figure 2.16(a), use values of Kikuchi band quality (stored at each incremental step of surface scanning) converted to a scaled value to depict the microstructure. Image quality is determined from Kikuchi band contrast and band slope values derived from Hough transformation. Band contrast describes the average intensity of the Kikuchi bands with regards to the overall intensity of the area of interest, while band slope describes the maximum intensity gradient across bands. Since Kikuchi band contrast is influenced by material structural aspects such as residual stress and dislocation density, band contrast and band slope can be used to indicate this (Wright *et al.*, 2011). This allows for sub-grain features to be identified that are not possible with orientation imaging (compare Figure 2.16(a) and (b)).
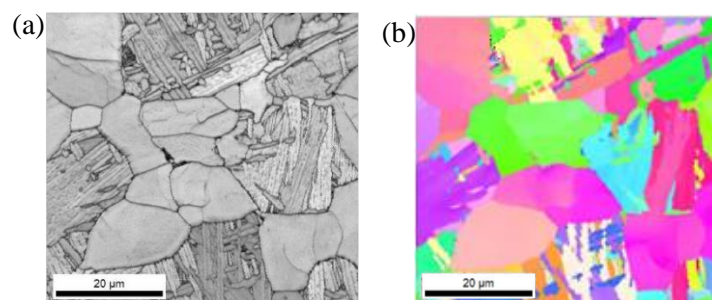
Figure 2.16. EBSD mapping of identical ROI using (a) image quality map, (b) orientation imaging (Brisset, 2010) (colouring defined in the next subsection).

2.5.7 Representing crystallographic orientation and texture

In addition to orientation imaging maps, Figure 2.16(b), another useful representation of orientation data, can be done through pole figures and inverse pole figures. These are commonly used to effectively present, identify and quantify the crystallographic texture of the material.

Representing orientation information can be challenging to visualise. To aid the reader's understanding to interpret pole figures (and inverse pole figures discussed subsequently), Figure 2.17 depicts the mental process by which this can be done. (a) The cubic lattice (or any crystal structure) is orientated with respect to the specimen coordinate system (X, Y, Z, or ND, RD, TD); (b) crystal miller ⟨100⟩ vectors (or any specified vector family) are traced to the outer hemisphere; (c) a stereographic projection is produced in which points on the hemisphere are traced towards the hemisphere's "south" pole. This causes the intersecting of the horizontal plane to generate; (d) the resultant ⟨100⟩ pole figure.
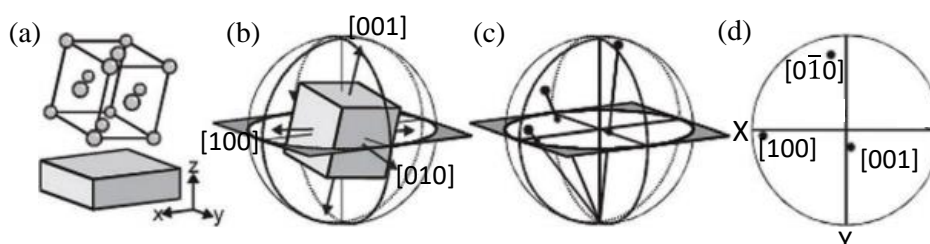
Figure 2.17. Schematic of the "mental steps" to generate a ⟨100⟩ pole figure for a single orientation (description in text). Adapted from Oxford Instruments (2015).

Inverse pole figures (IPF) use the same principles described in Figure 2.17, but use the symmetric nature of the crystalline material to depict only unique orientation information. For example, the three pole positions in Figure 2.17(d) describe a single crystal's orientation relative to the sample. In effect, only a single point is required to describe the unique crystal

36

orientation. Therefore, crystal symmetry allows for the intersected horizontal projection plane to be segmented into identical symmetric sections or triangles. Figure 2.18 depicts this for (a) hcp and (b) bcc symmetry. Each position in the unique triangle describes a unique crystal orientation. The triangle is coloured using, for example, hue-saturation-value (HSV), which allows for each unique orientation to have a unique colour. This can then be used to depict orientation maps using colour (see Figure 2.16(b)), or maps can be plotted as an inverse pole figure triangle to facilitate the identification and quantification of crystallographic texture.
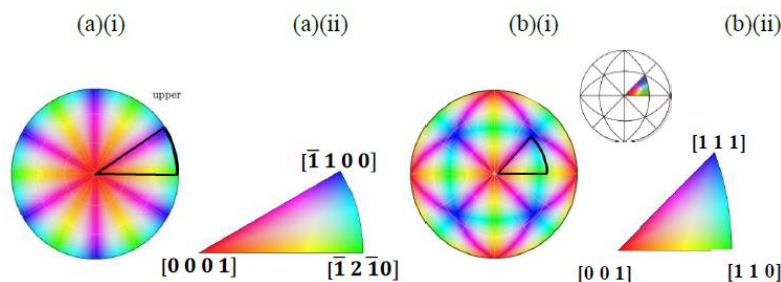
Figure 2.18. HSV-IPF plots of (a) hcp six-fold symmetry and (b) bcc 16-fold symmetry (i) complete hemisphere and (ii) unique orientation triangle (Ter Haar, 2017).

2.5.8   EBSD prior-β grain reconstruction

Prior-β orientations (i.e., the orientation of a parent β-grain) can be calculated from α orientation data through the BOR. The method was first published by Glavicic *et al.* (2003) and is discussed in more detail by the author elsewhere (Ter Haar, 2017). An algorithm to implement this using MATLAB and the toolbox MTEX was first published by Simonelli (2014). The author adapted the code that allows newer MTEX functionality (released in 2016) to be used. The author developed the algorithm during his master's studies (Ter Haar, 2017) and includes a variant identification subroutine. The reconstruction code and subroutine are included in Appendix F.

The prior-β reconstruction algorithm developed by the author is presented as a pseudocode in Figure 2.19. Sequential steps of the code (as labelled in the figure) are (a) MTEX functionality stores α-grain identification values of triple points (i.e., three grains that share a single common boundary point). (b) Each grain's mean orientation is multiplied by a BOR operator to calculate six unique prior-β orientations for each α-grain. (c) If all three α-grains belong to the same parent β-grain, then one unique β orientation exists that is shared by all. This unique β orientation solution is determined through a minimisation routine that finds a single β-orientation that is the least different between each of the three groups (below a threshold angle). These steps are repeated for all triple points until a data file containing a list of reconstructed orientations at each α triple point coordinate is generated. Post-processing involves either smoothing or using a mean PBG orientation to present the reconstructed data.

(a)

(b)

(c)

Triple point

α_1 $\quad$ α_2 $\quad$ α_3

$6 \times \beta_1$ $\quad$ $6 \times \beta_2$ $\quad$ $6 \times \beta_3$

Single prior β orientation
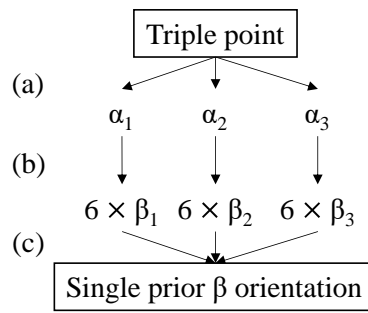
Figure 2.19. Prior-β reconstruction algorithm pseudocode (description in text).

3 Hypothesis development

This chapter presents the motivation and approach of selected methodologies to achieve the project's aim. This is followed by defining the project's objectives, describing their unique aims and tasks, and concludes by discussing the project scope and limitations.

3.1 Motivation for the experimental approach

The motivation for the broad structure of the project's experimental approach stems from both metallurgical and practical considerations. The motivation for specific laboratory techniques, Section 2.5, stems from their judged effectiveness in achieving the project's objectives based on recent literature findings and the project's scope. Since these laboratory techniques are, in most cases, considered standard recommended practice in the relevant study fields, these are discussed as part of the project's scope and limitations in Section 3.3.

Most studies on thermal treatment in LPBF metals have focused on post-process heat treatments. However, recent studies have found evidence that thermal treatments can also be done during the fabrication process (*in-situ*). Although both approaches are studied in this project, the post-process approach occupies 75 % of the total research output, while *in-situ* treatments occupy 25 %. The focus on post-process thermal treatments stems from their advantages over *in-situ* treatments with respect to achieving the project aim.

In-situ heating poses an experimental challenge for gaining fundamental understandings of thermal treatments' influence on the microstructure. This is due to the challenge of *in-situ* monitoring of the complex heating cycles, the replicability across sample sizes and differences in LPBF machine thermal response. A summary of the advantages of post-process versus *in-situ* thermal treatments is listed in Table 3.1. Ultimately, post-process thermal treatments were chosen since they allow for an experimental approach in which a fundamental understanding of the metallurgy could be developed. The research conducted of *in-situ* thermal treatments is an additional investigation to determine its feasibility as an alternative approach and serves as a point of departure for future research.

Table 3.1. Advantages of post-process versus *in-situ* thermal treatments.

Thermal treatment	Advantages
Post-process	Applicable across all machines
	Control of part temperature and hold time
	Comparable to previous studies
	Broader flexibility in the achievable microstructure
	Lower part oxidation
In-situ	Elimination of additional processing costs.

The project's experimental approach for post-process thermal treatments consisted in dividing the temperature range of the α+β phase-field into three separate regions, Figure 3.1. This was motivated by two factors. Firstly, from a metallurgical perspective, each of the three

temperature regions can be considered to have a unique impact on metallurgical response. Secondly, this allowed for the scope of research to be divided into practically manageable and focused portions with the intent of publishing each section as a stand-alone journal article. This also allowed for the formulation of key project objectives defined and described in the next section.

The two partitioning temperatures that segmented the three temperature regions were identified by key metallurgical transition points. The first identified partitioning temperature is the β-transus temperature ($T_β$). This is approximately 975 °C for Ti-6Al-4V ELI (Grade 23) (Lütjering & Williams, 2007). At this temperature, the equilibrium phase composition reaches 100 % β-phase and remains constant up until melting. The second identified partitioning temperature is based on Kelly's (2004) work, who identified that 708 °C is the α dissolution temperature (T_{diss}). However, it should be noted that there is no specific temperature at which a metallurgical dissolution of a solid solution "starts" since both phases are already present at room temperature. Rather, the range ~700 – 750 °C can be considered the transitional region at the start of a substantial change in phase fraction gradient with temperature. Thus, in summary, the three identified temperature ranges are:

- **Range 1:** Ambient to ~700 °C. This is referred to as a "stress relief" (SR) heat treatment based on conventional terminology.

- **Range 2:** From ~700 °C to $T_β$. This is referred to as the solid solution temperature region (SSTR).

- **Range 3:** Above the β-transus temperature. This is referred to as a β-anneal heat treatment.
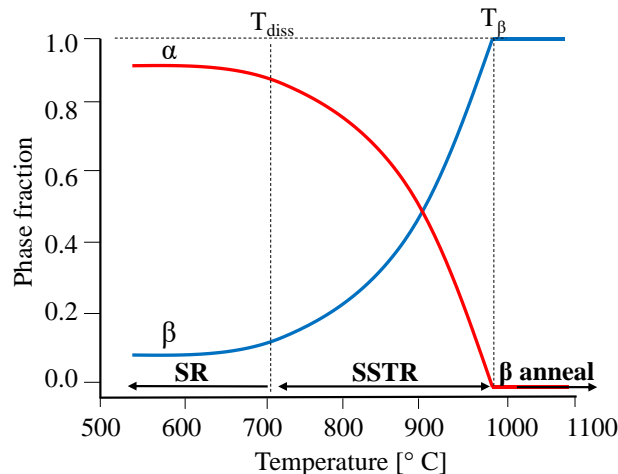
Figure 3.1. Equilibrium α/β phase fraction as a function of temperature and the division of identified temperature regions (SR—stress relief, SSTR—solid solution temperature region). Adapted from Kelly (2004).

3.2 Aims and objectives

As summarised in Chapter 1, this study's core aim is to develop a fundamental insight into the microstructural response of thermal treatments of LPBF-produced Ti-6Al-4V. In line with this and the motivation for the methodological approach discussed in the previous section, four primary objectives were formulated and organised into individual stand-alone chapters. Objectives 1, 2 and 3 were formulated based on unique research questions within the three temperature regions discussed in the previous section. Objective 4 concerned *in-situ* as opposed to post-process thermal treatments.

Objective 1: *Determine the structural response of post-process heat treatments in the solid-solution temperature region (SSTR).* This is driven by the aim to develop metallurgical insight and new microstructural morphologies that achieve tensile properties comparable to wrought-produced Ti-6Al-4V components. Specific tasks within this objective include applying post-process heat treatments in incremental temperatures followed by air cooling and water quenching; determining the microstructural response as a function of cooling rate and holding temperature; determining the tensile behaviour of the resultant microstructures, and explaining the mechanisms by which the unique morphological changes occur.

Objective 2: *Determine the structural response of post-process heat treatments in the SR temperature region.* This is driven by the aim to improve understandings of the initial stages of martensite decomposition and stress relaxation at low temperatures. Specific tasks within this objective include applying post-process heat treatments in incremental temperatures and hold times below 700 °C; determining the microstructural and residual stress response as a function of hold time and temperature; determining the deformation behaviour of the resultant microstructures, and explaining the formation mechanisms of the resultant microstructure and its influence on deformation behaviour.

Objective 3: *Determine the cause of deformation anisotropy by applying β-anneal heat treatments.* This is driven by the aim to fully describe the mechanisms that control anisotropic deformation in LPBF-produced Ti-6Al-4V. Since a strong PBG texture and a columnar morphology is believed to be the cause of anisotropic deformation behaviour, specific tasks within this objective include conducting β-anneal heat treatment strategies to alter the PBG structure; determining the influence of these heat treatments on PBG and α' morphology and texture; determining the deformation mechanisms of α' and their relation to the PBG texture, and formulating a theory of the likely dominant cause of deformation anisotropy based on the findings.

Objective 4: *Determine the structural response of intrinsic heating effects achieved by above-default energy density process parameters*. This is driven by the aim to eliminate post-process heat treatments by applying thermal treatments during the LPBF build process. Specific tasks within this objective include iteratively developing high-energy process parameters that achieve a high sample density; using micro XCT to determine the morphology and texture of internal defects; building cantilever-shaped samples to determine the effect of the process parameters on the residual stress, and using SEM imaging and EBSD mapping to determine the influence of the process parameters on microstructural texture, morphology, and phase.

3.3 Scope and project limitations

The project spans a range of engineering fields, including manufacturing, material science, and experimental mechanics. While experimental techniques in most of the fields can be considered standard practise, such as microscopy in metallurgy, specific existing laboratory techniques (for example, optical versus electron microscopy) were chosen based on the specific project aims and objectives. Important considerations influencing the choice of field-specific techniques were the project's budget, time limitations, and accessibility. Discussion of the project scope spans the following three fields (1) LPBF machines and powder, (2) heat treatments, (3) structural characterisation, and (4) the acquisition of mechanical properties.

3.3.1 LPBF machines and Ti-6Al-4V powder

As mentioned in Chapter 1, motivation for LPBF as the preferred metal AM processing technique, as opposed to the various alternative techniques summarised in Section 2.3, stem from several factors. These include (1) the desire to develop down-stream beneficiation of titanium mineral in powder form, (2) LPBF's advantages for aerospace and biomedical components in terms of its achievable high resolution, and (3), availability and affordability of LPBF part fabrication compared to other techniques.

Commercial LPBF machines used in this study are listed in Table 3.2. These machines were identified based on their availability and cost of part fabrication. The majority of fabrication was done at Stellenbosch University and the Central University of Technology in South Africa. Since both research institutes form part of the CPAM program, as discussed in Section 1.2, part fabrication was partially subsidised by the CPAM program. Parts were also fabricated at Katholieke Universiteit Leuven (KU Leuven)—a collaborative research partner—during a research visit to the university.

Powder suppliers were identified based on powder cost and powder delivery time. Gas atomised powder (purchased from TLS Technik GmbH & Co. and Praxair Surface Technologies GmbH) was chosen instead of plasma atomisation powder due to the former's lower cost.

Table 3.2. LPBF machines used in this study.

University / company	LPBF machine
Central university of technology	EOS M280
Stellenbosch University	Concept Laser M2
KU Leuven	Concept Laser M1

3.3.2 Heat treatments

A box-type muffle furnace without atmospheric control at the laboratories of Stellenbosch University's Materials Engineering research group was used. Heat treatment techniques and technologies that were outside the scope of the study include (1) HIP, (2) induction heating, (3) *in-situ* base plate heating, (4) inert-atmosphere heating, and (5) vacuum heating. The first three heat treatment technologies are not locally available, making them expensive and practically challenging for research purposes.

Due to titanium's propensity for oxidation at temperatures above ~400 °C, commercial titanium parts' thermal treatments are primarily done in a vacuum or inert-gas furnace. Although Stellenbosch University very recently acquired an inert-atmosphere furnace, this furnace-type was only available externally at the time of this study, thus making it a costly additional expense.

Although a vacuum-furnace is available in the Materials Engineering research group's laboratories, this vacuum furnace unfortunately, did not meet the required capabilities necessary to meet the project objectives. The shortcoming of the available vacuum furnace includes inaccurate and unreliable temperature monitoring and non-homogeneous thermal distribution. Critically, this available vacuum furnace does not allow for air cooling or quenching of samples.

Both vacuum and inert-atmosphere heating were not considered critical in achieving the project aims. This is because sample oxidation only occurs on the outer part surface, leaving the internal part uncontaminated and suitable for metallurgical analysis. For tensile testing, the influence of oxygen diffusion into the outer layer was assessed with incremental microhardness measurements. Figure 3.2 depicts an example of such a measurement of a sample heat-treated at 985 °C for three hours, followed by water quenching. After ~300 µm into the sample, the hardness remains constant at ~350 HV0.1. Thus, a conservative amount of surface material in the order of ~500 µm was removed through machining. Part machining was also used to improve surface roughness. Although part machining post-fabrication is not ideal or necessarily achievable in more complex parts, it allowed for addressing the research questions. For large complex parts, chemical milling will likely be more feasible and possibly faster (see Bezuidenhout *et al.* (2020)).
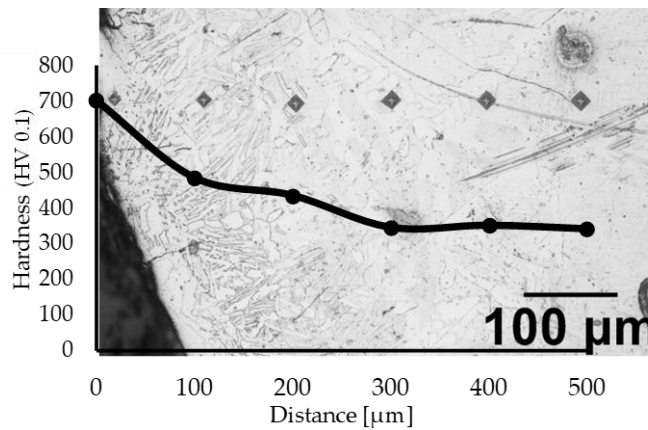
Figure 3.2. Incremental micro-indentation measurements from sample surface (heat-treated at 985 °C for 3 hours followed by WQ).

3.3.3 Structural characterisation

A broad range of structural aspects links process parameters with mechanical properties (see Figure 1.1). The term "structure" is used here to specifically refer to the quantifiable physical aspects that make up the material and contribute to the material's mechanical properties such as density, microstructure, residual stress, surface roughness, oxygen content, etc. Although microstructure was the primary structural consideration in this study, additional structural aspects considered essential for certain objective-specific tasks were sample density, defect morphology, residual stress, and oxygen-and-nitrogen concentration. Surface roughness, although a structural characteristic that is extremely detrimental to fatigue behaviour (Kahlin *et al.*, 2017; Vilardell *et al.*, 2018), was outside the scope of study. For a study in which the author contributed to applying chemical milling to improve surface roughness and fatigue life, see Bezuidenhout *et al.* (2020).

Since the focus of the research was on microstructural characterisation, a broad range of techniques were used. Since the martensitic microstructure of LPBF-produced Ti-6Al-4V is extremely fine, the SEM's higher resolution capability was essential. Furthermore, SEM has a wider range of functionality. For example, distinguishing features based on their chemical composition using EBS, measuring elemental composition of phases using EDS, and determining crystallographic structure and texture using EBSD. Due to its lower achievable resolution compared to SEM, optical microscopy was predominantly used to image larger structural features such as PBGs and microstructures of heat-treated samples. Optical microscopy was also used as an assessment technique of the polished surface quality before SEM imaging, microhardness indentations or XRD were undertaken.

Since the quantification of grain morphology and crystallographic texture were required tasks in the third and fourth objectives, EBSD was a necessary experimental technique. Although crystallographic texture can also be measured using certain XRD systems, for example, the Bruker D8 Advance, these systems were not freely available to the candidate, and since EBSD

44

mapping provided a range of additional quantified data of the microstructure, EBSD mapping was considered a more valuable experimental route.

X-ray diffraction can be used to characterise the microstructure and residual stress. For the prior, a benchtop X-ray diffraction machine, Bruker D2 Phaser, was used at Stellenbosch's Centre for Analytics Facilities. For the latter, a Bruker D8 Discover was used together with software LEPTOS S at KU Leuven, Department of Materials Engineering.

As opposed to microscopy methods such as EDS, XRD is a faster, more sensitive, and cost-effective approach to determining slight changes in chemical composition and average undistorted lattice size. This has been successfully applied in this study to determine subtle phase transformations in $\alpha' \rightarrow \alpha$ and the detection of the bcc phase.

Table 3.3 lists the utilised experimental techniques for structural characterisation and their respective laboratory facility. Laboratories at four universities and two state-owned institutions were used. The university institutes are Stellenbosch University (SU), Nelson Mandela University, and Katholieke Universiteit (KU) Leuven. Both the laboratories at the Engineering faculty and the University's Central Analytical Facilities were used.

Table 3.3. Experimental techniques and laboratory facility.

Facility / laboratory	Experimental technique
Department of mechanical and mechatronic engineering, Materials Engineering research group, SU	Sample preparation Optical imaging microscopy Archimedes method – density
Central Analytical Facilities, SU	SEM imaging (BSE and EDS) XRD – phase analysis micro XCT – porosity morphology
CHRTEM, Nelson Mandela University	SEM imaging (BSE and EDS) EBSD mapping STEM analysis EELS analysis
Department of materials engineering, KU Leuven, Belgium	Sample preparation Archimedes method – density XRD – residual stress Optical imaging microscopy SEM imaging (BSE and EDS) EBSD mapping
NECSA, Pretoria, South Africa	XRD – residual stress Sample oxygen and nitrogen measurement
CSIR, Pretoria, South Africa	Powder characterisation

3.3.4 Analysis software

This study's primary data processing software was MATLAB[2]—a powerful numerical computational package available through SU. Based on its merits and availability, it was chosen above other similar software packages such as Scilab or language-based computing packages such as Python or R.

In the research field, EBSD data processing is predominantly done using commercial software packages that are part of the EBSD acquisition suite. For example, Oxford instruments' data analysis package is AZtecCrystal (Oxford Instruments, 2020). Since EBSD mapping was outsourced to external universities (Table 3.3), these commercial software packages were not available to the candidate for data processing. Fortunately, open-source EBSD analysis software exists. The most attractive of these was MTEX (Bachmann *et al.*, 2010), a MATLAB-based toolbox for EBSD crystallographic and texture analysis. Due to its integration with MATLAB, MTEX is capable of additional data processing techniques not possible with commercial software. These additional data processing techniques most notably include prior-β reconstruction, the quantification of grain Schmid factors, and grain slip transmissibility.

While several open-source XRD programs exists, two software packages for XRD data analysis were used. For Rietfield refinement, MAUD (Lutterotti *et al.*, 1999) was used while peak identification, FWHM measurements, background filtering and plotting was done using XPowderX (Martin & Raheem, 2008). As opposed to other considerations such as FullProf, TOPAS and GSAS, the motivation for the chosen software was based on their ease-of-use and capabilities.

3.3.5 Mechanical properties

Mechanical properties determined in this study derived from uniaxial tensile tests and microhardness indentations. These were deemed adequate for describing the deformation behaviour in line with the project's aim. Although mechanical testing of properties such as fatigue life, fatigue threshold, material toughness and material creep behaviour was outside the scope of the project, certain tensile properties can be correlated with higher or lower fatigue life or part toughness. For example, higher part ductility has been shown to correlate with a higher fatigue life (Leuders *et al.*, 2014), and toughness can be determined from the area under the stress-strain curve.

The measurement of microhardness is a standard technique for assessing the material's deformation behaviour and can synthetically display materials' elasticity, plasticity, and tensile strength. For example, higher material hardness is empirically related to higher tensile strength (Zhang *et al.*, 2011). Microhardness is a fast and versatile experimental approach for assessing local material deformation, for example, measuring the hardness difference between phases and locations within a sample. Vickers hardness measurements were done at the Materials

---

[2] MATLAB release R2019a, The MathWorks Inc., Natick, MA, USA. Available:
https://www.mathworks.com/products/matlab.html

Engineering laboratories using a semi-automatic indentation machine EMCO-TEST DuraScan model 10 G5. For technical details, see ("DuraScan G5 - EMCO-TEST", n.d.).

4 Laser powder bed fusion produced Ti-6Al-4V: Post-process heat treatments to achieve superior tensile properties

Due to the novelty of metal AM, only a limited number of studies have been done to determine the influence of post-process heat treatments on the as-built microstructure of LPBF-produced Ti-6Al-4V. While published post-process heat treatments have shown to improve material ductility, the achieved mechanical properties are still lower than that achieved by wrought-produced bi-modal microstructures. This chapter addresses the first project objective by identifying the mechanisms of microstructural morphological transformations in the SSTR as a function of annealing temperature, holding time and cooling rate. Using this knowledge, new LPBF-produced Ti-6Al-4V microstructural morphologies, like bi-modal microstructures achieved by TMP, are developed, achieving superior deformation behaviour to current post-process strategies applied to LPBF-produced Ti-6Al-4V.

This chapter is published in the journal *Materials* (Ter Haar & Becker, 2018)[3] and is presented here in its pre-published form. A discussion of post-review considerations is included at the end of the chapter. This work has also been presented at the Fraunhofer Direct Digital Manufacturing Conference in Berlin and is published in their conference proceedings.[4]

Declaration by the candidate:

With regards to Chapter 4, the contributions of author and co-author are as follows:

Name	Email	Contribution	Extent (%)
G.M. Ter Haar (candidate)	gterhaar@sun.ac.za	Experimental design, completion of all tests and data analysis, writing and compilation of manuscript	90
T.H. Becker	tbecker@sun.ac.za	Supervision and reviewing	10

Signature of candidate: [GTH][5]
Date: 2021/02

Declaration by the candidate:

The undersigned hereby confirm that:

1. The declaration above accurately reflects the nature and extent of the contributions of the candidate and the co-authors to Chapter 4,

---

[3] DOI link: https://doi.org/10.3390/ma11010146
[4] ISBN 978-3-8396-1320-7 or http://hdl.handle.net/20.500.11850/312018
[5] Declaration with signature in possession of candidate and supervisor

2.   No other authors contributed to Chapter 4 besides those specified above, and

3.   Potential conflicts of interest have been revealed to all interested parties and that the necessary arrangements have been made to use the material in Chapter 4 of this dissertation.

Signature (see Footnote 5)	Institutional affiliation	Date
[TH Becker]	SU	2021/02

4.1 Introduction

Since the emergence of laser powder bed fusion (LPBF) as a humble rapid prototyping technology, the process has advanced exponentially to a point where it has become the most broadly used metal AM process in the industry (Xu *et al.*, 2017). LPBF-produced titanium alloys have been used for aircraft components and customised medical implants (Ford, 2014). The ability to produce complex part geometries, reduce manufacturing lead time and material waste has made LPBF-produced titanium a competitive alternative to conventional manufacturing processes. Considerable attention has been directed towards Ti-6Al-4V, a 6 wt% aluminium, 4 wt% vanadium titanium alloy that is considered the "workhorse" in the titanium industry due to its excellent material properties. LPBF-produced Ti-6Al-4V in its as-built state, is unable to achieve the high material performance of its wrought-produced counterpart. While parts are stronger (with regards to its ultimate tensile strength of up to ~1200 MPa (Yan & Yu, 2015)), ductility and toughness are low (with an elongation to failure reported at less than 6 % in some cases (Yan & Yu, 2015)). Low ductility is attributed to the presence of an undesired α' (martensite) microstructure within elongated columnar prior-β grains (Vrancken *et al.*, 2012; Simonelli, 2014; Xu, Brandt, *et al.*, 2015).

Microstructural morphology is the fundamental fingerprint for mechanical behaviour. In Ti-6Al-4V, the grain morphology (lamella versus equiaxed), grain size (fine versus coarse), and the dual-phase (α+β) microstructure prescribe the deformation behaviour of the material (Leyens & Peters, 2003). Wrought-produced Ti-6Al-4V is mechanically processed to achieve a bi-modal microstructure which consists of large equiaxed/globular α-grains in a matrix of elongated α+β lamellar grains. This is referred to as primary and secondary α, respectively, due to the order of formation in a duplex annealing process. A bi-modal microstructure allows for a balance in the advantages of combining fine lamellar and equiaxed microstructures. Bi-modal microstructures are achieved through thermomechanical processing (TMP), which allows for grain fragmentation and globularisation (Evans, 1998). According to Aerospace Material Specification H-81200C and findings by Semiatin *et al.* (2003), the microstructural morphology is first tailored using hot-working to induce dislocations that fragment α-grains followed by fast cooling (air cooling or water quenching) from a solid solution temperature (SST) between 900 – 970 °C. Equiaxial α-grains form because of preferential globularisation at prior-β grain triple point boundaries. Subsequently, a second anneal is used to relieve residual stresses and/or decompose α' into a dual α+β lamellar phase.

The challenge of achieving a bi-modal microstructure through post-processing in LPBF-produced Ti-6Al-4V is that the starting microstructure is martensitic. Since the LPBF

technology aims for near-net-shape part production, parts cannot be mechanically worked post-fabrication. The research aimed at improving part ductility have shown that annealing is effective in decomposing α' into a stable dual-phase lamellar α+β microstructure (Facchini *et al.*, 2010; Vrancken *et al.*, 2012; Becker *et al.*, 2015; Huang *et al.*, 2015; Kasperovich & Hausmann, 2015; Yan & Yu, 2015; Sallica-Leva *et al.*, 2016; Zhao *et al.*, 2016). However, the annealing strategies that are applied to wrought samples do not have the same effect on LPBF-produced Ti-6Al-4V; the α' forms into a coarse elongated lamella morphology. This improves ductility, however at the cost of strength (Facchini *et al.*, 2010; Vrancken *et al.*, 2012; Becker *et al.*, 2015; Huang *et al.*, 2015; Kasperovich & Hausmann, 2015; Yan & Yu, 2015; Sallica-Leva *et al.*, 2016; Zhao *et al.*, 2016). While this improvement in ductility is satisfactory according to ASTM standards (such as ASTM F2924), ductility versus strength is still significantly less than that of the wrought material (Donachie, 2000; Leyens & Peters, 2003). Potential lies in optimising mechanical properties of LPBF-produced Ti-6Al-4V; however, to accomplish this, grain morphological transformation as a function of annealing temperature and holding time needs to be understood.

This study aims to explain grain morphological transformation as a function of annealing temperature, holding time and cooling rate to contribute to the understanding of the mechanism of grain morphology transformation in the solid solution temperature region (SSTR). This allows for heat treatment strategies aimed at achieving a bi-modal microstructure to be tailored for the specific case in which the starting microstructure is martensitic. Annealing strategies are conducted in the low-, medium- and high-SSTR. While low- and medium-SSTR annealing is conducted to determine an annealing strategy for decomposing α' into a stable dual-phase lamellar α+β microstructure, a high-SSTR anneal approach is aimed at understanding fragmentation and globularisation of primary α-grains.

The study's scope focuses on improving the combined strength and ductility of the material to achieve tensile properties comparable to wrought-produced Ti-6Al-4V. For the first time, it is demonstrated that a bi-modal microstructure in LPBF-produced Ti-6Al-4V is possible, and that this microstructure is superior to that achieved by current annealing strategies proposed in the literature.

4.2 Materials and methods

4.2.1 Powder

Ti-6Al-4V ELI (Grade 23) atomised spherical powder was acquired from TLS Technik GmbH & Co. Collaborators to the study performed elemental and particle size analysis on the powder. Results of elemental composition and particle size distribution was first published by Thejane *et al.* (2016). Powder size distribution was measured using a MICROTRAC SI/S3500 laser scanner. The results thereof are plotted in Figure 4.1, which shows that the powder size distribution agrees with the manufacturer's specifications.

Powder elemental analysis was done through inductively coupled plasma optical emissions spectroscopy (ICP-EOS) to determine metallic composition. Inert gas fusion was used to

measure the composition of gas elements in the powder. ICP-EOS was done using a SPECTRO ARCOS machine, while inert gas fusion was done using an ELTRA OHN 2000. For technical details, see ELTRA GmbH (2020). The results of the elemental analysis on the powder are given in Table 4.1. This data shows that the powder's alloying elements are within the required standard set by ASTM F1580.
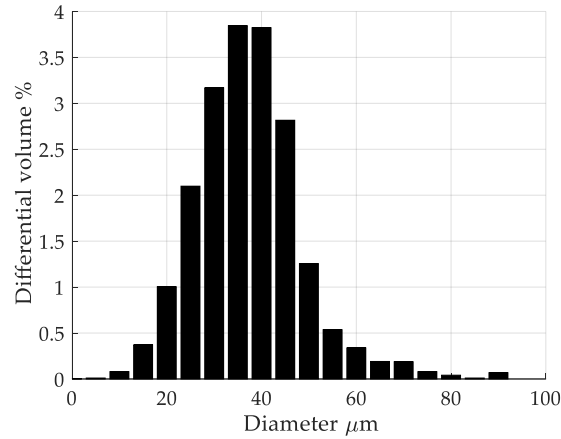
Figure 4.1. Powder size distribution.

Table 4.1. Powder elemental composition (wt%).

Al	V	Fe	N	O	Ti
6.08	3.88	0.170	0.023	0.090	90

Table 4.2. Printing process parameters.

Power (P) [W]	Velocity (v) [mm/s]	Layer thickness (t) [μm]	Hatch spacing (h) [μm]	Energy density ($E_v = P/vth$) [J/mm^3]
100	600	30	105	53
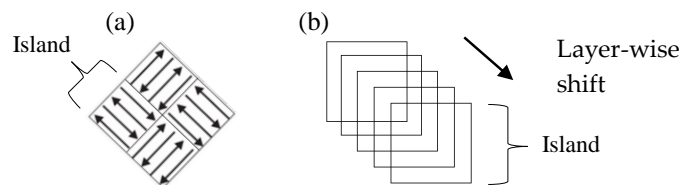
Figure 4.2. (a) island hatch strategy (Thijs, 2014) and (b) island shift strategy.

4.2.2 Build parameters and scan strategy

All samples were built using Concept Laser's M2 machine. Samples were deposited on a wrought Ti-6Al-4V substrate in an argon environment with oxygen concentration below 1200 ppm. Scan parameters are tabulated in Table 4.2. The scan strategy used was Concept Laser's "island" scan strategy, in which each layer is divided into 5×5 mm square islands and exposed in a zig-zag fashion. Scan vectors in each island are exposed at 90° with respect to the neighbouring island and alternating layers. A shift of 2 mm with respect to the previous island layer is used to limit porosity build-up. Figure 4.2(a) illustrates the exposure strategy, and Figure 4.2(b) the shift movement of a single island over five consecutive layers.

4.2.3 Samples and testing

Cylindrical samples with a 15 mm diameter were built, with a length of 93 mm for tensile tests, and a shorter length of 20 mm for microstructural investigations. All samples were built in the Z-orientation, i.e., with their longitudinal axis parallel to the build plane. After the respective heat treatment, long samples were machined into a cylindrical "dog bone" shape with a gauge length (G) of 25 mm and a gauge diameter (D) of 5 mm, in accordance with the 5-to-1 ratio stipulated by ASTM E8M. Finally, the gauge section was polished to a mirror finish. Tests were conducted using an MTS Criterion 44 tensile testing machine. All tests were displacement controlled with a strain rate of 0.001 s^{-1}. Elongation to failure (ε_f) was measured by putting the two broken halves together and measuring the gauge length after failure (G_f), as advised by ASTM E8M. Therefore, $\varepsilon_f = (G_f - G)/G$.

4.2.4 Density measurements

Sample density was measured using the Archimedes principle according to ASTM B311, complimented by micro X-ray computed tomography (XCT). For Archimedes measurements, a Kern and Sohn GmbH, model ABT 120-5DM scale was used. For technical details, see Kern and Sohn GmbH (2020). Instead of water, the suspension liquid used was isopropanol to reduce the formation of air bubbles on the rough sample surface and thereby achieving more consistent measurements. For XCT measurements, a General Electric Phoenix V|Tome|X L240 was used. The middle gauge section of the samples was scanned over a region of approximately 5×5 mm allowing for a voxel resolution of 3 µm.

4.2.5 Heat treatments

The heat treatments were undertaken before machining the samples using a 5 kW Gallenkamp muffle furnace and a EUROTHERM temperature controller. Sample temperature was measured by probing the sample surface with a Type-K thermocouple. Dwell times and cooling rates were heat treatment specific. A muffle furnace was chosen to allow for furnace cooling (FC), air cooling (AC) and water quenching (WQ). Oxidation effects such as scale and α-case hardening were removed through machining post-anneal.

4.2.6 Microstructural analysis

Metallographic samples were ground and polished using Buehler metallography equipment. Light optical microscopy (LOM) was undertaken using an Olympus GX51 optical microscope. Samples were etched using Kroll's Reagent (92 vol% H_2O, 6 vol% HNO_3 and 2 vol% HF) for 5 – 10 seconds to reveal the microstructure.

A Zeiss MERLIN scanning electron microscope (SEM) in conjunction with a backscattered electrons (BSE) detector was used for the electron microscopy analysis. Individual grain width measurements were done with Stream Essentials software tools. Area phase fractions of micrographs were considered realistic estimations of the volumetric α/β phase fractions. Minimum and maximum grain widths were measured using the line-intercept method automated in MATLAB 2017a with the help of MATLAB's Image Processing Toolbox. X-ray diffraction was performed using a Bruker D2 Phaser diffractometer (Cu-Kα source) with a standard Bragg Brentano geometry. Acquisition dwell time was 0.75 second at steps of 0.01°.

4.3 Heat treatment design and approach

The temperature region chosen for annealing in this study was within the SSTR, illustrated in Figure 4.3. In this solid solution, the α-phase is considered the solute and the β-phase the matrix. In this study, the SSTR was defined as the temperature region between the dissolution temperature (T_{dess}) and the β-transus temperature ($T_β$). The dissolution temperature (chosen as a single temperature point) is the temperature region where the β-phase starts to exponentially increase in volume percentage as the α-phase transforms into β-phase. This temperature has been defined as 705 °C (Kelly, 2004).
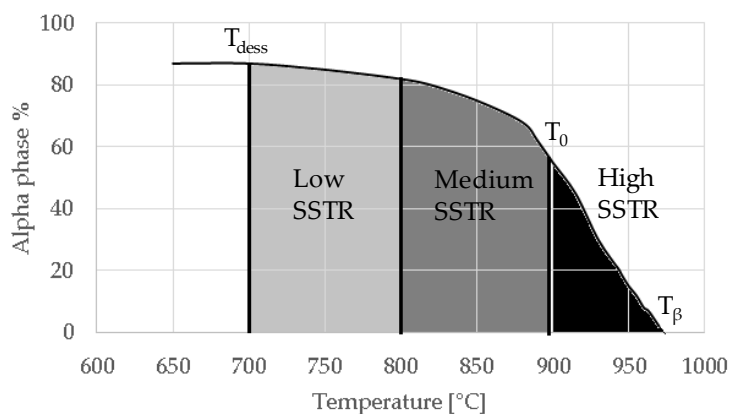
Figure 4.3. Schematic of temperature regions and key temperatures in the SSTR versus estimated α-phase fraction.

The SSTR was furthermore divided into low-, medium- and high-SSTR regions. The low- and medium-SSTRs lie below the critical temperature (T_0), and the high-SSTR lies above T_0. The

critical temperature is defined as the temperature above which α' forms upon fast cooling (water quenching—WQ or air cooling—AC). This temperature has been calculated based on thermodynamic database by Lu *et al.* (2016) and Ji *et al.* (2016), who respectively found T_0 to be 893 °C and 872 °C. The low- and medium-SSTR is separated by the temperature region where α' decomposes into α upon heating (Vrancken *et al.*, 2012; Huang *et al.*, 2015; Sallica-Leva *et al.*, 2016).

The heat treatments tabulated in Table 4.3 were designed to accentuate the effects of dwell temperature and time and cooling rate. Since α-grain growth is limited in low- and medium-SSTR heat treatments, variations in air and furnace cooling as a function of dwell time were considered. High-SSTR heat treatments used quenching, as opposed to furnace cooling, to "freeze" decomposed grains and thereby show the extent of α-grain growth and fragmentation. As such, the α/β phase fraction at the annealing temperature (i.e., *in-situ*) is determined by the α/α' phase fraction since β-phase fully transforms to α' upon quenching.

Table 4.3. Specifications for heat treatment strategies.

Annealing strategy	Temperature [°C]	Hold time [hours]	Method of cooling*
Low-SSTR	750	8	AC
Medium-SSTR	800	2	FC
	870	2	AC
		4	FC
High-SSTR	910	0.5	WQ
		2	WQ
		8	WQ
	945	4	WQ
	960	0.5	WQ
		4	WQ
		4	FC to 930 °C then WQ
		4	FC to 900 °C then WQ
Duplex	910 and 750	8 and 4	WQ and FC

* WQ—water quench, FC—furnace cooled, AC—Air cooled.

4.4 Results

4.4.1 As-built samples

Figure 4.4 shows the as-built microstructure. As expected, the microstructure consists of a fine single-phase α' needle-like grain structure. The measured range of grain sizes was found to be broad (between 10 nm and 3 µm). A hierarchical structure (similar to that measured by Yang, Yu *et al.* (2016)) was observed, consisting of primary, secondary, ternary and quartic α' grains. Table 4.4 lists the measured lengths of the major and minor axis of α' grains.

The BSE-SEM micrograph in Figure 4.4(b) shows the fineness of the ternary and quartic structure. This hierarchical structure forms naturally in α', but gets accentuated during the cyclic heating and cooling in the LPBF process (Yang, Yu *et al.*, 2016). The hierarchical microstructure and broad grain size range are key characteristics influencing the microstructural morphology transformation. This is further discussed in Section 4.5. Twinning dislocations were also observed and are indicated by arrows. This internal twinning has been observed numerous times in the LPBF induced α' phase (Murr *et al.*, 2009; Simonelli, 2014; Xu, Sun, *et al.*, 2015; Krakhmalev *et al.*, 2016; Yang, Yu *et al.*, 2016).

Table 4.4. Hierarchical structure of α'.

Type of α'	Length of major axis	Length of minor axis
Primary	(> 20 μm)	(1 – 3 μm)
Secondary	(10 – 20 μm)	(100 – 900 nm)
Ternary	(2 – 10 μm)	(10 – 90 μm)
Quartic	(< 2 μm)	(< 10 nm)
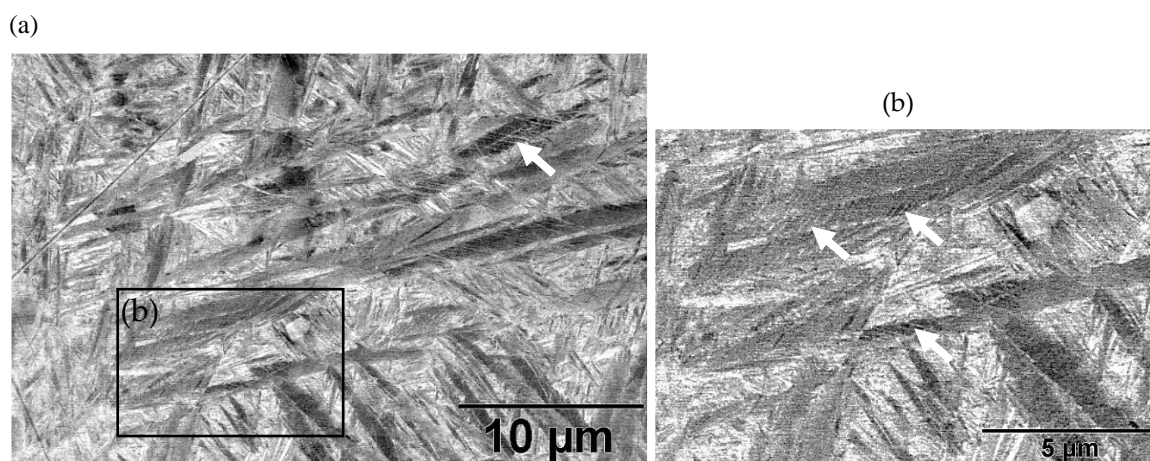
Figure 4.4. As-built microstructure: BSE-SEM image revealing the hierarchical α' grains and sub-grain twinning (indicated with arrows) and (b) an enlarge image indicating sub-grain twinning (indicated with arrows).

4.4.2 Samples annealed in the low- and medium-SSTRs

Table 4.5 provides LOM micrographs and measured grain sizes of samples annealed at low- and medium-SSTRs. The dark regions indicate the etched β-phase. Annealing in the low-SSTR shows the transformation from α' to lamella α+β phases. An increase of the fine as-built microstructure to a 0.5 μm minimum lamella grain width is seen. It is observed that quartic α' grains have been dissolved with little primary, secondary and ternary α-grain growth. The measured increase in the minimum grain size and insignificant growth in maximum grain size

suggests that the fine quartic α' grains have transformed to β-phase, whereas primary, secondary and ternary α' grains have transformed to α-phase grains with minimal grain growth.

Annealing in the medium-SSTR shows grain growth of primary, secondary and ternary α grains indicated by the maximum grain sizes given in Table 4.5. Significant grain growth is measured when comparing cooling rates, where furnace cooling (FC) allowed for a comparatively large amount of α-grain growth within a short period. β-grain width was found to be thicker, and the α-phase fraction was measured to be larger in FC samples compared to air-cooled (AC) samples. These α/β phase fractions agree with those published in the open literature (Semiatin *et al.*, 2003; Elmer *et al.*, 2004, 2005; Kelly, 2004; Murgau *et al.*, 2012).

4.4.3   Samples annealed in the high-SSTR

Table 4.6 summarises microstructure results of samples annealed at 910 °C for various dwell times, followed by water quenching (WQ). Light regions are α' phase (previously β-phase), while the dark grains are undissolved α grains. Annealing in the high-SSTR results in a microstructure that mainly consists of transformed primary and secondary α' grains. Tertiary and quadric α' grains have transformed to β-phase (in this case, transformed to α' upon quenching). This suggests that the hierarchical martensitic rank favours higher-order grains that remain undissolved/untransformed up until $T_β$.

By comparing α/α' phase fraction and therefore, the α/β-phase fraction at annealing temperature prior to quenching, it becomes apparent that a 30-minute dwell time is not sufficient for phase transformation to reach a steady-state equilibrium. Phase fraction equilibrium (41 % α-phase) is reached between 30 minutes and two hours. Grain growth is almost insignificant during this time, however, after eight hours a noticeable increase in grain width is measured. The micrograph of the sample annealed at 945 °C shows a larger amount of grain growth for a four-hour dwell time. α-grain fragmentation is evident (indicated by solid arrows) at prior-β grain boundaries and prior-β grain triple points, resulting in grain globularisation (indicated by hollow arrows). The given phase fractions agree with the equilibrium phase fraction given by open literature (Semiatin *et al.*, 2003; Elmer *et al.*, 2004, 2005; Kelly, 2004; Murgau *et al.*, 2012).

Table 4.7 summarises the microstructure of samples annealed at 960 °C. Similarly, a dwell time of 30 minutes does not allow for an equilibrium phase percentage to be reached. It is interesting to note that the α/α'phase fraction and grain size is similar to that of the sample annealed at 910 °C for 30 minutes. After four hours significant grain fragmentation of elongated α-grains was observed (indicated by solid arrows), resulting in globularisation (indicated by hollow arrows). Furnace cooling from 960 °C after four hours caused significant growth in grain width. Water quenching after furnace cooling to 930 and 900 °C, respectively, produced thick primary α-grains in a matrix of α'. These α-grains are no longer elongated and essentially become equiaxed due to the reduction in aspect ratio. The phase fractions agree with equilibrium phase fraction at these temperatures presented in the open literature (Semiatin *et al.*, 2003; Elmer *et al.*, 2004, 2005; Kelly, 2004; Murgau *et al.*, 2012).

Table 4.5. Microstructure—low and medium-SSTR annealing.
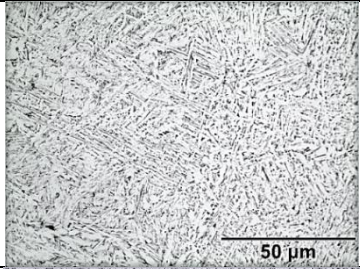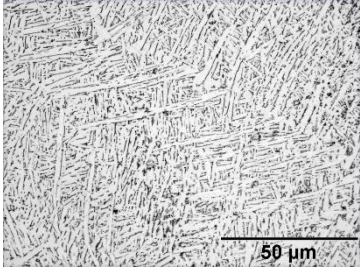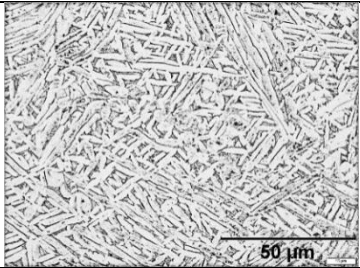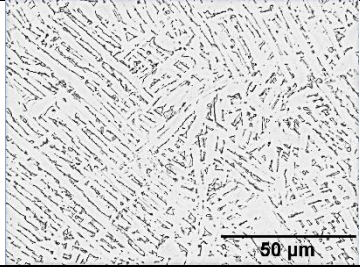
Temperature [°C], hold time	LOM micrograph	α/β phase fraction	α-grain width [min – max]
750, 8 hours AC		87 %	0.5 – 1.5 μm
800, 2 hours, FC		87 %	1 – 2 μm
870, 4 hours AC		65 %	1.5 – 2.5 μm
870, 2 hours, FC		88 %	1.5 – 3.5 μm

57

Table 4.6. Microstructure—annealing at 910 °C and 945 °C followed by WQ. Grain fragmentation and globularisation is indicated by solid and hollow arrows, respectively.
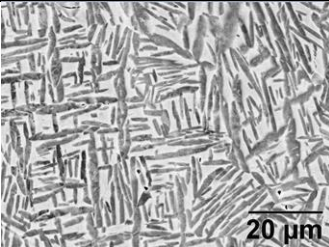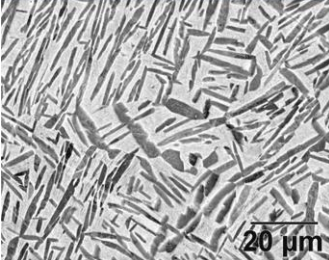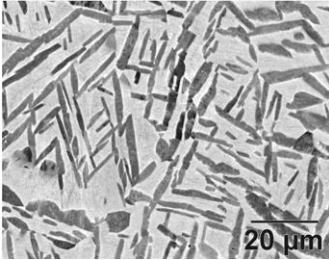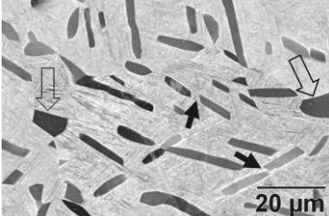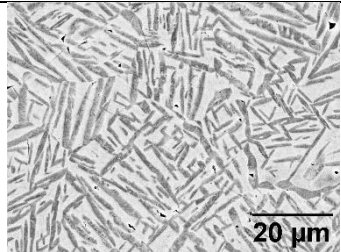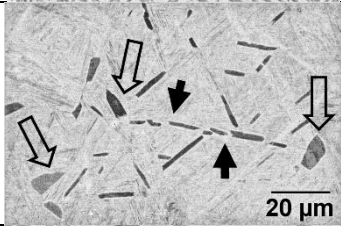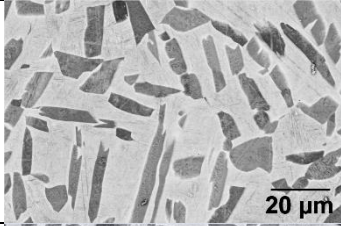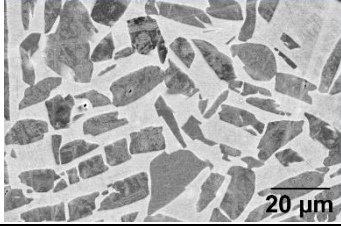
Temperature [°C], hold time	BSE-SEM micrograph	α/α' phase fraction	Median α-grain width
910, 30 minutes		60 %	1.5 μm
910 2 hours		41 %	1.5 μm
910, 8 hours		41 %	2.8 μm
945, 4 hours		20 %	3.5 μm

58

Table 4.7. Microstructure—annealing at 960 °C followed by WQ or FC+WQ.
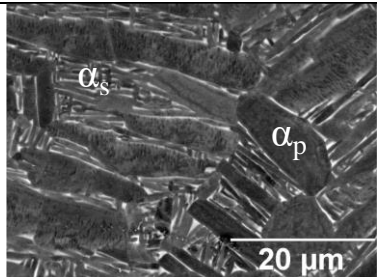
Temperature [°C], hold time	BSE-SEM Micrograph	α/α' phase fraction	Median α-grain width
960, 30 minutes	20 µm	58 %	1.5 µm
960, 4 hours	20 µm	8 %	1.5 µm
960, 4 hours, FC to 930	20 µm	30 %	8 µm
960, 4 hours FC to 900	20 µm	48 %	11 µm

4.4.4 Duplex annealed samples

Fast cooling by WQ from above T_0 in the high SSTR achieves a bi-modal microstructure of α in a matrix of α'. The α' is an unwanted phase due to its metastable and brittle nature. Thus, a second annealing step is introduced to decompose the newly formed α' into (α+β) lamellar using a low-SSTR anneal.

Table 4.8 summarises a bi-modal microstructure achieved through such a duplex annealing strategy. Shown is a bi-modal microstructure consisting of an equiaxed primary α-phase and lamella secondary α. Grain sizes vary from a relatively large 5 µm globular structure to an elongated 1 µm grain width.

Table 4.8. Bi-modal microstructure.

Temperature [°C], hold time	BSE-SEM micrograph*	α_p/α_s phase fraction	Median grain width
910, 8 hours WQ, followed by 750 4 hours FC		~41 %	Primary: 5 μm Secondary: 1 μm

*α_p—primary α, α_s—secondary α.

4.4.5   Tensile behaviour

The mean and median sample densities were measured at 99.25 % and 99.22 %, respectively, while the build's minimum and maximum density were measured at 98.78 % and 99.85 %, respectively. The geometry of porosity was observed to be spherical using micro XCT. The results of uniaxial tensile tests are presented in a plot of UTS versus % elongation-to-failure shown in Figure 4.5. Samples in the plot are grouped with ellipses which represent 1.5 standard deviation of the group's mean.

The ductility of the as-built group exceeded expectations. This could be attributed to the presence of compressive residual stresses in an as-built state that has been shown to act as strengthening mechanisms (Mercelis & Kruth, 2006). Low- and medium-SSTR samples both achieved a varied improvement in ductility at a significant cost of strength. Duplex samples achieved a noteworthy increase in ductility, with a strength similar to samples annealed in the medium-SSTR. On average, the ductility of low-SSTR samples was lower than both the as-built and medium-SSTR samples due to two samples performing poorly.
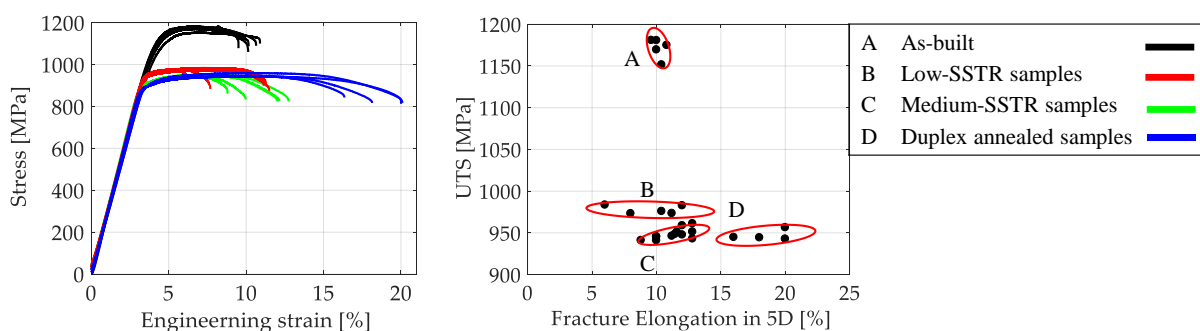
Figure 4.5. Plot of ultimate tensile strength (UTS) versus fracture elongation for the four groups of tensile samples.

4.5 Discussion

4.5.1   Background to morphological transformations

Two fundamental mechanisms that drive morphological transformation have previously been observed.

Type-1: is a phase transformation driven by the minimisation of Gibbs free energy (Ji *et al.*, 2016). The major contribution being the entropy or chemical potential energy of alloying elements in the respective α- and β-phases (Ji *et al.*, 2016). A change in α/β-phase fraction through phase transformation occurs until a stable/equilibrium alloy concentration is reached (Katzarov *et al.*, 2002). This is driven by atomic diffusion across the phase boundary. The diffusion rate (and therefore the phase transformation rate) is complexly dependent on a large range of parameters, including temperature, interface mobility, diffusivity and the fluctuating alloy concentration across the phase (Katzarov *et al.*, 2002). Upon cooling, the phase transformation mechanism is sensitive to the rate of change in temperature, where the phase transformation route of least energy is taken. Atomic diffusion is favoured during furnace, cooling while a shear displacement (non-diffusive) transformation is favoured during fast cooling—the latter route results in the formation of α' (Ji *et al.*, 2016).

Type-2: Grain morphology transformations are driven by grain surface-area minimisation; to minimise the total surface energy, smaller grains shrink in size while larger grains grow (Callister & Rethwisch, 2011). This mechanism is dependent on time and temperature, and the rate of grain growth increases with an increase in temperature. While both mechanisms occur simultaneously, the second mechanism becomes more noticeable at higher temperatures where grain globularisation is observed.

4.5.2   Low- and medium SSTR heat treatments

Annealing below T_0 is currently the most common annealing strategy for LPBF-produced Ti-6Al-4V. At low- and medium-SSTR heat treatments, the nucleation and growth of β-phase at grain boundaries and twinning dislocations start is observed. Due to the hierarchical structure of α', illustrated by Figure 4.6(a), the phase transformation (morphology transformation mechanism Type-1) of α' → β during annealing below T_0 is initiated by the transformation of the smallest α' grains first, followed by subsequent larger grains (quartic → ternary → secondary). Figure 4.6(b) and (c) demonstrate this mechanism by showing β-phase replacing the quartic α' grains. Since primary α' grains are the largest, complete transformation of these occur last (at T_β). As such, the transformed primary α' grains become more dominant in samples annealed at increasingly higher temperatures. This was observed by an increase in the measured minimum grain width of sub-T_0 treated samples. Thus, morphology transformation mechanisms Type-1 can be argued to be more dominant.

The rate of α-grain growth at isothermal temperature was measured to be low, increasing at higher temperatures. At low- to medium-SSTR heat treatments, primary and secondary α-phase growth was in the order of 1 μm. Morphology transformation mechanism Type-1 is also argued to be dominant during the isothermal hold. The dominant influence on grain growth at this

temperature range was shown to be the cooling rate, where furnace cooling allows for further α-grain growth by 1 – 2 µm and an increase in α-phase percentage.
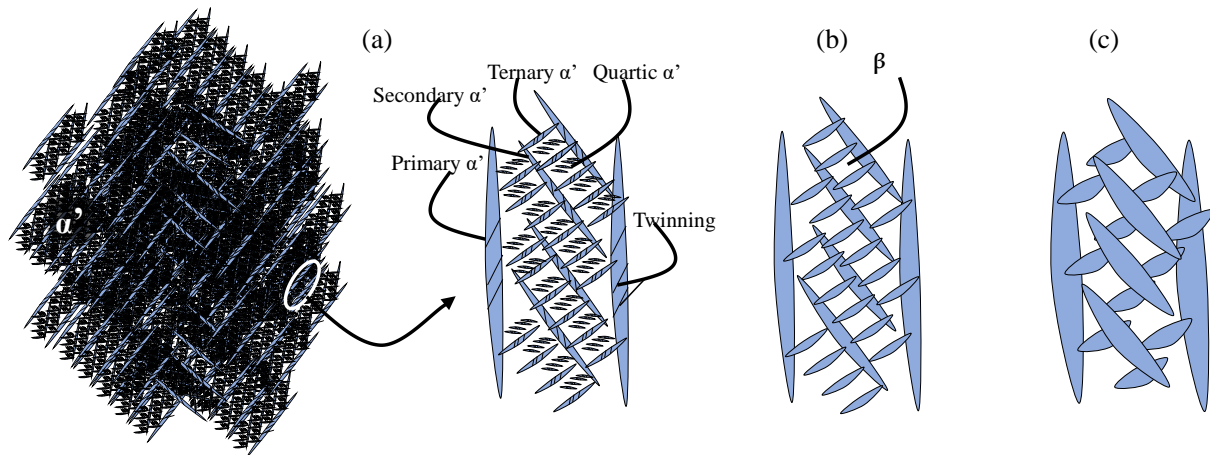
Figure 4.6. Schematic of (a) martensitic α' hierarchical structure and annealing in the (b) low- and (c) medium-SSTR.

Figure 4.7 depicts Bragg peaks between 2θ angles of 38° to 40° for low-, medium-SSTR annealed and powder samples. Both low- and medium-SSTR annealed samples show α-phase (hexagonal close-pack, hcp, lattice structure) Bragg peak positions aligned with one another. The martensite decomposes to the α phase, as can be seen by the shift of the peak from the higher angle to the lower angle. (Tan *et al.*, 2016).
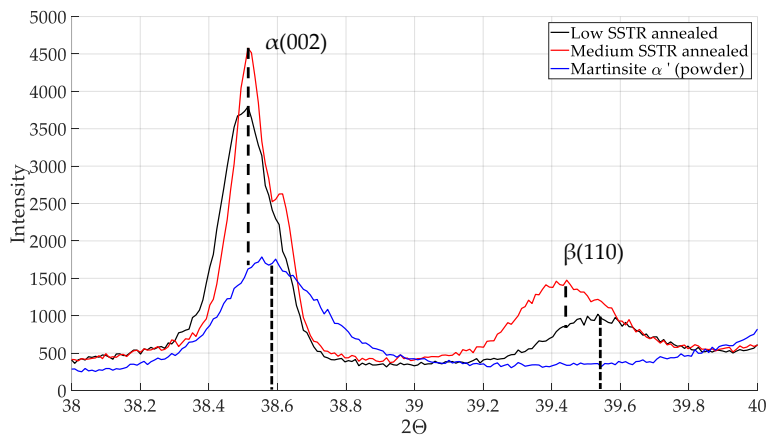
Figure 4.7. XRD plot of martensitic powder and samples annealed in the low and medium-SSTR.

62

During low-SSTR heat treatments, smaller quartic and ternary grain transformation are driven by diffusion (mechanism Type-1) whereby smaller α' grains shrink and dissolve to form β. This is visible in Figure 4.7 by the formation of the β-phase (body centred cubic, bcc, lattice structure) Bragg peak. At medium-SSTR the β-phase peak shift indicates higher concentrations in vanadium (low-SSTR samples have a smaller β-phase lattice spacing). Therefore, the observed morphological change in microstructure is seen to be driven by a combination of diffusion (mechanism Type-1) and surface energy minimisation (mechanism Type-2).

Furthermore, due to the reduction in the β lattice parameter, a larger mismatch of the α/β lattice parameters exists at the phase interfaces. This mismatch promotes the formation of dislocations once deformation begins (Tan *et al.*, 2016), and therefore, results in a higher interface strength and hence increased hardness and yield strength. Furthermore, a widening of α/β interface will weaken interface strength, while a narrower interface will increase strength (Tan *et al.*, 2016).

The low- and medium-SSTR annealed samples' tensile behaviour reveal two important considerations: (1) the medium-SSTR annealed samples achieved a lower strength compared to the low-SSTR annealed samples. This is due to a widening in the lamella α-laths and a larger β lattice spacing allowing for less mismatch between hcp and bcc slip planes. (2) the ductility of the low- and medium-SSTR annealed samples are similar. Therefore, is advised to anneal in the low-SSTR to achieve superior strength.

4.5.3   High-SSTR and duplex anneal

Figure 4.8 depicts the morphology of samples in the high-SSTR. Primary and secondary α-grain fragmentation is abundant, identifiable by the formation and widening of twinning sites where β-phase forms. The amount of β-phase formation enhances the fragmentation process, and therefore, grain fragmentation increases significantly with an increase in temperature above T_0. Grain growth is increased after fragmentation by surface energy minimisation (mechanism Type-2). In addition, the diffusion mechanism (mechanisms Type-1) is enhanced at slower cooling rates, resulting in massive α-grain growth. At high cooling rates, fragmented primary and secondary α-grains are "frozen" in a newly formed α' matrix. Since the brittle and metastable nature of α' is not always desired, a second anneal cycle at a low-SSTR is suggested to transform α' to α.

The large size of the fragmented primary α-grains greatly improves part ductility. The UTS of bi-modal samples coincided with that of the medium-SSTR samples. It is concluded that the secondary α+β structure has a dominant effect on strength since the addition of larger primary α-grains in the bi-modal microstructure did not significantly affect the UTS. A further increase in strength may be obtained by refining the secondary α+β structure, as argued in the previous section.
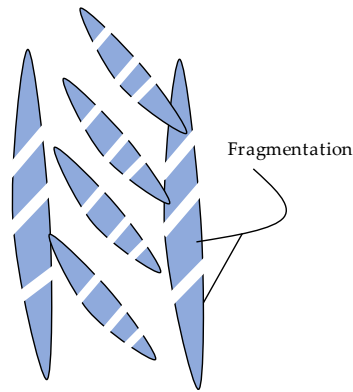
Figure 4.8. Schematic of morphology transformation during annealing in the high-SSTR.

4.6 Conclusions

This study pursued the improvement in tensile behaviour (UTS versus ductility) of LPBF-produced Ti-6Al-4V, beyond that which is currently achieved by post-process published annealing strategies. The study aimed to obtain a fundamental understanding of morphology transformation of LPBF-produced Ti-6Al-4V α' as a function of temperature, hold time and cooling rate in the SSTR. A bi-modal microstructure without the need for thermomechanical working was developed. Through understanding α-grain morphology transformation, the research demonstrated the advantages of internal twinning dislocations inherent in α', and the use thereof to fragment grains during a high-SSTR anneal. Bi-modal microstructures, consisting of fragmented equiaxial primary α-grains in a matrix of (α+β) lamellar, can be achieved through fast cooling from a high-SSTR, followed by a low-SSTR annealing step. The paper showed that a microstructure that achieves superior tensile properties to standard annealing strategies is possible for LPBF-produced Ti-6Al-4V.

4.7 Post-submission discussion

The following discussion stems from insights gained from reviewer feedback and literature published post-submission. At the time of writing, very few studies could be found that achieved a ductility of as-built LPBF-produced Ti-6Al-4V above 8 %, and thus the as-built ductility "exceeded expectations" (see Subsection 4.4.5). As the authors became aware of more publications on as-build Ti-6Al-4V, however, it became clear that the results of as-built samples lie in the upper-end of reported values and are therefore on-par with published results.

Due to the two outliers of the low-SSTR sample group, this group's average ductility is lower than that of the as-built group. It is possible that these outliers were caused by porosity in the samples. It is further argued that, once the outliers are excluded, the low-SSTR group will achieve a ~11 % ductility, which is slightly higher than the as-built group (as expected). Tensile stress-strain curves were also included post-submission to aid in data visualisation.

Although the powder's oxygen content is provided, no data of the oxygen concentration in the fabricated samples is reported. Significant take-up of oxygen in the samples during the build was considered negligible since the machine operates in a low oxygen environment (high purity argon environment) of less than 0.12 at% oxygen—measurements of oxygen concentration in powder after consecutive builds was added to the manuscript post-review, Table 4.9. After each build, the low increase in powder oxygen concentration supports the argument of a negligible oxygen pick-up of the built parts. Although slight oxygen pick-up is recorded after each build, the oxygen concentration is still below the 0.13 wt% recommended by the standard.

Table 4.9. Oxygen concentration of powder after three consecutive builds.

Build cycle	Oxygen concentration [wt%]
1	0.082
2	0.092
3	0.096

5 Low-temperature stress relief and martensitic decomposition in laser powder bed fusion-produced Ti-6Al-4V

A major quality concern in LPBF-produced Ti-6Al-4V is high residual stresses in as-built parts. Although post-processing in the SSTR, presented in Chapter 4, is effective in fully relieving these residual stresses, a significant loss in material strength is caused due to α-grain growth. Although thermal treatments at lower temperatures suppress α-grain growth and thereby achieve a higher material strength, little understanding of the microstructure and stress relief response of heat treatments at sub-SSTR temperatures exists, particularly of the initial stages of martensite decomposition. This chapter addresses the second project objective by investigating the response of residual stress and microstructure as a function of temperature and hold time below the SSTR.

This work was presented at the first European Conference on Structural Integrity of Additive Manufactured Materials (ESIAM) in Trondheim, Norway. This resulted in a shortened version of this chapter being published as a special article in the journal *Material Design and Process Communication* (Ter Haar & Becker, 2020)[6]. This work has also been presented at the 2018 RAPDASA conference and at the 56th Congress of the Microscopy Society of Southern Africa. The full version of the article is presented in this chapter.

Declaration by the candidate:

With regards to Chapter 5, the contributions of author and co-authors is as follows:

Name	Email	Contribution	Extent (%)
G.M. Ter Haar (candidate)	gterhaar@sun.ac.za	Experimental design, completion of all tests and data analysis, writing and compilation of manuscript	90
T.H. Becker	tbecker@sun.ac.za	Supervision and reviewing	10

Signature of candidate: [GTH] (see Footnote 5)
Date: 2021/02

Declaration by the candidate:

The undersigned hereby confirm that:

1.   The declaration above accurately reflects the nature and extent of the contributions of the candidate and the co-authors to Chapter 5,
2.   No other authors contributed to Chapter 5 besides those specified above, and

---

[6] DOI link: https://doi.org/10.1002/mdp2.138

3.   Potential conflicts of interest have been revealed to all interested parties and that the necessary arrangements have been made to use the material in Chapter 5 of this dissertation.

Signature (see Footnote 5)	Institutional affiliation	Date
[TH Becker]	SU	2021/02

5.1 Introduction

Metal additive manufacturing (AM) has the potential to revolutionise the metal manufacturing industry by bringing innovative and possibly disruptive capabilities to both design and manufacturing. Novel design capabilities, owing to the high level of achievable part complexity, allow for a reduced number of parts and optimised weight-to-strength ratio through techniques such as topology optimisation. Novel manufacturing capabilities include the democratisation of manufacturing, the decrease in manufacturing lead-time, and low-cost customisation. Furthermore, minimal material waste is achieved compared to traditional subtractive manufacturing methods such as milling and turning. Currently, the most commonly employed metal AM technique is a laser powder-bed fusion (LPBF) process, popularly referred to as selective laser melting (SLM). This technique entails the melting-and-solidification of fine spherical metal powder, using a high-power laser, in a layer-wise fashion.

The aerospace industry is particularly interested in the application of LPBF to produce Ti-6Al-4V components. This two-phase alloy boasts both high-temperature corrosion resistance and high specific strength, making it ideal for light-weight aerospace components. Furthermore, the alloy is biocompatible and therefore suitable for medical bone-replacement implantation. Together with the capabilities of AM, these material properties make LPBF-produced Ti-6Al-4V an attractive alternative to its wrought-produced counterpart.

This technology's process and manufacturing chains are still in its primary stages, and therefore the achievable mechanical properties of LPBF-produced parts are not optimal compared to their wrought produced counterparts (Shunmugavel *et al.*, 2015). While the LPBF-produced variant boasts exceptional strength—primarily due to the fine martensitic microstructure—this is countered by poor ductility, toughness and fatigue life (Shunmugavel *et al.*, 2015; Yan & Yu, 2015). Since the application of the material by aerospace is that of load-bearing and load-critical parts, such as turbine blades (Siemens, 2018), the enhancement of material performance of LPBF-produced Ti-6Al-4V is critical for its acceptance by industry leaders such as Boeing and Airbus.

The current research investigates two unfavourable LPBF-produced Ti-6Al-4V material properties, both caused by the high localised heating and cooling inherent in the LPBF process. Rapid localised heating and cooling rates of the Ti-6Al-4V melt pool and neighbouring local material of $10^3 – 10^8$ K/s (Vilaro *et al.*, 2011; Hodge *et al.*, 2014) causes (1) high non-uniform residual stresses and (2) a poor ductility caused by a fine hierarchical acicular martensitic microstructure.

High non-uniform macro residual stresses are caused by two thermal mechanisms in LPBF-produced metals: the thermal gradient mechanism (TGM) and the cool-down mechanism (Mercelis & Kruth, 2006). Both mechanisms rely on the principle of local material expansion and contraction that induces compressive and tensile stresses on neighbouring material in proportion to the material's thermal strain. The strain's magnitude is dependent on the coefficient of thermal expansion and the change in material's temperature. Ti-6Al-4V's poor thermal conductivity, together with the high rate of heating and cooling, results in high thermal gradients and consequently high residual stresses. While the TGM acts locally to the melt pool, the cool-down mechanism acts layer-wise. The resultant residual stress can lead to part distortion (warpage), inter-layer and/or build plate delamination (Anderson, 2017; DebRoy *et al.*, 2018), and the deterioration of fatigue properties and fracture toughness (Leuders *et al.*, 2013, 2014; Vrancken *et al.*, 2014; DebRoy *et al.*, 2018).

The second effect of rapid cooling is the formation of a fine acicular martensitic microstructure. Martensite is an unstable or metastable microstructure that forms from a body-centred cubic (bcc) phase through a non-diffusive phase transformation when the material is cooled at a high rate from above the martensite starting temperature. Two martensitic microstructures can form depending on the bcc solute (i.e., vanadium) concentration. The most abundant type has a hexagonal close-packed (hcp) structure (denoted α') known for its high internal dislocation twin structure and stacking faults (Yang, Yu *et al.*, 2016). The less abundant martensitic phase has a face-centred orthorhombic or distorted hexagonal structure (α'') (Murr *et al.*, 2009; Heo *et al.*, 2014). A full martensitic transformation (β → α'/α'') results from rapidly cooling from above the β-transus temperature (calculated as ~976 °C for Ti-6Al-4V ELI (Grade 23) by Ji *et al.* (2016)).

Varying the build process parameters (such as the scan strategy or layer thickness) has had limited success in reducing residual stress (Kruth *et al.*, 2010; Anderson, 2017). Recent studies into so-called "intrinsic heat treatments" produced an α+β lamellar microstructure by decreasing the hatch distance and thereby increasing the input energy density (Barriobero-Vila *et al.*, 2017). Currently, a more time-effective approach to achieve both a stress-free and stable (α+β) microstructure from as-built material is through post-process heat treatments or hot isostatic pressing.

Traditional thermo-mechanical processing (TMP) strategies applied to wrought-produced Ti-6Al-4V have been extensively developed and optimised over the years, and therefore, have become a standardised step in the fabrication of conventional titanium components. For example, the aerospace material specifications standard for heat treatments of titanium and titanium alloys (AMS H81200D). Since LPBF is a net-shape manufacturing process, mechanically deforming the as-built structure would be counterproductive. Thus, TMP is not a suitable process/strategy for improving the microstructure and properties of LPBF Ti-6Al-4V.

Ter Haar and Becker (2018) demonstrated the diffusion-controlled α' martensite decomposition process in the sub-β-transus solid solution temperature range of 750 – 960 °C and identified heat treatment processes that result in a fully stabilised α/β lamellar microstructure. While a slight increase in ductility is achieved, this comes at the cost of material strength reduction due to coarsening of α-plates following the Hall-Petch relationship (Cao *et al.*, 2018).

The influence of annealing strategies on residual stress and martensite decomposition at lower temperatures has also been reported. Tan *et al.* (2016) have found that annealing at 600 – 650 °C is sufficient for decomposing α' to a dual-phase α+β microstructure. AMS-H-81200D and Donachie (2000) recommend a stress relief annealing strategy for wrought Ti-6Al-4V of 480 – 650 °C for 1 – 4 hours. For LPBF-produced Ti-6Al-4V, it has been found that a stress relief heat treatment strategy of 650 °C for four hours is effective in relieving residual stresses (Vrancken *et al.*, 2014). A known phase formation in wrought Ti-6Al-4V when annealing below 600 °C is the precipitation hardening through the intermetallic Ti$_3$Al. These precipitates form in wrought-produced Ti-6Al-4V in the presence of more than ~5 wt% aluminium after long hold times (8 – 24 hours) at a temperature of 500 – 550 °C (Lütjering & Williams, 2007; Lunt *et al.*, 2017). A higher temperature of 622 °C has also been reported based on thermodynamic calculations (Ji *et al.*, 2016).

Although numerous studies can be found addressing stress relief and martensite decomposition at 600 °C and above, few have investigated lower temperature treatments in depth. Furthermore, the kinetics of martensite decomposition is not well understood, as expressed by Donachie (2000): "one of the least understood concepts in the behaviour of α-β titanium alloys is that of ageing." Research into the thermal effect of temperatures below 600 °C is particularly relevant to current research and industry application. This is because base plate pre-heating is a potentially valuable technique for minimising residual stress during the build (Kempen *et al.*, 2013; Vrancken, 2016) while lowering energy consumption (and thereby cost). Industrial companies such as ADC AeroSwift (South Africa) have started to manufacture parts with base-plate heating of 200 °C, although much higher temperatures are possible with the machine in question (Louw & Pistorius, 2019). See Appendix A.3.

This study complements the on-going research efforts to establish and improve post-process heat-treatment strategies to relieve residual stress and improve part ductility in LPBF-produced Ti-6Al-4V. This paper investigates thermal treatments' influence in the temperature range 427 – 610 °C on two aspects of LPBF-produced Ti-6Al-4V: residual stress and microstructure. This study demonstrates the nature of stress relief and the initial stages of martensitic decomposition at low temperatures.

5.2 Materials and methods

The experimental work is summarised in Table 5.1. The experimental approach in this study was aimed at measuring and monitoring changes in residual stress and microstructure over temperature and time. Subsequently, tensile tests were applied to specific heat treatment strategies to observe the effect of the resultant microstructure on tensile behaviour. Standard processing parameters were used to manufacture samples. The identified range was divided into four temperatures: 427, 480, 560, and 610 °C to observe residual stress and microstructural changes with respect to temperature. Each temperature was allocated four hold times to observe the material-change with respect to time.

To compare the progress of martensite decomposition to a stable α+β microstructure, a reference sample was produced through annealing an LPBF-built sample at 1000 °C for 2 hours, followed by furnace cooling to room temperature.

Table 5.1. Summary of experimental work. Temperatures reported in °C.

	Experiment/measurement					
	Residual stress	Hardness	SEM	STEM	Rietveld Refinement	Tensile test
As-built	✓	✓	-	-	✓	✓
Reference	-	✓	✓	-	✓	-
Hold time						
5 min	all	all	-	480	480	-
15 min	-	480, 560	-	-	480	-
1 hour	all	all	-	480	480	480, 560, 610
8 hours	-	610	-	-	-	610
30 hours	427, 480	all	all	480	all	-

5.2.1 Build parameters, scan strategy and geometry

Samples were built using powder from the same batch presented in the previous chapter (see Subsection 4.2.1). Samples were built using an EOS M280 machine with standard process parameters for Ti-6Al-4V. Samples were built on a wrought Ti-6Al-4V substrate in an argon environment with oxygen concentration below 1200 ppm. Cylindrical samples of diameter 15 mm and length 90 mm were built. All samples were built simultaneously on a single build plate. Samples were divided into two groups: one group intended for X-ray diffraction (XRD) analysis, microscopy inspection and micro-hardness indentations, and a second group for tensile tests. The first group samples were cut into shorter sections while samples intended for tensile testing were machined into "dog-bone" shaped samples. Details of the tensile testing procedure is given in Subsection 5.2.5.

5.2.2 Heat treatment design

A temperature range chosen for investigation was based on literature-reported effective stress relief temperatures. A minimum temperature of 427 °C was chosen, as it is the minimum annealing temperature to influence mechanical properties and the minimum of the traditional ageing strategy (Donachie, 2000). The upper limit of 610 °C was chosen as a minimum temperature of commonly applied stress relief heat-treatments. The heat treatments were undertaken using a 5 kW Gallenkamp furnace and a EUROTHERM temperature controller. Sample temperature was measured by probing with a Type-K thermocouple.

5.2.3 Microstructural analysis

Samples intended for XRD analysis were sectioned at using a low-speed precision cutter with a diamond-tip blade. Slow cutting speed and lubrication allowed for negligible temperature

increase. For XRD analysis, samples were left as-is after annealing (i.e., no further surface treatments were undertaken). The majority of samples had surface oxidation to a low enough degree to allow for the successful acquisition of XRD data. This is further discussed in the next subsection. The nature of the cutting allowed for a smooth surface.

SEM and micro-indentation samples were also cut as described above but afterwards ground and polished using the standard recommended Buehler metallography procedures and equipment. Samples prepared for Scanning Transmission Electron Microscopy (STEM) were cut using fine ion beam (FIB) milling in an FEI-HELIOS-Nanolab-650.

Both a Zeiss MERLIN and a JEOL JSM 7001F scanning electron microscope (SEM) were used in conjunction with a backscattered electron (BSE) detector to monitor phase transformation. For STEM analysis, a JEM-ARM200F microscope was used. Electron energy loss spectroscopy (EELS) was used in conjunction with STEM to map elemental composition. Both high-angle annular dark-field (HAADF) imaging and annular bright field (ABF) STEM imaging were used to image microstructural features at nano-scale resolution.

5.2.4 X-ray diffraction

When conducting residual stress measurements on the sample surface, an identified concern was the potential relaxation of the stress during sample preparation. For example, any mechanical cutting, grinding, or polishing procedure poses a risk of altering surface residual stress states. An initial solution to avoid mechanical cutting was to scan the samples final layer's top surface. However, it was found that the top layer's surface roughness was too great to reliably measure XRD. Therefore, an alternative solution was conducted: first, the sample was sectioned with a low-speed precision cutter using a diamond-tip blade at 5 mm below the top layer, after which residual stress was measured on the smooth cut surface both before and after annealing. It is acknowledged that the necessary mechanical cutting would have influenced the residual stress state of the as-built sample, but since only the nature of stress relaxation was of interest and not the actual stress state induced by LPBF, this was not deemed problematic. Therefore, the samples' residual stress state is not an accurate representation of the residual stress induced by the LPBF process but a representation of the level of stress relaxation from a similar initial state. The cutting procedure was identical for all samples, and the starting residual stress is assumed to be identical for each sample.

For residual stress measurements, the $\sin^2 \psi$ method was followed in accordance with BS EN15305:2008. A Bruker D8 Advanced XRD machine (at KU Leuven) with a Cu-K$_\alpha$ (1.541838 Å) radiation source set at 40 kV and 40 mA was used. The primary source was fitted with a 0.8 mm diameter collimator. Eleven ψ angles were scanned from -45° to +45°. A 2θ peak at ~142° (HKL plane 213) was chosen for stress analysis. The 2θ step size was set at 0.02° and the count time per frame was 2.1 seconds—data process software DIFFRAC.LEPTOS-7 was used together with a biaxial stress model. Material constants for Ti-6Al-4V hcp phase were selected from material database of the analysis software (S$_1$ = -2.86 $\times10^{-6}$ MPa^{-1} and ½S$_2$ = 11.69 $\times10^{-6}$ MPa^{-1}).

Wide-angle 2θ scans were done with a Bruker D2 PHASER XRD machine (goniometer primary and secondary radius 70.7° and detector 2θ angular range 5.638°) fitted with a 2.5 mm secondary Söller slit. The X-ray generator was set at 30 kV and 10 mA. Samples were scanned with a Cu-K$_\alpha$ (1.541838 Å) radiation source with a hold time of 0.75 second at 0.02° step size. Rietveld refinement was done on selected samples using MAUD (Lutterotti *et al.*, 1999) to obtain lattice parameter data.

5.2.5   Mechanical testing

Tensile tests specimens were machined to a sample geometry recommended by ASTM E8 (sample gauge diameter 5 mm and a gauge length of 25 mm). The reduced sectioned measured 35 mm, and the ends were machined and then cut with an M12 thread. Tensile tests were conducted using an MTS Criterion Model 44 tensile testing machine at a crosshead displacement rate of 0.13 mm/min.

A change in microhardness is a useful indicator of microstructural change. Vickers microhardness measurements were therefore taken to obtain qualitative information about microstructural transformation. Micro-indentations were conducted using an Emcotest DuraScan automatic indentation machine. A diamond-shaped indenter was used, and measurements were conducted according to ASTM standard E348-10. Load application was 2 kg-force for 10 seconds.

5.3 Results

This section presents (a) the results of stress relaxation as a function of annealing temperature and time and (b) the influence of annealing temperature and time on microstructure and tensile behaviour.

5.3.1   Residual stress profile

Figure 5.1 displays the compressive stress profiles with respect to the time of four temperatures. Broken lines indicate estimated paths while solid lines connect measured data points. While residual stresses are relieved for all temperatures, the rate of stress relaxation in the first 5 minutes increases with temperature. While samples annealed at 427 and 480 °C show a relatively slow stress relaxation rate, samples annealed at 560 and 610 °C show a significant increase in stress relief rate. It should be noted that the nature of stress relaxation is in agreement with that found by Donachie (2000). Due to surface oxidation of samples "560_30 hours" and "610_30 hours," XRD measurements of residual stress of these samples were unsuccessful but are assumed to decrease to a negligible low value as the trend in the data suggests. Raw data of the residual stress measurements obtained from KU Leuven and NECSA are provided in Appendix D.
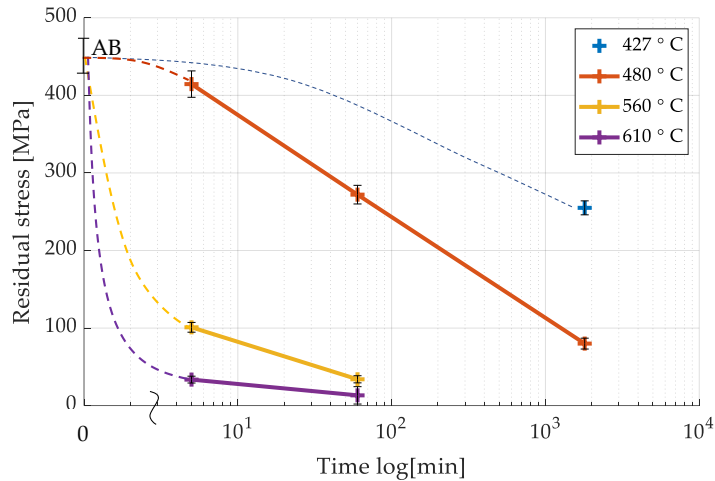
Figure 5.1. Compressive residual stress profiles as a function of time for the as-built and annealed samples (AB—as-built).

5.3.2 Microhardness profiles

Figure 5.2 displays plots of the microhardness profiles as a function of time for three temperatures as well as a single measurement for 427 °C. All three profiles indicate a rise in microhardness from the as-built hardness of ~345 HV2 until a peak in microhardness is reached and the microhardness starts to decrease. To determine whether the cause of the transitional hardness of the 610 °C samples (i.e., an increase, followed by a decrease in hardness) is the same for lower temperature samples, the sample "610_30hours" was further annealed at 480 °C for 30 hours. However, this resulted in no change in hardness. Therefore, it can be assumed that the transitional increase in hardness is due to a phase change that is completed when annealed at 610 °C for 8 hours (~350 HV2).

73
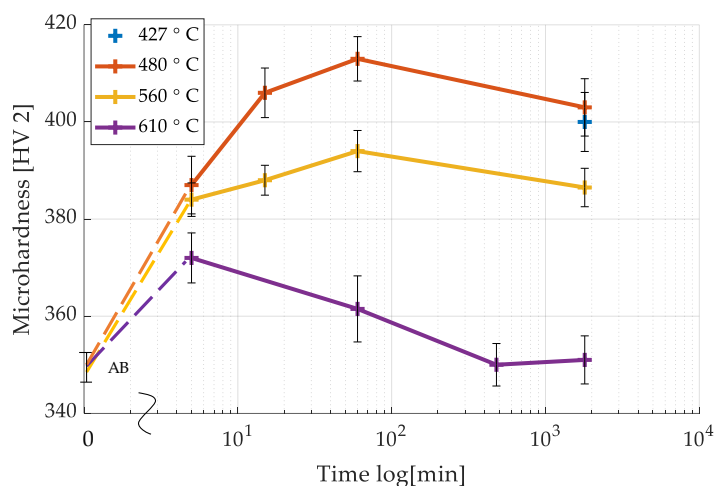
Figure 5.2. Microhardness profiles as a function of time for different annealing temperatures (AB—as-built).

5.3.3   Microstructural analysis

SEM micrographs and EDS analysis of the reference sample is provided in Figure 5.3. Approximate volume fractions of the phases were obtained through image processing. Bright precipitates homogeneously distributed on the inside of α-grains were observed as indicated by arrows. These precipitates appeared to be very similar to the observed Ti_3Al precipitates observed by Carreon *et al.* (2014) and Lee *et al.* (2008). Vickers micro hardness indentations of the α-grains further revealed a microhardness of ~430 HV0.1, which is much higher than the theoretical hardness of α, 310 HV (Crespo, 2011). This suggests that the precipitates are likely the Ti_3Al intermetallic phase.

74
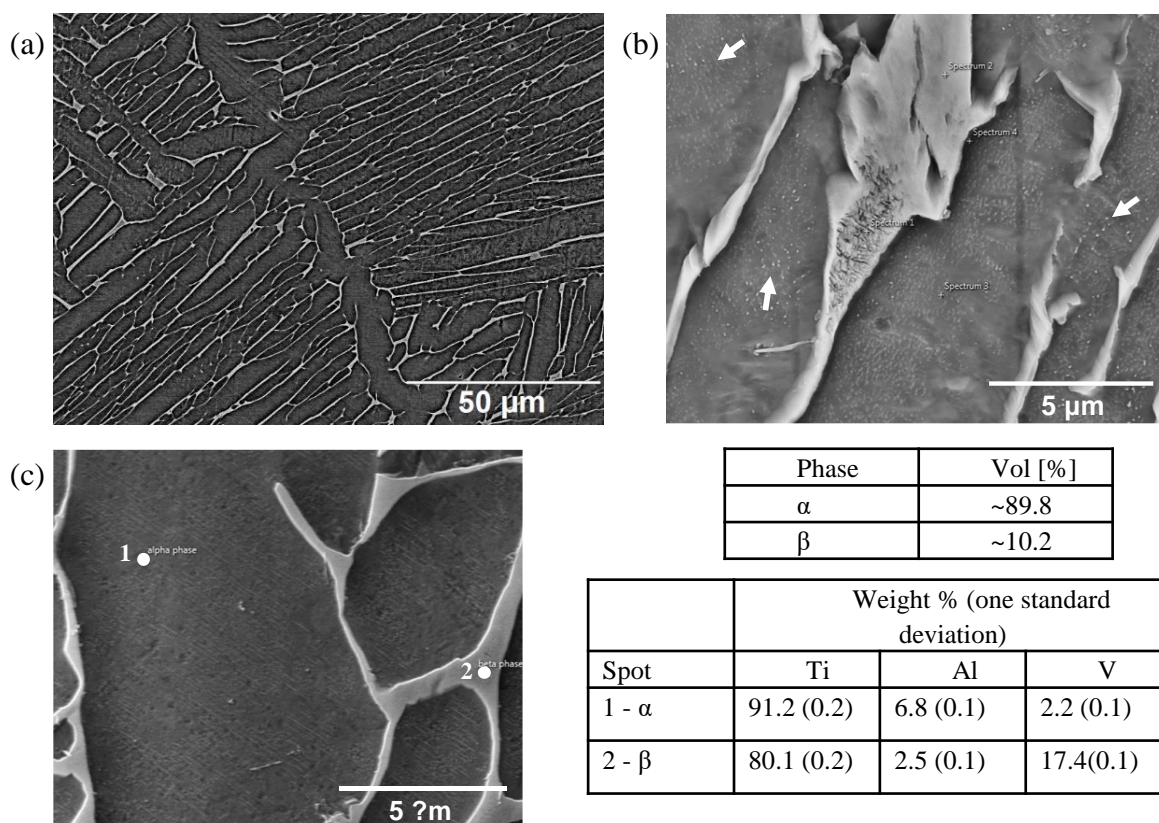
Figure 5.3. Reference sample SEM micrographs and elemental EDS analysis results. (arrows highlight Ti₃Al precipitates in the α-grains).

Phase	Vol [%]
α	~89.8
β	~10.2

Spot	Weight % (one standard deviation)		
	Ti	Al	V
1 - α	91.2 (0.2)	6.8 (0.1)	2.2 (0.1)
2 - β	80.1 (0.2)	2.5 (0.1)	17.4(0.1)

Due to the fine microstructure in the low temperature annealed samples, STEM was used to analyse phase transformation for three annealing hold-times at 480 °C (at 5 minutes, 1 hour, and 30 hours). The sample "480_30 hours" showed the most significant growth in precipitates and was mapped with EELS-STEM as depicted in Figure 5.4. Results show that bright regions in the HAADF-STEM images correspond to high vanadium regions of the EELS-STEM mapping. It can therefore be deduced that the bright regions at dislocation and grain boundaries observed in "480_5 minutes" and "480_1 hour" are also vanadium rich. Since the bcc phase is stabilised by ~15 wt% vanadium, the precipitated regions can be assumed to be β-phase (bcc) or pre-β phase (transitional structure). It is important to note that the aluminium concentration in both hcp and bcc phases are similar. Furthermore, the aluminium concentration in the hcp phase is lower than the as-built α' concentration (which can be assumed to be approximately ~6 % based on the measured LPBF-powder wt%).

Figure 5.5 depicts the same high-resolution area of sample "480_30 hours" depicted Figure 5.4(c) but uses ABF SEM settings to allow for the dislocations to become more visible. High dislocation density areas are visible as dark areas in the image. These appear to be concentrated on the boundaries of α-laths – likely the newly precipitated β-phase.

75

Spot/ area	Weight % (σ)		
	Ti	Al	V
1	89.4 (0.5)	4.3 (0.3)	4.3 (0.4)
2	89.5 (0.2)	4.3 (0.1)	6.2 (0.2)
3	81.9 (0.2)	4.5 (0.1)	13.6 (0.1)
4	78.5 (0.2)	3.8 (0.2)	17.8 (0.1)
5	80.7 (0.2)	4.3 (0.2)	15.0 (0.1)
6	79.7 (0.2)	4.2 (0.1)	16.1 (0.1)
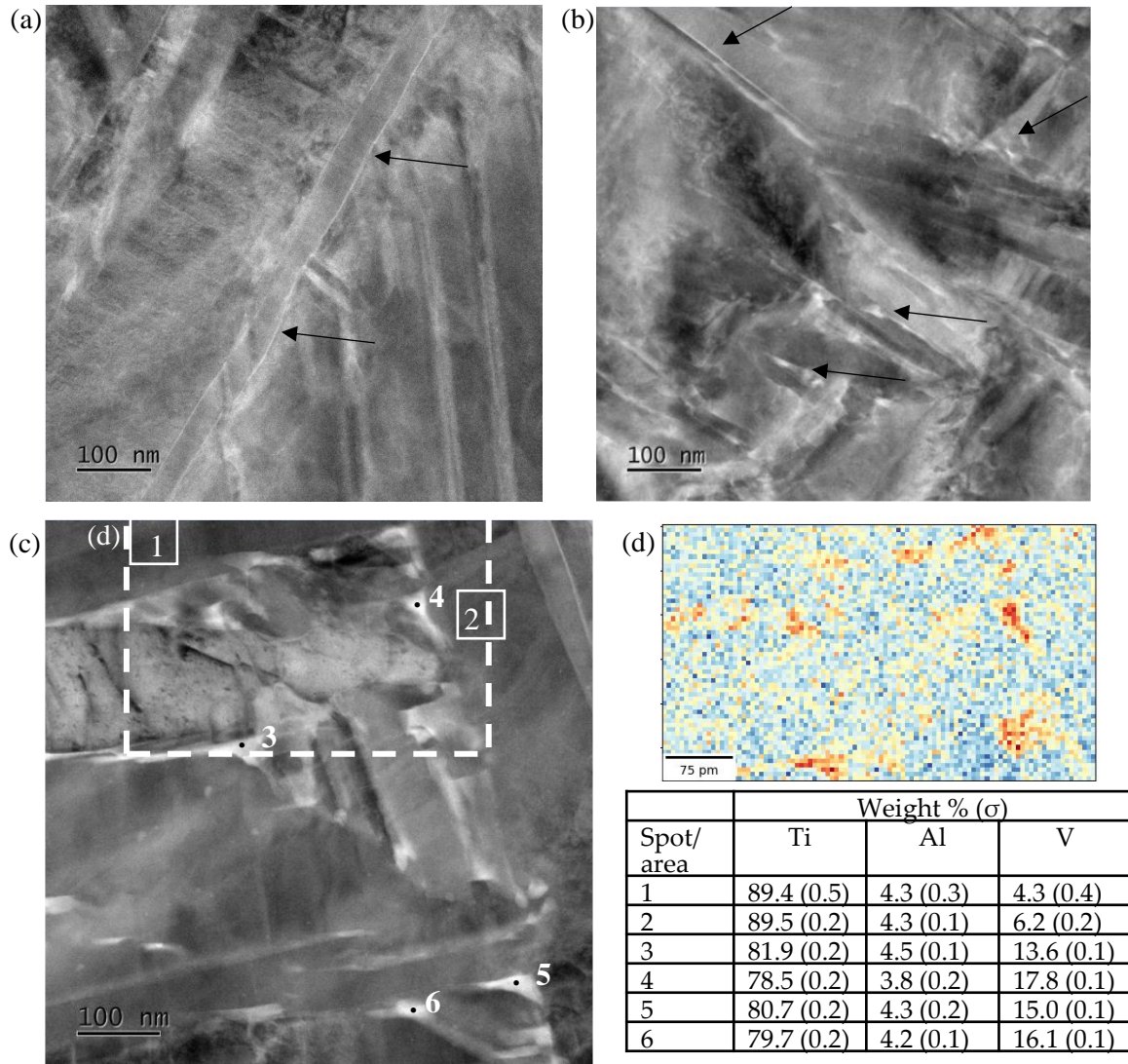
Figure 5.4. HAADF STEM images of sample 480 °C anneal different hold times: arrows point to bright vanadium enriched regions at (a) 5 minutes, (b) 1 hour, and (c) 30 hours. (d) EELS mapped region of vanadium, (c) EDS spot and area mappings of elemental weight analysis.
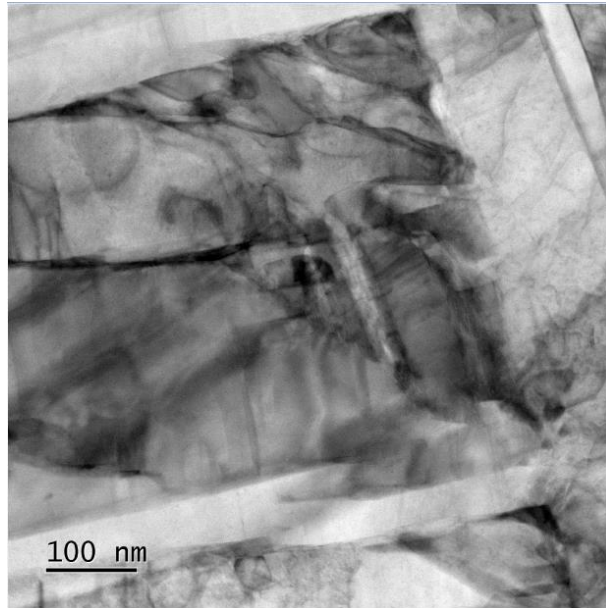
Figure 5.5. ABF STEM images of the same area as Figure 5.4. Dark regions correspond to areas of high dislocations density (and were shown to correspond to β-phase in the previous figure).

The growth of the vanadium-rich regions (bright spots) with temperature was mapped in Figure 5.6(a – d), which depicts BSE-SEM micrographs of samples annealed for 30 hours at the four temperatures investigated (427, 480, 560, and 610 °C).

(a)

(b)

(c)

(d)
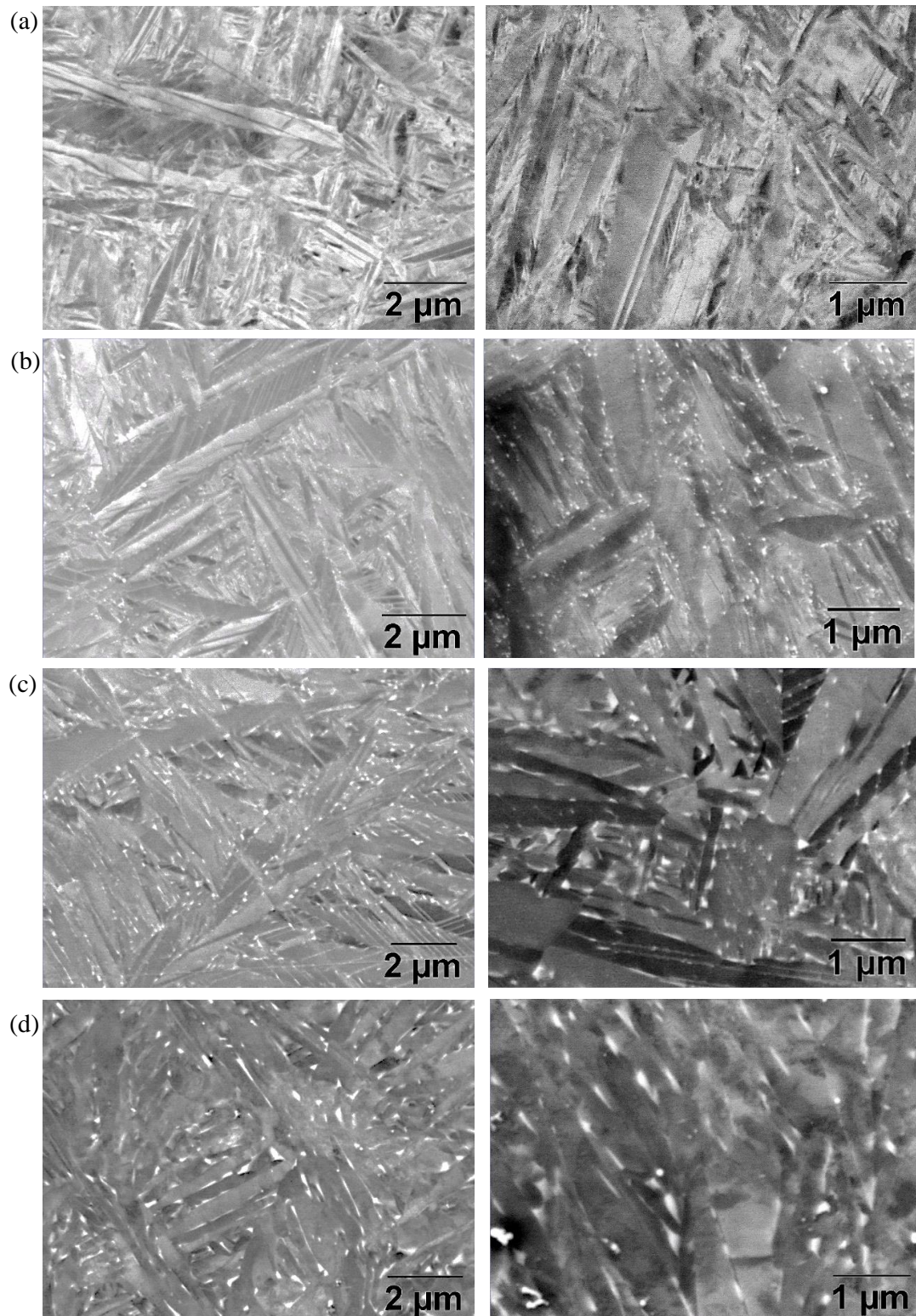
Figure 5.6. BSE-SEM images of samples annealed for 30 hours at (a) 427 °C (b) 480 °C, (c) 560 °C, and (d) 610 °C.

5.3.4   X-ray diffraction

Broad-angle XRD scans of an as-built sample and samples annealed for 30 hours at 427, 480, 560, and 610 °C, are plotted in Figure 5.7. Bragg peaks of bcc phase are observed in the "560_30 hours" and "610_30 hours" samples and are labelled β^1 and β^2 in Figure 5.7(b), respectively. The increase in bcc lattice parameters and peak intensity from β^1 to β^2 coincides with an increase in annealing temperature. The peaks on either side of the $\{10\bar{1}0\}_{hcp}$ peak in Figure 5.7(a) coincide with XRD peaks of α''-phase observed in Ti-6Al-4V by Zeng and Bieler (2005) and Sha & Malinov (2009). Due to the fine scale of the α''-phase, the peak profile clarity is too low to obtain reliable quantitative lattice values. The small peak at ~50° was determined to be caused by instrumental background noise.

Figure 5.8 plots quantitative lattice parameter results of Rietveld refinement. Peak broadening decreases with temperature due to a decrease in hcp lattice distortion. This lattice distortion is caused by the combination of residual stress and dislocations. The measured change in hcp lattice parameter ratio 'c/a' and bcc 'a' lattice parameter with annealing temperature is caused by a change in the chemical composition of respective phases due to phase transformation. The 'c/a' ratio reaches a stable value after 480 °C, and no further increase is observed at higher temperatures. Minor difference in the 'c/a' ratio exists between the one hour and 30 hour annealed samples. The reference sample's hcp and the bcc lattice parameter ratios are indicated with star and triangle symbols, respectively. Since the measured lattice parameters fall short of the stable $\alpha+\beta$ lattice parameters, it appears that the phase transformation $\alpha' \rightarrow \alpha+\beta$ is incomplete for these samples.
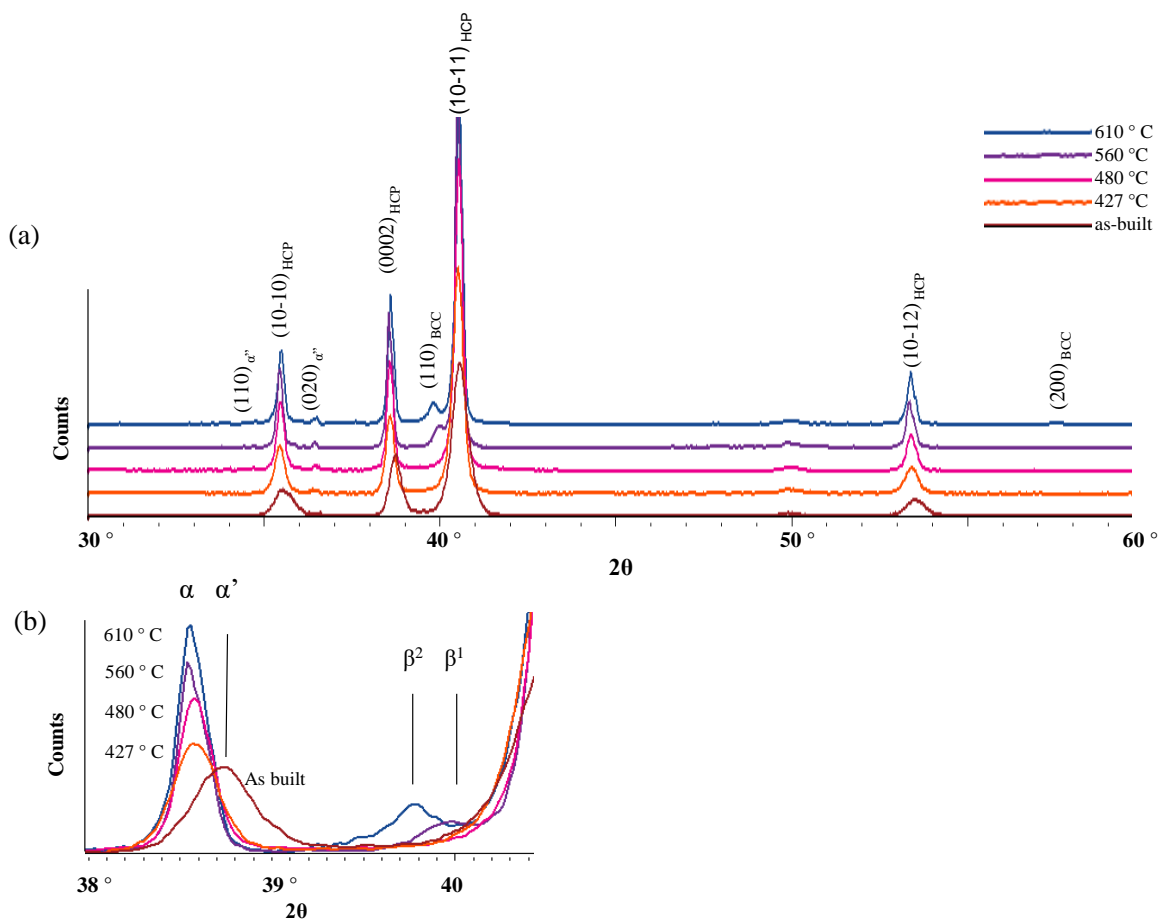
Figure 5.7. XRD plots of samples annealed for 30 hours. (a) large angle plot, (b) Enlarged section of (0002)ₐ and (110)β peaks. See legend for annealing temperatures.
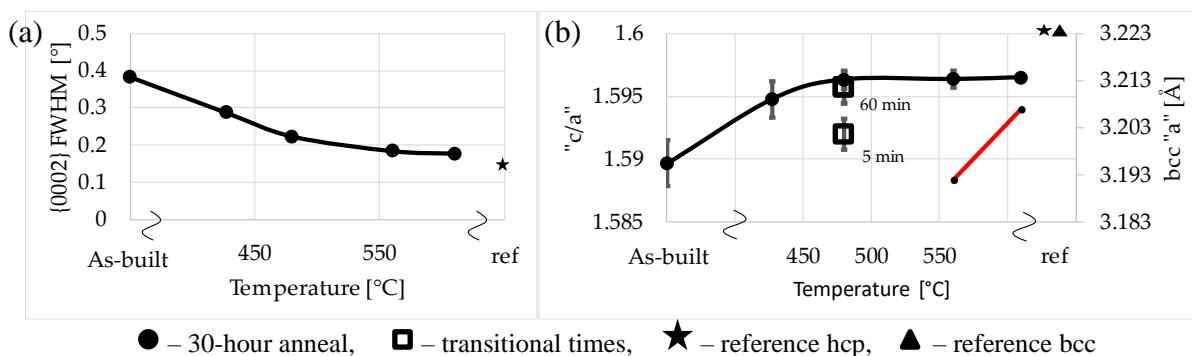
Figure 5.8. Quantitative data of (a) the FWHM of the {0002}hcp peak as a function of temperature, and (b) hcp 'c/a' ratio (black line) and bcc 'a' lattice parameter (red line) with temperature and time. Reference sample data points are included for comparison.

Rietveld refinement was applied to XRD peaks of samples annealed at 480 °C (hold times of five minutes, one hour and 30 hours). The α-phase lattice parameters, micro lattice strain (also known as RMS lattice strain) and average crystal size parameters are tabulated in Table 5.2. Sample thickness was determined from STEM-EELS data to be 190 nm (± 20 nm). A relationship developed by Williamson & Smallman (1956) to determine dislocation density from micro lattice strain (ε) and average crystal size (D) was used to estimate dislocation density of the three samples analysed: $\rho = (\rho_D \rho_s)^{\frac{1}{2}} = \frac{2\sqrt{3}\,\varepsilon}{b\,D}$. Where ρ_D is the dislocation density calculated from domain size, and ρ_s is the dislocation density calculated from lattice strain. Bragg's vector (b) is taken to be the thickness of the sample. Results indicate a ~50 % decrease in dislocation density after one hour and another 50 % decrease after 30 hours.

Table 5.2. Lattice parameters of the sample annealed at 480 °C determined from Rietveld refinement (measurement error value in brackets).

Anneal time	Lattice Constants (Å)		Average crystallite size (D) [nm]	Lattice strain (ε)	Dislocation density (ρ) [x10^{14} m^{-2}]
	a	c			
5 min	2.929	4.663	55.5 (4.3)	0.615 (0.030)	2.019
1 hour	2.924	4.666	90.6 (8.1)	0.549 (0.022)	1.105
30 hours	2.924	4.666	78.7 (7.1)	0.241 (0.043)	0.558

5.3.5 Tensile tests

Results of the ultimate tensile strength (UTS) versus elongation to failure are plotted in Figure 5.9. As expected from the hardness results, samples "480_1 hour" and "560_1 hour" show an increase in strength (from the as-built sample group) at the cost of ductility. Sample "610_1 hour" measured a decrease in strength and a similar ductility to the low temperature annealed samples. Further holding time at 610 °C showed an increase in ductility. It is likely that this ductility's recovery is caused by an increase in β-phase percentage. The loss in strength is caused by a decrease in dislocation density, average grain size and possibly due to the loss of localised compressive residual stresses.
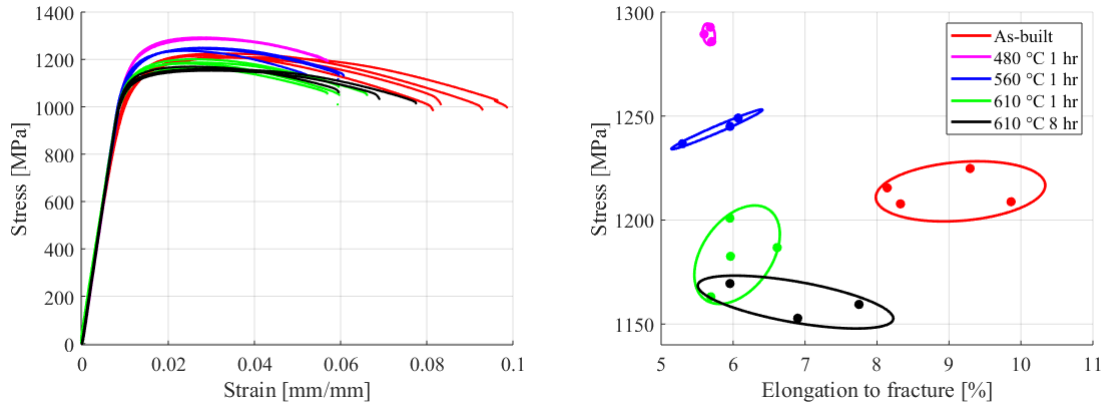
Figure 5.9. Stress-strain plots of as-built and annealed samples.

5.4 Discussion

5.4.1 Theoretical phase transformation pathways of martensitic decomposition

The β → α+β phase transformation upon equilibrium cooling from the high-temperature β-phase has been studied and simulated (Wang *et al.*, 2014; Ji *et al.*, 2016). The following subsection discusses more uncommon martensitic phase transformation pathways based on work by Heo *et al.* (2014). According to Ji *et al.* (2016),

> the presence of structural inhomogeneities such as grain boundaries and dislocations often alter the transformation pathways since it perturbs the relevant chemical and/or elastic strain energetics in alloys. This may cause spatially inhomogeneous distribution of alloying elements, which gives rise to the local variation of phase stabilities. For example, grain boundaries often induce solute segregation/ depletion to reduce the excess free energy (or grain boundary energy). As a result, the compositions of alloying elements at or near grain boundaries can be significantly different from the grain interior counterparts. Since transformation routes are dependent on chemical composition, more than one transformation route is possible for a single sample.

The thermodynamic stability of phases can be evaluated by their respective Gibbs free energy (G), as a function of composition (X) and order parameter (i.e., crystal structure) (η), i.e., $G = f(X, \eta)$ (Heo *et al.*, 2014). Kinematic phase transformation pathways of two-phase Ti-alloys can, therefore, be described in terms of these free energy curve functions. For simplicity, only α' is discussed due to its dominance in the material, although the following is also applicable to the metastable α'' phase. Furthermore, the free energy function is reduced to one dimension ($f(X)$), i.e., only a function of chemical composition.

An exaggerated sketch of the Gibbs free energy curves for hcp and bbc phases as a function of β-stabilizer alloy concentration is shown in Figure 5.10. Since there exists a miscibility gap for

the hcp-phase with respect to its β-stabilising alloy (Lütjering & Williams, 2007), a double-well type Gibbs energy curve is assumed for $f_{hcp}(X)$. This means that an intermediate α' phase that falls in an unstable region of the Gibbs free energy curve, will decompose through spinodal means into vanadium-rich and vanadium-poor phases. Spinodal phase transformation will theoretically occur when the vanadium composition in the hcp phase is such that $\partial^2 f/\partial X^2 < 0$ (unstable), while a nucleation and long-range diffusive phase transformation will occur when $\partial^2 f/\partial X^2 > 0$ (metastable), (Porter & Easterling, 1992) as demarcated in Figure 5.10.
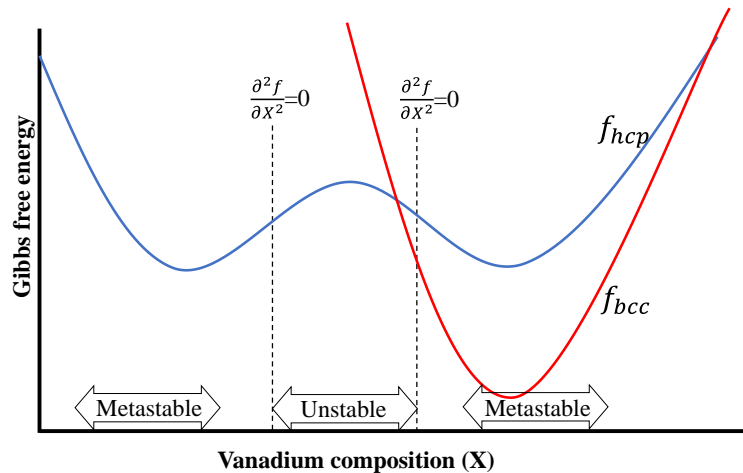
Figure 5.10. Schematic diagram of free energy curves of α- and β-phases (adapted from Heo *et al.* (2014)).

If the concentration of the vanadium in the martensite phase (α') is such that the phase falls in the unstable region of the α energy curve, the phase will transform through a continuous displacive spinodal mechanism, Figure 5.11(a). This would mean that α' will continuously transform both in concentration and structure without the need to overcome a nucleation barrier. Displacement structural transformation, which only requires shear and atomic shuffle (which takes place much faster than long-range diffusion) through the spinodal mechanism will cause the α' phase to decompose into vanadium-poor ($α_1$) and vanadium-rich ($α_2$) regions. The vanadium-poor ($α_1$) region will gradually reach a stable hcp α-phase while the vanadium-rich ($α_2$) region will experience an hcp to bcc structural change once the composition reaches a critical point where f_{hcp} and f_{bcc} intersect. Eventually, the bcc phase will reach an equilibrium vanadium concentration.

If the vanadium concentration in the α' phase is such that the formed α' is metastable, the kinetic pathway will cause the nucleation of stable β-phase at α' grain boundaries and dislocations, and a gradual phase transformation through long-range diffusion will lead to a stable α+β microstructure, represented by the broken arrow in Figure 5.11(b). If β-phase is already present or once a stable bcc phase has formed, phase transformation will continue through long-range atomic diffusion until an equilibrium concentration of elements in the phases is reached.
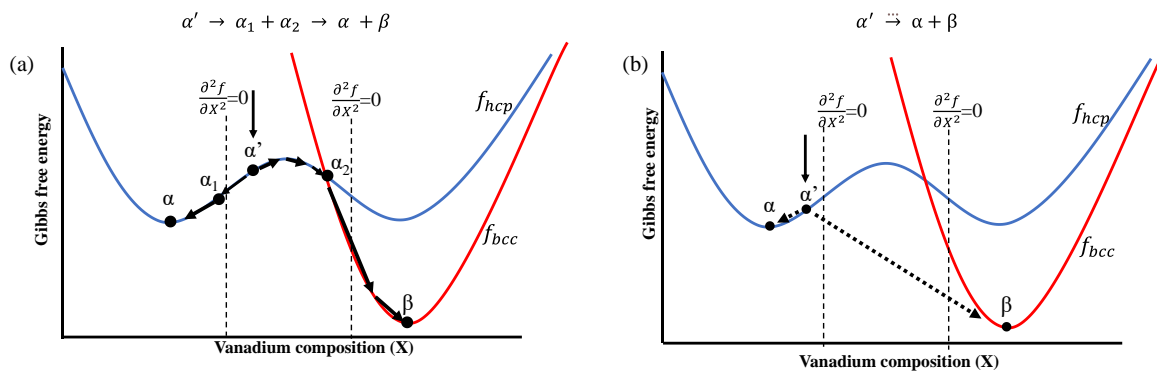
Figure 5.11. Kinetic pathways of (a) spinodal decomposition and (b) nucleation-and-growth (adapted from Heo *et al.* (2014)).

The fast rate of microhardness increase (after only five minutes) can be explained by both a spinodal and heterogeneous nucleation mechanism. Nucleation rate ($\dot{N}$) is known to peak at a temperature below the β-transus temperature, as illustrated by Figure 5.12(a), unlike growth rate that increases with temperature (Callister & Rethwisch, 2011). A lower temperature facilitates a faster nucleation rate but a slower growth rate. Furthermore, due to the high dislocation and twinning density, the nucleation density will also be high. This argument is reflected in the evidence of a high rate of initial phase transformation (short-range diffusion of the nucleation process) which slows down over time (illustrated by the lattice parameter change at 480 °C presented in Table 5.2). Due to the slow rate of grain growth, the overall phase transformation is slower at lower temperatures even though the nucleation rate might be high, illustrated in Figure 5.12(b).
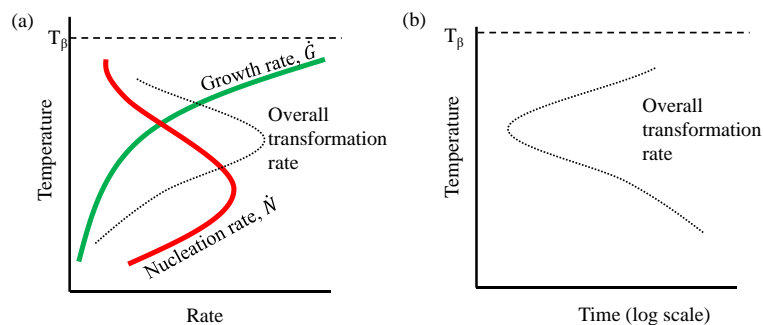
Figure 5.12. Schematic adapted from Callister and Rethwisch (2011) of (a) phase transformation rate – consisting of nucleation rate and growth rate and (b) time required for transformation to proceed to a certain percentage of completion.

The spinodal kinetic pathway is extremely difficult to observe both due to its fine scale and the small difference in lattice parameters of the resulting α₁ and α₂ phases. Figure 5.13 depicts a

84

TEM bright-field micrograph showing two different internal grain textures. Area-(a) depicts fine fluctuations in bright and darks spots with no grain boundaries. Area (b) depicts bright regions at clear dislocation and/or grain boundaries. The prior is argued to be evidence of spinodal decomposition, while the latter is argued to be due to the heterogeneous nucleation transformation route.
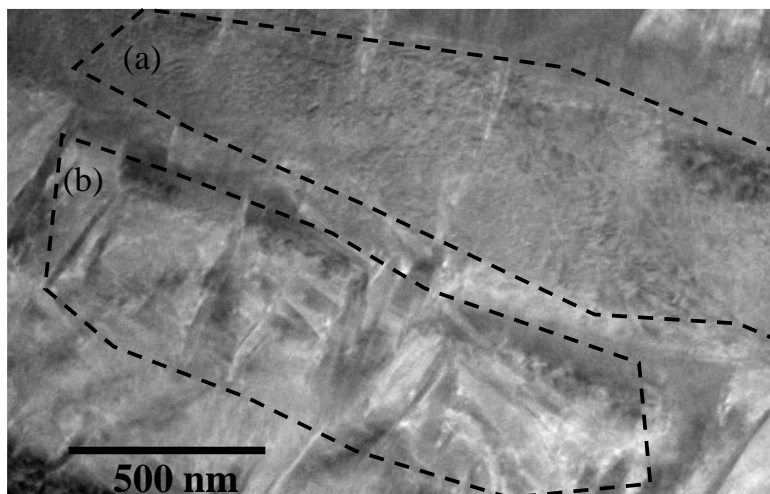
Figure 5.13. HAADF image of two surface textures as an indication of two different decomposition routes (sample "480_1 hour"): (a) Modulated / tweed-like texture inside α' grains and (b) β-nucleation at dislocations and grain boundaries.

Tan *et al.* (2016) observed the spinodal mechanism by measuring nano-scale fluctuations in atomic density and alloy concentration using atom probe tomography (APT). Spinodal decomposition observed through microscopy by Lee & Welsch (1990) and Davis *et al.* (1979) resemble the texture observed in area-(a) of Figure 5.13. Recent work by Haubrich *et al.* (2019) used APT to show the initiation of these fine β-precipitates at α' boundaries and internal dislocations.

5.4.2 Strengthening, embrittlement and ductility

It is well established that hardening of α-Ti can be accomplished by the homogeneous precipitation of high-strength Ti_3Al particles in the α-phase, see Subsection 2.2.2. Ti_3Al is known to form in the temperature range investigated in the study, specifically in the range of 500 – 600 °C (Lee *et al.*, 2008; Carreon *et al.*, 2014).

However, no evidence of Ti_3Al precipitates was found in this study. Additional investigation revealed that no increase in hardness was measured of the stable "610_30 hours" sample after further annealing at 480 °C for 30 hours. The lack of Ti_3Al is argued to be due to the concentration of aluminium in the α-phase being below the ~5 wt% needed for this phase to form (Radecka *et al.*, 2016).

It is argued that a further increase in β-phase volume fraction would cause an increase in aluminium concentration in the α-phase, thereby making Ti_3Al precipitation theoretically possible. This was observed to occur in the reference sample, which measured an aluminium concentration of above 5 wt% (6.8 wt%) compared to the "480_30 hours" sample, which measured an aluminium concentration in its hcp phase of ~4.3 wt%.

Studies of the formation of Ti_3Al have also found the precipitation to only occur after a prolonged period at elevated temperatures (Carreon *et al.*, 2014). Since the microhardness of the samples investigated in the current study reached a maximum value after just 1 hour, it is argued that the hardening effect is unlikely to have been caused by the slower forming Ti_3Al.

Since only ultra-fine vanadium-rich precipitates were observed, two theoretical non-classical hardening mechanisms are proposed. The first is the precipitation of bcc β-phase at dislocations and grain boundaries. The second hardening mechanism occurs due to subtle fluctuations of lattice parameters (caused by spinodal decomposition inside α' grains) associated with the alloy-rich and alloy-poor regions in the material. While both proposed mechanisms induce a crystallographic deformation mobility-barrier (i.e., a type of precipitation hardening) the first relies on the "quantity and fineness" of the precipitated β-phase (as argued by Donachie (2000)) while the latter mechanism additionally relies on the degree of structural difference (i.e., the magnitude of lattice strain) between the $α_1$ and $α_2$ phases.

Mayeur and McDowell (2007) argue that while slip transmission across α/α boundaries can be difficult due to low symmetry, "the most effective obstacles to dislocation motion are the α/β interfaces." Intense dislocation pileups have also been observed within single α+β colonies at the α/β interfaces. High dislocation density was also observed in the β-phase. This could result from residual stress in the α-phase being transmitted to form dislocations in the soft β-phase. Tsumoto *et al.* (2011) also argue that fine β-grains could act as strong barriers to dislocation motion, resulting in higher material strength.

The gradual decrease in hardness can be attributed to (1) the agglomeration and subsequent growth of precipitates through diffusion into lamellar β along α-laths or (2) the completion of the $α_2$(solute rich) → β transformation; both having the effect of a reduction in dislocation slip impediment.

The increase in hardness, as expected, is concomitant with the UTS from the as-built material. This strengthening comes at the cost of ductility for the annealing strategies investigated. Ageing could, however, be performed subsequently to a sub-β-transus quenching (i.e., to a bi-modal α+α' microstructure) to increase strength while still achieving acceptable ductility (as was demonstrated by de Formanoir *et al.* (2019)). The recovery of ductility of sample "610_8 hours" is argued to be due to an increase in β-phase fraction and lamella width between α-grains.

5.4.3 Lattice parameters and alloy concentration

Since crystal lattice parameters are influenced by alloy concentration, the second approach to monitoring the martensitic decomposition phase transformation was through measuring the

change in hcp and bcc lattice parameters. The increase in hcp lattice parameters 'c/a' ratio is caused by a decrease in vanadium concentration of the phase through the replacement of smaller vanadium atoms (0.134 nm) with larger titanium atoms (0.147 nm). The increase in bcc lattice parameter is likely caused by the decrease in aluminium concentration in this phase, where larger titanium atoms replace the smaller aluminium atoms (0.143 nm) as they diffuse to α. Due to the 'c/a' ratio of low temperature annealed samples falling below that of the reference α+β samples, the martensite decomposition phase transformation is incomplete.

While this study was unable to determine the vanadium-rich phase's crystal structure at initial formation, it can be assumed from microprobe analysis done on the stable reference Ti-6Al-4V sample that a phase consisting of ~15 vanadium wt% has a bcc structure (Haubrich *et al.*, 2019). The lack of bcc peaks in the 427 and 480 °C samples is either due to the extreme fine scale of the β-precipitates, or the lack of bcc phase at the early stage of the spinodal phase transformation in which a congruent bcc structure has not yet formed from the $α_2$ structure. The increase in hcp Bragg peak width is likely caused by a decrease in a distortion of hcp crystal, dislocation density and an increase in average grain size.

5.5 Conclusions

The motivation for the work conducted in this study grew from the limited knowledge of low-temperature heat treatments of LPBF-produced Ti-6Al-4V and the need for the qualification and improvement of material properties for acceptance in industrial application. This study investigated the influence of low-temperature ageing strategies in the range of 427 – 610 °C on residual stress and microstructure to further improve the achievable material properties.

The study was able to develop insight into the martensite decomposition phase transformation at low temperatures by proposing two possible kinematic transformation pathways and demonstrating their influence on material hardness and lattice parameters. It was shown that the degree of phase transformation at the low temperatures investigated produced α- and β-phases with alloy concentrations and lattice parameters different to that of the reference stable α+β phase sample. This shows that the phase transformation α'→ α+β is incomplete, compared to the reference material, when employing low-temperature heat treatments (even after 30 hours). Annealing strategies employed on LPBF-produced Ti-6Al-4V in the temperature range below 650 °C is popularly called "stress relief" heat treatments. This is misleading since evident microstructural transformation occurs that influence mechanical properties. Even though 90 % of residual stress was shown to relax after 1 hour at 560 °C and after only five minutes at 610 °C, this came at the cost of a loss in material ductility.

This loss in ductility is argued to be due to the precipitation hardening effect of β-phase or pre-β-phase particles ($α_2$) formation during the initial stages of martensite decomposition. The extremely slow phase transformation rate at 560 °C and below makes it more practical to anneal at ~610 °C for a minimum of 8 hours to improve ductility. The study's results further clarify that care should be taken when employing base plate heating in the temperature range below 610 °C since this could lead to part embrittlement.

5.6 Post-submission discussion

Although the feedback on this work has been overwhelmingly positive, two criticisms of this submission have been raised. The first was that the discussion section is heavily theoretical. Unfortunately, a study of microstructure and deformation below the nanoscale, for example, using atom-probe tomography, was outside the scope of the study. The author recommends the possible use of APT for future studies. The second comment/criticism was that other studies have been able to identify residual β-precipitation in the as-fabricated sample. Residual-β might change the α' decomposition mechanism, although, as discussed in this Subsection 5.4.1 and observed in Figure 5.13, more than one transformation pathway is possible. Further discussion and recommendation of this work are provided in Chapter 8.

6 The influence of microstructural texture and prior-β grain recrystallisation on the deformation behaviour of laser powder bed fusion produced Ti-6Al-4V

Although studies have hypothesised that the anisotropic deformation of LPBF-produced Ti-6Al-4V is caused by textured prior-β grains, to the candidate's knowledge, no study has demonstrated the fundamental mechanisms by which anisotropic deformation results. This study investigated the influence of PBG morphology and texture on the deformation behaviour on the grounds of this hypothesis. This chapter addresses the project's third objective by identifying a link between prior-β crystallographic texture and α-lath morphological texture, thereby forming a theory of the probable cause of material anisotropy.

This chapter was submitted to and unfortunately rejected by *Acta Materialia*. The post-submission discussion at the end of the chapter includes the insight gained from reviewer feedback. The work has subsequently been published in *Materials Science and Engineering: A* (Ter Haar & Becker, 2021)[7].

Declaration by the candidate:

With regards to Chapter 6, the contributions of author and co-author are as follows:

Name	Email	Contribution	Extent (%)
G.M. Ter Haar (candidate)	gterhaar@sun.ac.za	Experimental design, completion of all tests and data analysis, writing and compilation of manuscript	90
T.H. Becker	tbecker@sun.ac.za	Supervision and reviewing	10

Signature of candidate: [GTH] (see Footnote 5)
Date: 2021/02

Declaration by the candidate:

The undersigned hereby confirm that:

1.   The declaration above accurately reflects the nature and extent of the contributions of the candidate and the co-authors to Chapter 6,
2.   No other authors contributed to Chapter 6 besides those specified above, and

---

[7]DOI link: https://doi.org/10.1016/j.msea.2021.141185

3.   Potential conflicts of interest have been revealed to all interested parties and that the necessary arrangements have been made to use the material in Chapter 6 of this dissertation.

Signature (see Footnote 5)	Institutional affiliation	Date
[TH Becker]	SU	2021/02

6.1 Introduction

The build orientation of metal additively manufactured (AM) components have shown to influence mechanical properties such as strength, ductility, fracture toughness and fatigue life (Leicht & Wannberg, 2015; Shunmugavel *et al.*, 2015; Seifi *et al.*, 2017; Kok *et al.*, 2018; Liu & Shin, 2019; Ren *et al.*, 2019). Keeping in mind that the control of a material's mechanical properties is a crucial aspect in manufacturing, understanding the structural aspects that describe the material's microstructure, such as texture, is paramount. Once established, predictability and control of anisotropy can be accomplished.

Anisotropy of laser powder bed fusion (LPBF) produced material[8] can be caused by one or a combination of build defects (Seifi *et al.*, 2017; Ren *et al.*, 2019), residual stress (Anderson *et al.*, 2018), and microstructure (Leicht & Wannberg, 2015). Build defects, such as voids or unmelted powder particles, are either caused by non-optimum energy density (Dilip *et al.*, 2017) or uneven powder distribution (as noted from in-house studies). Defects can lead to anisotropy if heterogeneously dispersed in the sample or geometrically textured according to a particular direction (Seifi *et al.*, 2017). Part density (and thereby anisotropy) can be improved by optimising process parameters (Kasperovich *et al.*, 2016; Mishurova *et al.*, 2019a) or applying hot isostatic pressing (HIP). The formation of residual stress and microstructure and its influence on mechanical anisotropy is complex since residual stress and microstructure are hard to measure, quantify and predict (Qiu *et al.*, 2013). Residual stress is dependent on the nature of the thermal gradient during laser exposure. Non-uniform cooling will cause an unavoidable heterogeneous residual stress state (Anderson *et al.*, 2018). Residual stress can be reduced *in situ* by using a heated build plate (Vasinonta *et al.*, 2000; Kempen *et al.*, 2013; Vrancken *et al.*, 2015; Ali *et al.*, 2017), more effective scan strategies (Ali *et al.*, 2018), or through optimising process parameters where a higher laser energy density has been found effective (Mishurova *et al.*, 2019b). The most common method is post-process heat treatments (Ter Haar & Becker, 2020).

Qiu *et al.* (2013) found that the mechanical anisotropy of samples remained after HIP, which theoretically eliminates two out of three causes of mechanical anisotropy, leaving microstructure as the remaining cause to investigate. It should be noted that HIP of Ti-6Al-4V is done below the β-transus temperature, and therefore the prior-β grain (PBG) structure remains unaffected. It is, therefore, likely that the residual anisotropy is caused by microstructural texture. Microstructural texture of the columnar PBG has been proposed as a key contributor to mechanical anisotropy in LPBF (Leicht & Wannberg, 2015) and direct energy deposition (Carroll *et al.*, 2015). Few studies have described the causal mechanism by

---

[8] Not considering component attributes such as surface roughness.

which specific microstructural aspects control anisotropic deformation behaviour (Kumar *et al.*, 2018), and the understanding of the influence of PBG texture on anisotropy remains limited (Kumar & Ramamurty, 2019).

Microstructure is the focal point in this study. PBG size has shown to influence mechanical properties. For example, a smaller PBG microstructure achieves a higher strength and ductility compared to larger PBG microstructures (Liang & Wang, 2015; Chong *et al.*, 2017). A technique of rapid heat treatments and hydrogeneration have shown potential for refining PBG grain size and improving material strength and ductility in conventionally produced parts (Ivasishin & Teliovich, 1999). Recent work in wire-arc AM uses inter-layer cold rolling deformation to achieve PBG refinement (Donoghue *et al.*, 2016).

PBGs grow epitaxially (layer-wise) with a $\langle 001 \rangle_\beta$ texture parallel to the thermal gradient direction (usually the Z-axis direction) during cyclic heating of underlying layers (Antonysamy *et al.*, 2013). Ideally, the high energy-density of the laser melts all powder particles, thus eliminating them as nucleation sites and generating a sufficient thermal gradient within the meltpool to prevent nucleation ahead of the solidification front. Heterogeneous nucleation sites in the melt pool are absent, and therefore the growth of the underlying PBGs dominates (Kumar *et al.*, 2018). Critical parameters determining the solidification PBG microstructure are temperature gradient, solidification rate and undercooling. (Gockel & Beuth, 2013). In Louw and Pistorius's (2019) study on the influence of hatch distance and scan speed on PBG size and shape, it was found that an increase in scan speed can achieve a PBG refinement while a decrease in hatch distance increased PBG grain size.

Hexagonal close-packed (hcp) latticed alpha (α) and alpha prime (α' i.e., martensite) grains in Ti-6Al-4V form following the Burger's Orientation Relationship (BOR) which necessitates grains belonging to a single parent PBG to be oriented $\{0001\}_\alpha // \{101\}_\beta$ and $\langle 2\overline{1}\overline{1}0 \rangle_\alpha // \langle 111 \rangle_\beta$ (Burgers, 1934). Twelve possible unique grain crystallographic orientations (termed variants) can form from a single parent β-grain. If these variants form randomly, a weak hcp crystallographic texture will result (Sargent *et al.*, 2012). Typically only a small subset of variants form within each grain (Sargent *et al.*, 2012). Martensite laths have been observed to form along habit planes of approximately $\{334\}_\beta$ and $\{344\}_\beta$ (Gaunt & Christian, 1959; Banerjee & Krishnan, 1971). It has been suggested that an elongated grain morphology will have a larger influence on anisotropy than crystallographic texture (Thijs *et al.*, 2013).

Microstructural crystallographic and morphological texture play a prominent role in deformation anisotropy. Currently, the relationship between the two is not well understood for LPBF produced Ti-6Al-4V. By attaining a deeper understanding of this, function-specific design methodologies for AM and post-processing will possibly enable LPBF to become more attractive in industrial applications.

The aim of the study is to fully describe the mechanisms controlling anisotropic deformation in LPBF-produced Ti-6Al-4V. A strong PBG texture and a columnar morphology are believed to cause anisotropic deformation behaviour (Kok *et al.*, 2018). This hypothesis is investigated by conducting β-anneal (BA) heat-treatment strategies to globularise columnar PBGs by considering both the microstructure's morphological and crystallographic texture attributes.

Reported are the structural and crystallographic features of LPBF-produced Ti-6Al-4V in its as-fabricated (AF) and BA state that control deformation anisotropy, possible orientation-specific mechanisms that control plastic slip, and the respective tensile behaviour.

6.2 Materials and methods

The experimental approach is aimed at identifying anisotropic structural differences between AF and beta annealed and quenched (BAQ) microstructures to determine structural features that control deformation and respective tensile behaviour. This is done by quantitatively describing the microstructure in the AF state and changes due to a BAQ heat-treatment. The application of BAQ is important because it changes the PBGs. A change in PBG can then be correlated with a change in α' structure. This is both useful to assess how the PBG structure controls the α' structure, and how anisotropy can be improved through modification of the PBGs. Deformation is investigated to understand the dominant deformation mechanisms and how they are related to microstructural anisotropy—both PBG and α'.

6.2.1 Build parameters, scan strategy and sample geometry

All samples were built using a medically certified (ISO 13485) EOSINT M280 machine (EOS GmbH, Krailling, Germany). Samples were built in an argon gas flow environment with an oxygen content of < 0.12 at% (1200 ppm). Laser scan parameters used were 170 W laser power, a scan speed of 1200 mm/s, a laser spot size of 80 µm, and a hatch distance of 100 µm. Layers were scanned with 5 mm strips rotated at 67° between layers. Ti-6Al-4V ELI (Grade 23) powder with a nominal chemical composition (according to the production certificate) of Ti – balance, Al – 6.25, V – 4.1, C – 0.01, Fe – 0.2, O – 0.09, N – 0.01, H – 0.002 (wt%) was supplied. The 10th, 50th and 90th percentiles of sieve diameter normal distribution were 23 µm, 33 µm and 46 µm as measured by Laser Size Diffraction in accordance with ASTM B822.

Tensile test samples with a "dog-bone"-shape geometry were built in both the "vertical" and "horizontal" orientations with a net-shaped end diameter of 11.9 mm (to accommodate a post-cut M12 thread). The reference coordinate system ISO/ASTM52921 was used in which the plane of the base plate is the XY-plane, and the perpendicular direction the Z-axis. Due to the 67° scan rotation between layers, all directions parallel to the XY-plane experience the same process history making their respective microstructural planes, i.e., Z-axis planes, identical. To avoid confusion when discussing orientations, X-axis and Y-axis were used as default direction for axes perpendicular to the Z-axis. "Vertical sample" refers to samples with their longitudinal axis parallel to the Z-axis, and "horizontal sample" refers to samples with their longitudinal axis parallel to the Y-axis. Vertical samples were loaded in the Z-axis, while horizontal samples were loaded in the Y-axis. Sample density was measured using the Archimedes method as per standard ASTM B962. Both horizontal and vertical samples measured a mean sample density of 99.66 % ($\pm$ 0.05 %). Pore geometry was observed to be spherical using optical microscopy.

6.2.2   Heat treatment approach and method

To globularise PBGs, samples were annealed above the β-transus temperature. BA heat treatments were done at 985 °C (approximately 10 °C above the estimated β-transus temperature based on the measured oxygen content (Lütjering & Williams, 2007)). A 5 kW Gallenkamp muffle furnace (Type 2) was used instead of the conventional vacuum furnace to make quenching more practical. Surface oxidation was removed through machining, removing > 1 mm of the oxidised surface.

Preliminary heat treatments were done to establish the minimum approximate hold time at 985 °C for full PBG recrystallisation. A one hour hold time was adequate to recrystallise the sample based on stereoscopic optical microscopy imaging. One and three-hour hold times were consequently chosen to investigate PBG microstructure change over time. After the results were evaluated, three hours was considered to improve PBG globularisation to a larger degree than one hour. This hold time was therefore chosen for tensile testing to establish its effect on mechanical anisotropy.

Two cooling strategies were used: samples considered for tensile testing were water quenched (designated BAQ) to obtain a martensitic microstructure that is representative of an AF microstructure in that both have a α' phase (see Brandl & Greitemeier (2012)). Samples used for EBSD mapping were furnace cooled, as it was not feasible to map the fine martensitic structure over the required large area.[9] A furnace cool results in a lamella α+β structure that is only used for PBG reconstruction.

6.2.3   SEM imaging, EBSD mapping and microstructural analysis

Samples intended for scanning electron microscopy (SEM) imaging were prepared through mechanically polishing by sequential grinding with silicon carbide paper of grit size 600, 800, and 1200, followed by polishing with 9 µm diamond suspension and 0.04 µm colloidal silica (diluted with 30 vol% H_2O_2) for five minutes, respectively.

Microscopy imaging was done with a Zeiss MERLIN Field Emission (FE) SEM using a secondary electron detector. EBSD maps were acquired using an EOL JSM-7001F FE-SEM. For the AF samples, a single 700 µm square scan at 0.5 µm step size was done. For the BA furnace cooled samples, 3-by-3 maps (i.e., nine maps with a ~20 % overlap) were scanned and stitched post-process. These maps were scanned at a step size of 4 µm. EBSD data was processed post-acquisition using a MATLAB-based toolbox, MTEX (Bachmann *et al.*, 2010). MTEX is a free MATLAB toolbox for analysing and modelling crystallographic textures by

---

[9] The EBSD acquisition of fine martensite microstructure requires a small scan step size of 0.2 – 0.5 µm to achieve an adequate indexing percentage. Since the imaging of multiple PBGs of the BAQ samples required a map size in the millimeter range (due to the larger PBGs), using a 0.2 – 0.5 µm was not feasible due to the excessively large amount of data to be stored and time required. To use a larger step size, samples were furnace-cooled instead of quenched to produce a large-grained "colony" microstructure of lamellar (α+β). Since this caused a high area percentage of residual beta phase, a large step size could be used, making the scanning of a larger map feasible.

means of EBSD or pole figure data. All PBG reconstructions and EBSD figures were also done using MTEX.

The reconstruction of PBGs was done using one of two methods. The first method was applied to AF samples and is based on a method developed by Glavicic et al. (2003). The first method was necessitated by the low percentage of residual β-phase, which made interpolation of β-phase (the second method) impossible. Reconstruction code was developed in-house (Ter Haar, 2017) using code written by Simonelli as a starting point (2014). The second method was applied to BA samples which entailed interpolating β grain orientation of each PBG.

PBG were constructed from indexed orientations using a misorientation angle higher than 2.5°. All α' grains were constructed from 15° misorientation angles. Pole figures were constructed from mean grain orientations. Grains with less than five measurement points were excluded to minimise noise. All orientation maps were plotted using the mean grain orientation. All orientation maps were plotted from IPF of hue-saturation-value (HSV) colouring, as depicted in Figure 6.1.

Pole figure plots were created with 10° contours by generating the orientation distribution function from the orientation data. Measurements of grain shape parameters were calculated through MTEX functions by fitting a polygon boundary to an orientation region within the minimum specified misorientation angle. Grain length is defined as the longest distance between vectors of the polygon boundary. The shortest distance is taken as the perpendicular distance to this. Grain aspect ratio is defined as the longest distance divided by the shortest distance. Shape parameter data was fitted with a log-normal function in MATLAB.

6.2.4   Slip modes and slip transmissibility

Theoretical deformation was determined through mean grain orientation Schmid factors (denoted *m)* and geometric slip transmissibility criterion (denoted *m')*. The study used the Luster-Morris geometric transmissibility criterion to predict ease of slip transmission between two activated slip systems (Bayerschen *et al.*, 2016). A slip system is assumed to activate at a maximum *m*. The value of *m'* is calculated by multiplying the cosine of the angle between the two slip planes with the cosine of the angle of the two slip directions. Maximum *m'* exists when two active slip systems have parallel slip planes and parallel slip vectors. Deflection of slip across grain boundaries is therefore absent, making high-*m'* grain boundaries easy to cross. While various slip transmission criterion across two grains exist (Bayerschen *et al.*, 2016), this slip transmission criterion was chosen due to its practical applicability (i.e., all required data was accessible from EBSD data).

Of the possible hcp deformation slip modes, the basal and prismatic-$\langle a \rangle$ slip strengths are both the lowest and of similar magnitude (Nervo *et al.*, 2016). Reported critical resolved shear stress (CRSS) values for prismatic-$\langle a \rangle$ and basal slip have been reported as 442 MPa and 349 MPa, respectively (Habraken *et al.*, 2013), although reported values vary (Mayeur & McDowell, 2007). The first order pyramidal-$\langle a \rangle$ system has a 1 – 2 times higher CRSS (Mayeur & McDowell, 2007). Slip systems of pyramidal type $\langle c + a \rangle$, both 1st order and 2nd order, are typically 1.1 and 15 times higher than the CRSS for prismatic-$\langle a \rangle$ systems (Mayeur &

McDowell, 2007). In studies by Becker *et al.* (2020) and Bridier *et al.* (2005), only basal, prismatic and a small amount of pyramidal-⟨*a*⟩ slip systems were activated at room temperature. In a study by Ren *et al.* (2019) on the mechanical anisotropy of LPBF Ti-6Al-4V, only basal and prismatic-⟨*a*⟩ systems were considered. In this vein, only basal and prismatic-⟨*a*⟩ slip systems were considered in this study.

Schmid factor iso-curves plotted on an IPF were identified as useful to show both the grain's *m* value and its crystal orientation (Bridier *et al.*, 2005). MTEX's interpretation of IPF HSV colour key (a) and the maximum- (b) and minimum-*m* (c) orientation regions are plotted in Figure 6.1. Slip modes with a *m* < 0.35 are solely orientated with near-[0001] axis. Since basal slip Schmid factors are higher than prismatic slip factors for identical orientations in this orientation domain, the basal slip will always activate preferentially for *m* < 0.35. This is commonly known as "hard" slip.
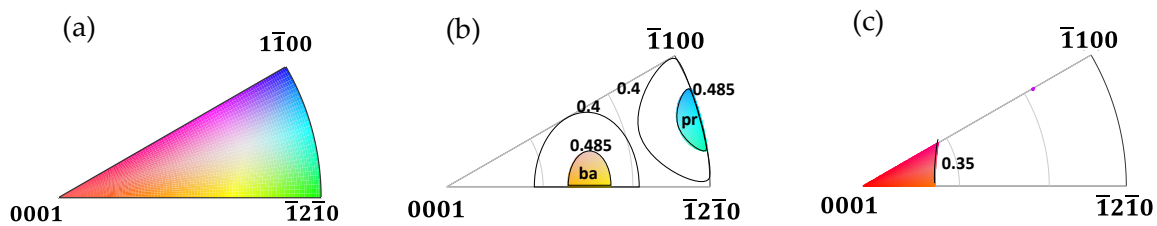
Figure 6.1. MTEX IPFs of (a) HSV-colour key map of hcp symmetry, (b) Schmid factor iso-lines of *m* = 0.485 and *m* = 0.4 (ba – basal, pr – prismatic-⟨*a*⟩), and (c) the region of *m* < 0.35 for both modes.

6.2.5 Mechanical testing

Tensile samples were built with a gauge diameter of 6.5 mm, which was machined to a final gauge diameter of 5 mm, and gauge length was 25 mm to satisfy ASTM E8. The gauge section of one sample of AF-vertical, AF-horizontal, BA-vertical, and BA-horizontal was milled flat on both sides (i.e., 2 mm thickness) before tensile load application to facilitate imaging of microstructural deformation (fractographic and EBSD analysis). Tensile tests were conducted using a Criterion Model 44 (MTS, Minnesota, USA) uniaxial tensile machine at a crosshead displacement rate of 0.13 mm/min.

6.3 Results

6.3.1 PBG morphology and texture

Figure 6.2 depicts the reconstructed PBG orientation maps of the XY and ZX-planes of the AF, one- and three-hour BA samples. The aim of this figure is two-fold, first to qualitatively compare the difference in PBG morphology between the AF XY- and ZX-planes and second, to qualitatively compare the change in morphology due to varying hold times' effect on BA

heat treatment. As observed in other studies of AF LPBF produced Ti-6Al-4V, the XY-plane PBG geometry is equiaxed in shape, while the ZX-plane consists of columnar PBGs orientated in the Z-axis direction (Kok *et al.*, 2018). When applying a BA heat treatment, grain growth, globularisation, and homogenisation occurs. The most notable morphological change is in the AF columnar grain structure and the increase in grain size of both planes.

Figure 6.2. Reconstructed prior-β grain orientation maps. In the XY-plane, showing (a) AF (b) BA 1 hour, and (c) BA 3 hours. In the ZX-plane, showing (d) AF (e) BA 1 hour, and (f) BA 3 hours. Note the scale difference between (a) and (d), versus (b), (c), (e) and (f).
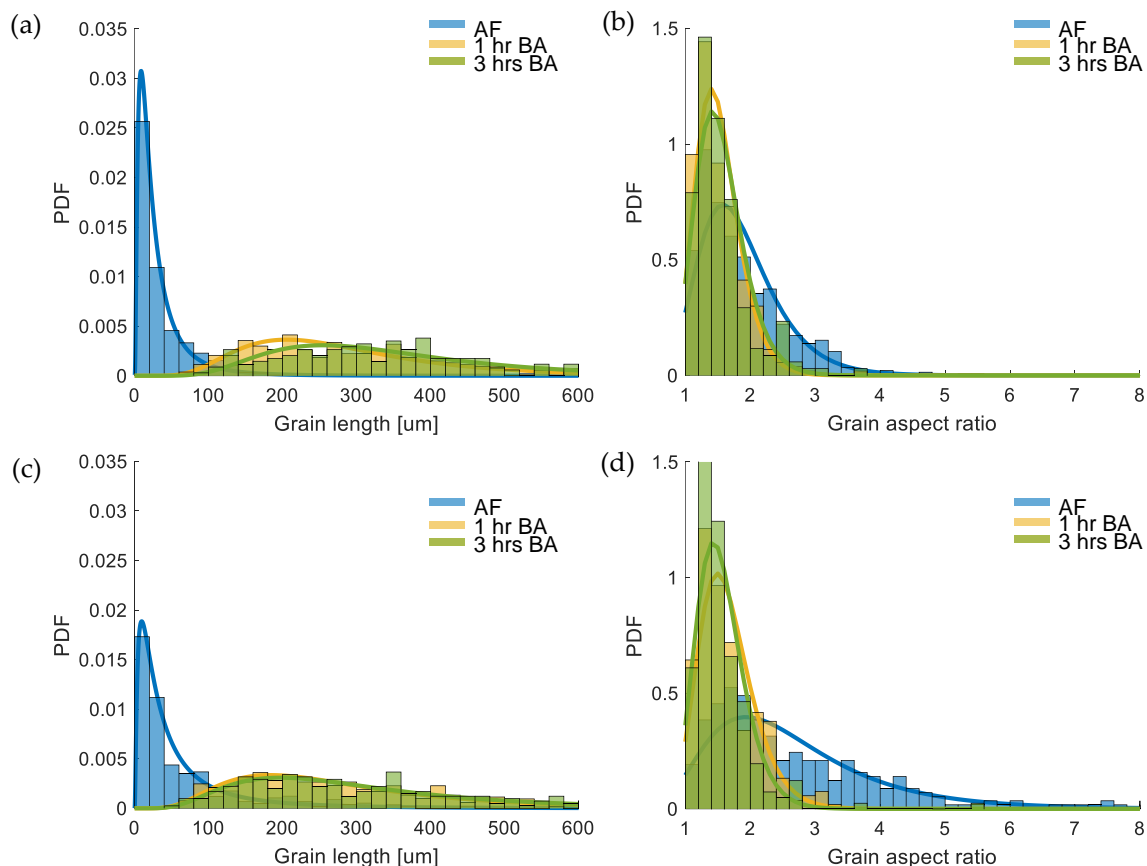
Figure 6.3. Probability distribution normalised histograms fitted with log-normal distribution function plots of PBG shape parameters of AF, BA 1 hour and BA 3 hours. In the XY-plane showing (a) grain length and (b) aspect ratio, and in the ZX-plane showing (c) grain length (d) aspect ratio. Bin width is 20 μm and 0.2 for grain length and aspect ratio, respectively.

In Figure 6.3, the change in AF PBG morphology resulting from BA at one and three hours is quantitatively described using histograms of grain length and grain aspect ratio. Mode, mean, and standard deviation values of the functions are given in Table 6.1. A notable decrease of 62 % in AF PBG mean aspect ratio in the ZX-plane occurs when applying one-hour BA. However, aspect ratio change is less significant in the XY-plane with a mean reduction of less than 1 %. Change in PBG aspect ratio between one and three hours is also less than 1 %. Mean grain growth from AF PBG grain size in both XY and ZX-planes is similar in both the one and three-hour BA.

To quantitatively compare the change in anisotropy of PBG morphology when applying a three-hour BA, histograms of the XY and ZX-plane PBG morphology of both the AF and three-hour BA samples are plotted in Figure 6.4. In the AF sample, the ZX-plane contains both longer and higher aspect ratio grains. After three-hour BA, the difference in XY and ZX-plane morphology

97

is much reduced—mean grain length and median difference of less than 1 % mean and median aspect ratio of less than 1 %.
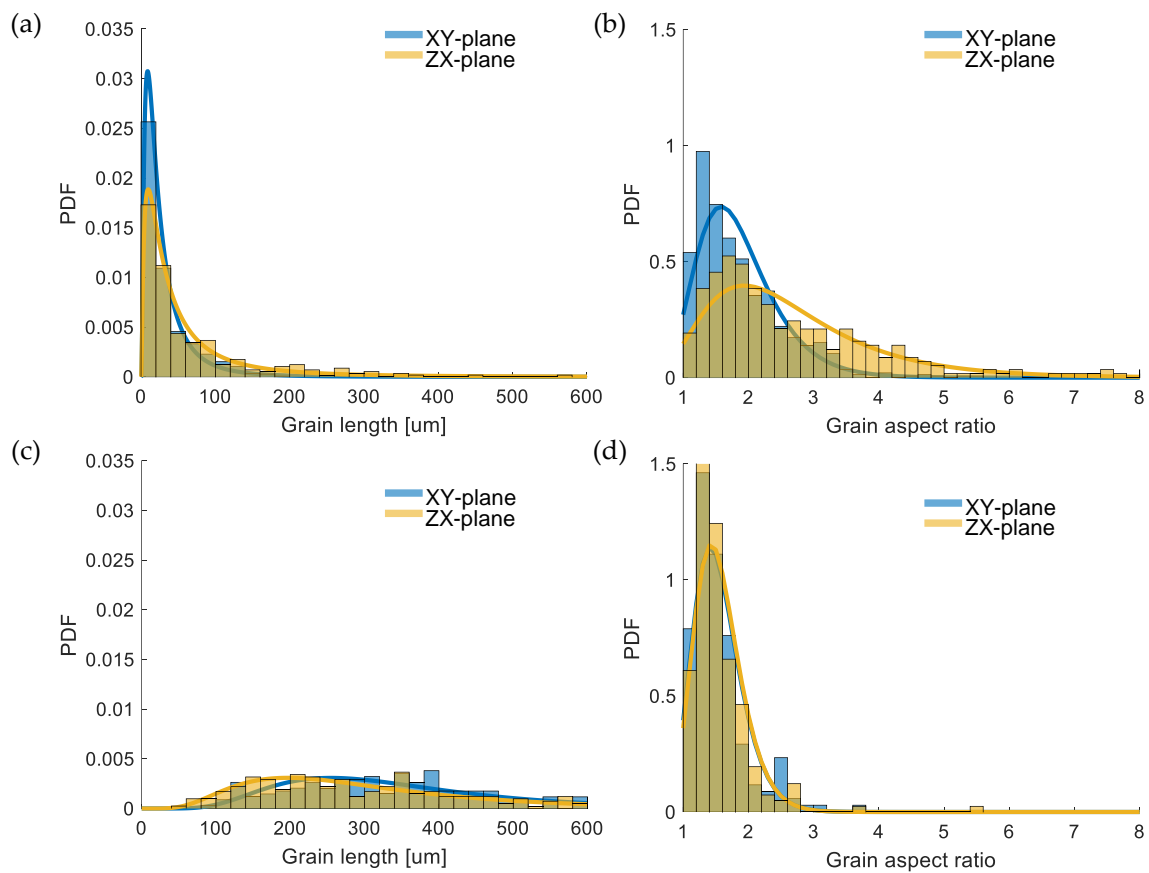
Figure 6.4. Probability distribution normalised histograms fitted with log-normal distribution function plots of PBG shape parameters. In the AF condition showing (a) length (b) grain aspect ratio, and in the 3-hour BA condition, showing (c) grain length (d) aspect ratio. Bin width is 20 μm and 0.2 for grain length and aspect ratio, respectively.

Table 6.1. Quantified data of PBG shape log normal fitting parameters.

Grain length [µm]	XY-plane			ZX-plane		
	AF	BA 1-hour	BA 3-hours	AF	BA 1-hour	BA 3-hours
Mode	8.83	206	255	9.64	184	197
Mean ± 1σ	33.5 ± 40.0	289 ± 146	349 ± 169	68.3 ± 112	292 ± 176	316 ± 197
Aspect ratio						
Mode	1.58	1.40	1.42	1.93	1.59	1.43
Mean ± 1σ	1.85 ± 0.618	1.51 ± 0.343	1.54 ± 0.375	2.68 ± 1.32	1.65 ± 0.425	1.55 ± 0.371

Figure 6.5 and Figure 6.6 depict the resulting (100) pole figure plots of the PBGs and the load-direction IPFs of the resulting α'/α grains in the XY and ZX-planes, respectively. Strong PBG ⟨001⟩$_β$ texture exists in the Z-axis direction. This is a well-established finding that has been made elsewhere in both LPBF and electron beam melting produced materials (Qiu *et al.*, 2013; Rafi *et al.*, 2013; Simonelli *et al.*, 2014b; de Formanoir *et al.*, 2016; Dilip *et al.*, 2017; Kok *et al.*, 2018).
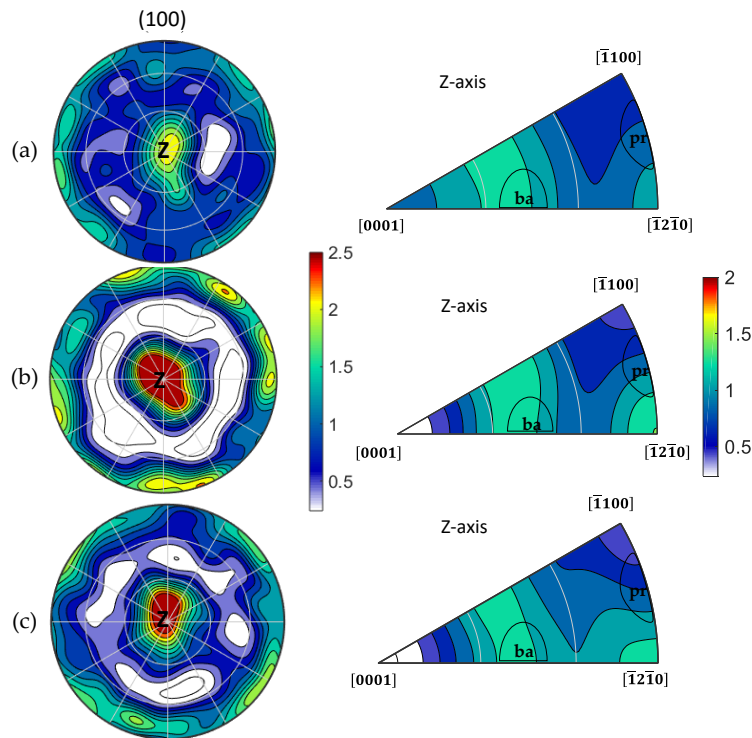
Figure 6.5. XY-plane – reconstructed PBG pole figures and Z-axis IPFs of α'/α laths of (a) AF, (b) BA 1-hour and (c) BA 3-hours.
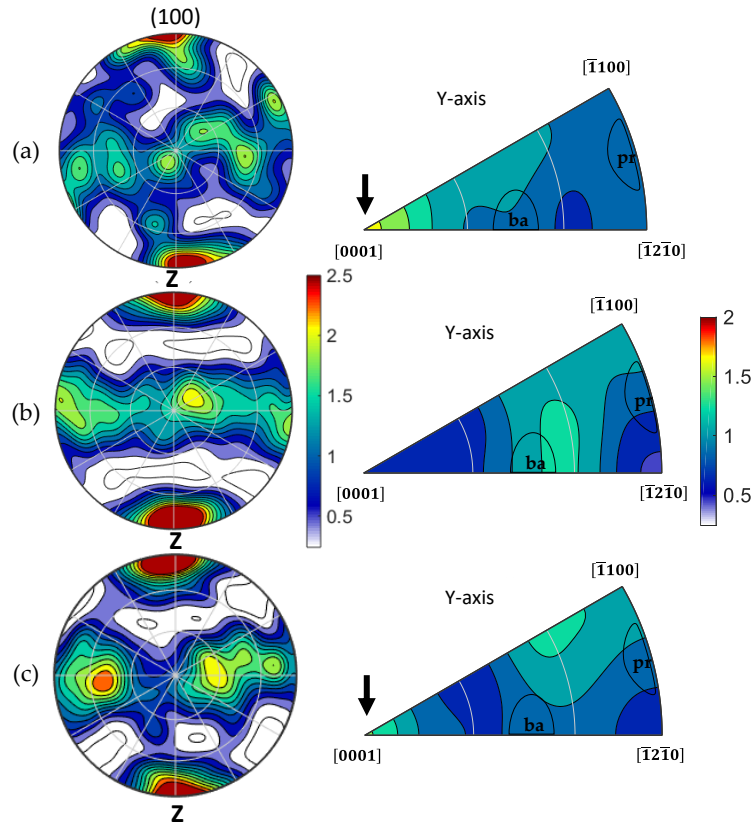
Figure 6.6. ZX-plane – reconstructed PBG pole figures and Y-axis IPFs of α'/α laths of (a) AF, (b) BA 1-hour and (c) BA 3-hours.

From the IPFs of the α'/α grains, it is observed that the AF and 3-hour BA microstructures have a stronger basal texture (indicated by arrows) in the ZX-plane than the XY-plane. A strong basal texture in the load direction is known to increase material strength and decrease ductility (Lütjering & Williams, 2007). In this case, the measured texture strength is weak and unlikely to have a noteworthy influence on material performance. The PBG pole figures indicate that no significant crystallographic texture change has occurred from the AF condition, suggesting grain growth dominating nucleation. IPFs show no notable change in texture from the AF at one- or three-hours BA in the XY-plane and no notable change from the AF to three-hour BA in the ZX-plane. A small difference in one hour BA ZX-plane texture is observed. This difference could be due to limited sample area size.

6.3.2   α' morphology and texture

Figure 6.7 depicts hcp grains using both EBSD orientation maps and quality maps of AF samples in both XY and ZX-plane orientations. The hierarchical structure is distinguishable and well described by Yang, Yu, *et al.* (2016) as a range in size-distribution of laths; primary α' laths are the largest, followed by secondary, tertiary and quaternary grains.
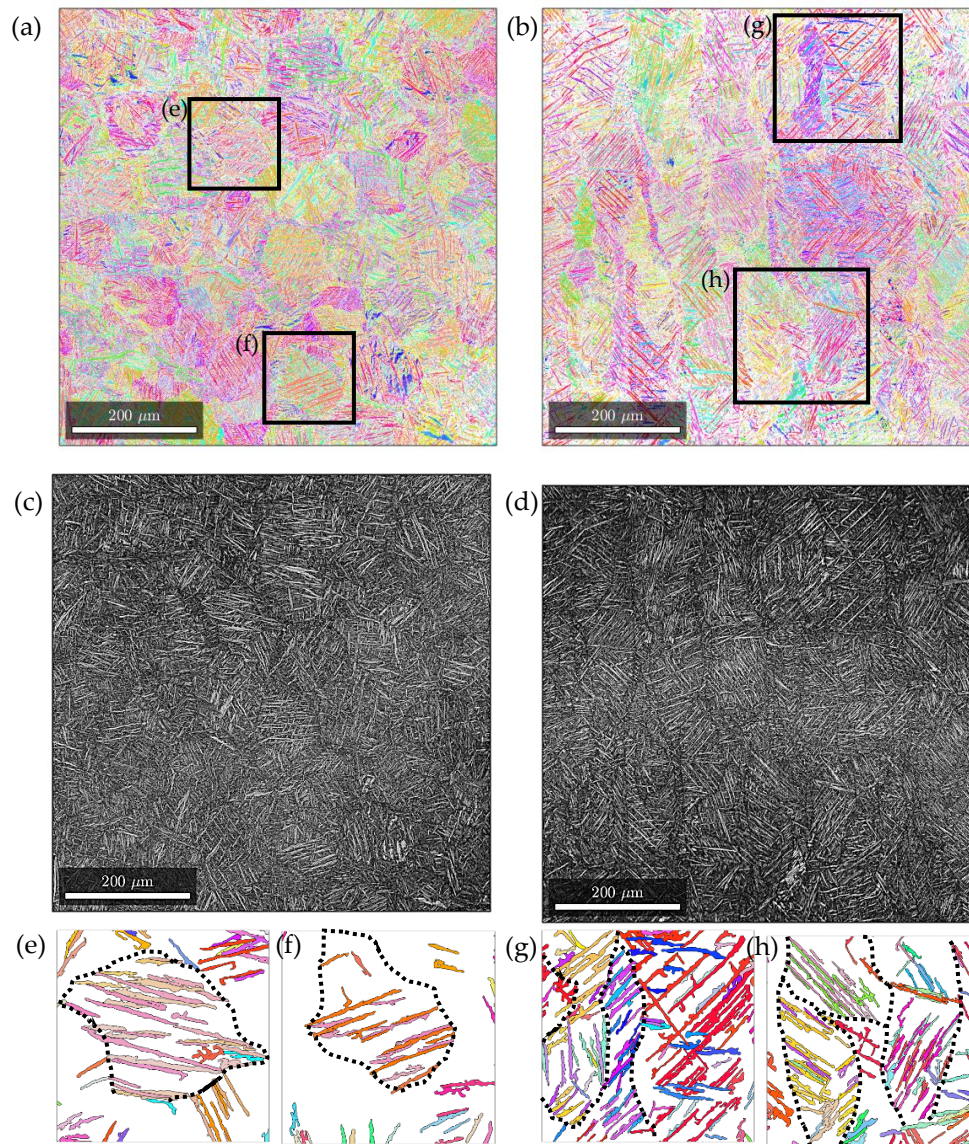
Figure 6.7. Qualitative comparison of AF lath morphology in XY-plane, showing (a) orientation map and (c) image quality map, and in ZX plane, showing (b) orientation map and (d) image quality map. Primary α' grain (grain length > 20 μm) sections (e & f) XY-plane, and (g & h) ZX-plane grains.

Microtexture refers to both the α' crystallographic and morphological texture local to a PBG. Unlike α+β colonies that form an α+β lamellar structure due to furnace cooling from above the β-transus, martensite lath "twins" are separated by finer secondary and tertiary laths. This repetition and the fraction to which the repetition dominates the PBG gives rise to texture and texture strength, respectively. Since the Ti-6Al-4V martensitic lath orientation has been shown to form along habit planes, PBG crystallographic texture controls α' lath-angle texture during the LPBF process (Gaunt & Christian, 1959; Banerjee & Krishnan, 1971). Figure 6.7(e – h)

illustrate the PBG-localised microtexture of primary α' laths. Primary α' laths were emphasised by selecting laths with a length of $> 20\,\mu\mathrm{m}$[10]. An interesting finding is that lath angle/orientation appears to be similar along layer-wise regions.

Figure 6.8 plots histograms of primary α' lath length, width, aspect ratio and lath angle for AF samples. Differences in these lath shape parameters between the two planes indicates that the ZX-plane has slightly larger grains, as quantified in Table 6.2. The dominant lath angle for the two planes also differs. For the XY-plane, peaks at ~0 and ~90° with respect to the X-axis can be seen. In the ZX-plane, a dominant lath angle at ~45° with respect to Z-axis is measured.
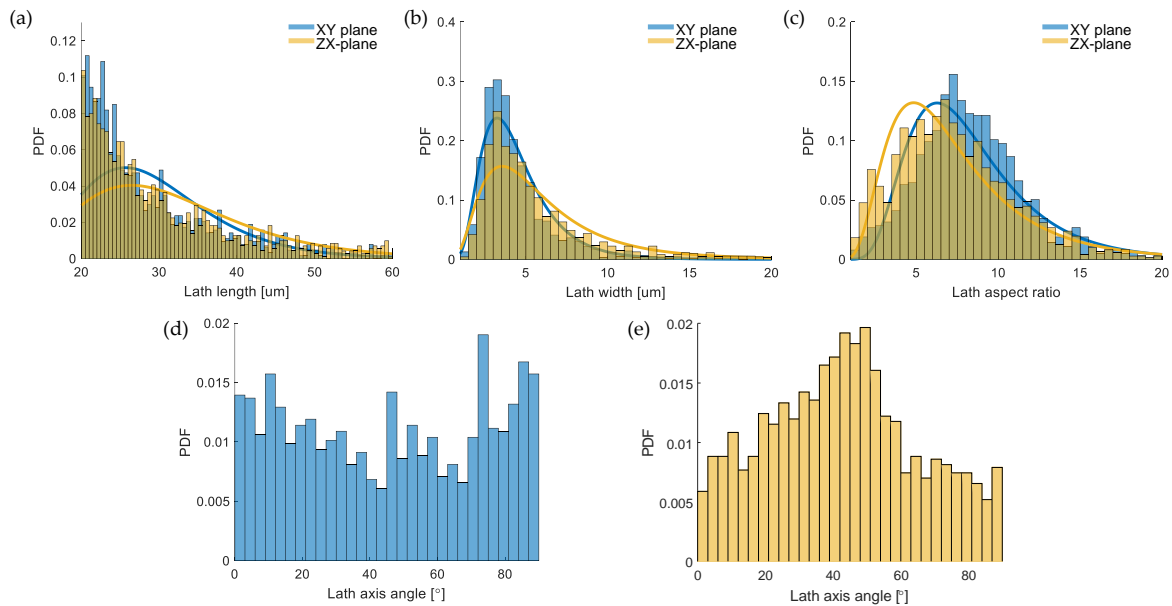
Figure 6.8. Quantification of primary α' lath morphology of AF showing (a) length and (b) width (c) aspect ratio. Bin width is 0.5 µm. AF lath-angle distribution showing (d) XY- and (e) ZX-planes. Bin width is 3°.

---

[10] The selection of 20 µm is based on the observed PBG column width, as shown in Figure 6.2.

Table 6.2. AF primary lath shape parameters from fitting functions.

	XY-plane	ZX-plane
Lath length [µm]		
Mode	25.7	26.46
Mean ± 1σ	29.3 ± 8.89	31.8 ± 11.5
Lath width [µm]		
Mode	3.25	3.55
Mean ± 1σ	4.48 ± 2.19	6.08 ± 4.00
Lath aspect ratio (length / width)		
Mode	6.27	4.83
Mean ± 1σ	8.37 ± 3.86	2.83 ± 1.41
Lath angle [°]		
Mode	~0° & 90°	~45°

6.3.3 Tensile behaviour

Tensile behaviour is shown in Figure 6.9 and summarised in Table 6.3. Clear anisotropy is noticeable when comparing the horizontal and vertical sample groups. AF horizontal samples achieved a higher strength and a lower percentage elongation-to-fracture, while the AF vertical samples achieved a lower strength and higher percentage failure elongation. After BAQ for three hours, both sample groups (horizontal and vertical) show a decrease in strength (horizontal: 9.6 %, vertical 5.9 %) and a decrease in the percentage elongation to failure (horizontal: 60 %, vertical 28 %). It should be noted that the largest change in mechanical properties occurs in the horizontal samples. This is likely a result of a larger change in microstructure in the horizontal sample, as observed from the change in PBG morphology of the ZX-plane. A decrease in the difference of the mean ultimate tensile strength between the vertical and horizontal orientations is noted (from 5.89 % to 1.80 %). A decrease in mean difference between percentage elongation to failure (from 31.6 % to 15.2 %) between the AF and BAQ groups was observed. A change in the difference in Young's modulus between the two orientations in the AF and BAQ state is less than one standard deviation.
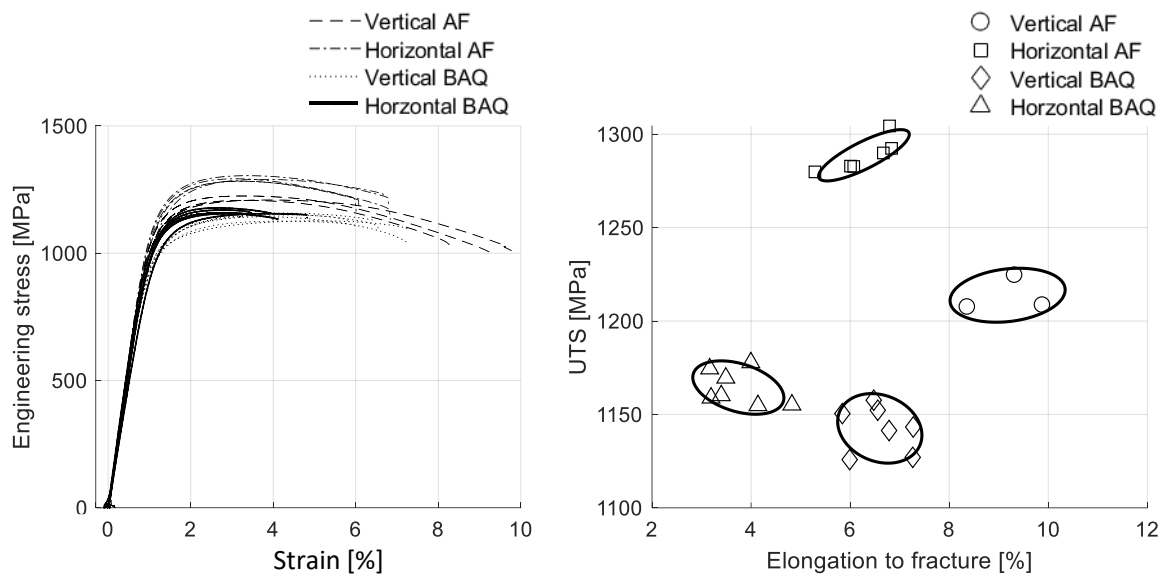
Figure 6.9. Tensile test results (a) Stress versus strain plot of all samples (b) plot of ultimate tensile strength (UTS) versus fracture elongation. Circles represent one standard deviation of the group.

Table 6.3. Mean tensile properties. ± range indicates one standard deviation.

	Yield stress [MPa]	UTS [MPa]	Fracture [%]	E [GPa]
AF Vertical	1054 ± 24.0	1 214 ± 9.54	9.18 ± 0.767	116 ± 2.47
AF Horizontal	1 113 ± 22.0	1 290 ± 9.06	6.28 ± 0.605	116 ± 6.05
BAQ Vertical	927 ± 15.7	1 140 ± 12.3	6.60 ± 0.561	108 ± 2.53
BAQ Horizontal	997 ± 19.3	1 160 ± 9.43	3.74 ± 0.607	105 ± 4.30

6.3.4 Surface deformation and microcracking

SEM micrographs of sample surface deformation, Figure 6.10(a & d), emphasise the influence of the PBGs on the deformation behaviour. PBGs are less distinguishable in the vertical sample than in the horizontal sample due to PBG-localised deformation in the horizontal sample causing shadow-lines (highlighted by arrows) along the PBG boundaries. The formation of shear lips (not directly shown) confirms a more ductile deformation of the vertical samples. With regards to the fracture plane edge, the XY fracture plane (vertical samples, Figure 6.10(a)) appears transgranular with respect to the PBGs, while the ZX fracture (horizontal samples, Figure 6.10(b)) plane appears intergranular with respect to the PBGs. This observation suggests that the PBGs in the horizontal sample inhibit deformation to a larger degree than in the vertical sample. Deformed α' laths also become visible after deformation. The α' lath deformation spread appears homogenous in the vertical sample and PBG-localised in the horizontal sample.

104
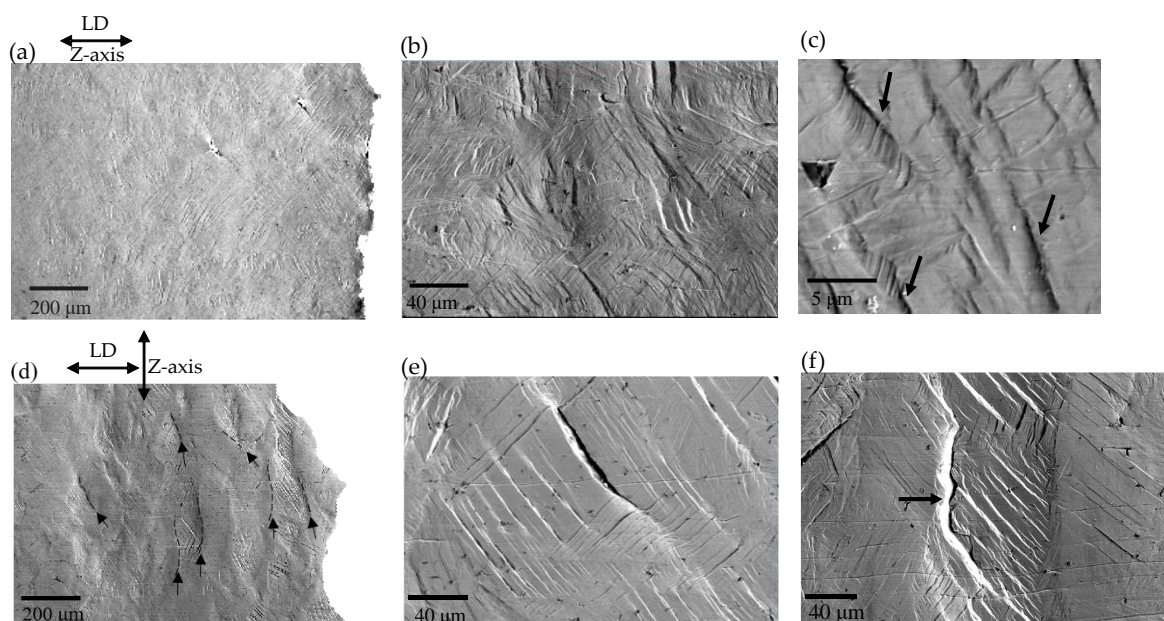
Figure 6.10. SEM micrographs of AF (a – c) vertical and (d – f) horizontal built samples. (e) PBG localised deformation trace lines showing PBG boundaries. Deformation and microcracks (arrows) on the surface of samples (c, f) (LD – load direction).

In the horizontal sample, Figure 6.10(e), large opening microcracks at ~45° to the load direction are visible. These are not present in the vertical sample, Figure 6.10(b). High-resolution image of the vertical sample, Figure 6.10(c) shows microcracking due to the accumulation of intergranular slip at the lath boundary (indicated by arrows). This mechanism of failure has also been observed elsewhere (Moridi *et al.*, 2019). Microcracking was also observed to propagate along PBG boundaries (indicated by arrow) in the horizontal sample, Figure 6.10(f).

Quasi-cleavage fracture planes consisting of planar cleavage facets as well as dimples, "crater holes" and fast fracture (FF) zones were observed and depicted in Figure 6.11. The large "crater holes" are likely the result of pores that have grown during loading. These features have also been observed in other studies (Khorasani *et al.*, 2017). The vertical AF sample, Figure 6.11(a), revealed many ductile dimple zones interspersed with inclined cleavage planes measuring approximately 100 µm in diameter. The facet planes in the horizontal sample, Figure 6.11(b), measure up to approximately 200 µm, but instead of dimples, areas of flat FF zones were observed. In both cases, the diameter of the facet planes approximately matches the length of their PBGs in the plane perpendicular to the load direction. The FF zones in the horizontal sample and the dimples zones in the vertical sample agree with the respective higher and lower ductility measured in the tensile tests. When comparing the AF, Figure 6.11(a & b), with the BAQ fracture surfaces of vertical samples, Figure 6.11(c, d, & e), the size of the facet planes appears larger in the BAQ sample. This is likely due to a larger PBG size in the BAQ sample.
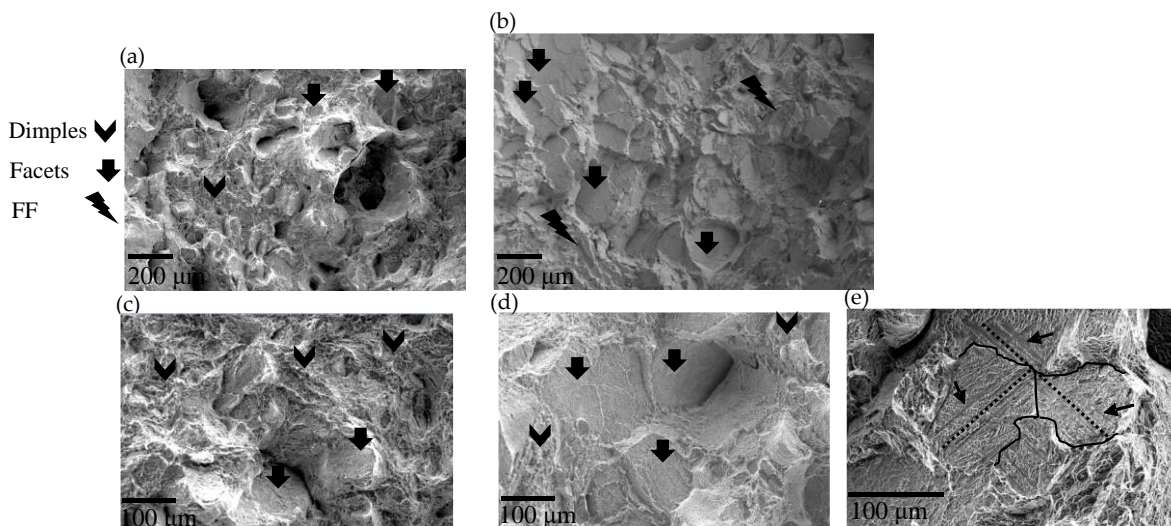
Figure 6.11. SEM fractographs of AF samples, showing (a) vertical and (b) horizontal orientations (FF – fast fracture). SE-SEM fractographs in the vertical orientation, showing (c) AF and (d, e) 3-hours BAQ samples. Cleavage trace-lines (e) of primary α' laths in neighbouring PBGs (pointed by arrows and traced with broken lines). PBG boundaries highlighted by black trace lines.

Figure 6.11(e) shows cleavage trace lines left by α' laths that span the diameter of the facet plane (likely to be primary α'). These cleavage laths appear to link at the PBG boundary triple point.

6.3.5 Slip and slip transmissibility

By careful observation of Figure 6.6(a), it appears that a texture intensity difference exists below $m < 0.35$, with the ZX-plane showing a higher texture intensity (as indicated by arrows). As noted in Subsection 6.2.3, slip of $m < 0.35$ predominantly occurs in basal slip mode. Figure 6.12(a – c) plots histograms of m for AF grains activated by basal, prismatic-⟨a⟩, and combined modes. Grains activated by "hard" basal slip of $m < 0.35$ in the XY-plane loaded in the Z-direction (representing vertical samples), Figure 6.12(a), have 16.1 % of all grains activated by basal mode (or 7.09 % of the total combined modes, Figure 6.12(c)) and the ZX-plane loaded in the Y-direction (representing horizontal samples), Figure 6.12(a), contains 20.3 % of all grains activated by basal mode (or 9.54 % of the total combined modes Figure 6.9(c)). This difference in percentage between the two orientations at $m < 0.35$ reflects the texture difference for near-[0001] grain orientations observed in Figure 6.6(a). However, the difference in the number of grains is only ~2.5 % of the total combined slip modes.
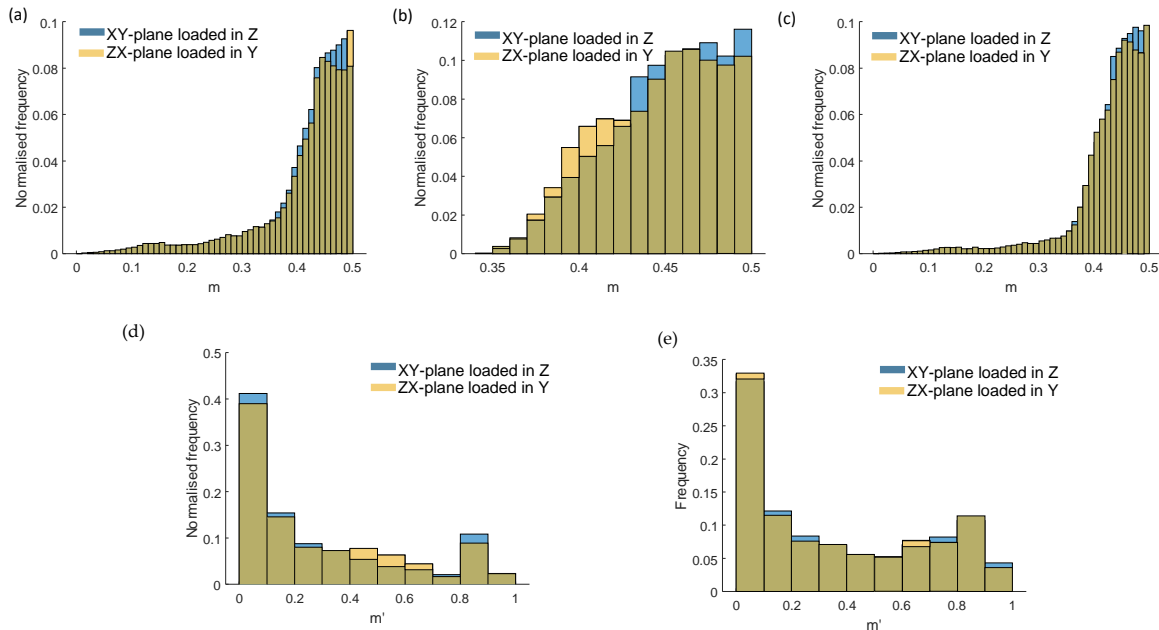
Figure 6.12. Normalised histogram plot comparing *m* and *m'* distribution between vertical and horizontal samples. Showing *m* of grains activated by (a) basal plane slip, (b) prismatic-⟨a⟩, and (c) combined slip modes (bin width is 0.01). Showing *m'* of α'-α' grain boundaries (d) internal to, and (e) across PBG boundaries (bin width is 0.1).

When considering the number of grains activated by basal slip, Figure 6.12(a), XY-plane has 76.3 % of basal mode grains of $m > 0.4$, and the ZX-plane has 72.7 % of $m > 0.4$ basal mode grains. When considering the number of grains activated by prismatic-⟨a⟩, Figure 6.12(b), the XY-plane has 89.8 % of $m > 0.4$ grains and the ZX-plane has 87.9 %. When considering the number of grains activated for a combined basal + prismatic modes, Figure 6.12(c), the XY-plane has 81.7 % of grains $m > 0.4$ and 47.6 % of grains $m > 0.45$. The ZX-plane has 79.1 % of grains $m > 0.4$ and 45.6 % of grains $m > 0.45$. While the ZX-plane loaded in the Y-axis (i.e., the horizontal sample) does show a lower *m,* it is only ~2 % for a combined basal + prismatic slip distribution. This small difference is in contrast to findings by Rem *et* al. (2019).

Slip transmissibility, *m',* is dependent both on activated grain slip mode and misorientation angles between grains (determined by BOR). Due to BOR, there exist five axis/angle misorientation types for α'-α' grain boundaries belonging to the same parent β-grain (Wang *et al.*, 2003). Since the misorientation distribution of grains in the XY- and ZX-planes is texture-independent, and an insignificant *m* difference exists between orientations, Figure 6.12(a – c), the distribution of *m'* for both planes are almost identical. Figure 6.12(d & e) plots histograms of the *m'* for active α-α slip both internal to and across PBGs. Since misorientation types have uneven amounts (for example, axis/angle pair $[\overline{1.377}, \overline{1}, 2.377, 0.359]/60.83°$ has the largest portion of high angle grain boundaries at a theoretical 36.4 % (Wang *et al.*, 2012)), peaks with high occurrence of low-*m'* exist. A large fraction of grain boundaries internal to PBGs, Figure 6.12(d), have $m' < 0.2$, with the XY-plane making up 56.6 % and the ZX-plane 53.5 %.

Furthermore, due to the preferential misorientation of PBGs (with a dominant axis/angle of [1 1 1] / 45°), this leads to a large fraction of low-m' of α'-α' slip across PBGs, Figure 6.12(e) with the XY-plane 43.8 % and the ZX-plane 44.3 % of grain boundaries $m' < 0.2$. This suggests that both internal and PBG boundaries function as slip inhibitors due to poor compatibility (transmissibility) of internal and neighbouring active α'-α' grains.

An EBSD map of a ~2 % strained sample was acquired by imaging the ZX-plane of a vertical BAQ fractured sample at some distance from the fracture plane. BOR necessitates the misorientation angles of hcp grains from the same parent β-grain to be: 10.53°, 60°, 60.83°, 63.26°, and 90° (Wang *et al.*, 2012). When plotting a histogram of misorientation angles, there are frequency peaks at these angles. Since laths on either side of two neighbouring PBGs do not hold to this rule, PBG boundaries can be identified by plotting "non-peak" misorientation angles (Wang *et al.*, 2012). Since the same is true for deformed laths, it was found that these too can be identified in this way. Deformed laths were identified by plotting the "non-peak" misorientation boundaries of α'-α' grains on top of the α' orientation map in Figure 6.13(a). To emphasise deformed α' laths identified, these were traced with broken lines while the reconstructed PBG map was overlaid, Figure 6.13(b). Letters signify PBGs while numbers signify identified deformed laths.
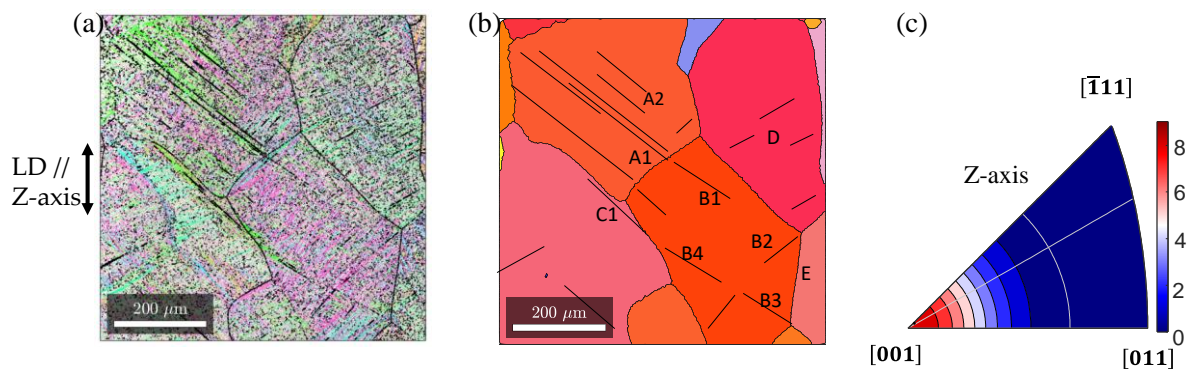
Figure 6.13. (a) overlay of non-BOR α'-α' boundaries on hcp orientation map, (b) identification and labelling of deformed laths using trace lines on Z-axis orientated reconstructed PBGs (c) Z-axis IPF of PBG orientations (LD – load direction).

Some lath deformations initiated at PBG boundary triple points (identified most clearly at B2 and B3 although C1 is a possibility) and interior to PBGs (laths in D, and A2). Deformed laths transverse PBG boundaries at two points: between A1 to B1 and between C1 and B4. Deformed lath groups A1, B1 and PBG E are further investigated using pole figures and IPFs to determine the active slip mode and the mechanism of slip transmission across PBG boundaries.

Colour hcp IPFs and pole figure plots of the selected regions A1, B1 and E are plotted in Figure 6.14. Iso-curves of high $m > 0.485$ (refer to Figure 6.1) are overlaid on IPFs. Lath deformation can be identified by a large orientation spread within a single grain. The lath's active slip system

undergoing deformation can be determined by the lath's proximity to a high *m* region (highlighted by the iso-curves in the IPFs).
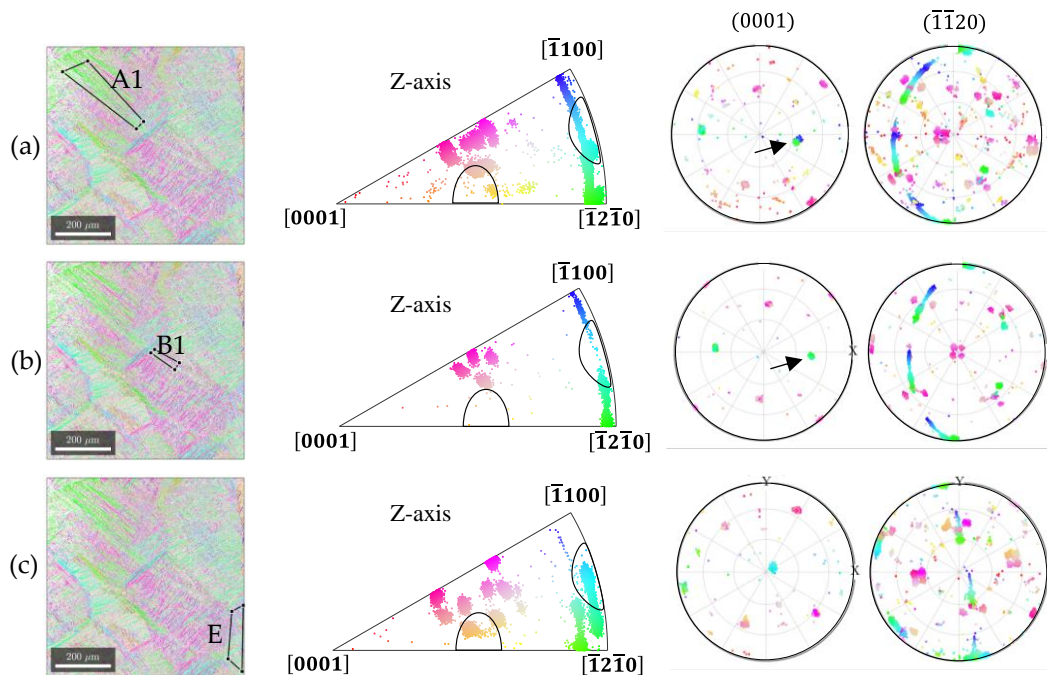
Figure 6.14. IPF and pole figures of lath groups (a) A1 and (b) B1, and area (c) PBG E, identifying primary deformation mechanisms for a ~2 % strained BAQ vertical sample.

Results show that a single α' variant of each PBG undergoes prismatic-⟨a⟩ slip. Interestingly, even though other laths have high Schmid factors in the basal system, they were not activated in the examples shown. Transmission of slip seems to occur when both deformation variants have parallel basal planes and, therefore, near-parallel slip vectors.

6.4 Discussion

6.4.1 Structural anisotropy of XY and ZX-plane in AF and BAQ samples

The microstructure of PBGs and α' grains was found to be textured both in morphology and crystallography. The crystallographic texture of the PBGs was seen in the strong uniformity of ⟨001⟩$_\beta$ axes parallel to the Z-axis. Due to the possible twelve variants forming in accordance with BOR, this leads to a weak α' crystallographic texture. A slight difference in α' crystallographic texture was observed between the two orientations, IPF of Figure 6.5 and Figure 6.6, causing a slight difference in *m* and *m'* distribution, Figure 6.12. PBGs were morphologically textured in that they had uniformly orientated columnar-shaped grains parallel to the Z-axis. This was shown to influence the α' lath shape parameters causing a difference in α' lath length, width, and aspect ratio between the XY and ZX-planes.

Furthermore, the α' lath-angle showed a strong uniformity at ~45° to the Z-axis. This dominant lath angle is likely caused by the combination of the ⟨001⟩$_β$ // Z-axis textured PBGs and the {334}$_β$, {344}$_β$ habit plane formation of martensitic laths (Banerjee & Krishnan, 1971)(Gaunt & Christian, 1959). The reconstructed PBG habit planes angles are plotted in Figure 6.15(a – d), and a pole plot of the habit planes is depicted in (e). This shows PBGs habit planes have a high affinity for angles at ~45° to the Z-axis. Good agreement between the measured dominant AF lath angles, Figure 6.8(c & d), and the AF habit plane angles, Figure 6.15(a & b), exist.
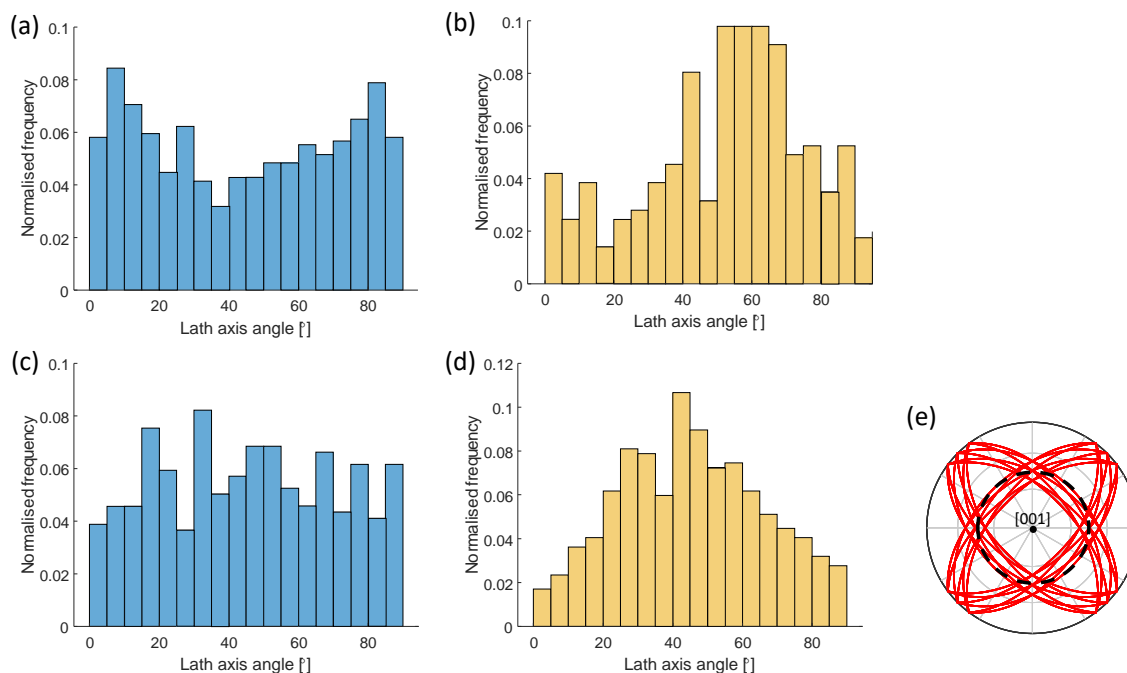
Figure 6.15. AF lath-angle distribution of reconstructed PBG habit planes trace lines with respect to Z-axis, showing AF (a) XY-plane and (b) ZX-plane, and BA (1-hour and 3-hours combined), showing (c) XY-plane and (d) ZX-plane. (e) Pole plot of the {334}$_β$ and {344}$_β$ habit planes with broken line at 45° from [001]. Bin width is 5°.

The recrystallisation of the PBGs through a BA heat treatment was effective in reducing the morphological texture of PBGs in the ZX-plane through globularising. However, the crystal texture of the PBGs remained unchanged, i.e., ⟨001⟩ // Z-axis. Due to the dependence of martensitic lath shape-orientation on the habit plane orientation of the PBG crystallography, it is likely that the ~45° dominant lath angle with respect to the Z-axis also remained unchanged, as derived from habit planes of Figure 6.15(c & d). This contrasts with wrought BA samples which undergo nucleation and growth of newly unstrained and differently textured PBGs (Pilchak *et al.*, 2018).

6.4.2   Preferential lath deformation and slip transmission

It was seen from the strained EBSD map, Figure 6.14, that prismatic-⟨a⟩ slip systems were activated even though they had a lower *m* value than variants of high-*m* basal slip laths. To explain this, it is argued that the α' morphology influences deformation of α' laths to a larger degree than their relative Schmid factors. Furthermore, since a negligible difference in the distribution of *m* and *m'* between the vertical and horizontal samples was found, but a significant difference between the XY and ZX-planes' dominant primary α' lath angle was found, Figure 6.8(d) versus (e), it is argued that the latter was a more significant differing structural feature, and therefore, had a dominant influence on anisotropy.

Primary α' laths orientated at ~45° to the load direction were shown to deform preferentially and acting as microcrack initiation sites. This phenomenon can be explained by noting that: (i) the maximum shear stress axis is at 45° with respect to the loading direction, and (ii) primary α' grains achieve a higher total plastic strain compared to shorter laths (i.e., secondary, tertiary and quaternary α' laths) and (iii) laths at ~45° have the longest slip distance along the maximum shear angle compared to laths orientated at angles of minimal shear angles of ~0 and ~90° to the load direction, as depicted on Figure 6.16. Moridi *et. al* (2019) further proposed that primary α' contain less dislocations due to auto-tempering during cyclic heating and therefore provide a "long dislocation mean free path."
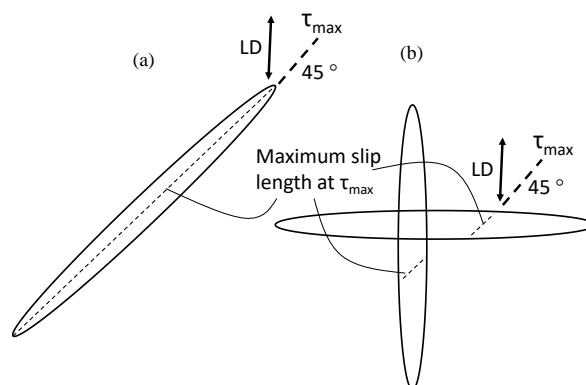
Figure 6.16. Sketch of slip length relative to maximum shear stress orientation of (a) 45° dominant lath orientation compared to (b) 0 and 90° lath orientations (LD – load direction).

Poor slip α'-α' transmissibility both internal and across PBGs was found. This provides evidence that PBG boundaries inhibit deformation. It follows that due to a relatively higher density of PBG boundaries in the XY-plane (compared to the Z-axis), deformation will be inhibited to a larger degree when material is loaded parallel to the XY-plane (i.e., horizontal samples). Slip translation across PBGs was seen to occur of near-parallel basal planes and parallel lath-angles. Therefore, it is clear that both crystallographic and morphological factors contribute to slip translation across PBG boundaries and to anisotropic deformation behaviour

in general. Persistent anisotropy is likely due to the unchanged ~45° dominant lath angle with respect to the Z-axis.

An improvement of mechanical anisotropy between sample orientations was measured after BAQ, however BAQ caused PBG growth and thereby led to the formation of longer primary α' laths compared to the AF microstructure. A larger α' lath length and fewer PBG boundaries are the likely causes of a decrease in material strength and ductility of the BAQ samples. While the former can be explained by the Hall-Petch relation, the latter is likely due to fewer PBG boundaries acting as slip obstructions.

6.4.3 Microcrack initiation, propagation, and final fracture

The mismatch of strain between primary and finer secondary, tertiary and quaternary α' laths resulted in strain localisation at their interface. The observed microcracks along lath boundaries occur due to the coalescence of nucleated voids. Void nucleation is a function of the strain state of the localised grain and/or grain boundary. The abovementioned morphological and crystallographic structural aspects control microcrack initiation and propagation. Void initiation and coalescence are argued to be preferential at (i) low-m grains (ii) a low-*m'* slip transmissibility, (iii) at the boundary of primary α' grains (iv) at the boundary of laths orientated ~45° to the load direction.

Due to their size, primary α' laths make up the majority of PBG area, and thus, can be regarded as the dominant α' microtexture. It is proposed that the dominant lath microtexture will control the PBG-localised deformation behaviour. Since microtextured regions will theoretically initiate the same slip systems at similar strain, microtextured regions function as a single grain in that they will deform at a single load level and in a single slip direction. Final fracture is caused by the coalescence of microcracks on the same plane, causing the fracture surface's facet appearance in a single PBG. This would continue until fast fracture. Larger regions of microtexture cause larger regions of uniform-textured deformation and crack coalescence. Since PBGs in the ZX-plane have larger regions of microtexture due to larger PBGs, this contributes to mechanical anisotropy. Globularisation was shown to homogenise PBGs between orientations and thereby improve anisotropy. By increasing the PBG size through BAQ treatment, however, the size of microtexture regions increased proportionally, reducing the mechanical properties.

In addition to this, PBG boundaries were shown to impede microcracks from propagating. The accumulation of slip and/or microcracks at PBG boundaries were shown to cause crack initiation and crack propagation along PBG boundaries. It is possible that microcracks could either have initiated from the same PBG triple point boundary, or a single microcrack could have propagated through this triple point to favourably orientated α' laths in other PBGs. Furthermore, PBG boundaries provide an unobstructed path for cracks to propagate. Since PBG boundary length is longer in the Z-axis direction, columnar PBG boundaries will be more susceptible to crack initiation. This is due to a larger stress concentration resulting from a larger number of laths impinging on a single PBG boundary in the ZX-plane, compared to the XY-plane.

6.5 Conclusions

This study was motivated by the need to understand the microstructural cause of anisotropic deformation behaviour with respect to the build direction (Z-axis) and the perpendicular direction (parallel to the XY-plane) in LPBF produced Ti-6Al-4V. Both crystallographic and morphological microstructural features differ in the two orientation planes. It is argued that the α' crystallographic texture difference is too small to cause significant difference in the *m* or *m'* distributions. However, significant α' morphological difference, particularly dominant lath angle difference, is observed. A BAQ heat treatment improved PBG morphological anisotropy by globularising and homogenising the PBGs, thereby improving mechanical anisotropy between vertical and horizontal samples. BAQ did not alter the PBG crystallographic texture (⟨001⟩ // Z-axis), however. Due to excessive PBG growth during BA, both strength and ductility decreased. Due to the dependence of α' lath habit planes on the PBG orientation, a dominant ~45° lath angle with respect to the Z-axis remained unaffected, and therefore, a residual anisotropy remains. Deformation behaviour of material studied through EBSD and fractography revealed that α' laths deformed local to PBGs and preferentially at angles of ~45° to the load direction. Fractography revealed crack propagation along α'-α' boundaries internal and at PBG boundaries.

6.6 Post-submission discussion

The following discussion stems from insights gained from reviewer feedback; literature published post-submission and post-submission analysis.

The paper does not include quantified analysis of BAQ α' laths, as was done of the as-fabricated samples. BAQ samples require a large map size in the range of 3×3 mm to include multiple PBGs. Due to the fine α' grain size, a small EBSD step size is required to achieve high indexing. The mapping of a 3×3 mm BAQ sample would be extremely computationally intensive in mapping duration, data volume, post-processing computation power and processing time. Furthermore, in email exchanges with the SEM facility operator, it was made clear that a map size larger than 1×1 mm would cause significant distortion, and that map size and step size are restricted based on scan time length.

Although the authors have not imaged large maps of BAQ samples, a theoretical deduction of α' lath angle is made from reconstructed PBG habit planes. This aims to at least provide a theoretical indication of the dominant α' formation angles in BAQ samples. In this regard, the authors have provided a theoretical analysis of BAQ α' morphology based on reconstructed PBGs.

The study uses furnace cooled samples to circumvent the above restrictions in EBSD maps size (see Footnote 9 in Subsection 6.2.3.). Furnace cooling was only used as an experimental approach to increase the volume percentage of β-phase in the material, thus allowing for a larger EBSD step size. Although the resultant furnace cooled microstructure will be significantly different to α' achieved by BAQ and as-fabricated LPBF, the analysis of deformation behaviour of furnace cooled material is not presented in this study since the study only focuses on the

influence of PBG texture and morphology on deformation anisotropy. The study's major contribution is in determining mechanisms by which PBG texture causes deformation anisotropy.

Grain boundary α (see Subsection 2.1.2) is known to cause a preferential path for damage accumulation along the PBG boundaries (Donachie, 2000). Therefore, it follows that since grain boundary α follows the morphology of the PBGs, this could influence anisotropic deformation behaviour. However, grain boundary α only forms through slow cooling from above T_β and was absent for all WQ samples in this study. Since no grain boundary α was observed, microcracks along PBG boundaries likely initiate internally and propagate along PBG boundaries.

The study found that β-annealing leads to a reduction in ductility. It should be noted that applying a BAQ heat treatment would likely not be advantageous for improving the material's mechanical performance. A key contribution of the paper is, however, not in using a BAQ to improve mechanical performance, but rather to provide a detailed explanation for why the anisotropy remains after globularisation of PBGs.

Additional investigation post-publication by the authors found that applying quenching-based heat treatments developed in Chapter 4, after β-annealing, was successful in improving the ductility above 10 %. Therefore, it follows that globular PBGs with adequate material properties are still achievable through following the correct heat treatment steps.

7 LPBF-produced Ti-6Al-4V: Influence of high-energy process parameters on *in-situ* martensite decomposition, stress relief and prior-β grain texture

Very few studies have investigated the use of high-energy process parameters for *in-situ* part heating and microstructural response. This chapter addresses the fourth project objective by investigating the influence of above-default-E_v process parameters on martensite decomposition, PBG structure and residual stress.

This paper has been submitted to the *Journal of Materials Processing Technology*. Since no reviewer feedback has yet been received for this chapter, the post-submission section is omitted, and all further discussion of this work is done in Chapter 8.

Declaration by the candidate:

With regards to Chapter 7, the contributions of author and co-author are as follows:

Name	Email	Contribution	Extent (%)
G.M. Ter Haar (candidate)	gterhaar@sun.ac.za	Experimental design, completion of all tests and data analysis, writing and compilation of manuscript	95
T.H. Becker	tbecker@sun.ac.za	Supervision and reviewing	5

Signature of candidate: [GTH] (see Footnote 5)
Date: 2021/02

Declaration by the candidate:

The undersigned hereby confirm that:

1. The declaration above accurately reflects the nature and extent of the contributions of the candidate and the co-authors to Chapter 7
2. No other authors contributed to Chapter 7 besides those specified above, and
3. Potential conflicts of interest have been revealed to all interested parties and that the necessary arrangements have been made to use the material in Chapter 7 of this dissertation.

Signature (see Footnote 5)	Institutional affiliation	Date
[TH Becker]	SU	2021/02

7.1 Introduction

Laser powder bed fusion (LPBF) is currently the most popular metal additive manufacturing (AM) method for the direct fabrication of functional components (Zhang *et al.*, 2017). LPBF additively fabricates parts by selectively melting sequential layers by scanning a fine metal-powder bed with a high-power laser. Compared to conventional metal manufacturing routes such as forging and rolling and subtractive processes such as milling and turning, LPBF boasts various advantages that ensure LPBF machines' continued market growth (Wohlers Associates, 2018). These advantages include high achievable part complexity, reduced manufacturing lead time, reduced specialised tooling requirements and low material waste during net-shaped fabrication.

Among other metals, LPBF has been applied to the titanium alloy, Ti-6Al-4V. This alloy has been extremely popular in aerospace and biomedical applications for a long time due to its high specific-strength, high-temperature corrosion resistance and biocompatibility (Boyer, 1996). Research efforts to qualify a LPBF process to achieve a high-quality Ti-6Al-4V material is on-going. Studies have found that a high part density > 99.9 % is achievable using optimal process parameters (Mishurova *et al.*, 2019a). Undesired martensitic microstructure (α') and residual stress caused by the high thermal gradients of the melt pool and surrounding material still pose an obstacle to achieving adequate material ductility, toughness, and fatigue properties in the as-fabricated (AF) state (Liu & Shin, 2019).

Post-process heat treatments have been demonstrated to successfully decompose α' into a more ductile (α+β) microstructure and relieve residual stress, thereby improving the aforementioned ductility (Vilaro *et al.*, 2011; Vrancken *et al.*, 2012; Huang *et al.*, 2015; Cao *et al.*, 2018; Ter Haar & Becker, 2018) and fatigue life (Vrancken *et al.*, 2014). Crucially, post-process heat treatments have been found to improve the material's elongation to failure to above 10 % required of Ti-6Al-4V by wrought (ASTM F1472) and LPBF standards (ASTM F2924-14). Furthermore, bi-modal post-process heat treatments conducted by the authors have achieved mechanical properties that are comparable to their conventional-produced counterpart (Ter Haar & Becker, 2018).

Post-processing is, however, an expensive and time-consuming step. Studies have shown potential in using *in-situ* thermal treatments (i.e., thermal treatments during LPBF fabrication) to decompose α' and reduce residual stress. In principle, as demonstrated in post-process heat treatments, martensite decomposition can occur *in-situ* at a temperatures as low as 400 (Xu, Sun, *et al.*, 2015) and 427 °C (Ter Haar & Becker, 2020). Therefore, it follows that increasing part temperature during fabrication to a high enough temperature will have a similar effect. Furthermore, sufficiently slow part cooling rates below the β-transus temperature can suppress martensitic transformation and allow for diffusional phase transformations (Kelly, 2004).

In addition to the brittle α' microstructure, high thermal gradients ($10^4 - 10^5$ K/cm) (Xu, Sun, *et al.*, 2015) in the melt pool lead to an epitaxial growth (EG) of a columnar prior-β grain (PBG) structure. This microstructure has been associated with an anisotropic mechanical behaviour in LPBF materials (DebRoy *et al.*, 2018; Kok *et al.*, 2018). A sufficient reduction in thermal gradient (G) has shown to induce the formation of equiaxed rather than columnar prior-β grains

when using CO_2 laser systems (Kobryn & Semiatin, 2003). Post-process heat treatments conducted by the authors have shown that post-process heat treatments above the β-transus temperature are successful in globularising and homogenising PBG structure (see Chapter 6). To the authors' knowledge, no research has been published that investigate the *in-situ* suppression of epitaxial PBG growth with commercially available fibre laser systems.

In-situ heating can be categorised into two approaches. The first route, being simpler to implement and having a larger number of published articles, is thermal treatments through base plate heating (Kempen *et al.*, 2013; Vrancken, 2016; Ali *et al.*, 2017). This has been shown to decompose martensite and reduce residual stress at a base plate temperature as low as 370 °C (Ali *et al.*, 2017). However, a study by Vrancken *et. al* (2015) indicated an increased oxygen and nitrogen pick-up with an increase base-plate temperature.

The second, less published route, uses process parameters to induce part heating, from either intensifying the energy density input of the laser (Xu, Brandt, *et al.*, 2015; Barriobero-Vila *et al.*, 2017; Haubrich *et al.*, 2019; Mishurova *et al.*, 2019a,b), or through using layer re-heating (Chen & Qiu, 2020). The specific parameters that have shown to facilitate martensite decomposition are shorter inter-layer time, larger layer thickness, less contact between the support structure and part, and larger part dimension (Xu *et al.*, 2017). A popular approach in quantifying the laser energy density input is through the volumetric energy density, calculated as $E_v = \frac{P}{v \cdot h \cdot l}$, where P is the laser power, v the laser scan velocity, h the distance between two consecutive scan tracks (called the hatch distance), and l the layer thickness. Since the first route of base plate heating requires specialised machine functionality or expensive machine customisation, the second route is likely more attractive as a cost and energy-efficient alternative.

Another promising avenue of research into *in-situ* processing is in altering the laser intensity or laser shape profile. This has been done by modulating the laser profile ellipticity, showing potential for reducing epitaxial columnar growth in 316L stainless steel (Roehling *et al.*, 2017; Shi *et al.*, 2020). Laser focal offset distance (FOD) is another route in altering the laser intensity profile. Due to the hour-glass shaped laser focal plane, altering the FOD by raising or lowering the base plate causes a broadening of laser spot size and a flattening of the gaussian-shaped laser intensity profile. Increasing the FOD causes an increased laser spot size in contact with the powder while decreasing the maximin laser intensity at the centre of the laser spot. This has the effect of decreasing the energy gradient with respect to the laser radius. Similarly, to the authors' knowledge, in-depth published research into the effects of altering the laser profile on the material response has not been done on Ti-6Al-4V.

The study was motivated by the desire to eliminate post-process heat treatments of LPBF-produced Ti-6Al-4V. The *in-situ* heating approach of altering laser scan parameters (as opposed to base plate heating) was chosen as a viable alternative *in-situ* route due to its promising outcomes in previous studies (Xu, Brandt, *et al.*, 2015; Barriobero-Vila *et al.*, 2017; Haubrich *et al.*, 2019; Mishurova *et al.*, 2019a, b; Chen & Qiu, 2020) and its practical implementation on current accessible commercial LBPF technologies.

The aim of the study is to determine the influence of above-default-E_v process parameters on martensite decomposition, PBG structure and residual stress. It is believed that a high laser energy input will allow for a favourable impact on microstructure and residual stress relief. This hypothesis is investigated by firstly determining a high-E_v process parameter range that achieves high part density. The influence of these process parameters on the microstructure, residual stress, oxygen + nitrogen content, material hardness and tensile behaviour is reported.
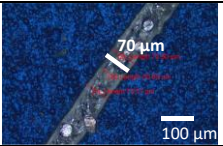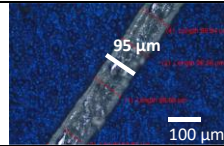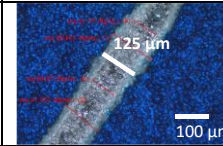
7.2 Materials and methods

7.2.1   Altering the laser profile

The laser system used in the study was manufactured by Rofin Baasel Lasertechnik (model YLR-200-WC) and has a wavelength of 1070 nm and a fundamental mode transverse electromagnetic profile (Gaussian or bell-shaped). The manufacturer reports a laser spot diameter (d) of 52.12 µm at the laser waist (d_0 – i.e., spot diameter at a FOD of zero). Laser spot diameter is defined as the diameter at which the laser intensity has fallen to $1/e^2$ (i.e., 13.5 %) of the maximum intensity. The maximum theoretical laser intensity, I, as a function of FOD distance from d can be calculated by $I = \frac{8P}{\pi\, d^2}$ (Svelto, 2010). A blue ionised plate was scanned at different FODs, and the width of the burnt tracks was measured using an optical microscope to measure the effect of FOD on laser spot diameter, as depicted by the micrographs in Table 7.1.

Calculated laser intensity from measured values and percentage change in relative laser intensity is also tabulated. The measured d of 70 µm is ~18 µm larger than the manufacturer-reported diameter from these results. This could be due to wear in the fibre optics. Measurements results further indicate that increasing the FOD from 0 to 2 mm increases the measured d from approximately 70 to 95 µm while decreasing the maximum theoretical laser intensity by 46 %. Increasing the FOD from 0 to 3.5 mm increases d from 70 to 125 µm and decreases the maximum laser intensity by 67 %.

Table 7.1. Measured laser spot size and theoretical maximum laser intensity at FOD of 0, 2 and 3.5 mm.

FOD [mm]	0	2	3.5
Micrograph			
Measured d [µm]	70	95	125
Theoretical I [×10⁸ W.m⁻²]	5.20·P	2.82·P	1.63·P
Relative decrease in I	-	46 %	67 %

7.2.2   Experimental approach, process parameters and sample geometry

Ti-6Al-4V ELI (Grade 23) gas-atomised powder was acquired from Praxair with a min/max chemical composition as supplied by the manufactured of (wt%): Ti – balance, Al – 6.32, V – 4.06, C – 0.01, Fe – 0.05, O – 0.11, N – 0.03, H – 0.002. Before using the powder, the powder was dried by heating at 120 °C for four hours followed by slow cooling to room temperature. This step, aimed at improving powder quality, was also conducted elsewhere (Yadroitsev *et al.*, 2014). Oxygen and nitrogen analysis was performed by inert gas fusion on the dried powder using an ON-ELTRA machine. Results indicated an oxygen content of 0.12 at% and a nitrogen content of 0.048 at%. While this indicates an increase from manufacturer specifications, the values still fall below the requirements of ASTM F3001 (0.13 at% for oxygen and 0.05 at% for nitrogen).

Sieve filtering was done according to ASTM B214, with the largest sieve mesh grid used measuring 45 µm. Particle size was analysed using laser diffraction according to ASTM B822. The 10th, 50th and 90th percentiles of the powder diameters measured 23, 33 and 46 µm, respectively.

It was noted from the literature that a FOD of 2 mm achieved *in situ* martensite decomposition in $10 \times 10 \times 10$ mm cubes (Xu, Brandt, *et al.*, 2015). Improved sample density with a larger spot size has also been found (Kasperovich & Hausmann, 2015). As a preliminary investigation, samples were built with a FOD of 2 mm using a Concept Laser M1 machine with a maximum laser power of 95 W. Results confirmed similar effects on martensite decomposition, and therefore, the possible advantage of using a non-zero FOD.

The experimental approach consisted of building samples with a range of above-default-E_v values through varying laser hatch distance and scan speed. Layer thickness was kept constant at 30 µm for all samples. Default scan parameters at zero FOD recommended by the machine manufacturer, Concept Laser, are $P = 100$ W, $v = 600$ mm/s, $h = 105$ μm and $t = 30$ μm, which results in a E_v of 53 J/mm^3.

The machine's achievable part density using default parameters and similar powder has previously been found to range from 98.78 – 99.85 %, with a mean of 99.25 % (Ter Haar & Becker, 2018). Since the default process parameter-set recommended by the machine manufacturer is optimised for sample density and build time, the study's first objective was to determine a range of parameters that achieved a similar or improved density range. A two-step iterative build-density optimisation approach was conducted to identify above-default-E_v process parameters that achieve an adequate sample density. Sample density was determined through the Archimedes method following the standard procedure recommended by ASTM B311. Iso-propanol, as opposed to water, was used to minimise surface tension to eliminate surface air-bubble entrapment.

Once a parameter range of hatch distance + scan velocity that achieved adequate density was identified, selected sample parameters were used to build cylindrical and cantilever-shaped samples, shown in Figure 7.5. Cylindrical samples were machined into tensile test specimens, which were used to evaluate tensile behaviour. Cantilever samples were built to evaluate macro

residual stress. This was done by partially wire-cutting cantilevers samples from the built plate to allow part deflection to be measured. Since the magnitude of part deflection is proportional to the parts' macro-residual stress (Vrancken, 2016), the relative part deflection was used to indicate relative part residual stress.

Figure 7.1 depicts the scan strategy used for (a) cubes, (b) cylinders and (c) cantilever geometry samples. Cubic and cylindrical samples were scanned with a "zig-zag" strategy with scan rotation of 90° for each layer. Cantilever samples were scanned with Concept Laser's "island" strategy. Islands were scanned at 5 mm and shifted 2 mm with each layer. No contour scanning was used for any samples. The oxygen sensor kept the oxygen content of the build chamber below 0.12 at% (1200 ppm).
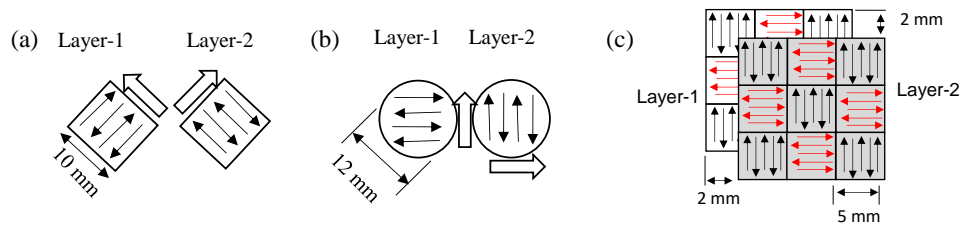
Figure 7.1. Scan strategy for (a) 10 mm cubes (b) Ø12 × 100 mm cylinders, and (c) cantilevers (Concept Laser "island" strategy).

7.2.3 Process optimisation for part density

The two density optimisation iterations entailed building $10 \times 10 \times 10$ mm cubic samples. The 1st iteration used a broad range of process parameters (P: 80 – 150 W; v: 200 – 1050 mm/s; h: 10 – 100 µm; FOD: 2 mm and 3.5 mm), at a constant $t = 30$ µm, to identify an overall relationship between laser power, hatch distance, scan velocity and FOD. The 2nd iteration used narrower ranges than those used in the 1st iteration in order to achieve high sample density over a larger range of process parameter sets. Table 7.2 depicts the build parameters of the 2nd build iteration, showing the narrower ranges of parameters investigated in these tests.

The influence of process parameters on sample density of the 1st build iteration indicated that a highest laser power was more effective in increasing sample density than lower power. Results showed that for a FOD = 2 mm and laser power larger than 130 W, scan speeds in the range of 500 – 650 mm/s and hatch distances larger than 20 µm were effective in achieving sample density above 99 %. The highest density for FOD of 3.5 mm was achieved by using a $P = 180$ W and a slower laser speed: 200 – 240 mm/s at a $h = 100$ µm.

Parameters chosen for cylindrical and cantilever builds, denoted with an '*', were chosen from the extremes of 2nd iteration process parameter ranges. These parameter sets, combined, covered three scan speeds, $v = 600, 700, 800$ mm/s, at $h = 60$ and 30 µm, respectively, and three hatch distances, $h = 30, 40$ and 60 µm, at $v = 800$ mm/s. Two samples at FOD = 3.5 mm were also built. A reference sample (ref) was fabricated using default parameters followed by a

recommended post-process heat treatment for martensite decomposition (800 °C for two hours followed by furnace cooling (Vrancken *et al.*, 2012; Ter Haar & Becker, 2018)). Since the reference sample was considered to have a stable α+β microstructure, its purpose was to serve as a "ideal" decomposed reference when evaluating the degree of martensite decomposition achieved in non-default parameter sets.

Table 7.2. Process parameter sets of the 2ⁿᵈ cubic build iteration grouped according to FOD and arranged in increasing E_v. Parameter sets chosen for cylindrical and cantilever samples are marked with an '*'.

Parameter set #	*FOD* [mm]	*P* [W]	*v* [mm/s]	*h* [μm]	*t* [μm]	*Ev* [J/mm³]
Default	0	100	600	105	30	53
Reference[11]	0	100	600	105	30	53
S10*	2	180	800	60	30	125
S5*	2	180	700	60	30	143
S11	2	180	800	50	30	150
S1*	2	180	600	60	30	167
S6	2	180	700	50	30	171
S12*	2	180	800	40	30	188
S2	2	180	600	50	30	200
S7	2	180	700	40	30	214
S3	2	180	600	40	30	250
S13*	2	180	800	30	30	250
S15	2	180	240	100	30	250
S16	2	180	220	100	30	273
S8*	2	180	700	30	30	286
S17	2	180	200	100	30	300
S4*	2	180	600	30	30	333
S18*	3.5	180	240	100	30	250
S19	3.5	180	220	100	30	273
S20*	3.5	180	200	100	30	300

The influence of process parameters on the sample density of the 2ⁿᵈ build iteration is plotted in Figure 7.2. Density is plotted as a function of E_v with constant scan velocities traced with solid lines and constant hatch distances traced with broken lines. For the range of parameters investigated, density is seen to increase with an increase scan speed and a decrease in hatch distance for most samples. The exception to this trend is two samples (S13 and S18) with hatch distances of 30 µm.

---

[11] Default parameters + post-process heat treatment at 800 °C for 2 hours followed by furnace cooling
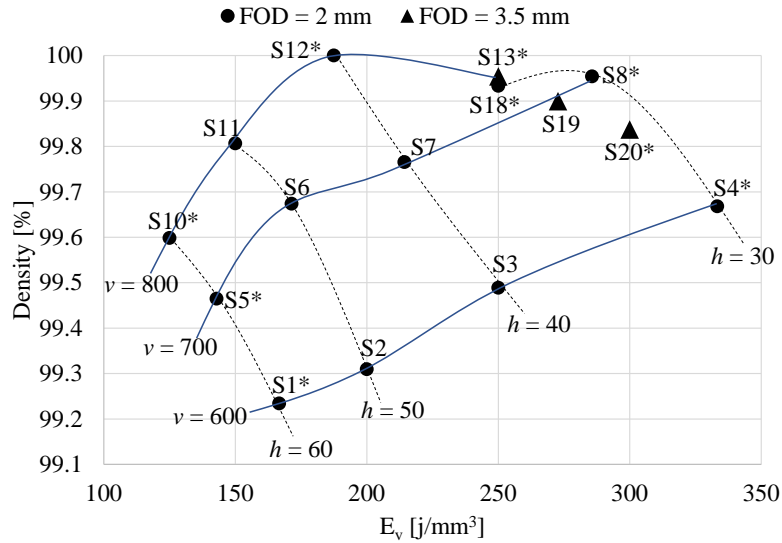
Figure 7.2. Second build iteration: sample density versus E_v matrix. Iso-lines of scan velocity (solid) and hatch distance (broken) (v [mm/s], h [µm]).

Micro X-ray computed tomography (XCT) scans were done on sectioned cubic samples to determine the pore distribution and morphology. A General Electric Phoenix Nanotom S X-ray machine was used. X-ray scan settings were 150 kV, 130 µA. Image acquisition time was 0.5 second per image. Copper beam filtration of 0.5 mm was done to reduce beam hardening artefacts. Scan resolution (voxel size) was set to 10 µm. Data processing was performed with Volume Graphics VGStudioMax. Processed data was viewed on software myVGL 3.4.

Figure 7.3 depicts the XY-planes (i.e., the plane of the build layer) of micro XCT scans of samples S1, S10, S13, S4, and two samples at different FOD values, 2 and 3.5 mm, samples S15 and S18. Four samples on the extreme points of the density matrix shown in Figure 7.2 (samples S1, S10, S13, and S4) depict pore accumulation predominantly on the sample boundaries in as can be seen in Figure 7.3(a – d). Samples S10 and S13 depict very few internal pores. The influence of decreasing FOD from 2 mm to 3.5 mm (S15 to S18) on porosity is depicted in Figure 7.3(e & f). Sample S15 measured a density of 93.5 %, which was likely caused by the above-optimal energy density input, which caused key-hole mode and/or gas formation in the meltpool. By lowering laser intensity through FOD increase, part density increases to above 99.9 % (S18) for the same hatch spacing and scan speed, $h = 100$ µm and $v = 240$ mm/s.

To determine the pore morphology, and thereby the meltpool mode of the four samples at the extremes of the density matrix, higher magnification images of pores were taken from the scans Figure 7.4(a – d). These images reveal a spherical-shaped pore morphology indicating a gas entrapment and/or key-holing meltpool formation.
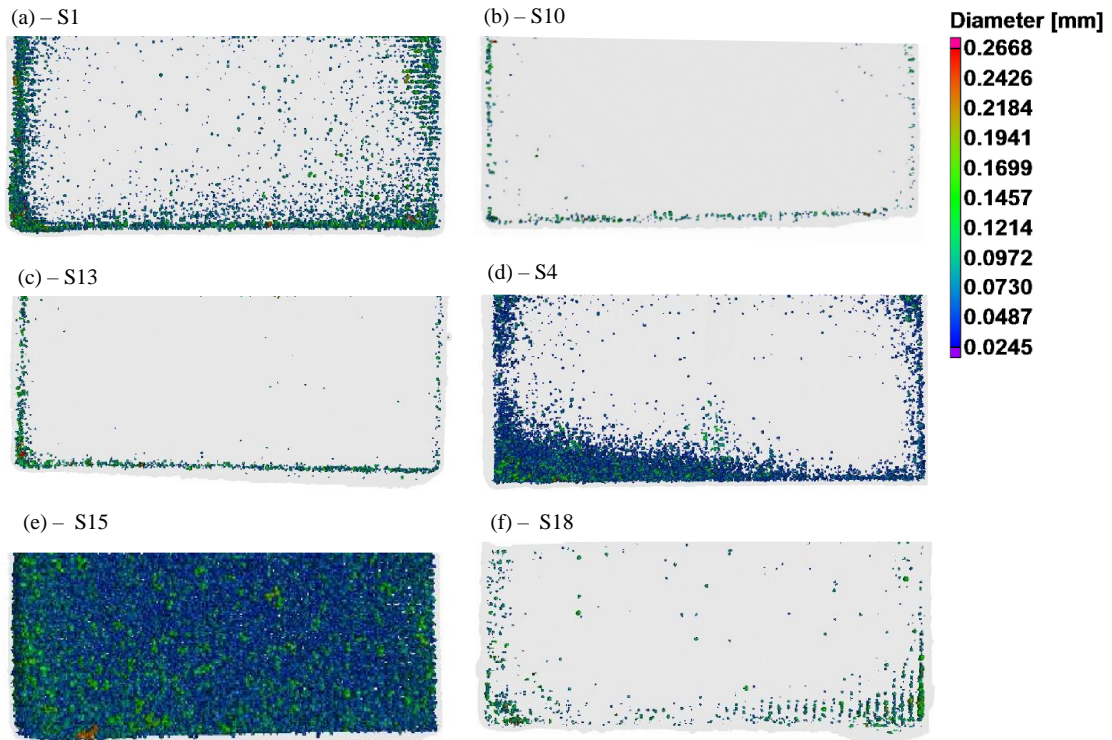
Figure 7.3. Micro XCT scans of the XY-plane of sectioned cubes.
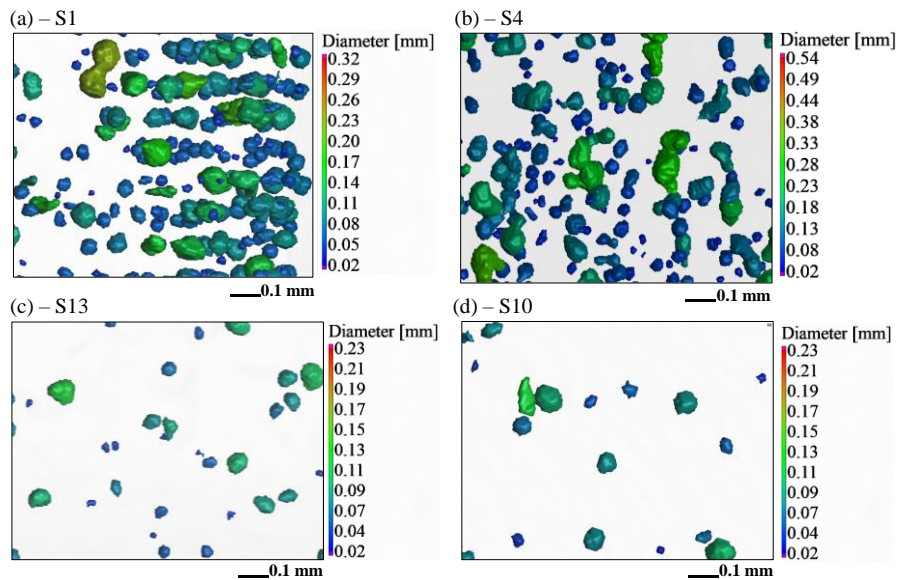
Figure 7.4. High magnification micro XCT images of samples showing spherical-like pores: (a) S1, (b) S4, (c) S13, and (d) S10.

123

7.2.4   Cylindrical and cantilever sample fabrication

As mentioned, chosen process parameter sets, indicated in the previous subsection, were used to build cylindrical and cantilever-shaped samples. Cylinders were built in a vertical orientation (longitudinal axis parallel to the build's Z-axis, as per ISO/ASTM 52900 designation) with dimensions of 12 mm in diameter and 100 mm in length (Figure 7.5(a)). For repeatability, three tensile cylinders of each process parameter were built. Cylindrical samples were machined post-build into "dog-bone" shape tensile samples with a gauge length of 25 mm and a gauge diameter of 5 mm (according to ASTM E8M and ISO 6892). Tensile tests were done in accordance with ASTM E8 at a crosshead displacement of 0.13 mm/min. Vickers microhardness indentations were done in accordance with ASTM E92 with 10 seconds hold time using 2 kg force (HV2).

Combustion analysis to measure oxygen and nitrogen content of cylindrical samples was done using an ON-ELTRA machine. For repeatability, five pieces of ~100 mg were sectioned at 5 mm from the bottom of selected cylinders.

The measured density of cylinders matched that of their respective cubes for all samples except those built with FOD = 3.5 mm (S18 and S20). Due to their poor density, these samples did not qualify according to the first objective criteria (achieving a high density) of the study, and therefore, microstructural analysis and tensile tests are not reported. The likely mechanism for this is further discussed in Section 7.4.

Cantilever beams, Figure 7.5(c), were built using dimensions of 9 mm × 10 mm × 62 mm. Beams were partially wire-cut from the build plate post-build to allow the resultant end-deflection to be measured.
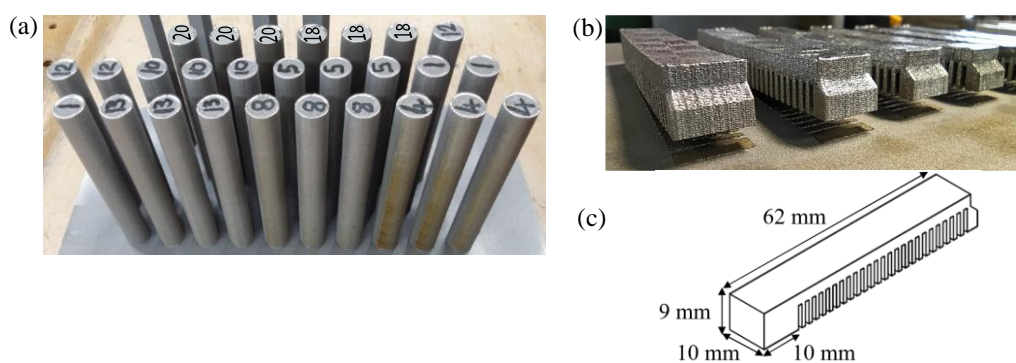
Figure 7.5. (a) cylindrical sample build and (b) cantilever build▬partially wire-cut showing curved deflection of end-tip (c) drawing of cantilever beam with outer dimensions.

7.2.5 Specimen preparation

All specimens intended for microstructural analysis and/or microhardness measurements were cut using a low-speed precision cutter from cylindrical samples. Two specimens from each cylindrical sample were cut: a top-end offcut 5 mm from the cylinder's top surface (i.e., final build layer) and a bottom-end offcut 5 mm from the sample's bottom surface.

Microstructural samples were prepared using standard polishing steps recommended by Buehler (2020). All microstructural specimens were chemically etched using Kroll's Reagent by swabbing the surface. Samples for SEM images were etched for a brief time of ~5 seconds, whereas samples for optical micrographs of PBG structure were etched for approximately 10 – 15 seconds to increase PBG contrast. Optical micrographs were stitched together from four neighbouring micrographs using the software Stream Essentials.

7.2.6 SEM imaging and EBSD analysis

SEM imaging was done with a Zeiss MERLIN electron microscope in combination with its secondary electron detector. EBSD maps were acquired using an EOL JSM-7001F. EBSD map scan dimensions were 450 µm × 450 µm at a step size of 0.3 µm. EBSD orientation data was processed using the MATLAB-based toolbox, MTEX (Bachmann *et al.*, 2010). The PBG orientation maps were reconstructed from in-house code developed by the authors (Ter Haar, 2017).

Prior-β grains were constructed from misorientation above angles of 5°. Orientation maps were plotted from inverse pole figure (IPF) hue-saturation-value colouring depicted in Figure 7.6(a). Pole figures were constructed from mean grain orientations created with 10° contours. Multiples of random distribution ranging from 0 – 4° were used (Figure 7.6(b)).

Since pole figures are constructed from stereographic projections of orientation directions Figure 7.6(c), quantification of texture orientation can be derived from their polar coordinates, (a, b). For these coordinates, anti-clockwise rotation about the Y-axis from the X-axis (or XY-plane) is measured by 'a', while the angle between the texture direction and Y-axis (stereographically projected onto the XY-plane) is measured by 'b'.
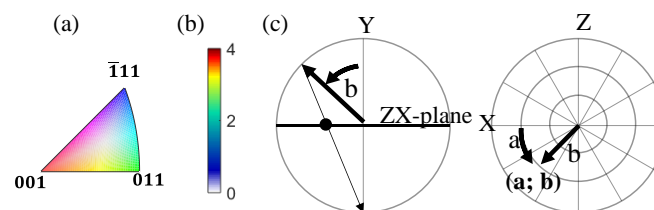
Figure 7.6. (a) bcc IPF HSV colour key, (b) orientation distribution intensity, (c) stereographic projection definition for pole figure coordinates.

7.2.7 Phase identification through X-ray diffraction

XRD was done with polished samples using a Bruker D2 phaser machine with a Cu-K$_\alpha$ radiation source (wavelength 1.5406 Å). Acquisition parameters used were a 0.02° step size, a 0.75 second hold time scanned between 30 – 80° (2θ) with sample rotation at 30 rotations per minute. Lattice parameters were quantified from Bragg peak positions through fitting the peaks using Rietveld refinement in open-source software MAUD. Bragg peak plots and the measurement of their full-width half-maximum values (FWHM) were done using XPowderX.

7.3 Results

7.3.1 XRD derived lattice parameters

Figure 7.7 plots 30 – 60° Bragg peaks of bottom offcut specimens from cylindrical samples. Samples are plotted in order of increasing E_v from the top-most (the default sample) to the parameter set of the highest E_v (S4). The reference sample XRD data set is included at the bottom-most position. A body centred cubic (bcc) Bragg peak is an indication of the presence of β-phase and is observed in all non-default parameter data sets, except for S10. Bcc peaks are observed to shift to higher angles and increase in intensity with increasing E_v. Hexagonal-close pack (hcp) Bragg peaks, indicative of α phase, are observed to shift to lower angles and narrow in width with an increase in E_v. Since these small effects are not easy to discern visually from Figure 7.7, quantification of the lattice parameters from the XRD data was conducted. Very subtle secondary phased peaks were observed and found to match those of the orthorhombic α'' structure.
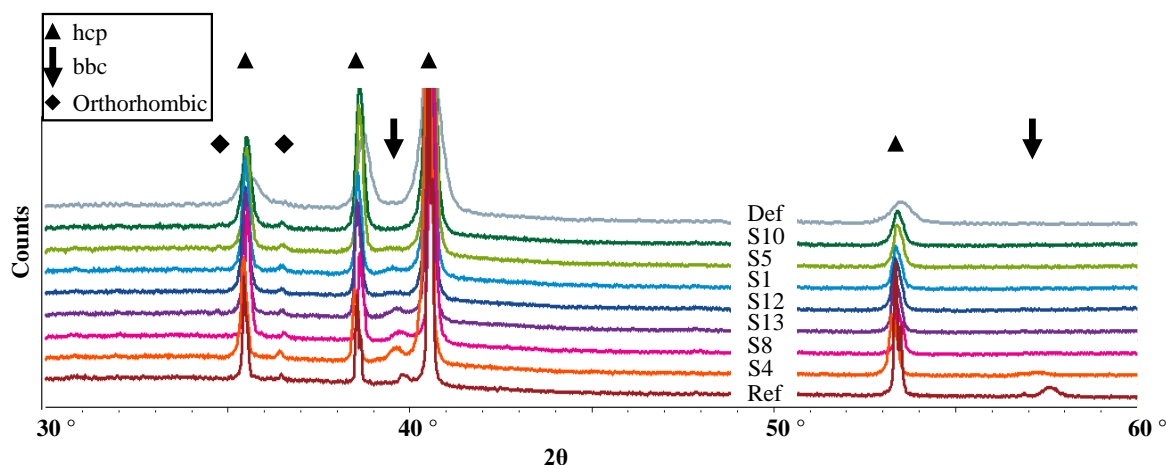
Figure 7.7. XRD Bragg peaks from bottom-offcut specimens, with build parameters correlating to cubic sample build parameter sets (see Table 7.2) as indicated.

Quantification of Bragg peaks in terms of hcp and bcc lattice parameters and $\{10\bar{1}1\}$-Bragg peak FWHM values, as a function of E_v, is plotted in Figure 7.8. A comparison of the bottom-to-top offcut specimens indicates that the top offcut hcp lattice parameters are generally larger

for each respective sample. Measurement trends with E_v are identical for both bottom- and top-offcuts and are highlighted by broken lines.

Data trends indicate that for an increasing E_v, both 'a' and 'c' hcp lattice parameters decrease from the default sample (martensite) up until S1 where they reached a minimum, as shown in Figure 7.8(a) and (b), respectively. The parameters ratio, 'c/a', increases from default up until S1, thereafter remaining constant for the remainder of the samples (Figure 7.8(c)). This likely indicates that martensite decomposition α'→ α is complete since lattice parameters of the top-offcut of S1 are observed to match that of the reference (α+β) sample. A similar difference in the 'c/a' ratio between α' and α phases have been reported elsewhere (Xu *et al.*, 2017).

Hcp lattice parameters increase from S1 onwards with an increase in E_v up until the highest E_v (S4) Figure 7.8(a) and (b). This is likely due to a combination of the diffusion of alloying elements and oxygen/nitrogen concentration increase and is further discussed in Subsection 7.3.2. The bcc lattice parameter 'a' measured near-identical values for both bottom and top offcuts and are observed to decrease with an increase in E_v. The bcc lattice parameter of the reference (α+β) sample matches that of S4 and similar bcc 'a' lattice parameters for (α+β) microstructures have been reported elsewhere (Xu *et al.*, 2017).

For the $\{10\bar{1}1\}$ lattice plane Bragg peaks, the measured FWHM decreases with an increase in E_v but remains above the reference parameter set value. The decrease from default is significantly higher than the rest of the samples. This indicates a decrease in dislocation density and an increase in grains size. This is further discussed in Subsection 7.3.2.
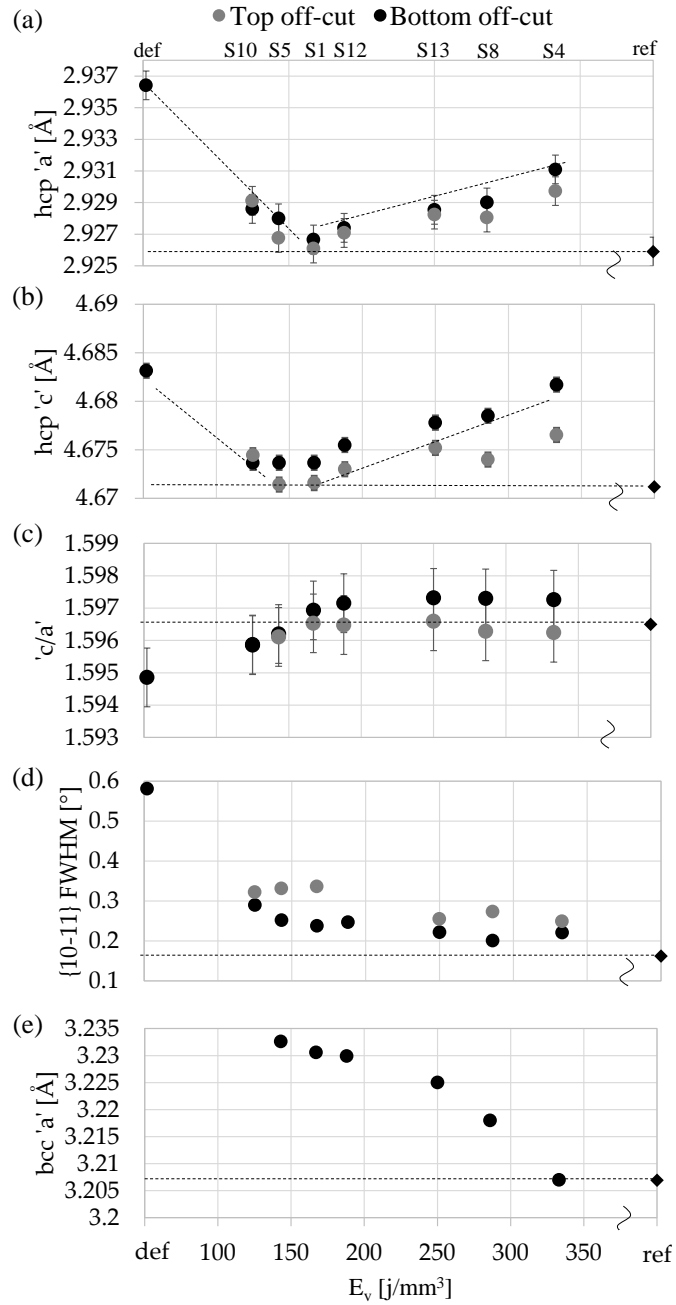
Figure 7.8. Quantified lattice parameters as a function of E_v. (a) hcp 'a', (b) hcp 'c', (d) hcp 'c/a', (e) {$10\bar{1}1$} FWHM, and (e) bcc 'a'.

7.3.2 SEM study of martensite decomposition

SEM analysis was used to qualitatively compare the degree of α' decomposition as well as to identify morphological changes in grain structure with increasing E_v. Figure 7.9 depicts SE-SEM micrographs of default and above-default-E_v samples at high resolution (20,000×

128

magnification) as well as the reference sample at low and high resolution. As expected, the default parameter set's microstructure, Figure 7.9(a), consists of typical fine hierarchical-structured martensite, while that of the reference sample at Figure 7.9(i) low- and (j) 20,000× magnification depicts a typical (α+β) lamellar structure.

Black-white contrast between laths is a function of lath chemical composition and dislocation density (Kumar *et al.*, 2018). This contrast is observed to decrease for above-default-E_v processed samples indicating a homogenisation of alloying elements within grains and/or a decrease in dislocation density. Furthermore, fine grains are no longer observed in these above-default-E_v samples indicating α-grain recrystallisation and grain growth. A fine β-phase (bright lamellar phase on the boundary of α-grains) is seen in S5 (c), which becomes more distinguishable in S1. Bright spots on the micrograph are possibly due to etching effects and/or β-precipitation.

β-grains are again identified on the boundary of α-laths and are observed to increase in width with an increasing E_v indicating a greater amount of phase transformation due to higher temperature heating of the sample. Note that the SEM images are ordered in increasing E_v from Figure 7.9(b) to (h). Energy density parameter sets above 250 J/mm^3 (S13) show a typical α+β lamellar structure. Grain width of the α-laths is also seen to increase with an increase in E_v. Compared to the reference sample's grain size, the grain size achieved by the highest E_v sample (S4) is still finer. This is a promising result which suggests a higher material strength will be achieved by S4 than the reference sample based on the Hall-Petch relation (Smith & Hashemi, 2006).
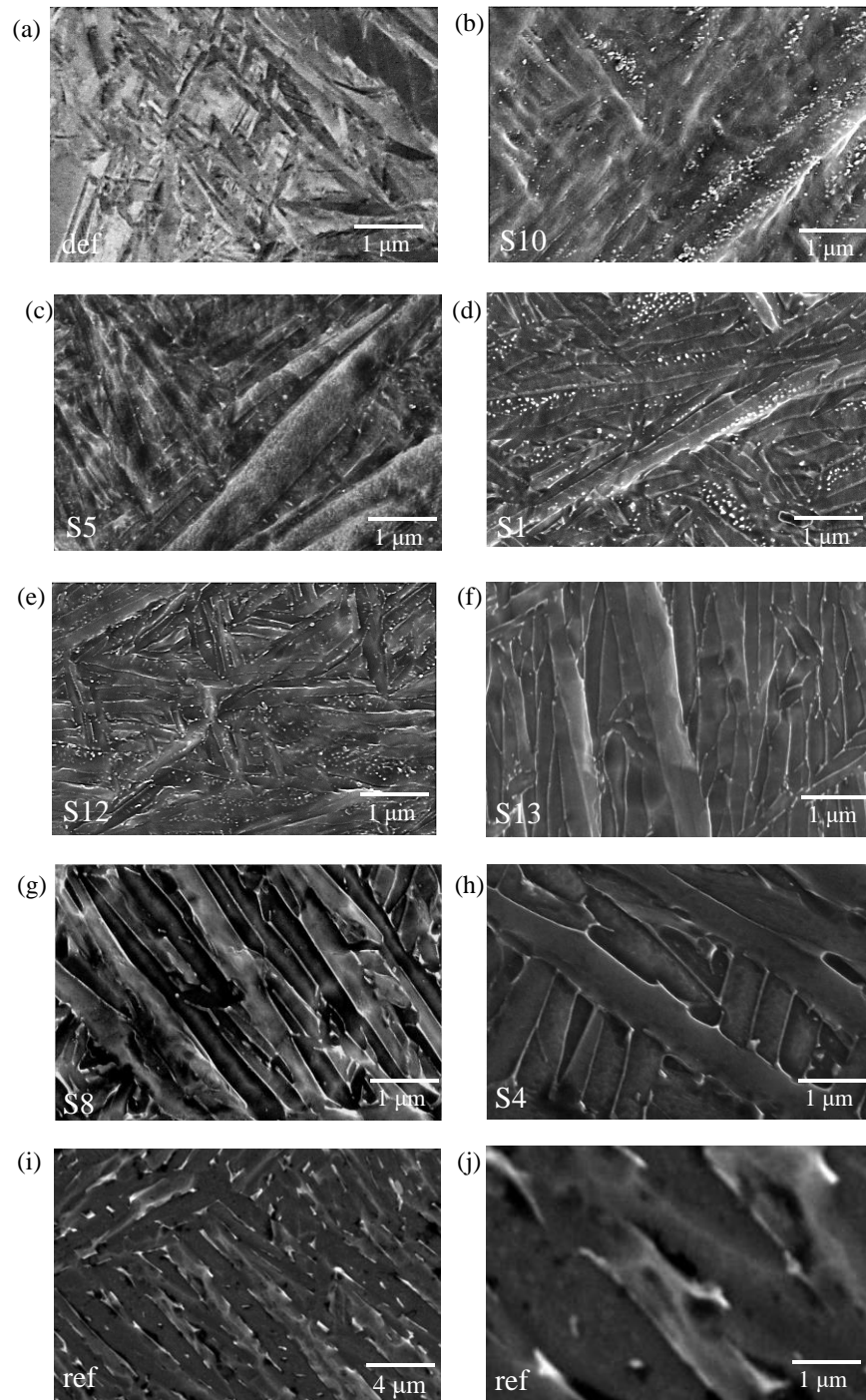
Figure 7.9. SEM micrographs at 20,000× magnification of SEM micrographs of (a) default parameter set, (b) S10 (125 J/mm³), (c) S5 (143 J/mm³), and (d) S1 (167 J/mm³), (e) S12 (188 J/mm³), (f) S13 (250 J/mm³) (g) S8 (286 J/mm³), (h) S4 (333 J/mm³), (i) reference sample at low- and (j) high magnification.

7.3.3 Prior-β texture dependence on process parameters

This section presents micrographs of PBG structure that aim to show the influence of hatch distance and scan speed on grain morphology and texture. Optical micrographs present the epitaxial-dominant PBG morphological texture, while small-area EBSD maps describe the dominant crystallographic and secondary texture.

Figure 7.10 presents optical micrographs in which dark and light chemically etched PBGs can be seen. Micrographs are arranged with rows of identical scan velocities and columns of identical hatch distances. Arrows and trace lines indicate the dominant morphological texture direction and angle rotation from the XY-plane.

For samples scanned at $v = 600$ mm/s, PBG grains are orientated vertically in the $h = 60$ μm sample (S1), while no discernible columnar structure can be distinguished for sample scanned at $h = 30$ μm (S4). For increased scan speed of 700 and 800 mm/s, columnar grains are seen to rotate/slant with respect to the XY-plane. This angle is measured to range from $85 - 80°$ for the 60 μm samples and decreases slightly to a minimum of ~70° for samples scanned at $h = 30$ μm. Variation within samples is seen to range in the order of ~10°.
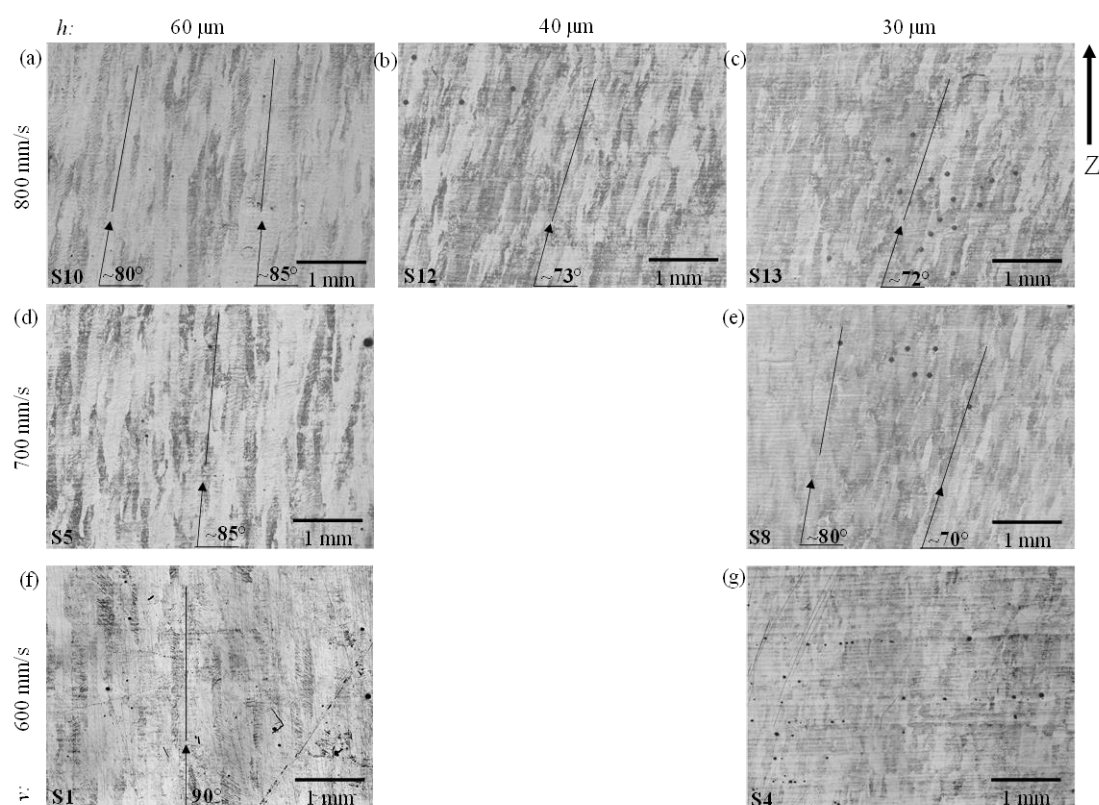
Figure 7.10. ZX-plane optical micrographs of PBG structure. Samples: (a) S10 (b) S12, (c) S13, (d) S5, (e) S8, (f) S1 and (g) S4 (black spots in S12, S13 and S8 were caused by microhardness indentations).

Reconstructed PBG orientation maps (450 μm square areas), Figure 7.11, are used to determine the local crystallographic texture in 3-dimensions due to local hatch and scan effects, as opposed to 2-dimensional morphological texture observed in the optical micrographs. Figure 7.11 depicts the reconstructed PBG orientations and ⟨100⟩ pole figures of samples scanned at $h = 60$ μm: S10, S5, and S1 and a sample scanned at $h = 30$ μm: S4.
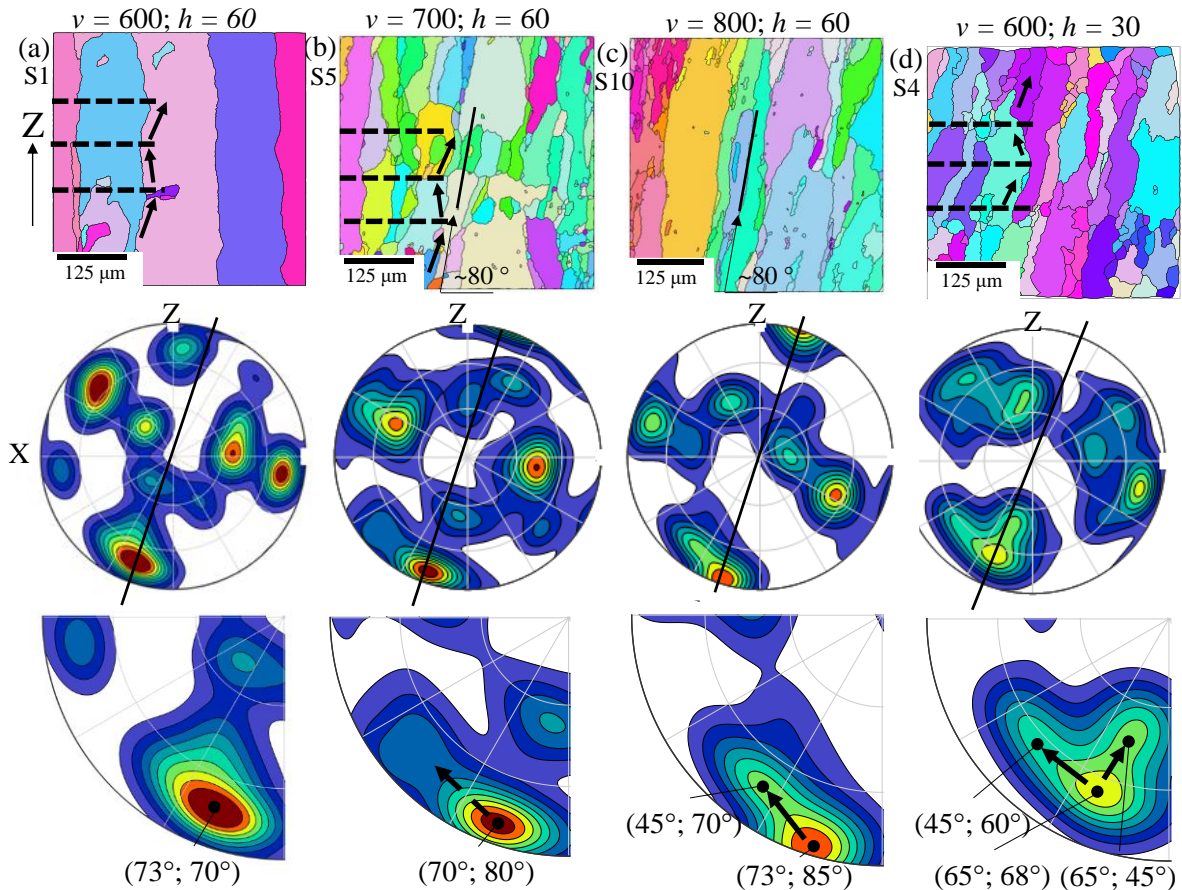
Figure 7.11. Reconstructed PBG orientation maps and {100} pole figures (10° contour lines of iso-intensity) (a) S10, (b) S5, (c) S1, (d) S4.

Dominant texture directions (i.e., highest intensity pole positions) do not change significantly for the same scan speed and remain in the region of 'a' = 70 – 73°, and 'b' = 70 – 85°. For a smaller hatch distance of 30 μm, the dominant texture direction changes to a lower angle (65°; 68°). In addition to the dominant texture directions labelled in the pole figures, the gradual formation of a secondary (45°; 70°) texture direction can be seen to form with an increase in scan speed from 700 – 800 mm/s, at $h = 60$ μm. At a smaller hatch distance of $h = 30$ μm, a similar secondary (45°; 60°) texture direction, as well as a (65°; 45°) texture direction, is observed. These can be considered non-epitaxial grains since they do not follow the dominant high-angle texture direction.

Furthermore, columnar grains appear to be dispersed, with shorter near-equiaxed grains alternating in left-to-right-slant in intervals of ~100 μm (indicated by arrows on the orientation maps). Texture strength is also seen to decrease with an increase in scan speed and a decrease in hatch distance. Lastly, a high-magnification optical micrograph of S4 (Figure 7.12) mimics the mixture of equiaxed and columnar grains observed in its orientation map (Figure 7.11(d)). The above findings suggest that a columnar to equiaxed transition (CET) is facilitated by a higher scan speed and smaller hatch distance. This is further discussed in the next section.

An increase in dark horizontal bands is seen in sample micrographs of higher E_v. This can be seen when comparing micrographs in Figure 7.10. A high-magnification images of S4, Figure 7.12, points out the dark bands with arrows. This effect has also been observed elsewhere and is likely caused by the etching of Ti_3Al (Welsch *et al.*, 1977; Thijs *et al.*, 2010). The formation of this interstitial phase is known to be facilitated by an increase in oxygen concentration (Welsch *et al.*, 1977). However, the average difference in hardness between dark and light regions is only ~3 – 4 HV0.1 Since this is in the error margin of individual measurements, it is unlikely to have a significant impact on anisotropic deformation behaviour.
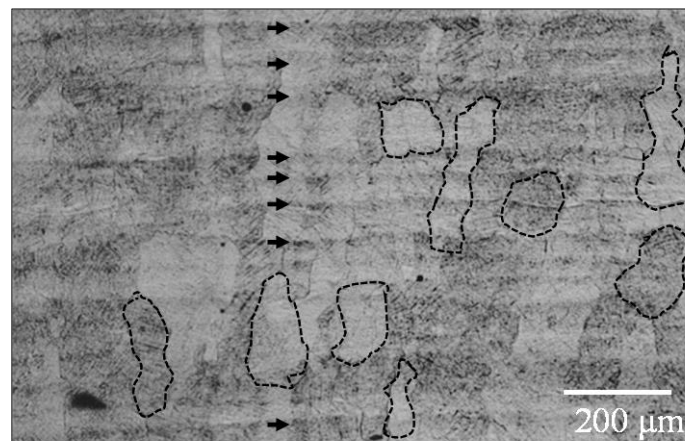
Figure 7.12. Mixed (columnar + equiaxed) morphological grain structure. PBG boundaries traced with broken lines. Black arrows show black horizontal etched planes.

7.3.4   Deformation behaviour – microhardness and tensile properties

A plot of microhardness measurements in the XY-plane of the cylindrical specimen offcuts is depicted in Figure 7.13. For top-end measurements, S10 and S5 measured a similar microhardness. Microhardness increases with an increase in E_v from S1 up to S4.

The microhardness of top offcuts versus bottom offcuts from default and S10 samples measured a near-identical hardness. A small difference of ~4 HV was measured between the top and bottom offcuts of S5. For samples S1 and S4, a larger hardness difference of ~10 HV was measured between the top and bottom of the sample. The reference sample measured a much lower mean microhardness of 323 HV.
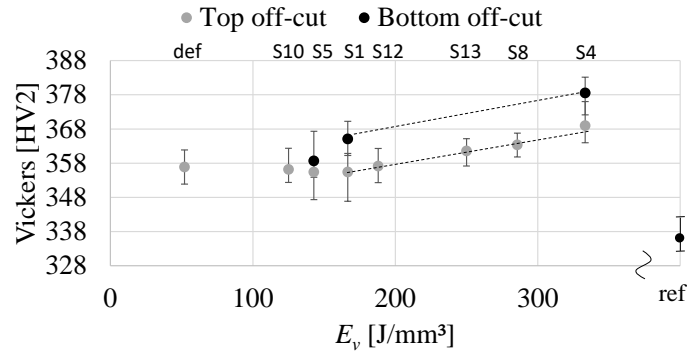
Figure 7.13. Vickers microhardness versus energy density of cylindrical samples.

Results of tensile tests are plotted in Figure 7.14. Sample S10 measured a slight increase in mean ductility and a slight decrease in strength from the default sample. For the remainder of the samples, material strength was seen to increase with an increase in E_v, while ductility decreases.
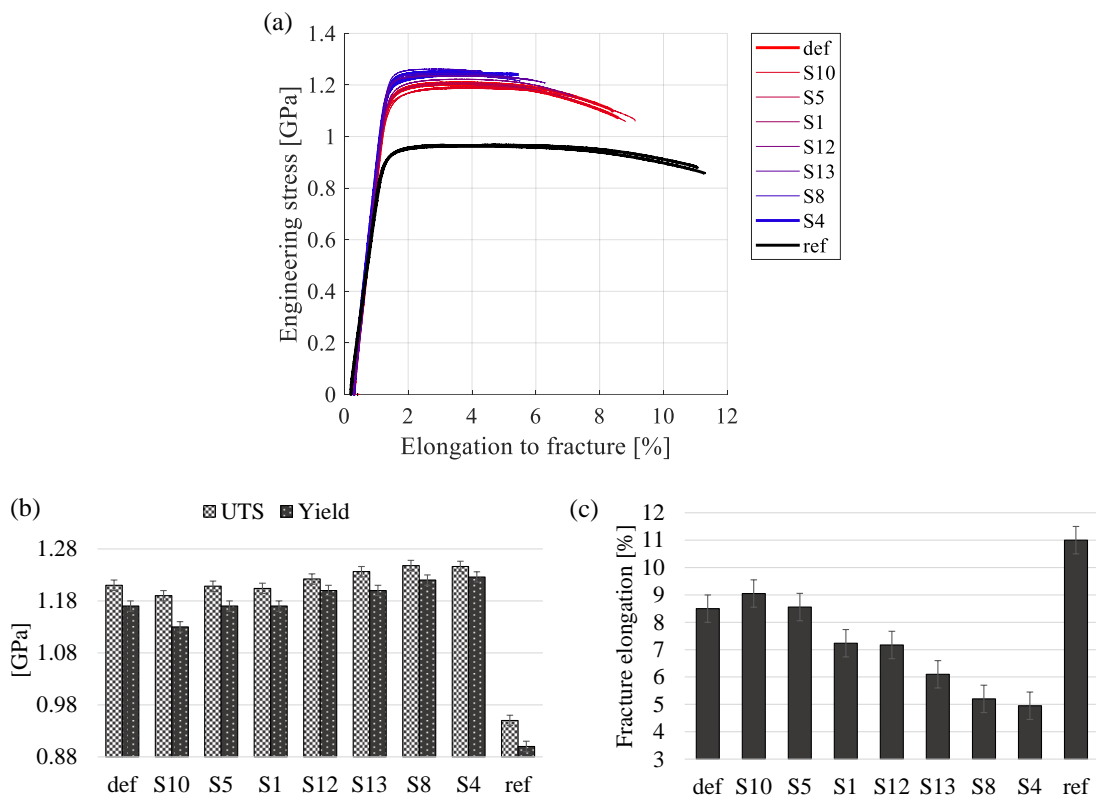
Figure 7.14. (a) Stress-versus-strain curves, (b) ultimate tensile strength (UTS) and 0.2 % proof yield values, and (c) % elongation-to-fracture values.

7.3.5 Oxygen and nitrogen measurements

Oxygen and nitrogen measurements of the bottom section offcut of selected cylindrical samples are plotted in Figure 7.15, together with results from Vrancken (2016) of samples built with default process parameters on a heated base plate. Results indicate that both the oxygen and nitrogen concentration increased with an increase in E_v. Oxygen was found to increase linearly and remain in the same range as that found from base-plate heating (0.13 – 0.23 at% oxygen). The measured nitrogen content was found to increase at a much higher gradient than oxygen, reaching just below 10× the value of the default parameters at the highest E_v (0.064 – 0.53 at% nitrogen). Compared to that measured of base-plate heating, the nitrogen is also approximately ten times higher.

This study			
	E_v [J/mm³]	O [at%]	N [at%]
def	52	0.13	0.064
S10	125	0.17	0.13
S1	167	0.16	0.14
S13	250	0.19	0.34
S4	333	0.23	0.53
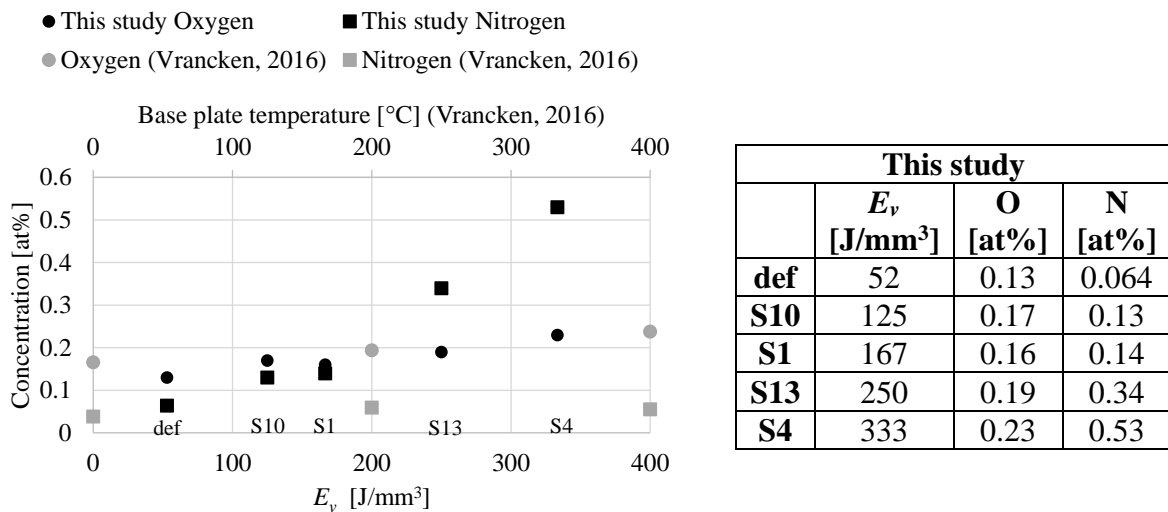
Figure 7.15. Oxygen and nitrogen concentration of the bottom-offcut of selected cylindrical samples. Comparative results of base plate heating 0 – 400 °C (Vrancken, 2016).

7.3.6 Residual stress

The results of Z-deflection of cantilever-shaped samples as a function of energy density is plotted in Figure 7.16. A steeper decrease in Z-deflection was observed when decreasing hatch distance compared to decreasing the laser speed. However, at a hatch distance of 30 μm, a similar steep gradient is observed when decreasing laser speed from 800 mm/s to 600 mm/s (S13-to-S4). Overall, beam deflection decreases with an increase in energy density, with parameter set S4 decreasing by 50 % of the beam deflection of the default parameter. The same percentage decrease deflection was achieved by a study of base plate pre-heating at 400 °C (Vrancken, 2016), which also measured a 50 % decrease in measured principle residual stress.

135
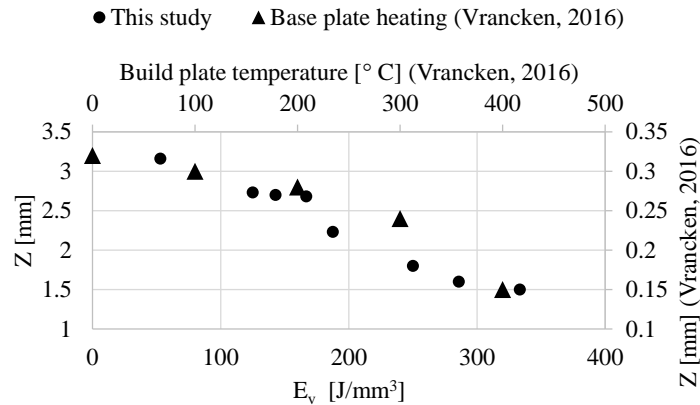
Figure 7.16. Measured Z-deflection of cantilever-shaped beam ends as a function of volumetric energy density. Comparative deflection results of base plate heating at 0 – 400 °C (Vrancken, 2016).

7.4 Discussion

7.4.1 Martensite decomposition and material embrittlement

The measured change in 'c/a' parameter ratios indicate a gradual increase in α' → α transformation with increased E_v up until a full transformation is reached at S1 (167 J/mm³). The α' → α transformation completion for energy densities 167 J/mm³ and higher is evident from the fact that (1) no further change in 'c/a' occurs, and (2) the reference sample measures a near-identical 'c/a', 'a' and 'c', to the top-offcut of sample S1. The decrease in lattice parameters 'a' and 'c' is likely due to micro residual stress relaxation and not a change in elemental composition. This is because, in a stress-free state, the α lattice parameters are larger than α' due to the former having a higher concentration of titanium.

Evidence for the formation of β-phase is deduced from bcc peaks, and β-phase observed in SEM images. Negligible change in β-phase volume up to 167 J/mm³ is deduced from unchanged bcc lattice parameters S10-to-S1. The increase in β-phase volume is deduced from the bcc Bragg peak intensity increase, the decrease of bcc lattice parameter, and β-phase width increase.

Since FWHM is proportional to ordered crystalline domains through the Scherrer equation (Patterson, 1939), the measured decrease in FWHM indicates a decrease in dislocation density and/or an increase in α-grain size with an increase in E_v. A decrease in dislocation density was evident from the decrease in dark-light contrast between α-grains, while the increased grain size was observed of α-laths in the SEM micrographs.

The influence of the above-mentioned microstructural changes is correlated with a slight decrease in microhardness, a decrease in UTS and an increase in elongation-to-failure of S10.

Since the reference sample has a much larger α-grain width and thicker β-phase than all samples, it achieved a higher elongation-to-failure and a lower strength.

For the medium-to-high E_v lattice parameters, S12 – S4, a trend of increasing lattice parameters with an increase in E_v was measured. This is argued to be caused by a combination of factors. The first is due to the diffusion of elements across phases due to phase transformation. Since α'→ α+β causes vanadium atoms to diffuse to the β-phase while titanium atoms diffuse to the α-phase, α lattice parameters will increase due to the larger relative size of the titanium atoms.

The second factor is the increase in interstitial elemental concentration, such as oxygen and nitrogen. This second factor is confirmed by the measured increase in oxygen and nitrogen concentration with increasing E_v conducted through combustion analysis. This led to the increase in the degree of embrittlement (measured by both microhardness and tensile properties) of samples with E_v of 167 J/mm^3 and higher (i.e., samples S1 to S4). This is measured by both microhardness and tensile properties. The mechanisms by which interstitial atoms cause part embrittlement on an atomic scale has been discussed in Subsection 2.4.2. An increase in sample microhardness with E_v has been reported elsewhere (Thijs *et al.*, 2010). An increased measure of oxygen and nitrogen uptake in the material with an increase in laser power has been reported for commercially pure Ti (Na *et al.*, 2018).

It is interesting to note the similarity of the oxygen concentration measured in this study to that measured by Vrancken (2016) of base plate heating. While both oxygen and nitrogen in titanium contribute to the embrittlement of the material, nitrogen contributes a larger degree according to findings in pure-Ti (Conrad, 1981: 128). Therefore, it is concerning to find a larger proportional increase in nitrogen compared to oxygen and a larger increase than that found from base plate heating. The cause of a larger increase in nitrogen is unknown, and further investigation is needed.

Both the larger α lattice parameters and the higher microhardness of each sample's bottom offcut indicate a higher oxygen + nitrogen contamination of the bottom of the samples. Since oxygen preferentially occupies octahedral interstitial sites in the hcp lattice, parameter 'c' increases to a larger degree than 'a'. This causes the bottom-offcut sample to measure a higher 'c/a' ratio than the top-offcut for all samples. Lastly, Figure 7.17 depicts a photograph of cylinder S4 which shows a higher degree of colourisation for the bottom versus the top of the sample. Therefore, this provides compelling evidence for the hypothesis of higher interstitial contamination of the bottom-half of the samples.
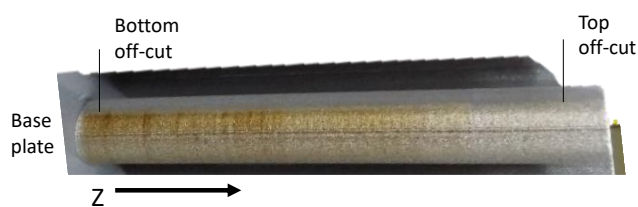
Figure 7.17. Tensile sample surface colourisation (parameter set S4).

Two plausible causes for the higher oxygen + nitrogen contamination of the lower section of the sample are proposed. The first hypothesis is that oxygen-and-nitrogen concentration was higher during the start of the build and slowly decreased over time. The second hypothesis is that the oxygen + nitrogen content of the top-most powder in the powder supply container, that is used for the first powder layer in the build, was higher.

7.4.2 Prior-β texture direction and columnar-to-equiaxed transition

The dominant epitaxial PBG texture direction has been observed to be influenced by scan strategies (Kruth *et al.*, 2010; Thijs *et al.*, 2010), although the mechanisms by which process parameters influence PBG texture have not been explored at length.

From the optical micrographs and EBSD pole figures, texture orientation direction is seen to decrease with an increase in hatch distance. This is likely due to an increase remelting of neighbouring scan tracks and thereby an increase in texture strength in the direction of the hatch. This proposed mechanism is depicted in Figure 7.18, which shows an increase in re-heating and remelting zones of the previous track. This zone increases with a decrease in hatch distance. Red arrows indicated neighbouring track re-heating changing the previous track's texture.
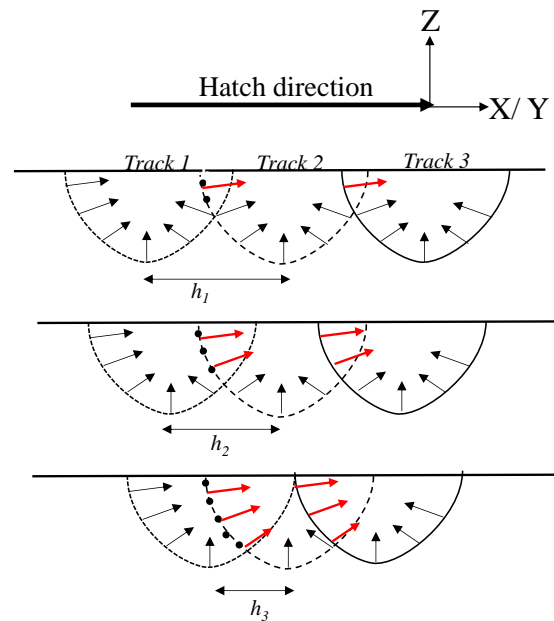
Figure 7.18. Influence of hatch distance on remelting and recrystallisation of previous neighbouring scan tracks ($h_3 < h_2 < h_1$).

Micrographs reveal that a dominant epitaxial PBG growth occurs at an angle with respect to the XY-plane. This means that there exists non-vertical resultant thermal gradient direction (∇T) during the build. The thermal field gradient is defined as $\nabla T = \frac{\partial T}{\partial x}\boldsymbol{i} + \frac{\partial T}{\partial y}\boldsymbol{j} + \frac{\partial T}{\partial z}\boldsymbol{k}$, where $\frac{\partial T}{\partial x}\boldsymbol{i}$

and $\frac{\partial T}{\partial y}\boldsymbol{j}$ are the thermal gradients in hatch direction when scan direction is along the Y-axis and X-axis, respectively. Since hatch direction alternates between only two directions, a heat flow resultant direction will be caused. However, the heat flow resultant caused by scan direction does not occur with scan rotation about 90° since four scan directions exist. This is schematically depicted in Figure 7.19.
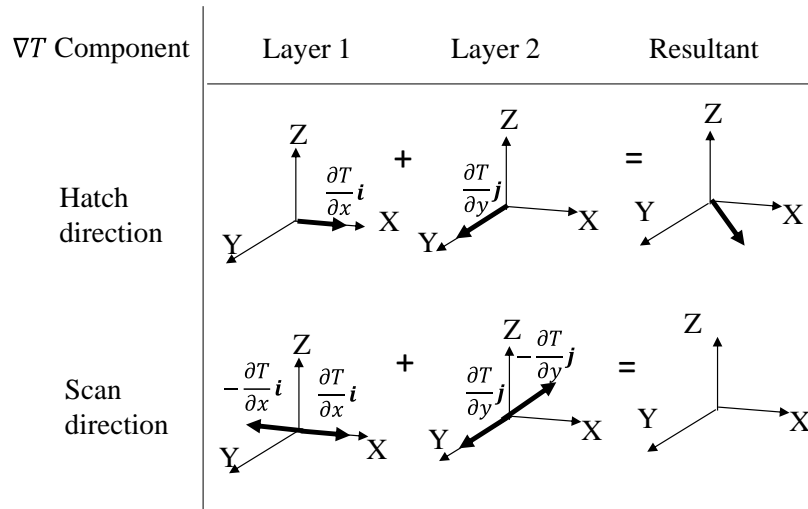
Figure 7.19. Resultant thermal flux component due to layer rotation of 90° – hatch versus scan direction components.

Columnar versus equiaxed morphological PBG structure is determined by the magnitude of the temperature field gradient ($G = \|\nabla T\|$) and the solidification rate at the solid-liquid interface, also called the interface velocity (R) (Spittle, 2006). The interface velocity for scan direction is calculated with $R = \boldsymbol{v} \cdot \cos\theta$, where θ is the angle between the heat flow direction (i.e., normal of the solid-liquid interface) and the scan direction. The relation between G, R and PBG morphology have been approximated experimentally by Kobryn and Semiatin (2003), as depicted in Figure 7.22.

Since local PBG texture direction follows the maximum heat flow direction (∇T) (Thijs *et al.*, 2010), PBG texture direction can be used to determine the thermal gradient direction, as shown in Figure 7.21. Figure 7.20 depicts the relation between the texture orientation (a, b) derived from the pole figure and the thermal gradient direction. Since 'b' represents the angle between the thermal gradient direction and the scan direction along the Y-axis, R for a scan direction along the Y-axis can be calculated.
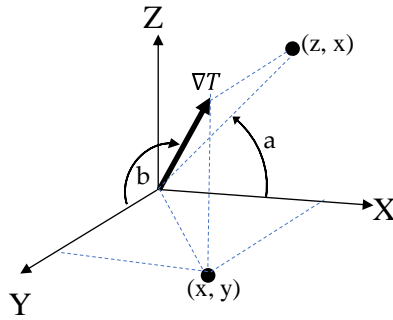
Figure 7.20. Thermal gradient with 'a' and 'b' rotation measured by pole figure coordinates.

Since the texture direction of underlying layers changes with each layer additions, this does not give the true thermal flow orientation of an individual scan track. However, from the local finer grain structure that has not undergone epitaxial growth and therefore remains unaffected by layer additions, Figure 7.21(b), their 'b' angle can be used as an estimation of the angle between the scan direction in Y-axis and the thermal gradient direction. Therefore, the minimum angle of ~45° is used to estimate the thermal flow direction. The R value for the scan velocities used in the study and the resultant range on the *G-R* chart is depicted in Figure 7.22.
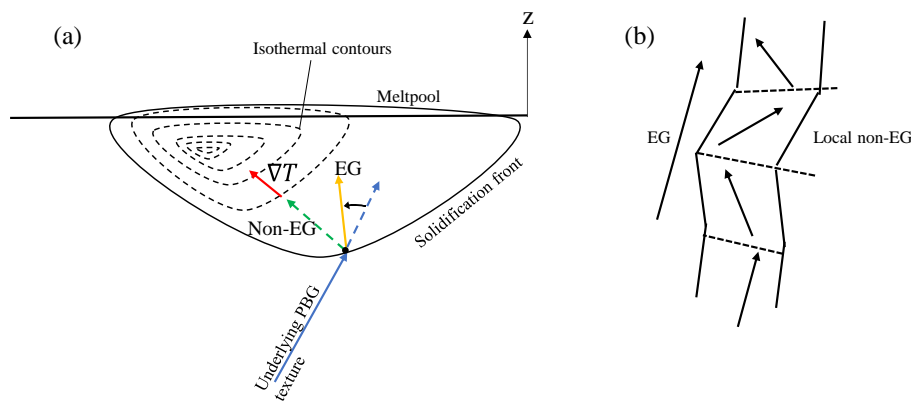
Figure 7.21. Epitaxial growth (EG) versus non-epitaxial growth (a) PBG texture direction relative to the maximum ∇T, (b) local non-EG versus global EG.

Meltpool thermal gradient has been reported to range from $10^4 - 10^5$ cm/s (Marshall *et al.*, 2016). This study was able to reduce the thermal gradient by using smaller hatch distances which is argued to induce a CET in sample S4.

140

(a)

(b)

R [mm/s]	v = 600	v = 700	v = 800
θ = 45°	424	495	566
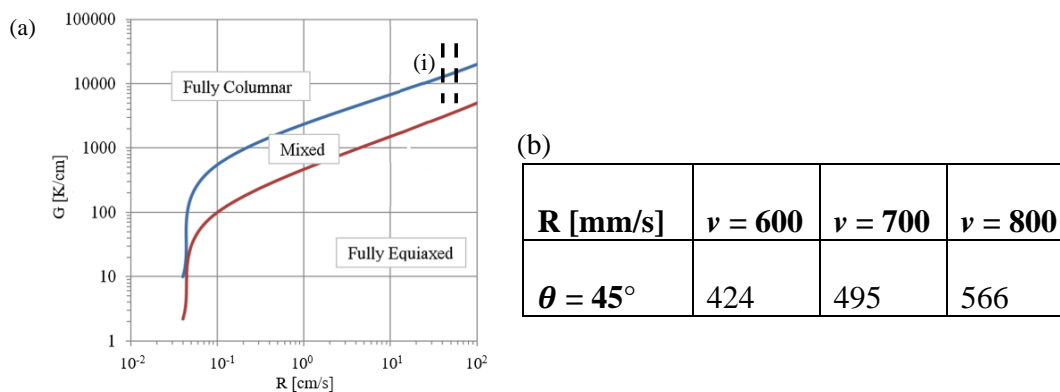
Figure 7.22. (a) G-R plot for Ti-6Al-4V PBG morphology from different solidification cooling operations, adapted from Kobryn & Semiatin (2003). (i) Identified CET zone (vertical parallel broken lines) from (b) calculated R for scan velocity 600 – 800 mm/s with θ approximated from local secondary PBG texture direction.

7.4.3 Influence of melt pool size on edge bulging and sample density

Cylinders built with a FOD of 3.5 mm measured significantly lower density than their cubic counterparts of the same parameter set. Cylindrical sample group S18 measured a mean density of 96.7 %, and S20 measured a mean density of 97.1 %. Due to their low density, these samples were discarded from the results discussion. This section discusses the probable cause of this disparity in density.

The top surface topology of samples FOD = 3.5 mm and slow scan speed (200 – 240 mm/s) caused severe edge bulging, as depicted in Figure 7.23(a). Since the severity of edge bulging increases with layer height, the impact of edge bulging on cubic samples was low enough to achieve adequate density (see Figure 7.2). With an increase in the number of layers, however, edge bulging increases, ultimately causing poor powder spreading due to obstruction of to the scraper blade. This effect was low enough for samples scanned at a FOD of 2 mm, Figure 7.23(b), to achieve high density in cylindrical samples.
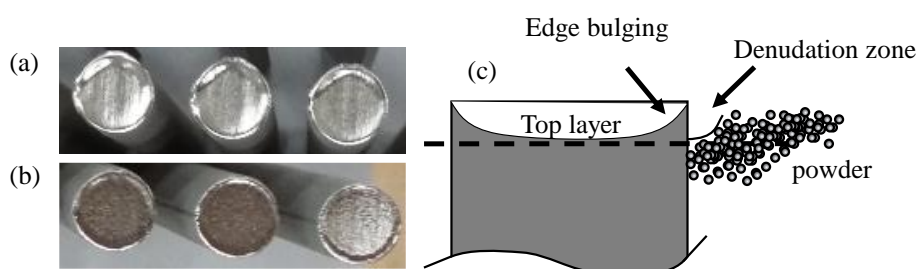
Figure 7.23. Comparison of sample top surface (a) S20 (FOD = 3.5 mm, v = 200 mm/s) and (b) S4 (FOD = 2, v = 600 mm/s). (c) Schematic of sectioned top ZX-plane showing the negative effect of edge bulging on powder spreading.

141

When comparing melt pool geometries, Figure 7.24, of samples scanned at an identical E_v = 250 J/mm^3 (S13 and S18), measurements indicated that at a FOD = 2 mm and v = 800 mm/s caused melt pool penetration depth of ~130 μm, while a FOD = 3.5 mm combined with a scan speed of 240 mm/s measured a penetration depth of ~220 μm.
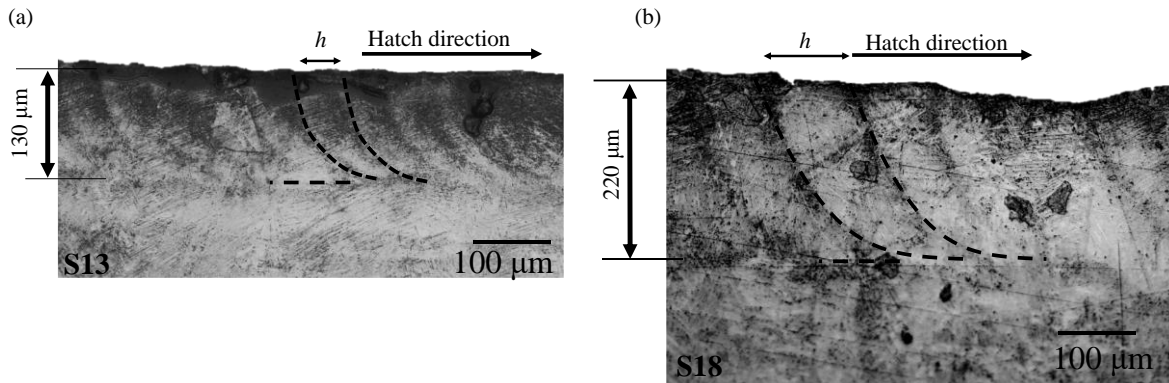
Figure 7.24. Melt pool depth comparison of samples both scanned at E_v = 250 J/mm (a) S13 (FOD = 2 mm, v = 800 mm/s), and (b) S18 (FOD = 3.5 mm, v = 240 mm/s).

Since a larger laser spot size and a slower scan speed is known to increase melt pool size (DebRoy *et al.*, 2018), powder denudation at sample edge increases since more powder is absorbed into the melt pool. Edge bulging, therefore, results due to a large, solidified melt pool on the sample's boundary.

7.4.4 Additional considerations of sample size and build time

Sample size could influence the degree to which the process parameters are effective in facilitating a phase transformation. The investigated process parameters significantly increased part-built time. While this is undesirable, the total process time of the presented *in-situ* route needs to be compared to the conventional process + post-process route before concluding the shortest route. Since process time is not this chapter's direct consideration, a calculation of process time is included in Appendix D.

7.5 Conclusions

Current default process parameters used in commercial machines cause high cooling rates and thermal gradients, which cause high residual stress, undesired brittle martensitic microstructure and a textured columnar PBG structure. Post-process heat treatments are currently applied to improve material ductility and fatigue properties by decomposing the martensite microstructure and relieving residual stress. Post-processing, is however, an expensive and time-consuming operation. The study investigated an alternative route to post-process heat treatments by using above-default-E_v process parameters to induce an *in-situ* heating effect in the samples.

The study found that above-default-E_v process parameters were effective in influencing the above-mentioned structural aspects. A decrease in hatch distance and laser scan speed both have the effect of increasing the E_v input to the material. Decreasing the scan speed lowers the thermal gradient in the direction of the scan track, while decreasing the hatch distance lowers the thermal gradient in the hatch direction. The combined effects of lower thermal gradients and higher E_v caused a heating effect on the underlying layers, thereby decomposing or suppressing martensite and residual stress formation.

Results indicate trends in data with changing E_v, hatch distance and scan speed. Martensite decomposition was found in all samples, with a full decomposition of $\alpha' \rightarrow \alpha$ being measured for E_v of 167 J/mm^3 and higher. β-phase volume was found to increase with an increase in E_v. An increase in E_v was correlated with a decrease in residual stress.

The influence of above-default-E_v process parameters on PBG morphology and texture revealed the dominant PBG growth occurred at an angle of $70 - 80°$ with respect to the XY-plane due to hatch rotation effects. A sufficiently high E_v at a hatch distance of 30 μm showed signs of columnar-to-equiaxed transition.

Oxygen and nitrogen pick-up with an increase in E_v was measured. An increase in these interstitial elements resulted in an increase in lattice parameters, material embrittlement, surface colourisation and horizontal dark bands in micrographs. Contamination was greater towards the bottom of the samples, and nitrogen content increased to a larger degree than oxygen.

Results show potential for using the proposed *in-situ* processing route to achieve a more desired α+β microstructure, lower residual stress and a more equiaxed, weaker PBG texture. However, future research needs to identify the cause of the oxygen + nitrogen contamination and reduce this effect for this to be successfully applied. This should enable improved ductility from that achieved by the default parameter set.

8 Discussion and recommendations

This chapter aims to expand on the discussions of the previous chapters in terms of the objectives outlined in Section 3.2. This chapter provides additional considerations for the broader implication of the findings, unanswered questions, potential additional experimental work, and poses recommendations for future research.

8.1 Tailoring microstructural morphology

Chapter 4 introduced an approach reported for the first time to post-process heat treatments in which the inherent dislocated structure of α' is used to achieve a fragmented and globular-like α-grain morphology. By annealing just below T_β, at ~960 °C, grain aspect ratio and grain size is significantly reduced. By furnace cooling and quenching from ~900 °C, a α_p-to-α' ratio of ~50 % and globular-shaped α-laths of ~11 µm is achieved (see Table 4.7).

The continuation of this study lies in the potential for further optimisation of the microstructural morphology. For example, optimisation in terms of the α_p-to-α' ratio should be considered since this ratio is shown to be a key factor in the mechanical properties of commercially produced Ti-6Al-4V (Semiatin *et al.*, 2003). Furthermore, improved homogeneity and uniformity in globularisation is likely possible through longer hold times in the high-SSTR. A technique that could complement this investigation is the use of nano-indentations, available at the CHRTEM, to measure the difference in hardness between the α_p and α' structures as was done by de Formanoir *et al.* (2019).

Further investigations that would complement the findings of Chapter 4 are in characterising an unknown internal acicular structure observed in samples quenched from ~910 °C. These are imaged in Figure 8.1.
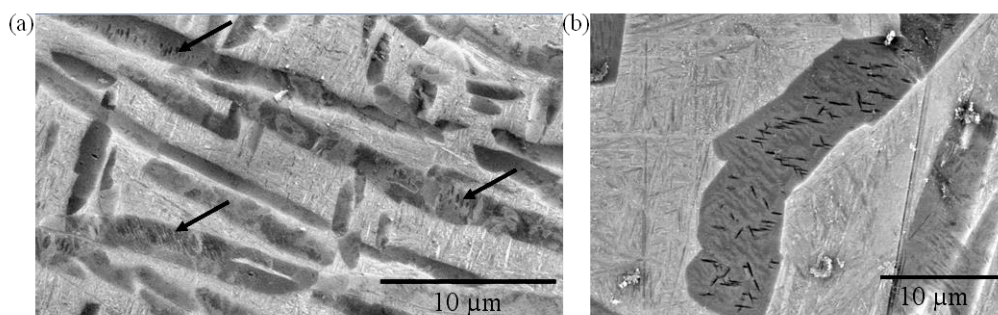
Figure 8.1. BSE-SEM micrographs of unidentified acicular structures (indicated by arrows) observed for samples annealed at 910 °C followed by water quenching, (a) low and (b) high magnification.

144

Challenges for implementing quenched-based heat treatments were identified. It is hypothesised that fast cooling could cause part distortion and the generation of residual stresses, particularly in thin structures. Since the thermal conductivity at room temperature of Ti-6Al-4V (6.7 $W.m^{-1}.K^{-1}$) is about ⅓ that of steel (~20 $W.m^{-1}.K^{-1}$) (Nuclear-power.net, n.d.), the cooling rate upon quenching would be slower for the former, thereby lowering the risks of part distortions and the magnitude of induced residuals stresses compared to ferrous-based metals.

For small scale experimental studies, the successful implementation of quenching without undesired surface oxidation remains a challenge. This is because conventional quenching methods require the sample to be removed from the furnace and placed in a water container, thereby exposing the heated sample to oxygen. Although the negative effects of surface oxidation on mechanical properties were removed through machining, machining of end-components with complex shapes might not be practical. An alternative to mechanical machining is chemical milling. An approach to avoid material oxidation in a research-based setting recommended for future studies is to encapsulate samples in quartz tubes filled with argon, as was done by de Formanoir *et al.* (2019).

In recent years, technological developments within HIP equipment now make it possible to perform ultrahigh-pressure gas quenching, which enables high cooling rates in a HIP unit (Ahlfors, 2020). It is therefore highly recommended for future studies to investigate the use of similar HIP and ultrahigh-pressure gas quenching procedures. This would not only improve tensile behaviour through the bi-modal microstructure, but also eliminate internal porosity, which would greatly improve porosity-sensitive fatigue properties.

The potential of rapid heating for the formation of finer grain structures in titanium alloys exist (Ivasishin & Teliovich, 1999). Rapid heating is accomplished by induction-heating. Although the author is not aware of local laboratories with this technology, future investigation into induction-heating could be of value for further development and optimisation of microstructural morphologies and textures. However, the low electrical and thermal conductivity in titanium alloys poses a challenge to uniform fast heating (Smolyanov *et al.*, 2019). Induction heating remains a novel research field. For further reading on the topic, see Rycroft (2016) and Smolyanov *et al.* (2020). For further demonstration, detailed schematics and instruction of building a small scale, 1.4 kW, induction heater for future research, see Schematix (2020).

8.2 The initiation of martensite decomposition and stress relaxation

Chapter 5 investigated the influence of low-temperature post-process thermal treatments on residual stress relaxation and martensite decomposition. A key finding was that 90 % of compressive residual stress was relaxed at 550 °C after only one hour. The contribution of this chapter was in characterising the initial stages of martensite decomposition at low annealing temperatures. Extremely fine precipitates at the boundaries and dislocations were observed and identified as β-phase. Fine topographic textures internal to laths, which indicate possible spinodal decomposition, was also observed, Figure 5.13(a). Based on these observations and the increase in microhardness over time, two kinematic transformation routes were

hypothesised: (1) nucleation-and-growth of β-precipitates and (2) a spinodal decomposition. Both are theorised to cause a precipitation hardening.

Worth exploring but not addressed in Chapter 5 is the extent to which compressive residual stress contributes to material ductility and microhardness. According to Surech and Giannakopoulos (1998), compressive residual stress will make it harder for the micro-indenter to penetrate the material, thereby increasing the apparent material hardness. However, results presented in Section 5.3 indicated that the relaxation of compressive residual stress was correlated with an increase in microhardness. Therefore, residual stress can be discarded as a dominant cause of an increase in material microhardness. The question that remains is, to what extent internal compressive residual stress (observed in multiple studies of LPBF-produced Ti-6Al-4V (Vrancken, 2016; Anderson, 2017)) contributes to material ductility? Theoretically, compressive residual stress would lower the effect of internal defects on crack initiation. The challenge is separating the influence of residual stress and microstructure on material deformation since these cannot be independently altered by using thermal treatments.

The main challenge of this study was characterising extremely fine structures. Although this study was unable to detect bcc phase using XRD in as-built, "427_30hours" or "480_30hours" samples (Figure 5.7), this finding should not be considered overwhelming evidence for ruling out small traces of residual bcc phase. The reasons for this is firstly that the detection limit of conventional XRD is believed to be ~3 vol% of a given phase (Tan *et al.*, 2015), and secondly, Mengucci *et al.* (2019) observed small traces of residual β-phase using the high-penetration-depth approach of neutron diffraction.

Jia (2016) used selected area diffraction to image α_2 particles at oxygen concentrations as low as 1200 ppm in LPBF-produced Ti-6Al-4V. A valuable addition to Chapter 5 would be in repeating this experimental characterisation used by Jia to investigate the presence of α_2 particles.

The local research nuclear reactor (SAFARI-1 at NECSA) has a neutron strain scanning instrument (Materials Probe for Internal Strain Investigations – MPISI). This instrument enables deeper penetration (in the millimetre range) for measuring residual stress and crystal texture (Anderson *et al.*, 2018; Venter *et al.*, 2018). International X-ray synchrotron facilities such as BESSY II or PETRA III (by DESY) could also be considered. Atom probe tomography would be an ideal experimental technique to characterise perceived spinodal decomposition.

De Formanoir *et al.* (2019) applied the resultant increase in hardness of α' found in this chapter to similar bi-modal microstructures as that developed in Chapter 4. This had the effect of lowering the work-hardening rate of the material. Therefore, a recommendation is to combine the heat treatment strategies of Chapter 4 with the low-temperature heat treatments of Chapter 5.

The final recommendation for future investigations related to the work presented in Chapter 5 is using an induction-heating approach. Rapid heating rates are hypothesised to cause a "reverse martensite transformation" in titanium alloys (Ivasishin & Teliovich, 1999) which might be an avenue of research to achieve finer decomposed α+β structures.

8.3 PBG texture-induced deformation anisotropy

Chapter 6 investigated the cause of anisotropic deformation behaviour of as-fabricated LPBF-produced Ti-6Al-4V. Morphological and crystallographic texture differences in the two orientations were quantified. Deformation was studied through the quantification of Schmid factors and transmissibility factors. The chapter's main findings were that the crystallographic texture of α' is relatively weak and that plastic slip does not initiate at the lowest Schmid factors. Rather, micro-crack initiation is observed to form along lath boundaries at ~45° to the load direction. Laths were quantitatively measured to be mainly orientated at ~45° with respect to the Z-axis (i.e., morphological angle-texture). The study contributes an insight to explain how this is related to the PBG-texture. The study hypothesises that a dominant lath angle due to PBG crystallographic texture is the probable cause of anisotropic deformation behaviour.

Post-process heat treatments in the SSTR are likely to increase the α-texture strength, which might cause crystallographic effects to become dominant (see Hayes *et al.* (2017)). As demonstrated in Chapter 4, laths can be globularised by annealing in the high-SSTR. Since anisotropy was related to the morphology of α' laths, anisotropy could be theoretically reduced by reducing the lath aspect ratio. Future work could be to investigate the influence of α-lath fragmentation and globularisation on deformation anisotropy.

Additional experimental techniques could complement the theoretical-based Schmid-factor approach of this study. Sub-grain *in-situ* digital image correlation has been effectively used to investigate deformation and failure behaviour of LPBF-produced Ti-6Al-4V (Leicht & Wannberg, 2015; Book & Sangid, 2016; de Formanoir *et al.*, 2019; Moridi *et al.*, 2019) and conventionally produced Ti-6Al-4V (Sandala, 2012). These studies successfully used Schmid Law and slip transmissibility to predict deformation behaviour and found evidence of high strain accumulation along high aspect ratio α-grains with high Schmid factors orientated at 45° with respect to the load direction. Lastly, rapid heat treatments of titanium alloys were successfully applied to yield smaller PBG grain sizes (Ivasishin & Teliovich, 1999; Ivasishin *et al.*, 2002).

8.4 *In-situ* thermal treatments

Chapter 7 investigated the use of non-default process parameters that achieve a high energy input with the aim of inducing an *in-situ* heating effect. This was hypothesised to decompose or suppress martensitic phase formation and lower residual stresses. This chapter's findings exposed the immense potential for using high-energy process parameters for martensite decomposition and stress relief. Undesirable aspects from *in-situ* thermal treatments can serve as starting points for future research. These undesirable aspects include the increased oxygen and nitrogen content, long build times and part defects. Furthermore, although not quantified in this study, the achievable dimensional accuracy might be affected by larger laser diameter and melt pool size.

Although the cause of the increased oxygen and nitrogen content is unknown, a few hypotheses are proposed. Preliminary investigation of high-energy process parameters using KU Leuven's

Concept Laser M1 machine also indicated part surface contamination (as observed by surface colourisation). Other studies have indicated similar part oxygen pick-up and embrittlement results using higher energy process parameters (Thijs *et al.*, 2010; Na *et al.*, 2018). This means that part oxidation is unlikely to be due to abnormal machine functionality, such as an air leak or sensor error. Since the powder used in the study measured normal interstitial content, the probable cause of part oxygen + nitrogen contamination is the build chamber's atmosphere or heterogeneous air composition in the powder container. Even though the oxygen sensor kept the oxygen content below 1200 ppm, this was likely still too high for above-default-E_v process parameters and thereby causing surface oxidation. Future investigation would also benefit from monitoring the nitrogen content of the build chamber since this increased to larger degree than oxygen content and has a larger theoretical influence of part embrittlement.

Micro XCT indicated internal defects situated predominantly at the turning point of the laser (on the part boundary). This was likely caused by a transient increase in energy density at the end of the scan tracks as demonstrated by Martin *et al.* (2019). The presence of these pores could be reduced by applying a contour scan before internal hatching, or by applying a mitigation strategy in which the process parameters are adjusted *in-situ* to achieve a constant energy density (Martin *et al.*, 2019). Other suggestions for future research to eliminate boundary defects are alternative hatch strategies, such as a spiral-type strategy, or remelting contour scan track.

The developed process parameters presented in Chapter 7 have the disadvantage of increasing the build time (see **Error! Reference source not found.**). Although process time was not a f ocus of this study, it is an important consideration in the feasibility of using these parameters in an industrial/commercial setting. The reduction in build time is ultimately limited by laser power. A higher laser power would allow for a faster scan speed and larger hatch distances while still maintaining a high energy density. A higher laser power, however, would cause higher laser intensity which might cause key-pore or gas entrapment. Issues of high laser intensity could be overcome by using a higher FOD. A viable machine with higher laser power that could serve as a research focus with the aim of *in-situ* thermal treatments with shorter build time is the AeroSwift machine (this machine has a laser power of 2 kW, see Appendix A.3).

Quench-based heat treatments developed in Chapter 4 to globularise the α-laths might be less effective for the α+β lamellar structures achieved through high energy parameters in Chapter 7. This is because the mechanism that allows for α globularisation relies on the inherent dislocation structure of the as-fabricated martensitic microstructure, which is not present in decomposed microstructures.

9 Conclusions

This project was motivated by the potential for socio-economic growth by (1) increased beneficiation of the locally mined titanium mineral, and (2) to prepare local industrial infrastructure and markets to allow for the fully beneficiation of the 4IR. LPBF-produced Ti-6Al-4V was identified as an innovative titanium manufacturing approach of the 4IR, thus satisfying both (1) and (2). Structural quality concerns about the material, such as achievable tensile properties, prevents it from being accepted by industries such as aerospace and biomedical. Currently, understanding the process-structure-property interactions of LPBF-produced Ti-6Al-4V is limited due to the technology's novelty. Thus, this serves as the study's primary scientific motivation. The study contributes to the development of scientific knowledge of the influence of thermal strategies on the microstructural response for improving the achievable part quality.

The aim of this research study was to develop fundamental insights into the microstructural response of thermal treatments and the influence of resultant microstructures on deformation behaviour. This was done through post-process heat treatments in three temperature regions and an investigation of high-energy process parameters through *in-situ* thermal treatments. The key contributions are outlined below:

- Post-process annealing strategies in the temperature range $700 - T_\beta$ °C were developed to improve tensile behaviour. Optical and electron microscopy was used to study α-grain morphology as a function of annealing temperature, hold time and cooling rate. Unique contributions of Chapter 4 are (1) describing the mechanisms of large-scale morphological transformation, (2) developing thermal strategies that involve both furnace cooling and water quenching to achieve a fragmentation and globularisation of α-laths and (3) developing a bi-modal microstructure that achieves superior tensile behaviour to conventional thermal treatments applied to LPBF-produced Ti-6Al-4V.

- Low-temperature post-process thermal treatments below 700 °C were applied to develop an understanding of the initial stages of martensite decomposition and residual stress relief. Material embrittlement as a function of temperature and time was measured. XRD was used to observe subtle changes in alloy composition of phases. High-resolution transmission electron microscopy was used to image and characterise fine precipitates in the martensitic microstructure. Unique contributions of Chapter 5 are (1) insight into initial stages of α'→ α+β phase transformation, (2) developing theories for probable cause of material embrittlement based on two possible transformation routes.

- The microstructural cause of anisotropic deformation in LPBF-produced Ti-6Al-4V was investigated by applying β-anneal strategies. Large reconstructed EBSD maps were used to quantify microstructural anisotropy between two orientations. The influence of microstructure on deformation and crack initiation was studied through tensile tests and EBSD maps. Unique contributions of Chapter 6 are (1) insight into the influence of β-anneal on LPBF-produced Ti-6Al-4V PBG morphology and texture and (2) identifying a link between prior-β crystallographic texture and α-lath morphological texture to formulate a theory of the probable cause of material deformation anisotropy.

- An approach to thermal treatments was investigated by using high-energy-inducing LPBF process parameters. Variations in hatch distance and laser scan speed were used to generate above-default laser energy densities ranging from 125 to 333 J/mm^3. XRD was used to monitor subtle differences in the alloy composition. Micro XCT was used to characterise internal defects. Optical electron micrographs and EBSD maps were used to characterise PBG texture directions. The unique contribution of Chapter 7 is in demonstrating the feasibility of using *in-situ* thermal strategies to decompose martensite and relieve residual stress.

List of references

Abubakr, M., Abbas, A.T., Tomaz, I., Soliman, M.S., Luqman, M. & Hegab, H. 2020. Sustainable and Smart Manufacturing: An Integrated Approach. *Sustainability*. 12(6): 2280.

Aeroswift South Africa. 2018. *Gallery – Aeroswift*. [Online], Available: https://www.aeroswift.com/gallery/ [2020, November 19].

Ahlfors, M. 2020. *Hot Isostatic Pressing with Integrated Heat Treatment*. [Online], Available: https://www.industrialheating.com/articles/95589-hot-isostatic-pressing-with-integrated-heat-treatment [2020, November 11].

Ahmed, T. & Rack, H.J. 1998. Phase transformations during cooling in α+β titanium alloys. *Materials Science and Engineering: A*. 243(1–2): 206–211.

Ali, H., Ma, L., Ghadbeigi, H. & Mumtaz, K. 2017. In-situ residual stress reduction, martensitic decomposition and mechanical properties enhancement through high temperature powder bed pre-heating of Selective Laser Melted Ti6Al4V. *Materials Science and Engineering: A*. 695: 211–220.

Ali, H., Ghadbeigi, H. & Mumtaz, K. 2018. Effect of scanning strategies on residual stress and mechanical properties of Selective Laser Melted Ti6Al4V. *Materials Science and Engineering: A*. 712: 175–187.

AM Chronical. 2019. *Aeroswift develops 0.5 m tall titanium frame for UAV using 3D Printing*. [Online], Available: https://www.amchronicle.com/news/aeroswift-develops-0-5-m-tall-titanium-frame-for-uav-using-3d-printing/ [2020, May 28].

AMFG. 2020. *40+ 3D Printing Industry Stats You Should Know*. [Online], Available: https://amfg.ai/2020/01/14/40-3d-printing-industry-stats-you-should-know-2020/?cn-reloaded=1 [2020, October 13].

Anderoglu, O. 2004. Residual stress measurement using X-ray diffraction. Texas A&M University. [Online], Available: http://oaktrust.library.tamu.edu/bitstream/handle/1969.1/1507/etd-tamu-2004C-MEEN-Anderog.pdf?isAllowed=y&sequence=1 [2020, June 11].

Anderson, L.S. 2017. Evaluating measurement techniques: establishing a testing framework for residual stress in selective laser melted Ti-6Al-4V. Stellenbosch University. [Online], Available: http://scholar.sun.ac.za/handle/10019.1/102816 [2018, July 27].

Anderson, L.S., Venter, A.M., Vrancken, B., Marais, D., van Humbeeck, J. & Becker, T.H. 2018. Investigating the Residual Stress Distribution in Selective Laser Melting Produced Ti-6Al-4V using Neutron Diffraction. In *Mechanical Stress Evaluation by Neutron and Synchrotron Radiation*. Vol. 4. Materials Research Forum LLC. 73–78.

Antonysamy, A.A., Meyer, J. & Prangnell, P.B. 2013. Effect of build geometry on the β-grain structure and texture in additive manufacture of Ti6Al4V by selective electron beam melting. *Materials Characterization*. 84: 153–168.

Atkinson, H. V. & Davies, S. 2000. Fundamental aspects of hot isostatic pressing: An overview. *Metallurgical and Materials Transactions A: Physical Metallurgy and Materials Science*. 31(12): 2981–3000.

Attar, H., Ehtemam-Haghighi, S., Kent, D. & Dargusch, M.S. 2018. Recent developments and opportunities in additive manufacturing of titanium-based matrix composites: A review. *International Journal of Machine Tools and Manufacture*. 133(June): 85–102.

Bachmann, F., Hielscher, R. & Schaeben, H. 2010. Texture Analysis with MTEX – Free and Open Source Software Toolbox. *Solid State Phenomena*. 160: 63–68.

Bae, C.J., Diggs, A.B. & Ramachandran, A. 2018. Quantification and certification of additive manufacturing materials and processes. In *Additive Manufacturing: Materials, Processes, Quantifications and Applications*. Elsevier. 181–213.

Bagot, P.A.J., Radecka, A., Magyar, A.P., Gong, Y., Bell, D.C., Smith, G.D.W., Moody, M.P., Dye, D. & Rugg, D. 2018. The effect of oxidation on the subsurface microstructure of a Ti-6Al-4V alloy. *Scripta Materialia*. 148: 24–28.

Baldi, A. 2014. Residual Stress Measurement Using Hole Drilling and Integrated Digital Image Correlation Techniques. *Experimental Mechanics*. 54(3): 379–391.

Banerjee, D. & Williams, J.C. 2013. Perspectives on Titanium Science and Technology. *Acta Materialia*. 61(3): 844–879.

Banerjee, S. & Krishnan, R. 1971. Martensitic transformation in zirconium-niobium alloys. *Acta Metallurgica*. 19(12): 1317–1326.

Barriobero-Vila, P., Gussone, J., Haubrich, J., Sandlöbes, S., Da Silva, J., Cloetens, P., Schell, N. & Requena, G. 2017. Inducing Stable α + β Microstructures during Selective Laser Melting of Ti-6Al-4V Using Intensified Intrinsic Heat Treatments. *Materials*. 10(3): 268.

Bayerschen, E., McBride, A.T., Reddy, B.D. & Böhlke, T. 2016. Review on slip transmission criteria in experiments and crystal plasticity models. *Journal of Materials Science*. 51(5): 2243–2258.

BCCPublishing. 2019. *2019 Manufacturing Research Review*. [Online], Available: https://www.bccresearch.com/market-research/manufacturing/manufacturing-research-review.html.

Becker, T.H., Beck, M. & Scheffer, C. 2015. Microstructure and mechanical properties of direct metal laser sintered Ti-6Al-4V. *South African Journal of Industrial Engineering*. 26(May): 1–

10.

Becker, T.H., Dhansay, N.M., Haar, G.M. Ter & Vanmeensel, K. 2020. Near-threshold fatigue crack growth rates of laser powder bed fusion produced Ti-6Al-4V. *Acta Materialia*. 197: 269–282.

de Beer, D., du Preez, W., Greyling, H., Prinsloo, F., Sciammarella, F., Trollip, N., Vermeulen, M. & Wohlers, T. 2016. *A South African Additive Manufacturing Strategy*. [Online], Available: https://site.rapdasa.org/wp-content/uploads/2017/02/South-African-Additive-Manufacturing-Strategy.pdf.

Bester, D., Wichers, H. & Moller, H. 2017. Evaluation of a carbon fibre powder scraper used in metal additive manufacturing. In *RAPDASA 2017 Conference Proceedings*. [Online], Available: https://site.rapdasa.org/wp-content/uploads/2019/10/RAPDASA-2017-Conference-Proceedings.pdf.

Bester, D., Vermeulen, M. & Prinsloo, J. 2017. Design for metal additive manufacturing: Printing the AHRLAC flight grips. In *RAPDASA 2017 Conference Proceedings*. [Online], Available: https://site.rapdasa.org/wp-content/uploads/2019/10/RAPDASA-2017-Conference-Proceedings.pdf.

Bezuidenhout, M., Ter Haar, G.M., Becker, T., Rudolph, S., Damm, O. & Sacks, N. 2020. The effect of HF-HNO3 chemical polishing on the surface roughness and fatigue life of laser powder bed fusion produced Ti6Al4V. *Materials Today Communications*. 25: 101396.

Bissett, H., Van Der Walt, I.J., Havenga, J.L. & Nel, J.T. 2015. Titanium and zirconium metal powder spheroidization by thermal plasma processes. *Journal of the Southern African Institute of Mining and Metallurgy*. 115(10): 937–942.

Blanter, M.S., Granovskiy, E.B. & Magalas, L.B. 2004. Interaction of dissolved atoms and relaxation due to interstitial atoms in hcp metals. *Materials Science and Engineering A*. 370(1–2): 88–92.

Bogue, R. 2013. 3D printing: The dawn of a new era in manufacturing? *Assembly Automation*. 33(4): 307–311.

Bonneau, V., Yi, H., Probst, L., Pedersen, B. & Lonkeu, O.-K. 2017. *The disruptive nature of 3D printing The disruptive nature of 3D printing : offering new opportunities for verticals*. [Online], Available: https://ec.europa.eu/growth/tools-databases/dem/monitor/sites/default/files/DTM_The disruptive nature of 3D printing v1.pdf.

Book, T.A. & Sangid, M.D. 2016. Strain localization in Ti-6Al-4V Widmanstätten microstructures produced by additive manufacturing. *Materials Characterization*. 122: 104–112.

Boyer, R.R. 1996. An overview on the use of titanium in the aerospace industry. *Materials*

Science and Engineering A. 213(1–2): 103–114.

Boyer, R., Collings, E.W. & Welsch, G. 1994. *Materials Properties Handbook: Titanium Alloys*. ASM International.

Brandl, E. 2010. Microstructural and mechanical properties of additive manufactured Ti-6Al-4V using wire. Brandenburg Technical University of Cottbus.

Brandl, E. & Greitemeier, D. 2012. Microstructure of additive layer manufactured Ti–6Al–4V after exceptional post heat treatments. *Materials Letters*. 81: 84–87.

Bridier, F., Villechaise, P. & Mendez, J. 2005. Analysis of the different slip systems activated by tension in a α/β titanium alloy in relation with local crystallographic orientation. *Acta Materialia*. 53(3): 555–567.

Brisset, F. 2010. *EBSD Workshop Electron BackScattered Diffraction basics and applications*. [Online], Available: http://www.semat.lab.uminho.pt/Documentos/EBSD-compilation.pdf.

British Broadcasting Corporation. 2012. *Transplant jaw made by 3D printer claimed as first*. [Online], Available: https://www.bbc.com/news/technology-16907104 [2020, October 15].

Buehler. 2020. *Titanium Specimen Testing & Preparation*. [Online], Available: https://www.buehler.com/titanium-specimen-testing-and-preparation.php [2020, June 10].

Burgers, W.G. 1934. On the process of transition of the cubic-body-centered modification into the hexagonal-close-packed modification of zirconium. *Physica*. 1(7–12): 561–586.

Callister, W.D.. & Rethwisch, D.G. 2011. *Materials Science and Engineering*. 8th ed. John Wiley & Sons.

Campbell, T., Williams, C., Ivanova, O. & Garrett, B. 2011. Could 3D Printing Change the World?: Technologies, Potential, and Implications of Additive Manufacturing. *Atlantic Council*. 3–7.

Cao, S., Chu, R., Zhou, X., Yang, K., Jia, Q., Lim, C.V.S., Huang, A. & Wu, X. 2018. Role of martensite decomposition in tensile properties of selective laser melted Ti-6Al-4V. *Journal of Alloys and Compounds*. 744: 357–363.

Capucine Lonjon. 2017. *The history of 3d printer: from rapid prototyping to additive fabrication*. [Online], Available: https://www.sculpteo.com/blog/2017/03/01/whos-behind-the-three-main-3d-printing-technologies/ [2020, October 14].

Carreon, H., Ruiz, A. & Santoveña, B. 2014. Study of aging effects in a Ti-6AL-4V alloy with Widmanstätten and equiaxed microstructures by non-destructive means. In *AIP Conference Proceedings*. Vol. 1581. 739–745.

Carroll, B.E., Palmer, T.A. & Beese, A.M. 2015. Anisotropic tensile behavior of Ti–6Al–4V components fabricated with directed energy deposition additive manufacturing. *Acta Materialia*. 87: 309–320.

Central Intelligence Agency. 2020. *The World Factbook - South Africa*. [Online], Available: https://www.cia.gov/library/publications/resources/the-world-factbook/geos/sf.html [2020, May 28].

Central University of Technology. 2019. *South Africa top of additive manufacturing innovation*. [Online], Available: https://www.cut.ac.za/news/south-africa-top-of-additive-manufacturing-in [2020, October 16].

Chen, X. & Qiu, C. 2020. In-situ development of a sandwich microstructure with enhanced ductility by laser reheating of a laser melted titanium alloy. *Scientific Reports*. 10(1): 15870.

Chen, G., Zhao, S.Y., Tan, P., Wang, J., Xiang, C.S. & Tang, H.P. 2018. A comparative study of Ti-6Al-4V powders for additive manufacturing by gas atomization, plasma rotating electrode process and plasma atomization. *Powder Technology*. 333: 38–46.

Chivel, Y. & Smurov, I. 2010. On-line temperature monitoring in selective laser sintering/melting. *Physics Procedia*. 5: 515–521.

Chong, Y., Bhattacharjee, T., Yi, J., Shibata, A. & Tsuji, N. 2017. Mechanical properties of fully martensite microstructure in Ti-6Al-4V alloy transformed from refined beta grains obtained by rapid heat treatment (RHT). *Scripta Materialia*. 138: 66–70.

Clarke, C. 2017. *South African Aeroswift 3D printing project in talks with Boeing and Airbus*. [Online], Available: https://3dprintingindustry.com/news/south-african-aeroswift-3d-printing-project-talks-boeing-airbus-107057/ [2020, June 09].

Conrad, H. 1981. Effect of interstitial solutes on the strength and ductility of titanium. *Progress in Materials Science*. 26(2–4): 123–403.

Crespo, A. 2011. Modelling of Heat Transfer and Phase Transformations in the Rapid Manufacturing of Titanium Components. In *Convection and Conduction Heat Transfer*. InTech. 315–340. [Online], Available: http://cdn.intechopen.com/pdfs/22262.pdf.

de Damborenea, J.J., Larosa, M.A., Arenas, M.A., Hernández-López, J.M., Jardini, A.L., Ierardi, M.C.F., Zavaglia, C.A.C., Filho, R.M. & Conde, A. 2015. Functionalization of Ti6Al4V scaffolds produced by direct metal laser for biomedical applications. *Materials & Design*. 83: 6–13.

Davis, R., Flower, H.M. & West, D.R.F. 1979. The decomposition of Ti-Mo alloy martensites by nucleation and growth and spinodal mechanisms. *Acta Metallurgica*. 27(6): 1041–1052.

DebRoy, T., Wei, H.L., Zuback, J.S., Mukherjee, T., Elmer, J.W., Milewski, J.O., Beese, A.M.,

Wilson-Heid, A., De, A. & Zhang, W. 2018. Additive manufacturing of metallic components – Process, structure and properties. *Progress in Materials Science*. 92: 112–224.

Desktop Metal^{TM}. 2020. [Online], Available: https://www.desktopmetal.com/ [2020, October 10].

Dilberoglu, U.M., Gharehpapagh, B., Yaman, U. & Dolen, M. 2017. The Role of Additive Manufacturing in the Era of Industry 4.0. *Procedia Manufacturing*. 11(June): 545–554.

Dilip, J.J.S., Zhang, S., Teng, C., Zeng, K., Robinson, C., Pal, D. & Stucker, B. 2017. Influence of processing parameters on the evolution of melt pool, porosity, and microstructures in Ti-6Al-4V alloy parts fabricated by selective laser melting. *Progress in Additive Manufacturing*. 2(3): 157–167.

Ding, R., Guo, Z.X. & Wilson, A. 2002. Microstructural evolution of a Ti–6Al–4V alloy during thermomechanical processing. *Materials Science and Engineering: A*. 327(2): 233–245.

Donachie, M.J. 2000. *Titanium: A Technical Guide*. 2nd ed. Materials Park, Ohio, U.S.A.: ASM International.

Donoghue, J., Antonysamy, A.A., Martina, F., Colegrove, P.A., Williams, S.W. & Prangnell, P.B. 2016. The effectiveness of combining rolling deformation with Wire–Arc Additive Manufacture on β-grain refinement and texture modification in Ti–6Al–4V. *Materials Characterization*. 114: 103–114.

DuraScan G5 - EMCO-TEST. n.d. [Online], Available: https://www.emcotest.com/en/products-services/hardness-testing-machines/durascan-g5/ [2020, June 12].

Dutta, B. & (Sam) Froes, F.H. 2015. The additive manufacturing (AM) of titanium alloys. In *Titanium Powder Metallurgy*. Elsevier. 447–468.

Dworzanowski, M. 2013. The role of metallurgy in enhancing beneficiation in the South African mining industry. *Journal of the Southern African Institute of Mining and Metallurgy*. 113(9): 677–683.

Elmer, J.W., Palmer, T. a., Babu, S.S., Zhang, W. & DebRoy, T. 2004. Phase transformation dynamics during welding of Ti-6Al-4V. *Journal of Applied Physics*. 95(12): 8327–8339.

Elmer, J.W., Palmer, T. a., Babu, S.S. & Specht, E.D. 2005. In situ observations of lattice expansion and transformation rates of α and β phases in Ti-6Al-4V. *Materials Science and Engineering A*. 391(1): 104–113.

ELTRA GmbH. 2020. *Elementrac ONH-p*. [Online], Available: https://www.eltra.com/products/onh-analyzers/onh-p/function-features/ [2020, June 12].

Ernst & Young Global Limited. 2019. *3D printing: hype or game changer? - A Global EY Report 2019*. [Online], Available: https://assets.ey.com/content/dam/ey-sites/ey-com/en_gl/topics/advisory/ey-3d-printing-game-changer.pdf.

Evans, W.J. 1998. Optimising mechanical properties in alpha+beta titanium alloys. *Materials Science and Engineering: A*. 243(1–2): 89–96.

Facchini, L., Magalini, E., Robotti, P., Molinari, A., Höges, S., Wissenbach, K. & Facchini, L. 2010. Ductility of a Ti-6Al-4V alloy produced by selective laser melting of prealloyed powders. *Rapid Prototyping Journal*. 16(6): 450–459.

Fan, Z. & Miodownik, A.P. 1994. TEM study of metastable β-phase decomposition in rapidly solidified Ti-6Al-4V alloy. *Journal of Materials Science*. 29(24): 6403–6412.

Fitzpatrick, M., Fry, A., Holdway, P., Kandil, F., Shackleton, J. & Suominen, L. 2005. *Determination of Residual Stresses by X-ray Diffraction*. [Online], Available: https://www.researchgate.net/publication/42795493_Determination_of_Residual_Stresses_by_X-ray_Diffraction.

Forbes. 2019. *Significant 3D Printing Forecast Surges To $35.6 Billion*. [Online], Available: https://www.forbes.com/sites/tjmccue/2019/03/27/wohlers-report-2019-forecasts-35-6-billion-in-3d-printing-industry-growth-by-2024/#bc1c1507d8a6 [2020, October 12].

Ford, S.L.N. 2014. Additive Manufacturing Technology: Potential Implications for U.S. Manufacturing Competitiveness. *Journal of International Commerce and Economics*. September(9): 1–35. [Online], Available: http://www.usitc.gov/journals.

Ford, S. & Despeisse, M. 2016. Additive manufacturing and sustainability: an exploratory study of the advantages and challenges. *Journal of Cleaner Production*. 137: 1573–1587.

de Formanoir, C., Michotte, S., Rigo, O., Germain, L. & Godet, S. 2016. Electron beam melted Ti–6Al–4V: Microstructure, texture and mechanical behavior of the as-built and heat-treated material. *Materials Science and Engineering: A*. 652: 105–119.

de Formanoir, C., Martin, G., Prima, F., Allain, S.Y.P., Dessolier, T., Sun, F., Vivès, S., Hary, B., Bréchet, Y. & Godet, S. 2019. Micromechanical behavior and thermal stability of a dual-phase α+α' titanium alloy produced by additive manufacturing. *Acta Materialia*. 162: 149–162.

Fraţila, D. & Rotaru, H. 2017. Additive manufacturing-a sustainable manufacturing route. In *MATEC Web of Conferences*. Vol. 94.

Gammon, L.M., Briggs, R.D., Packard, J.M., Batson, K.W., Boyer, R. & Domby, C.W. 2004. Metallography and Microstructures of Titanium and its Alloys. In *ASM Handbook*. Vol. 9. 899–917.

Gaunt, P. & Christian, J.W. 1959. The crystallography of the β-α transformation in zirconium

and in two titanium-molybdenum alloys. *Acta Metallurgica*. 7(8): 534–543.

GE Aviation. 2017. *GE Aviation Announces First Run of the Advanced Turboprop Engine*. [Online], Available: https://www.aviationpros.com/engines-components/aircraft-engines/turbine-engines-parts/press-release/12388459/ge-aviation-ge-aviation-announces-first-run-of-the-advanced-turboprop-engine [2020, October 09].

Geetha, M., Singh, A.K., Asokamani, R. & Gogia, A.K. 2009. Ti based biomaterials, the ultimate choice for orthopaedic implants – A review. *Progress in Materials Science*. 54(3): 397–425.

Glavicic, M.G., Kobryn, P.A., Bieler, T.R. & Semiatin, S.L. 2003. A method to determine the orientation of the high-temperature beta phase from measured EBSD data for the low-temperature alpha phase in Ti-6Al-4V. *Materials Science and Engineering: A*. 346(1–2): 50–59.

Gockel, J. & Beuth, J. 2013. Understanding Ti-6Al-4V Microstructure Control in Additive Manufacturing via Process Maps. In *Solid Freeform Fabrication Proceedings*. 666–674.

Gong, H., Rafi, K., Gu, H., Janaki Ram, G.D., Starr, T. & Stucker, B. 2015. Influence of defects on mechanical properties of Ti–6Al–4V components produced by selective laser melting and electron beam melting. *Materials & Design*. 86: 545–554.

Grand View Research. 2018. *3D Printing Market Size To Expand At CAGR Exceeding 16.5% From 2018-2025*. [Online], Available: https://www.grandviewresearch.com/industry-analysis/3d-printing-industry-analysis [2020, October 09].

Ter Haar, G.M. 2017. Selective Laser Melting-produced Ti6Al4V: Influence of annealing strategies on crystallographic microstructure and tensile behaviour. Stellenbosch University. [Online], Available: http://hdl.handle.net/10019.1/102946.

Ter Haar, G.M. & Becker, T.H. 2018. Selective Laser Melting Produced Ti-6Al-4V: Post-Process Heat Treatments to Achieve Superior Tensile Properties. *Materials*. 11(01): 146–160.

Ter Haar, G.M. & Becker, T.H. 2020. Low temperature stress relief and martensitic decomposition in selective laser melting produced Ti6Al4V. *Material Design & Processing Communications*. (January, 21).

Ter Haar, G.M. & Becker, T.H. 2021. The influence of microstructural texture and prior beta grain recrystallisation on the deformation behaviour of laser powder bed fusion produced Ti–6Al–4V. *Materials Science and Engineering: A*. 814(March): 141185.

Habraken, A., Gilles, G., Tuninetti, V., Duchene, L., Hammami, W. & Delannay, L. 2013. Identification and validation of CRSS values for Ti6Al4V alloy. In *Conference of the Balkan Network for the Animal Reproduction Biotechnology*.

Hanson, K. 2020. *Metal Milestones in 3D Printing*. [Online], Available: https://www.sme.org/technologies/articles/2020/march/metal-milestones-in-3d-printing/ [2020, October 13].

Haria, R. 2018. *GE successfully tests ATP engine featuring over 30% 3D printed alloys - 3D Printing Industry*. [Online], Available: https://3dprintingindustry.com/news/ge-successfully-tests-atp-engine-featuring-30-3d-printed-alloys-126756/ [2020, October 09].

Haubrich, J., Gussone, J., Barriobero-Vila, P., Kürnsteiner, P., Jägle, E.A., Raabe, D., Schell, N. & Requena, G. 2019. The role of lattice defects, element partitioning and intrinsic heat effects on the microstructure in selective laser melted Ti-6Al-4V. *Acta Materialia*. 167(April): 136–148.

Hayes, B.J., Martin, B.W., Welk, B., Kuhr, S.J., Ales, T.K., Brice, D.A., Ghamarian, I., Baker, A.H., Haden, C. V., Harlow, D.G., Fraser, H.L. & Collins, P.C. 2017. Predicting tensile properties of Ti-6Al-4V produced via directed energy deposition. *Acta Materialia*. 133: 120–133.

Hémery, S., Villechaise, P. & Banerjee, D. 2020. Microplasticity at Room Temperature in α/β Titanium Alloys. *Metallurgical and Materials Transactions A*. 51: 4931–4969.

Heo, T.W., Shih, D.S. & Chen, L.-Q. 2014. Kinetic Pathways of Phase Transformations in Two-Phase Ti Alloys. *Metallurgical and Materials Transactions A*. 45(8): 3438–3445.

Hodge, N.E., Ferencz, R.M. & Solberg, J.M. 2014. Implementation of a thermomechanical model for the simulation of selective laser melting. *Computational Mechanics*. 54(1): 33–51.

Hollander, D.A., Von Walter, M., Wirtz, T., Sellei, R., Schmidt-Rohlfing, B., Paar, O. & Erli, H.-J. 2006. Structural, mechanical and in vitro characterization of individually structured Ti-6Al-4V produced by direct laser forming. *Biomaterials*. 27(7): 955–963.

Hornick, J. 2016. *How Patents Die: Expiring 3D Printing Patents*. [Online], Available: https://www.finnegan.com/en/insights/articles/how-patents-die-expiring-3d-printing-patents.html [2020, October 12].

Hu, S.J. 2013. Evolving Paradigms of Manufacturing: From Mass Production to Mass Customization and Personalization. In *Procedia CIRP*. Vol. 7. Elsevier B.V. 3–8.

Huang, Q., Liu, X., Yang, X., Zhang, R., Shen, Z. & Feng, Q. 2015. Specific heat treatment of selective laser melted Ti–6Al–4V for biomedical applications. *Frontiers of Materials Science*. 9(4): 373–381.

International Monetary Fund. 2018. *World Economic Outlook Database - Groups and Aggregates Information*. [Online], Available: https://www.imf.org/external/pubs/ft/weo/2018/02/weodata/groups.htm [2020, November 16].

International Monetary Fund. 2020. *World Economic Outlook Update: June 2020 - A Crisis Like No Other, An Uncertain Recovery*.

InvestSA. 2020. *Invest in South Africa*. [Online], Available: http://www.investsa.gov.za/whysouthafrica/ [2020, November 16].

Ivasishin, O.M. & Teliovich, R. V. 1999. Potential of rapid heat treatment of titanium alloys and steels. *Materials Science and Engineering: A*. 263(2): 142–154.

Ivasishin, O.M., Semiatin, S.L., Markovsky, P.E., Shevchenko, S. V. & Ulshin, S. V. 2002. Grain growth and texture evolution in Ti-6Al-4V during beta annealing under continuous heating conditions. *Materials Science and Engineering A*. 337(1–2): 88–96.

Jahan, S.A. & El-Mounayri, H. 2016. Optimal Conformal Cooling Channels in 3D Printed Dies for Plastic Injection Molding. *Procedia Manufacturing*. 5: 888–900.

Ji, Y., Heo, T.W., Zhang, F. & Chen, L.-Q. 2016. Theoretical Assessment on the Phase Transformation Kinetic Pathways of Multi-component Ti Alloys: Application to Ti-6Al-4V. *Journal of Phase Equilibria and Diffusion*. 37(1): 53–64.

Jia, G. 2016. The Effect of Oxygen Content on the Tensile Properties of SLMed Ti6Al4V alloy. Monash University.

Kahlin, M., Ansell, H. & Moverare, J.J. 2017. Fatigue behaviour of additive manufactured Ti6Al4V, with as-built surfaces, exposed to variable amplitude loading. *International Journal of Fatigue*. 103: 353–362.

Karkina, L.E. & Yakovenkova, L.I. 2012. Dislocation core structure and deformation behavior of Ti 3 Al. *Modelling and Simulation in Materials Science and Engineering*. 20(6): 065003.

Kasperovich, G. & Hausmann, J. 2015. Improvement of fatigue resistance and ductility of TiAl6V4 processed by selective laser melting. *Journal of Materials Processing Technology*. 220: 202–214.

Kasperovich, G., Haubrich, J., Gussone, J. & Requena, G. 2016. Correlation between porosity and processing parameters in Ti6AlV4 produced by selective laser melting. *Materials and Design*. 105(May): 160–170.

Katzarov, I., Malinov, S. & Sha, W. 2002. Finite element modeling of the morphology of beta to alpha phase transformation in Ti-6Al-4V alloy. *Metallurgical and Materials Transactions a-Physical Metallurgy and Materials Science*. 33(4): 1027–1040.

Kazantseva, N., Krakhmalev, P., Thuvander, M., Yadroitsev, I., Vinogradova, N. & Ezhov, I. 2018. Martensitic transformations in Ti-6Al-4V (ELI) alloy manufactured by 3D Printing. *Materials Characterization*. 146(September): 101–112.

Kelly, S.M. 2004. Thermal and Microstructure Modeling of Metal Deposition Processes with Application to Ti-6Al-4V. State University. [Online], Available: https://theses.lib.vt.edu/theses/available/etd-11242004-211009/.

Kempen, K., Thijs, L., Vrancken, B., Buls, S., Van Humbeeck, J. & Kruth, J.-P. 2013. Lowering thermal gradients in selective laser melting by pre-heating the baseplate. In *Solid Freeform Fabrication Symposium Proceedings*. [Online], Available: https://lirias.kuleuven.be/retrieve/233232 [2019, January 25].

KERN & SOHN GmbH. 2020. *Analytical balance ABT*. [Online], Available: https://www.kern-sohn.com/shop/en/laboratory-balances/analytical-balances/ABT/ [2020, June 12].

Khorasani, A.M., Gibson, I., Goldberg, M. & Littlefair, G. 2017. On the role of different annealing heat treatments on mechanical properties and microstructure of selective laser melted and conventional wrought Ti-6Al-4V. *Rapid Prototyping Journal*. 23(2): 295–304.

Klostermann, J.A. 1972. The concept of the habit plane and the phenomenological theories of the martensite transformation. *Journal of The Less-Common Metals*. 28(1): 75–94.

Knowles, C. 2012. Residual Stress Measurement and Structural Integrity Evaluation of SLM Ti-6Al-4V. Univesity of Cape Town.

Kobryn, P.. & Semiatin, S.. 2003. Microstructure and texture evolution during solidification processing of Ti–6Al–4V. *Journal of Materials Processing Technology*. 135(2–3): 330–339.

Kok, Y., Tan, X.P.P., Wang, P., Nai, M.L.S.L.S., Loh, N.H.H., Liu, E. & Tor, S.B.B. 2018. Anisotropy and heterogeneity of microstructure and mechanical properties in metal additive manufacturing: A critical review. *Materials & Design*. 139: 565–586.

Krakhmalev, P., Fredriksson, G., Yadroitsava, I., Kazantseva, N., Plessis, A. du & Yadroitsev, I. 2016. Deformation Behavior and Microstructure of Ti6Al4V Manufactured by SLM. *Physics Procedia*. 83: 778–788.

Kruth, J., Badrossamay, M., Yasa, E., Deckers, J., Thijs, L., Van Humbeeck, J. & Humbeeck, J. Van. 2010. Part and material properties in selective laser melting of metals. In *Proceedings of the 16th International Symposium on Electromachining*. SHANGHAI JIAO TONG UNIV PRESS. [Online], Available: https://lirias.kuleuven.be/retrieve/106724 [2013, September 20].

Kumar, P. & Ramamurty, U. 2019. Microstructural optimization through heat treatment for enhancing the fracture toughness and fatigue crack growth resistance of selective laser melted Ti6Al4V alloy. *Acta Materialia*. 169: 45–59.

Kumar, P., Prakash, O. & Ramamurty, U. 2018. Micro-and meso-structures and their influence on mechanical properties of selectively laser melted Ti-6Al-4V. *Acta Materialia*. 154(May): 246–260.

Leary, M. 2020. *Design fo Additive Manufacturing*. Elsevier.

Lee, Y.T. & Welsch, G. 1990. Young's modulus and damping of Ti-6Al-4V alloy as a function of heat treatment and oxygen concentration. *Materials Science and Engineering: A*. 128(1): 77–89.

Lee, D.-G., Lee, S. & Lee, Y. 2008. Effect of precipitates on damping capacity and mechanical properties of Ti–6Al–4V alloy. *Materials Science and Engineering: A*. 486(1–2): 19–26.

Leicht, A. & Wannberg, E.O. 2015. Analyzing the Mechanical Behavior of Additive Manufactured Ti-6Al-4V Using Digital Image Correlation Analyzing the Mechanical Behavior of Additive Manufactured Ti-6Al-4V Using Digital Image Correlation. Chalmers University of Technology.

Leuders, S., Thöne, M., Riemer, A., Niendorf, T., Tröster, T., Richard, H.A. & Maier, H.J. 2013. On the mechanical behaviour of titanium alloy TiAl6V4 manufactured by selective laser melting: Fatigue resistance and crack growth performance. *International Journal of Fatigue*. 48(1): 300–307.

Leuders, S., Lieneke, T., Lammers, S., Tröster, T. & Niendorf, T. 2014. On the fatigue properties of metals manufactured by selective laser melting – The role of ductility. *Journal of Materials Research*. 29(17): 1911–1919.

Leutenecker, B., Klahn, C. & Meboldt, M. 2015. Indicators And Design Stratagies For Direct Part Production By Additive Manufacturing. In *International conference on engineering design*. 1–10.

Leyens, C. & Peters, M. 2003. *Titanium and Titanium Alloys: Fundamentals and Applications*. Weinheim: Wiley. [Online], Available: http://onlinelibrary.wiley.com/book/10.1002/3527602119.

Li, P., Warner, D.H., Fatemi, A. & Phan, N. 2016. Critical assessment of the fatigue performance of additively manufactured Ti-6Al-4V and perspective for future research. *International Journal of Fatigue*. 85(December): 130–143.

Li, Z., Li, J., Zhu, Y., Tian, X. & Wang, H. 2016. Variant selection in laser melting deposited α + β titanium alloy. *Journal of Alloys and Compounds*. 661: 126–135.

Liang, Y. & Wang, H. 2015. Influence of prior-β-grain size on tensile strength of a laser-deposited α/β titanium alloy at room and elevated temperatures. *Materials Science & Engineering A*. 622: 16–20.

Liu, S. & Shin, Y.C. 2019. Additive manufacturing of Ti6Al4V alloy: A review. *Materials & Design*. 164: 107552.

Liu, R., Wang, Z., Sparks, T., Liou, F. & Newkirk, J. 2017. Aerospace applications of laser

additive manufacturing. In *Laser Additive Manufacturing*. M. Brandt, Ed. Elsevier. 351–371.

Lott, P., Schleifenbaum, H., Meiners, W., Wissenbach, K., Hinke, C. & Bültmann, J. 2011. Design of an Optical system for the In Situ Process Monitoring of Selective Laser Melting (SLM). *Physics Procedia*. 12: 683–690.

Louw, D.F. 2016. Maximising the build rate for laser powder bed fusion of Ti6Al4V with a 3 kW laser. University of Pretoria.

Louw, D.F. & Pistorius, P.G.H. 2019. The effect of scan speed and hatch distance on prior-beta grain size in laser powder bed fused Ti-6Al-4V. *The International Journal of Advanced Manufacturing Technology*. 103: 2277–2286.

Lu, S.L., Qian, M., Tang, H.P., Yan, M., Wang, J. & StJohn, D.H. 2016. Massive transformation in Ti-6Al-4V additively manufactured by selective electron beam melting. *Acta Materialia*. 104: 303–311.

Lunt, D., Busolo, T., Xu, X., Quinta da Fonseca, J. & Preuss, M. 2017. Effect of nanoscale α_2 precipitation on strain localisation in a two-phase Ti-alloy. *Acta Materialia*. 129: 72–82.

Lütjering, G. 1998. Influence of processing on microstructure and mechanical properties of ($\alpha+\beta$) titanium alloys. *Materials Science and Engineering: A*. 243(1): 32–45.

Lütjering, G. & Williams, J.C. 2007. *Titanium*. 2nd ed. (Engineering Materials, Processes). Berlin, Heidelberg: Springer Berlin Heidelberg.

Lutterotti, L., Wenk, H. & Matthies, S. 1999. MAUD (Material Analysis Using Diffraction): a user friendly Java program for Rietveld Texture Analysis and more. In *Proceeding of the Twelfth International Conference on Textures of Materials*. Vol. 2. Montreal, Canada: NRC Research Press. 1599–1604. [Online], Available: https://iris.unitn.it/handle/11572/57067#.XL7Zoej7TIU [2019, April 23].

Maitland, T. & Sitzman, S. 2007. Electron Backscatter Diffraction (EBSD) Technique and Materials Characterization Examples. In *Scanning Microscopy for Nanotechnology - Techniques and Materials Characterization Examples*. W. Zhou & Z.. Wang, Eds. Springer. 41–76.

Marshall, G.J., Young, W.J., Thompson, S.M., Shamsaei, N., Daniewicz, S.R. & Shao, S. 2016. Understanding the Microstructure Formation of Ti-6Al-4V During Direct Laser Deposition via In-Situ Thermal Monitoring. *JOM*. 68(3): 778–790.

Martin, J.D. & Raheem, Z. 2008. *User guide: 'XPowder ' A software package for powder X-ray diffraction analysis*. [Online], Available: https://www.researchgate.net/publication/331984613.

Martin, A.A., Calta, N.P., Khairallah, S.A., Wang, J., Depond, P.J., Fong, A.Y., Thampy, V.,

Guss, G.M., Kiss, A.M., Stone, K.H., Tassone, C.J., Nelson Weker, J., Toney, M.F., van Buuren, T. & Matthews, M.J. 2019. Dynamics of pore formation during laser powder bed fusion additive manufacturing. *Nature Communications*. 10(1): 1987.

Masako, N., Kaori, I. & Masahiko, A. 2016. *Features and applications of Hitachi tabletop microscope TM3030Plus*. [Online], Available: https://www.hitachi-hightech.com/file/global/pdf/sinews/technical_explanation/07071.pdf [2020, October 23].

Matsumoto, H., Yoneda, H., Sato, K., Kurosu, S., Maire, E., Fabregue, D., Konno, T.J. & Chiba, A. 2011. Room-temperature ductility of Ti–6Al–4V alloy with α′ martensite microstructure. *Materials Science and Engineering: A*. 528(3): 1512–1520.

Mayeur, J.R. & McDowell, D.L. 2007. A three-dimensional crystal plasticity model for duplex Ti–6Al–4V. *International Journal of Plasticity*. 23(9): 1457–1485.

Meiners, W., Wissenbach, K. & Gasser, A. 1996. *Patent No. DE19649865C1*. Germany. [Online], Available: https://patents.google.com/patent/DE19649865C1/en.

Mengucci, P., Santecchia, E., Gatto, A., Bassoli, E., Sola, A., Sciancalepore, C., Rutkowski, B. & Barucca, G. 2019. Solid-State Phase Transformations in Thermally Treated Ti-6Al-4V Alloy Fabricated via Laser Powder Bed Fusion. *Materials*. 12(18): 2876.

Mercelis, P. & Kruth, J. 2006. Residual stresses in selective laser sintering and selective laser melting. *Rapid Prototyping Journal*. 12(5): 254–265.

Milkert, H. 2014. *Two South African Cancer Patients Receive 3D Printed Titanium Jaw Implants*. [Online], Available: https://3dprint.com/10210/3d-printed-jaw-south-africa/ [2020, October 08].

Mishurova, T., Cabeza, S., Artzt, K., Haubrich, J., Klaus, M., Genzel, C., Requena, G. & Bruno, G. 2017. An Assessment of Subsurface Residual Stress Analysis in SLM Ti-6Al-4V. *Materials*. 10(4): 348–362.

Mishurova, T., Artzt, K., Haubrich, J., Requena, G. & Bruno, G. 2019a. New aspects about the search for the most relevant parameters optimizing SLM materials. *Additive Manufacturing*. 25: 325–334.

Mishurova, T., Artzt, K., Haubrich, J., Requena, G. & Bruno, G. 2019b. Exploring the Correlation between Subsurface Residual Stresses and Manufacturing Parameters in Laser Powder Bed Fused Ti-6Al-4V. *Metals*. 9(2): 261.

Montanari, R., Costanza, G., Tata, M.E. & Testani, C. 2008. Lattice expansion of Ti-6Al-4V by nitrogen and oxygen absorption. *Materials Characterization*. 59(3): 334–337.

Moridi, A., Demir, A.G., Caprio, L., Hart, A.J., Previtali, B. & Colosimo, B.M. 2019. Deformation and failure mechanisms of Ti–6Al–4V as built by selective laser melting.

Materials Science and Engineering: A. 768: 138456.

Motyka, M., Kubiak, K., Sieniawski, J., Waldemar, Z. & Waldemar Ziaja. 2012. Hot Plasticity of Alpha Beta Alloys. In *Titanium Alloys - Towards Achieving Enhanced Properties for Diversified Applications*. InTech. 87–116.

Murgau, C.C., Pederson, R. & Lindgren, L.E. 2012. A model for Ti–6Al–4V microstructure evolution for arbitrary temperature changes. *Modelling and Simulation in Materials Science and Engineering*. 20(5): 1–23.

Murphy, D.B., Salmon, E.D., Spring, K.R., Parry-Hill, M., Sutter, R.T. & Davidson, M.W. 2012. *Wavefront Shear in Wollaston and Nomarski Prisms*. [Online], Available: https://www.olympus-lifescience.com/en/microscope-resource/primer/java/dic/wollastonwavefronts/ [2020, December 03].

Murr, L.E., Quinones, S. a., Gaytan, S.M., Lopez, M.I., Rodela, A., Martinez, E.Y., Hernandez, D.H., Martinez, E.Y., Medina, F. & Wicker, R.B. 2009. Microstructure and mechanical behavior of Ti-6Al-4V produced by rapid-layer manufacturing, for biomedical applications. *Journal of the mechanical behavior of biomedical materials*. 2(1): 20–32.

Na, T.-W., Kim, W.R., Yang, S.-M., Kwon, O., Park, J.M., Kim, G.-H., Jung, K.-H., Lee, C.-W., Park, H.-K. & Kim, H.G. 2018. Effect of laser power on oxygen and nitrogen concentration of commercially pure titanium manufactured by selective laser melting. *Materials Characterization*. 143: 110–117.

Najmon, J.C., Raeisi, S. & Tovar, A. 2019. Review of additive manufacturing technologies and applications in the aerospace industry. In *Additive Manufacturing for the Aerospace Industry*. Elsevier Inc. 7–31.

Nalla, R.K., Boyce, B.L., Campbell, J.P., Peters, J.O. & Ritchie, R.O. 2002. Influence of microstructure on high-cycle fatigue of Ti-6Al-4V: Bimodal vs. lamellar structures. *Metallurgical and Materials Transactions A*. 33(13): 899–918.

Narayana, P.L., Lee, S., Choi, S.-W., Li, C.-L., Park, C.H., Yeom, J.-T., Reddy, N.S. & Hong, J.-K. 2019. Microstructural response of β-stabilized Ti–6Al–4V manufactured by direct energy deposition. *Journal of Alloys and Compounds*. 811: 152021.

National Planning Commission. 2020. *Digital Futures: South Africa's Digital Readiness for the Fourth Industrial Revolution*. [Online], Available: https://www.ellipsis.co.za/wp-content/uploads/2020/07/Digital-Futures-SAs-readiness-for-the-Fourth-Industrial-Revolution-6-July-2020.pdf [2020, October 29].

Nayak, S.K., Hung, C.J., Sharma, V., Alpay, S.P., Dongare, A.M., Brindley, W.J. & Hebert, R.J. 2018. Insight into point defects and impurities in titanium from first principles. *npj Computational Materials*. 4(11).

Nervo, L., King, A., Fitzner, A., Ludwig, W. & Preuss, M. 2016. A study of deformation twinning in a titanium alloy by X-ray diffraction contrast tomography. *Acta Materialia*. 105(January): 417–428.

Niewczas, M. 2007. Chapter 75 Dislocations and Twinning in Face Centred Cubic Crystals. In *Dislocations in Solids*. Vol. 13. 263–364.

Niinomi, M. 2008. Mechanical biocompatibilities of titanium alloys for biomedical applications. *Journal of the mechanical behavior of biomedical materials*. 1(1): 30–42.

Nuclear-power.net. n.d. *Steel vs Titanium - Comparison - Pros and Cons*. [Online], Available: https://www.nuclear-power.net/nuclear-engineering/metals-what-are-metals/alloys-composition-properties-of-metal-alloys/steel-vs-titanium-comparison-pros-and-cons/ [2020, November 17].

Olympus. n.d. *Olympus GX Series*. [Online], Available: https://grimas.hu/wp-content/uploads/2018/12/GX71_51.pdf [2020, June 11].

Oosthuizen, S.J. & Swanepoel, J.J. 2018. Development status of the CSIR-Ti Process. *IOP Conference Series: Materials Science and Engineering*. 430(1).

Oxford Instruments. 2015. *EBSD Explained - From data acquisition to advanced analysis*. Oxford instruments.

Oxford Instruments. 2020. *AZtecCrystal*. [Online], Available: https://nano.oxinst.com/azteccrystal [2020, November 16].

Panesar, A., Abdi, M., Hickman, D. & Ashcroft, I. 2018. Strategies for functionally graded lattice structures derived using topology optimisation for Additive Manufacturing. *Additive Manufacturing*. 19: 81–94.

Patterson, A.L. 1939. The scherrer formula for X-ray particle size determination. *Physical Review*. 56(10): 978–982.

Paul, B., Tony, C. & Simon, J. 2006. *Bragg's Law*. [Online], Available: http://pd.chem.ucl.ac.uk/pdnn/powintro/braggs.htm [2020, October 24].

Pike, J. 2017. *Air Force Equipment Introduction*. [Online], Available: https://www.globalsecurity.org/military/world/rsa/airforce-equipment-intro.htm [2020, June 01].

Pilchak, A.L., Sargent, G.A. & Semiatin, S.L. 2018. Early Stages of Microstructure and Texture Evolution during Beta Annealing of Ti-6Al-4V. *Metallurgical and Materials Transactions A*. 49(3): 908–919.

du Plessis, A., Sperling, P., Beerlink, A., Tshabalala, L., Hoosain, S., Mathe, N. & le Roux,

S.G. 2018. Standard method for microCT-based additive manufacturing quality control 1: Porosity analysis. *MethodsX*. 5: 1102–1110.

Ponor. 2020. *Electron-matter interaction volume and various types of signal generated*. [Online], Available: https://commons.wikimedia.org/wiki/File:Electron-matter_interaction_volume_and_various_types_of_signal_generated_-_v2.svg [2020, October 23].

Porter, D.A. & Easterling, K.E. 1992. *Phase Transformations in Metals and Alloys*. 2nd Editio ed. Chapman & Hall.

du Preez, W. 2014. *Qualification of Additive Manufacturing of Ti6Al4V for Medical Implants and Aerospace Components - Proposed business plan to the Department of Science and Technology*.

Presidential Commission on the Fourth Industrial Revolution. 2020. *Summary Report & Recommendations*. [Online], Available: https://www.ellipsis.co.za/wp-content/uploads/2020/10/201023-Report-of-the-Presidential-Commission-on-the-Fourth-Industrial-Revolution.pdf [2020, October 29].

Prevéy, P.S.. & Hornbach, D.J. 2019. X-Ray Diffraction Residual-Stress Techniques. In *Materials Characterization*. Vol. 10. ASM International. 440–458.

Prince, J.D. 2014. 3D Printing: An Industrial Revolution. *Journal of Electronic Resources in Medical Libraries*. 11(1): 39–45.

Pushilina, N., Panin, A., Syrtanov, M., Kashkarov, E., Kudiiarov, V., Perevalova, O., Laptev, R., Lider, A., Koptyug, A., Pushilina, N., Panin, A., Syrtanov, M., Kashkarov, E., Kudiiarov, V., Perevalova, O., Laptev, R., Lider, A. & Koptyug, A. 2018. Hydrogen-Induced Phase Transformation and Microstructure Evolution for Ti-6Al-4V Parts Produced by Electron Beam Melting. *Metals*. 8(5): 301.

Qiu, C., Adkins, N.J.E. & Attallah, M.M. 2013. Microstructure and tensile properties of selectively laser-melted and of HIPed laser-melted Ti-6Al-4V. *Materials Science and Engineering A*. 578: 230–239.

Radchenko, T.M., Tatarenko, V.A. & Zapolsky, H. 2008. Statistical Thermodynamics and Ordering Kinetics of $D0_{19}$-Type Phase: Application of the Models for H.C.P.-Ti–Al Alloy. *Solid State Phenomena*. 138: 283–302.

Radecka, A., Bagot, P.A.J.J., Martin, T.L., Coakley, J., Vorontsov, V.A., Moody, M.P., Ishii, H., Rugg, D. & Dye, D. 2016. The formation of ordered clusters in Ti-7Al and Ti-6Al-4V. *Acta Materialia*. 112: 141–149.

Rafi, H.K., Karthik, N. V., Gong, H., Starr, T.L. & Stucker, B.E. 2013. Microstructures and Mechanical Properties of Ti6Al4V Parts Fabricated by Selective Laser Melting and Electron

Beam Melting. *Journal of Materials Engineering and Performance*. 22(12): 3872–3883.

Ramaswamy, V., Schwarzkopf, M.D., Randel, W.J., Santer, B.D., Soden, B.J. & Stenchikov, G.L. 2006. Anthropogenic and natural influences in the evolution of lower stratospheric cooling. *Science*. 311(5764): 1138–1141.

Ramosena, L., Parker, B., Dzogbewu, T., Du Preez, W. & Blaine, D. 2019. Optimum Process Parameters for Dmls in-Situ Alloying of a Ti-10(60Al40V) Powder Blend. In *RAPDASA 2019 Conference Proceedings*. Vol. 10. 78–93.

Ren, S., Chen, Y., Liu, T. & Qu, X. 2019. Effect of Build Orientation on Mechanical Properties and Microstructure of Ti-6Al-4V Manufactured by Selective Laser Melting. *Metallurgical and Materials Transactions A: Physical Metallurgy and Materials Science*. 50(9): 4388–4409.

Robinson, J.M., Van Brussel, B.A., De Hosson, J.T.M. & Reed, R.C. 1996. X-ray measurement of residual stresses in laser surface melted Ti-6Al-4V alloy. *Materials Science and Engineering*. 208: 143–147.

Roehling, T.T., Wu, S.S.Q., Khairallah, S.A., Roehling, J.D., Soezeri, S.S., Crumb, M.F. & Matthews, M.J. 2017. Modulating laser intensity profile ellipticity for microstructural control during metal additive manufacturing. *Acta Materialia*. 128: 197–206.

Rokita, P.S. 2017. Socio-economic and Techno-economic Factors Associated with Establishing a Titanium Machining Industry in South Africa, a Qualitative Study. Stellenbosch University. [Online], Available: http://hdl.handle.net/10019.1/101293.

Roskil. 2013. *Titanium Metal: Market Outlook to 2018*. London.

Rubenchik, A.M., King, W.E. & Wu, S.S. 2018. Scaling laws for the additive manufacturing. *Journal of Materials Processing Technology*. 257(October): 234–243.

Rycroft, M. 2016. *Induction heating applications in the metals industry*. [Online], Available: https://www.ee.co.za/article/induction-heating-applications-metals-industry.html [2020, November 17].

SAE International. 2014. AMSH81200D - Heat Treatment of Titanium and Titanium Alloys.

Sallica-Leva, E., Caram, R., Jardini, A.L. & Fogagnolo, J.B. 2016. Ductility improvement due to martensite a' decomposition in porous Ti-6Al-4V parts produced by selective laser melting for orthopedic implants. *Journal of the Mechanical Behavior of Biomedical Materials*. 54: 149–158.

Sames, W.J., List, F.A., Pannala, S., Dehoff, R.R. & Babu, S.S. 2016. The metallurgy and processing science of metal additive manufacturing. *International Materials Reviews*. 61(5): 315–360.

Sandala, R.S. 2012. Deformation Mechanisms of Two-Phase Titanium Alloys. The University of Manchester.

Santer, B.D., Taylor, K.E., Wigley, T.M.L., Johns, T.C., Jones, P.D., Karoly, D.J., Mitchell, J.F.B., Oort, A.H., Penner, J.E., Ramaswamy, V., Schwarzkopf, M.D., Stouffer, R.J. & Tett, S. 1996. A search for human influences on the thermal structure of the atmosphere. *Nature*. 382(6586): 39–46.

Sargent, G.A., Kinsel, K.T., Pilchak, A.L., Salem, A.A. & Semiatin, S.L. 2012. Variant selection during cooling after beta annealing of Ti-6Al-4V ingot material. *Metallurgical and Materials Transactions A: Physical Metallurgy and Materials Science*. 43(10): 3570–3585.

Saunders, S. 2018. *GE Reports Looks to The Future While Celebrating 10th Anniversary of First 3D Printed Hip Implant*. [Online], Available: https://3dprint.com/206019/ge-reports-3d-printed-hip-implant/ [2020, October 14].

Schematix. 2020. *How to: 1.4kW Induction Heater*. [Online], Available: https://www.schematix.co.nz/forum/how-to-s/1-4kw-induction-heater [2020, November 17].

Scholtz, L. 2013. *The SADF in the Border War 1966-1989*. Cape Town: Tafelberg.

Seifi, M., Salem, A., Beuth, J., Harrysson, O. & Lewandowski, J.J. 2016. Overview of Materials Qualification Needs for Metal Additive Manufacturing. *JOM*. 68(3): 747–764.

Seifi, M., Salem, A., Satko, D., Shaffer, J. & Lewandowski, J.J. 2017. Defect distribution and microstructure heterogeneity effects on fracture resistance and fatigue behavior of EBM Ti–6Al–4V. *International Journal of Fatigue*. 94: 263–287.

Semiatin, S.L., Knisley, S.L., Fagin, P.N., Barker, D.R. & Zhang, F. 2003. Microstructure evolution during alpha-beta heat treatment of Ti-6Al-4V. *Metallurgical and Materials Transactions A*. 34(10): 2377–2386.

Serwale, M.R., Coetsee, T. & Fazluddin, S. 2020. Purification of crude titanium powder produced by metallothermic reduction by acid leaching. *Journal of the Southern African Institute of Mining and Metallurgy*. 120(5): 349–354.

Seshacharyulu, T., Medeiros, S.., Morgan, J.., Malas, J.., Frazier, W.. & Prasad, Y.V.R.. 2000. Hot deformation and microstructural damage mechanisms in extra-low interstitial (ELI) grade Ti–6Al–4V. *Materials Science and Engineering: A*. 279(1–2): 289–299.

Sha, W. & Malinov, S. 2009. *Titanium alloys: modelling of microstructure, properties and applications*. CRC Press.

Shahrubudin, N., Lee, T.C. & Ramlan, R. 2019. An Overview on 3D Printing Technology: Technological, Materials, and Applications. *Procedia Manufacturing*. 35: 1286–1296.

Shi, R., Khairallah, S.A., Roehling, T.T., Heo, T.W., McKeown, J.T. & Matthews, M.J. 2020. Microstructural control in metal laser powder bed fusion additive manufacturing using laser beam shaping strategy. *Acta Materialia*. 184: 284–305.

Shunmugavel, M., Polishetty, A. & Littlefair, G. 2015. Microstructure and Mechanical Properties of Wrought and Additive Manufactured Ti-6Al-4V Cylindrical Bars. *Procedia Technology*. 20(July): 231–236.

Siemens. 2018. *Additive Manufacturing: Siemens uses innovative technology to produce gas turbines*. [Online], Available: https://press.siemens.com/global/en/feature/additive-manufacturing-siemens-uses-innovative-technology-produce-gas-turbines [2019, August 08].

Simonelli, M. 2014. Microstructure and mechanical properties of Selective Laser Melted. Loughborough University. [Online], Available: https://dspace.lboro.ac.uk/2134/15070.

Simonelli, M., Tse, Y.Y. & Tuck, C. 2014a. Effect of the build orientation on the mechanical properties and fracture modes of SLM Ti–6Al–4V. *Materials Science and Engineering: A*. 616: 1–11.

Simonelli, M., Tse, Y.Y. & Tuck, C. 2014b. On the texture formation of selective laser melted Ti-6Al-4V. *Metallurgical and Materials Transactions A: Physical Metallurgy and Materials Science*. 45(6): 2863–2872.

Skapinyecz, R., Illés, B. & Bányai, Á. 2018. Logistic aspects of Industry 4.0. *IOP Conference Series: Materials Science and Engineering*. 448(1): 012014.

Smith, W.F. & Hashemi, J. 2006. *Foundations of Materials Science and Engineering*. 4th ed ed. McGraw-Hill.

Smolyanov, I., Sarapulov, F. & Sarapulov, S. 2019. Induction Heating Control of Titanium Alloys. In *2019 XXI International Conference Complex Systems: Control and Modeling Problems (CSCMP)*. IEEE. 252–256.

Smolyanov, I.A., Kotlan, V. & Doležel, I. 2020. Optimal heat induction treatment of titanium alloys. *COMPEL - The International Journal for Computation and Mathematics in Electrical and Electronic Engineering*. 39(1): 53–65.

Soundararajan Rajan, S., Vishnu, J., Manivasagam, G. & Rao Muktinutalapati, N. 2020. Heat Treatment of Metastable Beta Titanium Alloys. In *Welding*. IntechOpen.

Spittle, J.A. 2006. Columnar to equiaxed grain transition in as solidified alloys. *International Materials Reviews*. 51(4): 247–269.

Stamp, R., Fox, P., O'Neill, W., Jones, E. & Sutcliffe, C. 2009. The development of a scanning strategy for the manufacture of porous biomaterials by selective laser melting. *Journal of Materials Science: Materials in Medicine*. 20(9): 1839–1848.

Stockholm International Peace Research Institute. 2020. *UN arms embargo on South Africa*. [Online], Available: https://www.sipri.org/databases/embargoes/un_arms_embargoes/south_africa/un-arms-embargo-on-south-africa [2020, June 01].

Stratview Research. 2020. *Aerospace Prepreg Market Size, Share, Trend, Forecast, & Competitive Analysis: 2020-2025*. [Online], Available: https://www.prnewswire.com/news-releases/aerospace-3d-printing-market-size-to-reach-us-6-7-billion-in-2027--says-stratview-research-300984367.html [2020, October 14].

Sun, P., Fang, Z.Z., Zhang, Y. & Xia, Y. 2017. Review of the Methods for Production of Spherical Ti and Ti Alloy Powder. *JOM*. 69(10): 1853–1860.

Suresh, S. & Giannakopoulos, A.E. 1998. A new method for estimating residual stresses by instrumented sharp indentation. *Acta Materialia*. 46(16): 5755–5767.

Svelto, O. 2010. *Principles of Lasers*. Boston, MA: Springer US.

Tammas-Williams, S., Zhao, H., Léonard, F., Derguti, F., Todd, I. & Prangnell, P.B. 2015. XCT analysis of the influence of melt strategies on defect population in Ti–6Al–4V components manufactured by Selective Electron Beam Melting. *Materials Characterization*. 102: 47–61.

Tammas-Williams, S., Withers, P.J., Todd, I. & Prangnell, P.B. 2016. Porosity regrowth during heat treatment of hot isostatically pressed additively manufactured titanium components. *Scripta Materialia*. 122: 72–76.

Tan, X., Kok, Y., Tan, Y.J., Descoins, M., Mangelinck, D., Tor, S.B., Leong, K.F. & Chua, C.K. 2015. Graded microstructure and mechanical properties of additive manufactured Ti–6Al–4V via electron beam melting. *Acta Materialia*. 97: 1–16.

Tan, X., Kok, Y., Toh, W.Q., Tan, Y.J., Descoins, M., Mangelinck, D., Tor, S.B., Leong, K.F. & Chua, C.K. 2016. Revealing martensitic transformation and α/β interface evolution in electron beam melting three-dimensional-printed Ti-6Al-4V. *Scientific Reports*. 6(April): 26039.

The Department of Trade and Industry. 2014. *Industrial Policy Action Plan 2014/15 - 2016/17*. [Online], Available: http://www.thedti.gov.za/DownloadFileAction?id=851.

Thejane, K., Chikosha, S. & du Preez, W.B. 2016. Characterisation of Ti6Al4V (ELI) Powder Used by the South African Collaborative Program in Additive Manufacturing. In *RAPDASA 2016 Conference Proceedings*.

Thijs, L. 2014. Microstructure and texture of metal parts produced by Selective Laser Melting. KU Leuven.

Thijs, L., Verhaeghe, F. & Craeghs, T. 2010. A study of the microstructural evolution during

selective laser melting of Ti–6Al–4V. *Acta Materialia*. 58(9): 3303–3312.

Thijs, L., Montero Sistiaga, M.L., Wauthle, R., Xie, Q., Kruth, J.-P. & Van Humbeeck, J. 2013. Strong morphological and crystallographic texture and resulting yield strength anisotropy in selective laser melted tantalum. *Acta Materialia*. 61(12): 4657–4668.

Thomas, M., Baxter, G.J. & Todd, I. 2016. Normalised model-based processing diagrams for additive layer manufacture of engineering alloys. *Acta Materialia*. 108: 26–35.

Thompson, M.K., Moroni, G., Vaneker, T., Fadel, G., Campbell, R.I., Gibson, I., Bernard, A., Schulz, J., Graf, P., Ahuja, B. & Martina, F. 2016. Design for Additive Manufacturing: Trends, opportunities, considerations, and constraints. *CIRP Annals*. 65(2): 737–760.

Tromans, D. 2011. Elastic Anistropy Of HCP Metal Crystals And Polycrystals. *International Journal of Research and Reviews in Applied Sciences*. 6(4): 463–483. [Online], Available: http://www.arpapress.com/volumes/vol6issue4/ijrras_6_4_14.pdf [2016, October 17].

U.S. Geological Servey. 2018. *Mineral Commodity Summaries*. Reston, Virginia.

Unruh, D.K. & Forbes, T.Z. 2019. X-ray Diffraction Techniques. In *Analytical Geomicrobiology*. Cambridge University Press. 215–237.

US Geological Survey. 2020. *Mineral Commodity Summaries 2020*. [Online], Available: https://doi.org/10.3133/ mcs2020.

Vasinonta, A., Beuth, J. & Griffith, M. 2000. Process Maps for Controlling Residual Stress and Melt Pool Size in Laser-Based SFF Processes. In *International Solid Freeform Fabrication Symposium*.

Venter, A.M., van Heerden, P.R., Marais, D. & Raaths, J.C. 2018. MPISI: The neutron strain scanner materials probe for internal strain investigations at the SAFARI-1 research reactor. *Physica B: Condensed Matter*. 551: 417–421.

Vilardell, A.M., Krakhmalev, P., Fredriksson, G., Cabanettes, F., Sova, A., Valentin, D. & Bertrand, P. 2018. Influence of surface topography on fatigue behavior of Ti6Al4V alloy by laser powder bed fusion. *Procedia CIRP*. 74: 49–52.

Vilaro, T., Colin, C. & Bartout, J.D. 2011. As-fabricated and heat-treated microstructures of the Ti-6Al-4V alloy processed by selective laser melting. *Metallurgical and Materials Transactions A: Physical Metallurgy and Materials Science*. 42(10): 3190–3199.

Vrancken, B. 2016. Study of Residual Stresses in Selective Laser Melting. KU Leuven.

Vrancken, B., Thijs, L., Kruth, J.-P. & Van Humbeeck, J. 2012. Heat treatment of Ti6Al4V produced by Selective Laser Melting: Microstructure and mechanical properties. *Journal of Alloys and Compounds*. 541: 177–185.

Vrancken, B., Cain, V., Knutsen, R. & Van Humbeeck, J. 2014. Residual stress via the contour method in compact tension specimens produced via selective laser melting. *Scripta Materialia*. 87: 29–32.

Vrancken, B., Buls, S., Kruth, J.-P. & Van Humbeeck, J. 2015. Influence of preheating and oxygen content on Selective Laser Melting of Ti6Al4V. *Proceedings of the 16th RAPDASA Conference*.

van Vuuren, D.S. 2009. Keynote address : Titanium — an opportunity and challenge for South Africa. In *The 7th International Heavy Minerals Conference*. The Southern African Institute of Mining and Metallurgy. 1–8. [Online], Available: https://www.saimm.co.za/Conferences/HMC2009/001-007_vanVuuren.pdf.

Wang, D., Shi, R., Zheng, Y., Banerjee, R., Fraser, H.L. & Wang, Y. 2014. Integrated Computational Materials Engineering (ICME) Approach to Design of Novel Microstructures for Ti-Alloys. *JOM*. 66(7): 1287–1298.

Wang, S.C., Aindow, M. & Starink, M.J. 2003. Effect of self-accommodation on α/α boundary populations in pure titanium. *Acta Materialia*. 51(9): 2485–2503.

Wang, S.C., Starink, M.J., Ubhi, H.S. & Li, W.S. 2012. Identification of transformed grain boundaries and reconstruction of the prior grains from EBSD data in pure Ti and α-Ti alloys. *Reviews on Advanced Materials Science*. 32(1): 47–51.

Washington, M.N. 2018. Investigation on upscaling selective laser meling process parameters using 17-4PH stainless streel powder. Central University of Technology.

Waziers, S., Roy, S., Suwas, S., Tamirisakandala, S., Srinivasan, R. & Miracle, D. 2009. Solidification Microstructure and Texture in Grain-Refined Titanium Alloys. *Microstructure and Texture in Steels*. 475–482. [Online], Available: http://www.springerlink.com/index/h207u72145l2144n.pdf.

Weiss, I. & Semiatin, S.L. 1999. Thermomechanical processing of alpha titanium alloys - an overview. *Materials Science and Engineering: A*. 263: 243–256.

Welsch, G., Lütjering, G., Gazioglu, K. & Bunk, W. 1977. Deformation characteristics of age hardened Ti-6Al-4V. *Metallurgical Transactions A*. 8(1): 169–177.

Williamson, G.K. & Smallman, R.E. 1956. III. Dislocation densities in some annealed and cold-worked metals from measurements on the X-ray debye-scherrer spectrum. *Philosophical Magazine*. 1(1): 34–46.

Wohlers, T. & Gornet, T. 2014. History of additive manufacturing. In *Wohlers Report 2014*. 1–34.

Wohlers Associates. 2013. *Wohlers Report 2013*.

Wohlers Associates. 2018. *Wohlers Report 2018*.

Wohlers Associates. 2019. *Wohlers Report 2019*.

Wright, S.I., Nowell, M.M. & Field, D.P. 2011. A review of strain analysis using electron backscatter diffraction. *Microscopy and microanalysis : the official journal of Microscopy Society of America, Microbeam Analysis Society, Microscopical Society of Canada*. 17: 316–329.

Xu, W., Brandt, M., Sun, S., Elambasseril, J., Liu, Q., Latham, K., Xia, K. & Qian, M. 2015. Additive manufacturing of strong and ductile Ti–6Al–4V by selective laser melting via in situ martensite decomposition. *Acta Materialia*. 85(November): 74–84.

Xu, W., Sun, S., Elambasseril, J., Liu, Q., Brandt, M. & Qian, M. 2015. Ti-6Al-4V Additively Manufactured by Selective Laser Melting with Superior Mechanical Properties. *JOM*. 67(3): 668–673.

Xu, W., Lui, E.W., Pateras, A., Qian, M. & Brandt, M. 2017. In situ tailoring microstructure in additively manufactured Ti-6Al-4V for superior mechanical performance. *Acta Materialia*. 125: 390–400.

Xu, Z.W., Liu, A. & Wang, X.S. 2019. The influence of building direction on the fatigue crack propagation behavior of Ti6Al4V alloy produced by selective laser melting. *Materials Science and Engineering: A*. 767(August): 138409.

Yadroitsev, I., Krakhmalev, P. & Yadroitsava, I. 2014. Selective laser melting of Ti6Al4V alloy for biomedical applications: Temperature monitoring and microstructural evolution. *Journal of Alloys and Compounds*. 583: 404–409.

Yager, T.R. 2015. *The Mineral Industry of South Africa [Advanced release]*. [Online], Available: https://prd-wret.s3-us-west-2.amazonaws.com/assets/palladium/production/atoms/files/myb3-2015-sf.pdf.

Yan, M. & Yu, P. 2015. Chapter 5 - An Overview of Densification, Microstructure and Mechanical Property of Additively Manufactured Ti-6Al-4V — Comparison among Selective Laser Melting, Electron Beam Melting, Laser Metal Deposition and Selective Laser Sintering, and with Convent. In *Sintering Techniques of Materials*. A. Lakshmanan, Ed. InTech. 76–106.

Yan, R., Luo, D., Huang, H., Li, R., Yu, N., Liu, C., Hu, M. & Rong, Q. 2018. Electron beam melting in the fabrication of three-dimensional mesh titanium mandibular prosthesis scaffold. *Scientific Reports*. 8(1): 1–10.

Yang, F., Chen, C., Zhou, Q., Gong, Y., Li, R., Li, C., Klämpfl, F., Freund, S., Wu, X., Sun, Y., Li, X., Schmidt, M., Ma, D. & Yu, Y. 2017. Laser beam melting 3D printing of Ti6Al4V based porous structured dental implants: fabrication, biocompatibility analysis and photoelastic study. *Scientific Reports*. 7(1): 45360.

Yang, J., Yu, H., Yin, J., Gao, M., Wang, Z. & Zeng, X. 2016. Formation and control of martensite in Ti-6Al-4V alloy produced by selective laser melting. *Materials & Design*. 108: 308–318.

Yang, J., Han, J., Yu, H., Yin, J., Gao, M., Wang, Z. & Zeng, X. 2016. Role of molten pool mode on formability, microstructure and mechanical properties of selective laser melted Ti-6Al-4V alloy. *Materials and Design*. 110: 558–570.

Zeng, L. & Bieler, T.R. 2005. Effects of working, heat treatment, and aging on microstructural evolution and crystallographic texture of α, α', α'' and β phases in Ti-6Al-4V wire. *Materials Science and Engineering A*. 392(1–2): 403–414.

Zhang, J. & Li, D. 2003. Preferred precipitation of ordered α2 phase at dislocations and boundaries in near-α titanium alloys. *Materials Science and Engineering A*. 341(1–2): 229–235.

Zhang, L.C. & Liu, Y. 2018. Additive manufacturing of titanium alloys for biomedical applications. *Additive Manufacturing of Emerging Materials*. (January): 179–196.

Zhang, D., Qiu, D., Gibson, M.A., Zheng, Y., Fraser, H.L., StJohn, D.H. & Easton, M.A. 2019. Additive manufacturing of ultrafine-grained high-strength titanium alloys. *Nature*. 576(7785): 91–95.

Zhang, P., Li, S.X. & Zhang, Z.F. 2011. General relationship between strength and hardness. *Materials Science & Engineering A*. 529: 62–73.

Zhang, Y., Wu, L., Guo, X., Kane, S., Deng, Y., Jung, Y.-G., Lee, J.-H. & Zhang, J. 2017. Additive Manufacturing of Metallic Materials: A Review. *Journal of Materials Engineering and Performance 2017 27:1*. 27(1): 1–13.

Zhao, X., Li, S., Zhang, M., Liu, Y., Sercombe, T.B., Wang, S., Hao, Y., Yang, R. & Murr, L.E. 2016. Comparison of the microstructures and mechanical properties of Ti–6Al–4V fabricated by selective laser melting and electron beam melting. *Materials & Design*. 95: 21–31.

Zhong, H.Z., Zhang, X.Y., Wang, S.X. & Gu, J.F. 2018. Examination of the twinning activity in additively manufactured Ti-6Al-4V. *Materials and Design*. 144: 14–24.

Appendix A Additional background reading relevant to South Africa

A.1 South African military history

The initiation of locally developed and manufactured military aircraft was driven by two factors. The first factor was the Cuban intervention in Angola and the escalation of the Border War (also known as the "bush war") (1966 – 1989). For a comprehensive book on the subject see Scholtz (2013). The second factor was the increased international military sanctions due to the South African government's apartheid regime. Sanctions were largely a result of the United Nation's arms embargo on South Africa, promulgated in 1964, mandatory in 1977 (Stockholm International Peace Research Institute, 2020). These factors led to the dire need for locally manufactured military equipment leading to the founding of the Atlas Aircraft Corporation in 1965, owned by the Armaments Corporation of South Africa (ARMSCOR). Atlas manufactured military aircraft, avionics, and support equipment in support of the South African Air Force. At the peak of development, South Africa had the strongest military in Africa.

With the ending of the Border War in 1988, after South Africa signed the Tripartite Accord with Cuba and Angola, and a transition to a democratic government in 1994, military funding was drastically cut. This was due to reduced military activity, a redefinition of the role of the South African National Defence Force and a growth in social-humanitarian needs (such as education, training, and housing) (Pike, 2017).

A.2 The CSIR-powder production plant

Titanium powder has not been produced directly at commercial scale from titanium tetrachloride (TiCl4), which is the precursor for both pigment and metal production. In 2013, an experimental titanium powder production plant was commissioned by the CSIR. This plant produces 2 kg of titanium powder per hour directly by metallothermic reduction of TiCl4 in molten salt. The process invented and patented by Prof D. S. Van Vuuren and Dr S. J. Oosthuizen (titled the "CSIR-Ti Process") is a potential cost-effective alternative method for titanium metal production. Figure A.1(a) depicts the CSIR process and conventional metal production processes route for metal powder and part fabrication. The shorter production route of the CSIR-process is predicted to allow for a cost reduction in titanium powder and finished components. This is more clearly depicted in Figure A.1(b) where the estimated costs of conventional powder production and the cost of titanium powder production through the CSIR-process is depicted.

For further background to the project, process and technical challenges (2014 – 2017) see Oosthuizen & Swanepoel (2018). Research into local plasma spheroidization to refine and improve the quality of the "unique morphology" output powder has also been undertaken (Bissett *et al.*, 2015). Recent development of a purification step through acid leaching has also shown promising results (Serwale *et al.*, 2020).
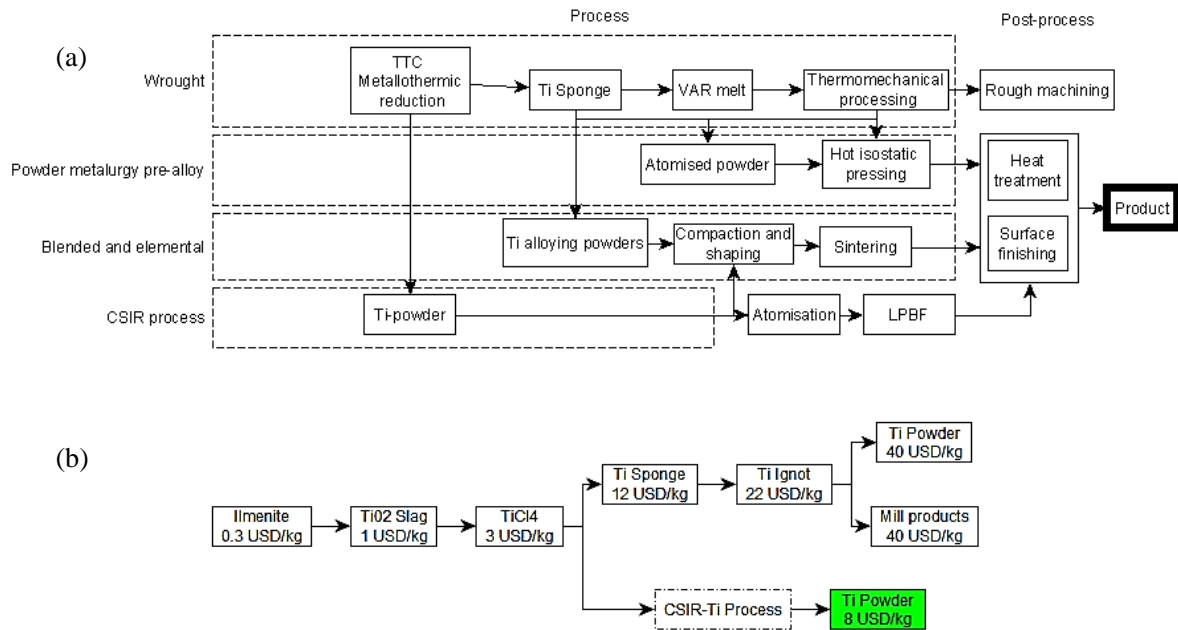
Figure A.1. (a) Ti production routes including the CSIR process (adapted from Serwale *et al.* (2020)) (b) cost analysis (in United Stated Dollar – USD) of the CSIR-Ti route versus conventional route. Conventional mineral costs (Roskil, 2013) and novel powder production cost estimation (Oosthuizen & Swanepoel, 2018).

A.3 Aeroswift project

The CSIR and Aerosud Innovation Centre, through the Aeroswift project established in 2011, developed and built one of the largest and fastest LPBF machines in the world. The machine measures a build area of 2×0.6 meter and a 0.6-meter build hight. The current utilized volume is 0.3×0.6-meter base area with 0.6 m build hight. The default laser power is 2 kW. Proof-of-concept trials indicated an achievable laser speed up to $10\times$ that of commercial machines. Preliminary process parameter optimisation with the intention of upscaling to a higher laser speed and power has been conducted by Louw (2016) and Washington (2018). Potential machine modifications were investigated by Bester, Wichers, *et al.* (2017). Ti-6Al-4V microstructural characterisation of parts building on the Aeroswift machine has also been done (Louw & Pistorius, 2019).

Commercial parts built on the Aeroswift machine include parts for the Advanced High-Performance Reconnaissance Light Aircraft (AHRLAC) (Bester, Vermeulen, *et al.*, 2017). Other projects include a topologically optimised 0.5 meter tall unmanned aerial vehicle (drone) frame build from Ti-6Al-4V (AM Chronical, 2019), depicted still on the base 0.3×0.6 m base-plate in Figure A.2.

Figure A.2. Topology-optimised drone frame built using LPBF from Ti-6Al-4V (Aeroswift South Africa, 2018)

A.4 RAPDASA

AM market development and technical research in South Africa would not have been possible without RAPDASA (a member of ASTM International Committee F42 and seat holder on the Executive Committee). Terry Wohler, principal author of the Wohlers Report is also a founding member of RAPDASA. RAPDASA holds an annual international conference (of which the 21st was held in 2020) which is a key anneal event for both industry and researchers to share latest AM research and developments. RAPDASA's conference proceedings, together with the South African Journal of Industrial Engineering, are important publication platforms for local AM related research and development.

Appendix B   Examples of metal AM application

Examples of metal AM used in the medical sciences go as far back as 2007 when the first recorded AM titanium hip cup implantation was performed (Saunders, 2018). The world's first metal AM lower jaw implant was done in the Netherlands in 2012 (British Broadcasting Corporation, 2012), followed closely by a historic moment in July 2014 when two South African patients, suffering from facial misconfigurations due to cancer, received AM-produced titanium hemi-mandible (lower jaw) implants (Milkert, 2014) (for a research example of this, see Figure B.1.) This was followed by another further sixty successful AM cases, including full- and hemi-maxilla (upper jaw) implants (Central University of Technology, 2019). These were produced by the Centre for Rapid Prototyping and Manufacturing at the Central University of Technology who received medical certification of their AM design and manufacturing process in 2016, making it the first in Africa to do so.

The application of metal AM in the biomedical industry was earlier than its application in aerospace likely due to certification of the metal AM process for aerospace (AS9100D certification) being more stringent than that for fabrication of biomedical components (ISO 13485). Recently, the Aerospace Material Specification committee on Additive Manufacturing SAE International issued the first technical standards for aerospace additive manufacturing. These include 4 standards including AMS7003 on Laser Powder Bed Fusion.
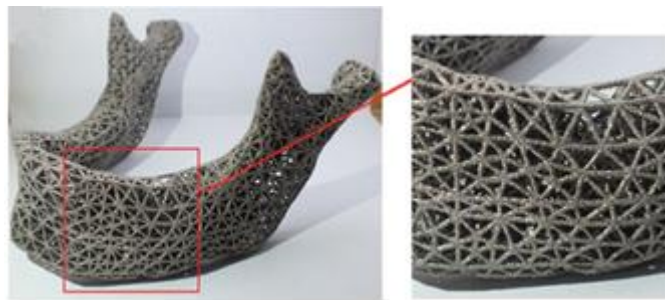
Figure B.1. Lattice-design mandibular prosthesis fabricate EBM technology (Weight: 107 g; Porosity: 81.38 %; Strut size: 0.7 mm) (Yan *et al.*, 2018).

Examples of AM application for production of functional aerospace parts have grown in recent years. A historic moment in April of 2016 marked the first jet engine (General Electric Aviation's LEAP-1A) to incorporate metal additively manufactured fuel nozzles. This reduced the number of parts from 18 to just one and the weight by 25 %. Due to intricate cooling pathways and supports, the nozzle measured a five-fold increase in durability. After only three years of production, General Electric completed its 30,000[th] fuel nozzle in 2018 show the extent of metal AM's application as a production method. Even though each engine contains 19 fuel nozzles, the company expects to meet the planned ramp-up production reaching 2,000 engines by 2020—indicating the enormous scale of production. Another example is Airbus's A350 XWB (serial production aircraft since 2017) which, in addition to more than 1 000 plastic AM

parts, boasts with 20 AM-produced titanium-alloy cabin brackets and 16 door-locking latch shafts (using a Concept Laser M2 machine). The latter part has a 10-to-1 reduction in number of parts and an integrated and improved functionality (Ernst & Young Global Limited, 2019).

Lastly, in 2015, Textron Aviation's Cessna Denali announced their first clean-sheet design turboprop in decades (the Advanced Turboprop (ATP) engine) which consists of 35 % titanium AM parts – the most of any production engine in history (GE Aviation, 2017). This design has a component reduction of 855 to 12 resulting in a 40 % weight reduction (45.4 kg) (Haria, 2018). The impact of this is an impressive 60 % cost reduction with 20 % less fuel and 10 % higher cruise power than other engines in the same class.

Appendix C Specific LPBF standards

The development of AM standardisation in areas of terminology, design, and test methods and materials and processes lead by the collaborative effort of ASTM International Committee F42 (established in 2009), the ISO technical committee 261 (established in 2011) and the National Institute of Standards and Technology, US Department of Commerce (Bae *et al.*, 2018). ASTM F42 has approved 22 AM standards as of May 2020.

Table C.1 Relevant standards.

Standard Designated code	Standard	Last Revision Date
ASTM F2924	Standard Specification for Additive Manufacturing Titanium-6 Aluminum-4 Vanadium with Powder Bed Fusion	2014
ASTM F3001	Standard Specification for Additive Manufacturing Titanium-6 Aluminum-4 Vanadium ELI (extra low interstitial) with Powder Bed Fusion	2014
ASTM F3122	Standard Guide for Evaluating Mechanical Properties of Metal Materials Made via Additive Manufacturing Processes	2014
ASTM F3301	Standard for Additive Manufacturing–Post Processing Methods–Standard Specification for Thermal Post-Processing Metal Parts Made Via Powder Bed Fusion	2018
ASTM F3302	Standard for Additive Manufacturing—Finished Part Properties—Standard Specification for Titanium Alloys via Powder Bed Fusion	2018
ASTM F3303	Standard for Additive Manufacturing—Process Characteristics and Performance: Practice for Metal Powder Bed Fusion Process to Meet Critical Applications	2018

Appendix D   Residual stress data

D.1 KU Leuven

The following raw data was obtained at KU Leuven using a Bruker D8 Advanced together with DIFFRAC.LEPTOS-7 software (refer to Subsection 5.2.4). The same samples were measured by NECSA, but no raw data was provided by them. The following two raw data sets from the as-built and 480_30 hours samples aim to show the possible non-linearity in the data and peak profiles. Similar data trends are seen in the other data sets, although due to the page restriction of the dissertation, these are not provided.

Sample: As-built

Material	H K L	Wavelength	2Theta	Poisson	Young	S1	1/2 S2	Arx
Ti6Al4V-ELI	2 1 3	Cu_Ka1	141.700	0.324	113302	-2.864E-6	1.169E-5	1.000
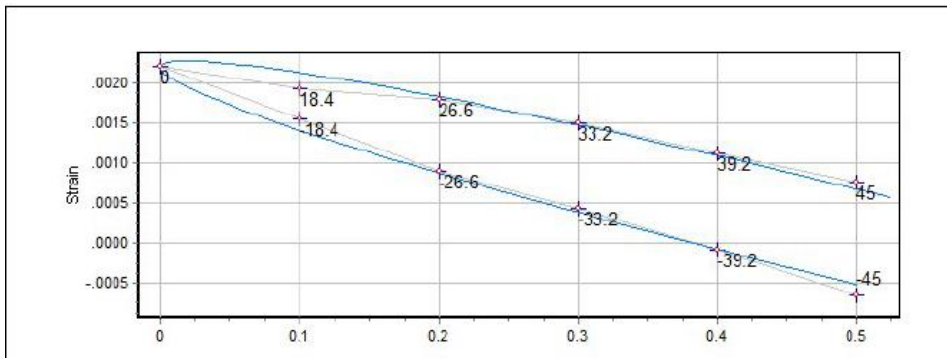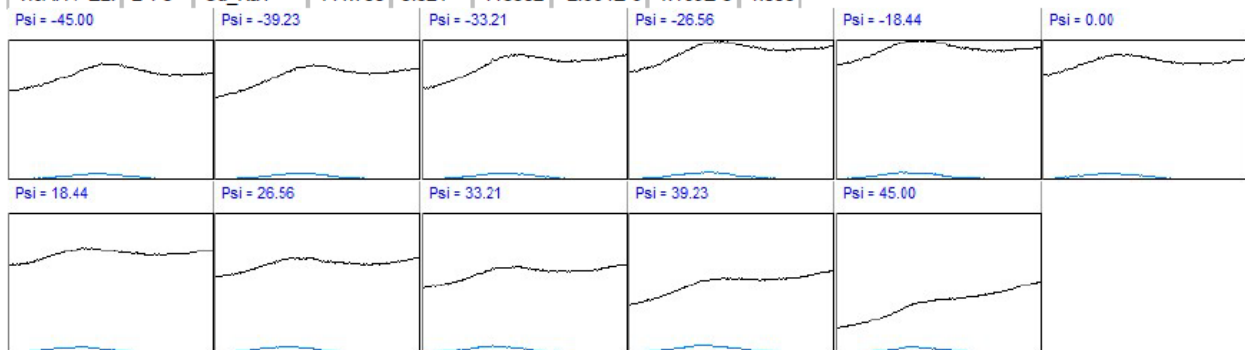
Measured:

03/21/2018 10:48:1

Peak Evaluation Method:

Sliding Gravity

(10, 20, 30, 40, 50, 60, 70, 80)

Stress Model:

Normal + Shear

Normal:

-361.6 ± 17.1

Shear:

51.2 ± 3.3

Corrections: Absorption , Background (5) , Polarisation , Smooth , K alpha 2 (0.50)

Phi: 0

Psi values: -45.00, -39.23, -33.21, -26.56, -18.44, 0.00, 18.44, 26.56, 33.21, 39.23, 45.00

138-147	0.0	-45.0	141.907
138-147	0.0	-39.2	141.720
138-147	0.0	-33.2	141.551
138-147	0.0	-26.6	141.398
138-147	0.0	-18.4	141.189
138-147	0.0	0.0	140.975
138-147	0.0	18.4	141.056
138-147	0.0	26.6	141.105
138-147	0.0	33.2	141.198
138-147	0.0	39.2	141.328
138-147	0.0	45.0	141.454

Sample: 480_30 hours

Material	H K L	Wavelength	2Theta	Poisson	Young	S1	1/2 S2	Arx
Ti6Al4V-ELI	2 1 3	Cu_Ka1	141.700	0.324	113302	-2.864E-6	1.169E-5	1.000

Psi = -45.00   Psi = -39.23   Psi = -33.21   Psi = -26.56   Psi = -18.44   Psi = 0.00

Psi = 18.44   Psi = 26.56   Psi = 33.21   Psi = 39.23   Psi = 45.00
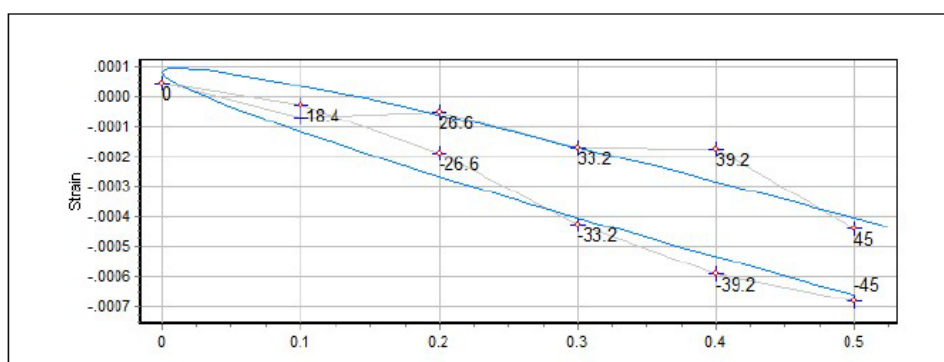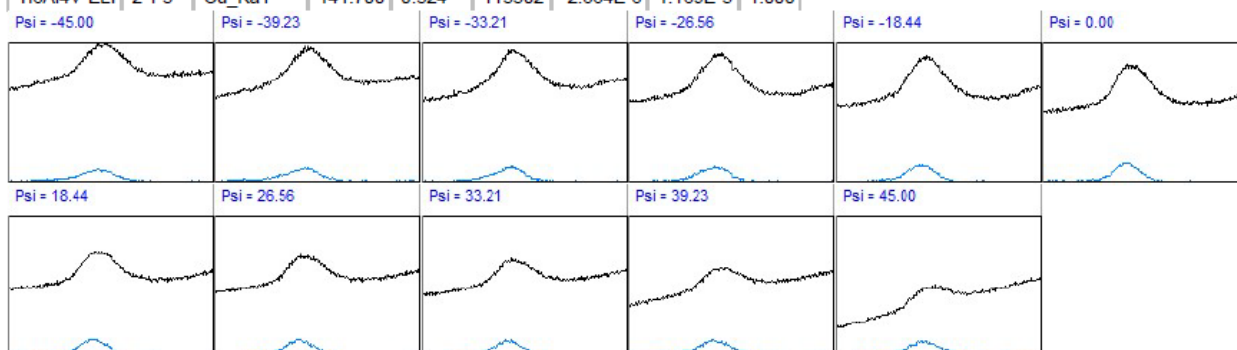
Measured:

03/21/2018 12:08:5

Peak Evaluation Method:

Sliding Gravity

(10, 20, 30, 40, 50, 60, 70, 80)

Stress Model:

Normal + Shear

Normal:

-105.4 ± 12.1

Shear:

11.0 ± 2.3

Corrections: Absorption , Background (5) , Polarisation , Smooth , K alpha 2 (0.50)

Phi: 0

Psi values: -45.00, -39.23, -33.21, -26.56, -18.44, 0.00, 18.44, 26.56, 33.21, 39.23, 45.00

138-147	0.0	-45.0	141.923
138-147	0.0	-39.2	141.893
138-147	0.0	-33.2	141.837
138-147	0.0	-26.6	141.756
138-147	0.0	-18.4	141.706
138-147	0.0	0.0	141.685
138-147	0.0	18.4	141.721
138-147	0.0	26.6	141.717
138-147	0.0	33.2	141.754
138-147	0.0	39.2	141.754
138-147	0.0	45.0	141.845

183

D.2 NECSA

The following presents the residual stress measured by NECSA. The average of measurement points 1 and 2 of each sample, Table D.1, was used to describe the residual stress presented in Chapter 5. Data for shorter hold times of 5 minutes and 1 hour for temperatures 427 and 550 °C were obtained from measurements at KU Leuven. Raw data of these follow similar trends to that of Appendix D.1 but are not included here due to the dissertation page restriction.
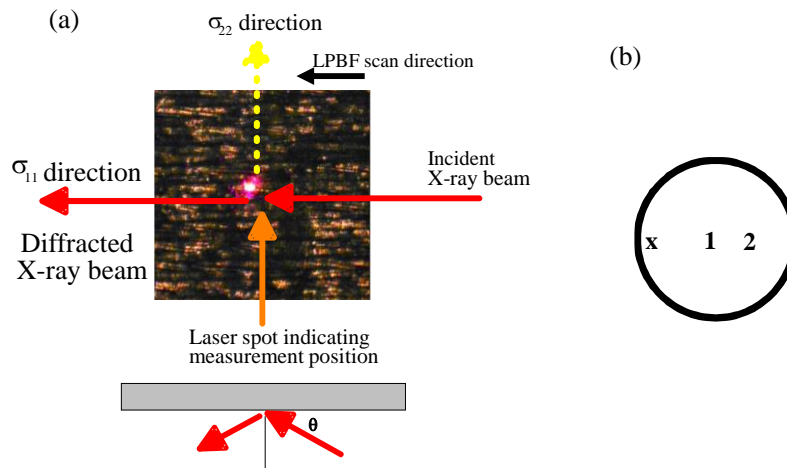
Figure D.1. NECSA report (a) Schematic diagram showing side and top views of the measurement geometry (b) 'x' corresponds to the marker made by the client with positions 1 and 2 being where stress measurements were taken (i.e., centre, and off-centre measurement points).

Table D.1. Residual stress data obtained from NECSA

Sample description	Measurement Point	Stress components [MPa]		Shear stress [MPa]	Principal stresses [MPa]		Principal stress angle [°]
		σ_{11}	σ_{22}	σ_{12}	σ_{I}	σ_{II}	θ_P
As-built	1	-541 ± 32	-507 ± 30	-173 ± 31	-350	-697	42
	2	-347 ± 38	-396 ± 36	-176 ± 37	-194	-549	-41
427_30 hours	1	-286 ± 9	-256 ± 8	31 ± 8	-236	-305	-32
	2	-224 ± 9	-244 ± 8	-4 ± 9	-224	-244	-10
480_30 hours	1	-93 ± 7	-86 ± 6	-1 ± 16	-85	-94	10
	2	-67 ± 7	-89 ± 6	7 ± 6	-64	-83	23
550_30 hours	1	102 ± 7	73 ± 7	-4 ± 8	103	73	-8
	2	60 ± 6	40 ± 5	-2 ± 6	60	40	-6
480_5 min	1	-445 ± 17	-362 ± 16	35 ± 16	-349	-458	-20
	2	-384 ± 18	-328 ± 17	76 ± 18	-275	-437	-35
480_1 hour	1	-298 ± 12	-235 ± 12	16 ± 12	-231	-302	-14
	2	-246 ± 13	-213 ± 12	21 ± 12	-203	-256	-26

Appendix E   Process time of novel build parameters

Simplified process time per sample layer (denoted t) is calculated by multiplying time per track by the number of tracks, $t = \frac{WL}{hv}$, Figure E.1.

Figure E.1. Schematic of single cubic layer.

Due to scan rotation with each layer, width and length of the sample have the same effect on total scan time of the sample and the equation can be simplified to, $t = \frac{A}{hv}$, where A is the sample layer area.
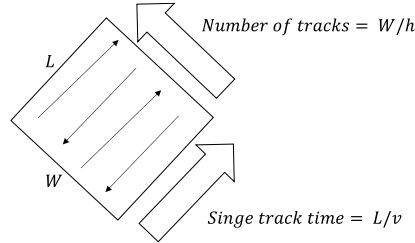
The percentage time increase of each parameter set from the default parameter set is related to the product of default-to-novel ratio of scan velocity and hatch distance. This percentage change in terms of the ratio of default to novel parameters can be derived as follows: change in layer time from default parameters layer time (t_1) to novel parameter set layer time (t_2) proportional to t_1 can be calculated as $\frac{t_2-t_1}{t_1}$. By expressing the default layer time as $t_1 = \frac{A}{h_1 v_1}$ and novel parameter layer time as $t_2 = \frac{A}{h_2 v_2}$, this becomes $\frac{h_1 v_1}{h_2 v_2} - 1$.

By substituting the novel parameters in terms of default parameters by using the ratio $h_2 = x_h h_1$ and $v_2 = x_v v_1$, the fractional time change from default to novel parameters in terms of the novel parameters to default scan parameters ratio is

$$\frac{t_2-t_1}{t_1} = \frac{1}{x_h x_v} \tag{1}$$

Interestingly, the same formula is derived for fractional change in E_v for constant P, and l. In other words, the percentage change in energy density is therefore identical to percentage change in layer time, as expected, i.e., $\frac{(E_v)_2-(E_v)_1}{(E_v)_1} = \frac{t_2-t_1}{t_1} = \frac{1}{x_h x_v}$.

Relative process time per 1 cm square area for selected process parameters are plotted in Figure E.2. Percentage time increase is plotted on novel parameter bars.
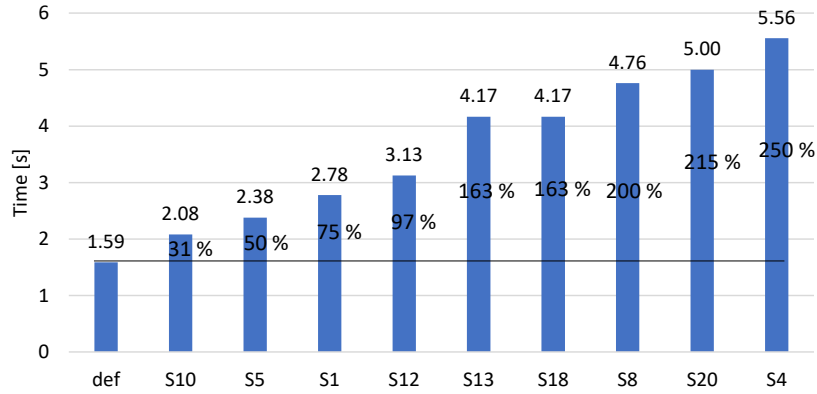
Figure E.2. Process time and percentage increase from default parameters for 1 cm^2 scan surface

An evaluation of total process time using novel parameters versus total default process time (which included a post-process heat treatment) was done. It is assumed that post-process time is independent of sample size and number of samples (batch size). This is assuming that the entire build batch can fit into the furnace volume space. Built process time, on the other hand, is dependent on these factors. In-direct time delays, such as powder layer addition, is the same for both routes and therefore cancel out. Simplified build time for a single sample can be expressed by:

$$f(A, L) = \frac{L \, A}{h \, v} \qquad (2)$$

A is the layer area, L is the number of layers, and h and v are constant values of hatch distance and scan speeds. The default process route has a constant time addition (C) which represents the total post-process time. This includes thermal treatment time, transporting and handling time.

In-situ process routes have a fixed increase from the default process time per sample, denoted as K (previously calculated as $\frac{1}{x_h x_v}$). Time functions for default process time and novel process time as a function of layer area and number of layers can therefore be expressed as (where N is the number of samples):

$$total \; time \; of \; default \; process \; route \; = \; N \left\{ f(A, L) \right\} + C \qquad (3)$$

$$total \; time \; of \; novel \; process \; route = \; N \, K \left\{ f(A, L) \right\} \qquad (4)$$

Since the novel process route time is multiplied by an additional gradient K, this would mean that for small-sized samples, the *in-situ* heating route could be shorter in total process time compared to the default route. This is highlighted by the shaded region in Figure E.3. Additional cost factors besides process time need to be considered such as the fact that post-process will add additional costs, whereas the *in-situ* route will not.
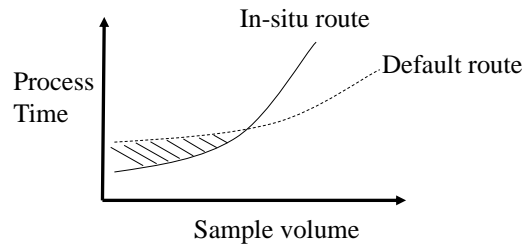
Figure E.3. Sketch-plot projecting likely *in-situ* versus post-process route process time as a function of sample size

Appendix F   Prior-β reconstruction code

MATLAB R2018a and MTEX version 5.2.beta2

```matlab
function [ebsd] = main_reconstruction()

threshold = 30; % degrees difference between parent beta phase solutions
ebsd_a = ebsd('Ti-Hex'); %store only hcp data. Use user-specific mineral
name

[grains_a,ebsd_a.grainId] =
calcGrains(ebsd_a('indexed'),'angle',15*degree);

% FILTER fine grains
grains_sel = grains_a(grains_a.grainSize > 5); %5 index points per grain
ebsd_a = ebsd_a(grains_sel);
[grains_a,ebsd_a.grainId] = calcGrains(ebsd_a('indexed'),'angle',5*degree);

% Triple Points
tP = grains_a.triplePoints('Ti-Hex','Ti-Hex','Ti-Hex');
totgrains = length(tP); %number of triple points

cs=crystalSymmetry('cubic');
ss=specimenSymmetry('triclinic');
X = [0 0 0];

% Parallel processing MAIN LOOP
parfor g=1:totgrains

    [TPgrains_id] = tP.grainId(g,:); %trip alpha ids (1x3)
    % calc beta to return sigle beta solution
    [solutionbeta,quest] = calc_beta(grains_a,TPgrains_id,threshold);

    % Question: is flag 1? (has a solution found? If yes, then continue)
    if quest=0
        [a,b,c,~] = Euler(solutionbeta,'Bunge');
        phibeta=rad2deg(a); %convert Euler angle to degree
        thetaneta=rad2deg(b);
        psibeta=rad2deg(c);

        %write solution to trip point coordinate in text file
        hoeke_pix = [phibeta,thetaneta,psibeta,tP(g).x,tP(g).y];
        dlmwrite('ebsd_file1.txt',hoeke_pix,'-append','delimiter','\t')

%%~~~~~~~~ Variant identification subroutine.~~~~~~~~~~~~~~~~~~~~~~~~~~~~~
Not necessary for reconstruction and can be commented out.
        r=rotation('Euler', phibeta*degree, thetaneta*degree,
        psibeta*degree); %Beta solution rotation (B)
        hoek = orientation(r, cs,ss); %beta solution orientation (S*B)

%X represents variants 1-12
        X(g,:) = variant_distribution (hoek, TPgrains_id,grains_a);
```

```
%store hex trip grain IDs and variant number
        sto(g,:) = [TPgrains_id,X(g,:)];
%write separate variants into separate text files
        variantSub(sto(g,:),ebsd_a);
%%~~~~~~~~~~~~~~~~~~~~~~~~~~~~~~~~~~~~~~~~~~~~~~~~~~~~~~~~~~~~~~~~~~~~~~~~~~~~~~


    end
end % end of function main_reconstruction
```

Theory in comments based on Glavicic et al. (2003)

```
function [solution, q] = calc_beta(grains,TPgrains_id,threashold)


q=0; %flag variable

%the mean orientation of each triple point alpha grain
%(1x3) euler angles in radians
var1=grains(TPgrains_id(1,1)).meanOrientation.Euler;
var2=grains(TPgrains_id(1,2)).meanOrientation.Euler;
var3=grains(TPgrains_id(1,3)).meanOrientation.Euler;


ori_1 = rotation('Euler',var1); % rotation matrix
ori_2 = rotation('Euler',var2);
ori_3 = rotation('Euler',var3);


% Indexing software uses a different specimen reference orientation
% than MTex. This means that the reference orientation of the data is out
% by 30degrees CCW to that of the hex crystal in MTex.
% REFERENCE: XisEast || to [1 0 -1 0]. YisSouth.
% CRYSTAL: a is 4oclock b is 12oclock. (both -2 1 1 0)
% Therefore, when
% specimen to reference parallelism is enforced (X||a*) the crystal is
% rotated 30 CCW. Or, for example, the (Y||b*) is enforced, the crystal is
% rotated 90deg CCW. This rotation needs to be carried through to all
% calculations such as the BOR of (135,90,325+30) or (135,90,325+90)

cs=crystalSymmetry('6/mmm', [2.954 2.954 4.729], 'X||a*', 'Y||b', 'Z||c',
'mineral', 'Ti-Hex');
ss=specimenSymmetry('triclinic');

rot1 = orientation(ori_1,cs,ss); %(G^alpha)(P^alpha)
rot2 = orientation(ori_2,cs,ss);
rot3 = orientation(ori_3,cs,ss);


s=symmetrise(rot1,cs,ss); %(S_j^alpha)(G^alpha)(P^alpha) ALL symmetry
s2=symmetrise(rot2,cs,ss);
s3=symmetrise(rot3,cs,ss);
s = s(s.i==0); %get rid of inverses
s2 = s2(s2.i==0);
s3 = s3(s3.i==0);


% If this does not work try using 325*degrees instead of 355
```

```matlab
% (see notes above)
d=rotation('Euler', 135*degree, 90*degree, 355*degree);

%select the correct variants (variants a,b,c according to Glavicic et al)
for i=1:2:5
    betaa(i)=s(i)*inv(d); %(B_li^beta) = (D^-1)*(S_l)^alpha * GP
    betaa2(i)=s2(i)*inv(d);          % = TGP
    betaa3(i)=s3(i)*inv(d);
end

%select the correct variants (variants f,d,e according to Glavicic et al)
for i=8:2:12
    betaa(i)=s(i)*inv(d); %Burgers orientation relationship
    betaa2(i)=s2(i)*inv(d); %(B_mi^beta) = (D^-1)*(S_m)^alpha * GP
    betaa3(i)=s3(i)*inv(d);
end

betaa=betaa.unique; %get rid of zero rows
betaa2=betaa2.unique;
betaa3=betaa3.unique;
betaa(1,:) = [];  %6 Beta rotations (rotation matrix) from single variant s
betaa2(1,:) = []; %6 Beta rotations from single variant s2
betaa3(1,:) = []; %6 Beta rotations from single variant s3
mis12 = zeros([6 6]);
mis13 = zeros([6 6]);
mis32 = zeros([6 6]);
cs=crystalSymmetry('m-3m', [3.192 3.192 3.192], 'mineral', 'Titanium
cubic');
ss=specimenSymmetry('triclinic');

%6x1 matrix 6 variants (6rows) each 3 Euler angles
ori = orientation(betaa(:), cs,ss);
ori2 = orientation(betaa2(:), cs,ss);
ori3 = orientation(betaa3(:), cs,ss);

beta_1=ori; %6 beta solutions orientations from a single alpha variant
beta_2=ori2; %CLASS orientation. Lowercase bold g - pg 55 Galvicic
beta_3=ori3;

%3 or 6 depending on variants chosen (a,b,c) or (a,b,c,d,e,f)
%trip point beta misorientation minimization routine
parfor i=1:6
    for j=1:6   %calc angle between beta solutions of trip grians
        mis12(i,j)=angle(beta_1(i),beta_2(j))/degree;
        mis13(i,j)=angle(beta_1(i),beta_3(j))/degree;
        mis32(i,j)=angle(beta_3(i),beta_2(j))/degree;
    end
end

% Find minimum angle between 3 solutions under given threshold
[x,y]=find(mis12==min(min(mis12)));
value=mis12(x(1),y(1));
if (value < threashold)
    beta1=beta_1(x(1));
```

```matlab
        [xx,yy]=find(mis13==min(mis13(x(1),:))); %find second min

    value2 =mis13(xx(1),yy(1));
    if (value2 < threashold)

        value3=mis32(yy(1),y(1));

        if (value3 < threashold)

            solution=beta1; %single solution found!!
        else
            solution=0;
            q=0;

        end
    else
        solution=0;
        q=0;

    end
else
    solution=0;
    q=0;


end
end % end of function calc_beta
%~~~~~~~~~~~~~~~~~~~~~~~~~~~~~~~~~~~~~~~~~~~~~~~~~~~~~~~~~~~~~~~~~~~~~~~
%% GENERATE SOLUTION variable ONCE RECONSTUCTION IS DONE

cs=crystalSymmetry('cubic','mineral','Titanium cubic');
ss=specimenSymmetry('triclinic');

% Reconstructed beta EBSD-class variable map
ebsd_b =loadEBSD_generic('ebsd_file1.txt', 'CS', cs, 'SS', ss,
'ColumnNames', {'Euler1', 'Euler2', 'Euler3', 'x','y'},'Bunge');
%~~~~~~~~~~~~~~~~~~~~~~~~~~~~~~~~~~~~~~~~~~~~~~~~~~~~~~~~~~~~~~~~~~~~~~~`

function [x] = variant_distribution(hoek, TPgrains_id,grains_a)

%ebsd_a is the alpha phase from which it was deduced.

d=rotation('Euler', 135*degree, 90*degree, 355*degree,'Bunge');

 % orientation reconstructed beta %HOEK variable in main_reconstrauction.m

    s=symmetrise(hoek); %hoek - beta orientation (C_all*S*B)
    s = s(s.i==0); %exclude inverse rotations (s.i==1)


    %12 variants according to Simonelli's thesis page 200
    % Orientation matrix - - Glavicic, M.G. et al (2003)
    var(1) = s(5)*d;
    var(2) = s(11)*d;
```

```matlab
    var(3)  = s(17)*d;
    var(4)  = s(23)*d;
    var(5)  = s(3)*d;
    var(6)  = s(9)*d;
    var(7)  = s(15)*d;
    var(8)  = s(21)*d;
    var(9)  = s(1)*d;
    var(10) =s(4)*d;
    var(11) =s(16)*d;
    var(12) =s(10)*d;

%hexagonal crystal symmetry
    cs=crystalSymmetry('6/mmm', [2.954 2.954 4.729], 'X||a*', 'Y||b',
'Z||c', 'mineral', 'Ti-Hex');
    ss=specimenSymmetry('triclinic');

for i=1:12
    or(i) = orientation(var(i), cs,ss);
end

for j=1:3
   for i=1:12
      misOrientat(i)=angle(or(i),grains_a(TPgrains_id(j)).meanOrientation.E
      uler)/degree;
   end
   st=find(misOrientat==min(min(misOrientat)));
   x(j)=st(1);
end
end


function [] = variantSub(sto,ebsd_a)

clear ebsd_1 ebsd_2 ebsd_3 T

% is this variant 1? Then store it.
if sto(4) == 1;
    ebsd = ebsd_a(ebsd_a.grainId==sto(1));
%export variants who's orientation is parent beta solution
    export(ebsd,'tempV.txt');
%read it (out.txt is a temporary file who's content changes with each loop)
    T = dlmread('tempV.txt','',1,0);
%Write variant to file
    dlmwrite('var1.txt',T,'-append','delimiter',' ');

% is this variant 2? Then store it, etc.
elseif sto(4) == 2;
    ebsd = ebsd_a(ebsd_a.grainId==sto(1));
    export(ebsd,'tempV.txt');
    T = dlmread('tempV.txt','',1,0);
    dlmwrite('var2.txt',T,'-append','delimiter',' ');
elseif sto(4) == 3;
    ebsd = ebsd_a(ebsd_a.grainId==sto(1));
    export(ebsd,'tempV.txt');
```

```matlab
    T = dlmread('tempV.txt','',1,0);
    dlmwrite('var3.txt',T,'-append','delimiter',' ');
elseif sto(4) == 4;
    ebsd = ebsd_a(ebsd_a.grainId==sto(1));
    export(ebsd,'tempV.txt');
    T = dlmread('tempV.txt','',1,0);
    dlmwrite('var4.txt',T,'-append','delimiter',' ');
elseif sto(4) == 5;
    ebsd = ebsd_a(ebsd_a.grainId==sto(1));
    export(ebsd,'tempV.txt');
    T = dlmread('tempV.txt','',1,0);
    dlmwrite('var5.txt',T,'-append','delimiter',' ');
elseif sto(4) == 6;
    ebsd = ebsd_a(ebsd_a.grainId==sto(1));
    export(ebsd,'tempV.txt');
    T = dlmread('tempV.txt','',1,0);
    dlmwrite('var6.txt',T,'-append','delimiter',' ');
elseif sto(4)== 7;
    ebsd = ebsd_a(ebsd_a.grainId==sto(1));
    export(ebsd,'tempV.txt');
    T = dlmread('tempV.txt','',1,0);
    dlmwrite('var7.txt',T,'-append','delimiter',' ');
elseif sto(4) == 8;
    ebsd = ebsd_a(ebsd_a.grainId==sto(1));
    export(ebsd,'tempV.txt');
    T = dlmread('tempV.txt','',1,0);
    dlmwrite('var8.txt',T,'-append','delimiter',' ');
elseif sto(4) == 9;
    ebsd = ebsd_a(ebsd_a.grainId==sto(1));
    export(ebsd,'tempV.txt');
    T = dlmread('tempV.txt','',1,0);
    dlmwrite('var9.txt',T,'-append','delimiter',' ');
elseif sto(4) == 10;
    ebsd = ebsd_a(ebsd_a.grainId==sto(1));
    export(ebsd,'tempV.txt');
    T = dlmread('tempV.txt','',1,0);
    dlmwrite('var10.txt',T,'-append','delimiter',' ');
elseif sto(4) == 11;
    ebsd = ebsd_a(ebsd_a.grainId==sto(1));
    export(ebsd,'tempV.txt');
    T = dlmread('tempV.txt','',1,0);
    dlmwrite('var11.txt',T,'-append','delimiter',' ');
elseif sto(4) == 12;
    ebsd = ebsd_a(ebsd_a.grainId==sto(1));
    export(ebsd,'tempV.txt');
    T = dlmread('tempV.txt','',1,0);
    dlmwrite('var12.txt',T,'-append','delimiter',' ');
end

%~~~~~~~~~~~~~~Second triple point
if sto(5) == 1;
    ebsd = ebsd_a(ebsd_a.grainId==sto(2));
    export(ebsd,'tempV.txt');
    T = dlmread('tempV.txt','',1,0);
    dlmwrite('var1.txt',T,'-append','delimiter',' ');
elseif sto(5) == 2;
```

```
    ebsd = ebsd_a(ebsd_a.grainId==sto(2));
    export(ebsd,'tempV.txt');
    T = dlmread('tempV.txt','',1,0);
    dlmwrite('var2.txt',T,'-append','delimiter',' ');
elseif sto(5) == 3;
    ebsd = ebsd_a(ebsd_a.grainId==sto(2));
    export(ebsd,'tempV.txt');
    T = dlmread('tempV.txt','',1,0);
    dlmwrite('var3.txt',T,'-append','delimiter',' ');
elseif sto(5) == 4;
    ebsd = ebsd_a(ebsd_a.grainId==sto(2));
    export(ebsd,'tempV.txt');
    T = dlmread('tempV.txt','',1,0);
    dlmwrite('var4.txt',T,'-append','delimiter',' ');
elseif sto(5) == 5;
    ebsd = ebsd_a(ebsd_a.grainId==sto(2));
    export(ebsd,'tempV.txt');
    T = dlmread('tempV.txt','',1,0);
    dlmwrite('var5.txt',T,'-append','delimiter',' ');
elseif sto(5) == 6;
    ebsd = ebsd_a(ebsd_a.grainId==sto(2));
    export(ebsd,'tempV.txt');
    T = dlmread('tempV.txt','',1,0);
    dlmwrite('var6.txt',T,'-append','delimiter',' ');
elseif sto(5)== 7;
    ebsd = ebsd_a(ebsd_a.grainId==sto(2));
    export(ebsd,'tempV.txt');
    T = dlmread('tempV.txt','',1,0);
    dlmwrite('var7.txt',T,'-append','delimiter',' ');
elseif sto(5) == 8;
    ebsd = ebsd_a(ebsd_a.grainId==sto(2));
    export(ebsd,'tempV.txt');
    T = dlmread('tempV.txt','',1,0);
    dlmwrite('var8.txt',T,'-append','delimiter',' ');
elseif sto(5) == 9;
    ebsd = ebsd_a(ebsd_a.grainId==sto(2));
    export(ebsd,'tempV.txt');
    T = dlmread('tempV.txt','',1,0);
    dlmwrite('var9.txt',T,'-append','delimiter',' ');
elseif sto(5) == 10;
    ebsd = ebsd_a(ebsd_a.grainId==sto(2));
    export(ebsd,'tempV.txt');
    T = dlmread('tempV.txt','',1,0);
    dlmwrite('var10.txt',T,'-append','delimiter',' ');
elseif sto(5) == 11;
    ebsd = ebsd_a(ebsd_a.grainId==sto(2));
    export(ebsd,'tempV.txt');
    T = dlmread('tempV.txt','',1,0);
    dlmwrite('var11.txt',T,'-append','delimiter',' ');
elseif sto(5) == 12;
    ebsd = ebsd_a(ebsd_a.grainId==sto(2));
    export(ebsd,'tempV.txt');
    T = dlmread('tempV.txt','',1,0);
    dlmwrite('var12.txt',T,'-append','delimiter',' ');
end
```

```matlab
%%~~~~~~~~~~~Third triple point
if sto(6) == 1;
    ebsd = ebsd_a(ebsd_a.grainId==sto(3));
    export(ebsd,'tempV.txt');
    T = dlmread('tempV.txt','',1,0);
    dlmwrite('var1.txt',T,'-append','delimiter',' ');
elseif sto(6) == 2;
    ebsd = ebsd_a(ebsd_a.grainId==sto(3));
    export(ebsd,'tempV.txt');
    T = dlmread('tempV.txt','',1,0);
    dlmwrite('var2.txt',T,'-append','delimiter',' ');
elseif sto(6) == 3;
    ebsd = ebsd_a(ebsd_a.grainId==sto(3));
    export(ebsd,'tempV.txt');
    T = dlmread('tempV.txt','',1,0);
    dlmwrite('var3.txt',T,'-append','delimiter',' ');
elseif sto(6) == 4;
    ebsd = ebsd_a(ebsd_a.grainId==sto(3));
    export(ebsd,'tempV.txt');
    T = dlmread('tempV.txt','',1,0);
    dlmwrite('var4.txt',T,'-append','delimiter',' ');
elseif sto(6) == 5;
    ebsd = ebsd_a(ebsd_a.grainId==sto(3));
    export(ebsd,'tempV.txt');
    T = dlmread('tempV.txt','',1,0);
    dlmwrite('var5.txt',T,'-append','delimiter',' ');
elseif sto(6) == 6;
    ebsd = ebsd_a(ebsd_a.grainId==sto(3));
    export(ebsd,'tempV.txt');
    T = dlmread('tempV.txt','',1,0);
    dlmwrite('var6.txt',T,'-append','delimiter',' ');
elseif sto(6)== 7;
    ebsd = ebsd_a(ebsd_a.grainId==sto(3));
    export(ebsd,'tempV.txt');
    T = dlmread('tempV.txt','',1,0);
    dlmwrite('var7.txt',T,'-append','delimiter',' ');
elseif sto(6) == 8;
    ebsd = ebsd_a(ebsd_a.grainId==sto(3));
    export(ebsd,'tempV.txt');
    T = dlmread('tempV.txt','',1,0);
    dlmwrite('var8.txt',T,'-append','delimiter',' ');
elseif sto(6) == 9;
    ebsd = ebsd_a(ebsd_a.grainId==sto(3));
    export(ebsd,'tempV.txt');
    T = dlmread('tempV.txt','',1,0);
    dlmwrite('var9.txt',T,'-append','delimiter',' ');
elseif sto(6) == 10;
    ebsd = ebsd_a(ebsd_a.grainId==sto(3));
    export(ebsd,'tempV.txt');
    T = dlmread('tempV.txt','',1,0);
    dlmwrite('var10.txt',T,'-append','delimiter',' ');
elseif sto(6) == 11;
    ebsd = ebsd_a(ebsd_a.grainId==sto(3));
    export(ebsd,'tempV.txt');
    T = dlmread('tempV.txt','',1,0);
    dlmwrite('var11.txt',T,'-append','delimiter',' ');
```

```
elseif sto(6) == 12;
    ebsd = ebsd_a(ebsd_a.grainId==sto(3));
    export(ebsd,'tempV.txt');
    T = dlmread('tempV.txt','',1,0);
    dlmwrite('var12.txt',T,'-append','delimiter',' ');

end
end
```